Revealing DNA's Secret Structures: Development of an i-Motif Specific Ruthenium-based Probe

A thesis submitted to the School of Pharmacy at the University of East Anglia for the degree of Doctor of Philosophy

Philip Spence

July 2020

Declaration

This thesis is submitted to the University of East Anglia for the Degree of Doctor of Philosophy and has not been previously submitted at this or any university assessment or for any other degree. Except where stated, and reference and acknowledgement are given, this work is original and has been carried out by the author alone.

Acknowledgements

There are many people to whom I owe a lot of gratitude for helping me along the journey of completing my PhD. Firstly, I'd like to thank my two supervisors, Dr. Zoë Waller and Dr. John Fielden for their encouragement and guidance throughout the process. I could not have asked for better supervisors. I'd also like to thank the past and present members of both the Waller and Fielden groups who are too numerous to name, but I'd especially like to thank Dr. Mahmoud Abdelhamid for the many conversations and for being a great sounding board, Dr. Kevin Vincent for all his help with crystallography and for the numerous ideas and interests shown in my research.

I'd also like to thank my parents, for without whom I would not exist. You have always encouraged me to ask big questions and be unsatisfied with the easy answers to them. Without this encouragement, I certainly would not have pursued a career in science.

I'd finally like to thank my wife, Emma, for all the love and support over the years and the many sacrifices you have made. David Hume once wrote "Let all the powers and elements of nature conspire to serve and obey one man, let the sun rise and set at his command: The sea and rivers roll as he pleases, and the earth furnish spontaneously whatever may be useful or agreeable to him. He will still be miserable, till you give him some one person at least, with whom he may share his happiness, and whose esteem and friendship he may enjoy."

Abstract

Chapter 1 is general introduction to DNA and the secondary structures that it forms, leading into an introduction to ruthenium-based polypyridyls and their application as secondary structure probes.

Chapter 2 discusses the DNA interactions of *mer-*, *trans,fac-*, and *cis,fac*-$[Ru(bqp)_2]^{2+}$. This explores the photophysical changes that occur upon DNA binding and the discovery that the *cis,fac-* isomer behaves as a light switch with DNA. It explores the specificity of this isomer and its two enantiomers (Δ and Λ) to i-motif DNA. This culminates in a hypothesis for the unique light switching mechanism caused by the steric and electronic interactions with DNA, rather than solvent exclusion.

Chapter 3 explores the synthesis of various bqp analogues. Here the discovery of a new synthetic route for the high yielding synthesis of *cis,fac*-$[Ru(bqp)_2]^{2+}$ that also enables the synthesis of heteroleptic bqp complexes, is also discussed, as well as the application of this synthetic route to the synthesis of facial bqp-containing complexes that incorporate metals other than ruthenium.

Chapter 4 discusses the results of a high-throughput screen using *in silico* and biophysical techniques with a library of 1584 molecules and an i-motif forming DNA sequence. The correlations between these three techniques is discussed as well as identification of the hits that are produced by each one.

Chapter 5 summarises Chapters 2, 3 and 4, and explores the future work that this project could take.

Chapter 6 describes the experimental procedures used in Chapters 2, 3 and 4.

Contents

List of Figures

List of Tables

List of Abbreviations

Å	Ångstrom
A	Adenine
bqp	2,6-bis(8′-quinolinyl)pyridine
C	Cytosine
CD	Circular dichroism
D_{TO}	Thiazole orange displacement
DCM	Dichloromethane
DMSO	Dimethyl sulphoxide
DNA	Deoxyribonucleic acid
dppz	dipyrido[3,2-a:2′,3′-c]phenazine
EtOH	Ethanol
FAM	6-Carboxyfluorescein
FID	Fluorescence intercalator displacement
FRET	Förster resonance energy transfer
G	Guanine
HPLC	High performance liquid chromatography
MeCN	Acetonitrile

MeOH	Methanol
NMR	Nuclear magnetic resonance
PEG	Polyethylene glycol
PDB	Protein data bank
T	Thymine
TAMRA	6-Carboxytetramethyl rhodamine
TFA	Trifluoroacetic acid
TO	Thiazole orange
$\boldsymbol{T_m}$	Melting temperature
UV	Ultraviolet

1. Introduction

1.1. DNA Structure

Since Watson and Crick proposed that DNA secondary structure is a double-helix with the bases on the inside, the phosphates on the outside, and stabilised by hydrogen bonds between nucleic acids, the investigation into DNA's secondary structure has not stopped.[1–4] Their discovery in 1953, along with evidence presented by Franklin and Wilkins,[5,6] confirmed, by the use of X-ray crystallographic techniques, the secondary structure of DNA for the first time. These three components are found in equimolar amounts with the phosphoric acid residue bound to the ribose sugar at the 5′position (Figure 1.1).[7]

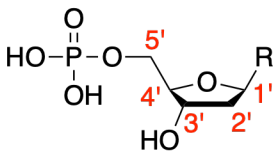

Figure 1.1: Structure of a 5′- DNA monomer displaying a phosphate group and sugar group where R is the heterocyclic base

Monocyclic pyrimidines and bicyclic purines form the bases present in nucleic acids. Pyrimidines consist of a 6-membered heterocycle with a nitrogen at the 1 and 3 position, whereas purines consist of both 5 and 6-membered rings containing a nitrogen at positions 1, 3, 7 and 9 (Figure 1.2).

The positions of the donor and acceptor groups within the bases leads to the complementarity of their Watson-Crick pairing. Cytosine (C) possesses two acceptors and one donor, while guanine (G) contains two donors and one acceptor. Similarly, adenine (A) contains one donor and one acceptor, while thymine (T) contains one donor and two acceptors. In 1950, Chargaff coined his famous rule after observing the molar contribution of C and G to be equivalent in a number of different DNA sequences, with the same obser-

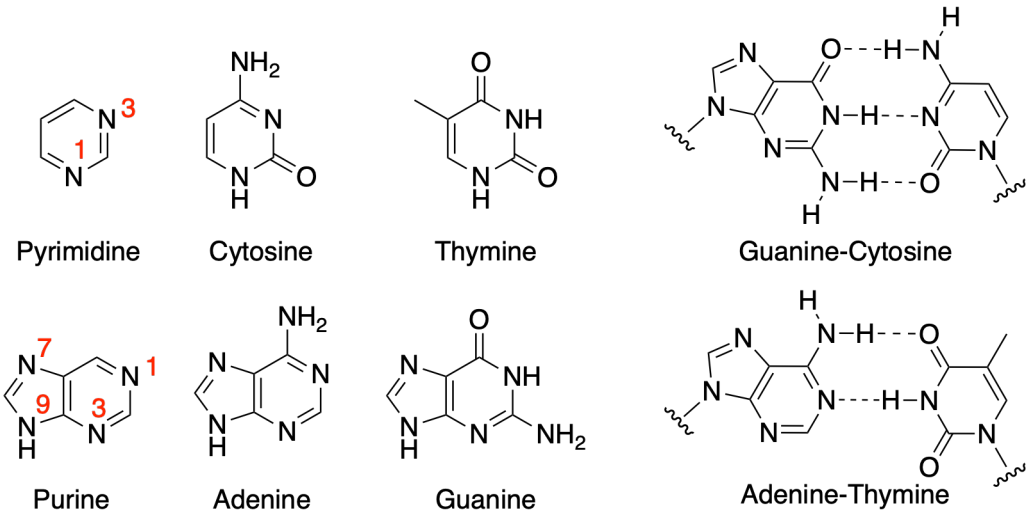

Figure 1.2: Pyrimidine and purine structures (left) with Watson-Crick base-pairing (right)

vation made for A and T (Figure 1.2).[8] This type of complementary pairing is found in B-form DNA, the secondary structure elucidated from the work of Watson, Crick, Franklin, and Wilkins.[1,5] The base pairs stack to give a twisted helical structure, with each turn containing just over 10 base pairs, with 3.4 Å between each pair (see Table 1.1).[1] B-form DNA contains two grooves, one major and one minor. The major groove is much wider (11.7 Å) than the minor groove (5.7 Å) (Figure 1.3).

Table 1.1: The structural properties of A-, B-, Z-, G-quadruplex and i-motif DNA secondary structures

	A-DNA	B-DNA	Z-DNA	G-quadruplex	i-Motif
Handedness	Right	Right	Left	N/A	Right
Helical Twist (°)	33	36	-30	N/A	17
Base pair distance (Å)	2.6	3.4	3.7	3.1	3.1 (6.2)
Length per turn (Å)	28.6	34.0	44.4	N/A	N/A
Major groove width (Å)	2.7	11.7	8.8	N/A	15.2 - 16.0
Minor groove width (Å)	11.0	5.7	2.0	N/A	3.1

This type of pairing, however, is also found in other forms of DNA. The A-form of DNA (Figure 1.3), normally formed in low water conditions,[9] is composed of a more condensed helix than B-form. This can be seen when comparing the length per turn of the helix (28.6 Å) compared with B-form (34 Å). One of the more unusual DNA structures is the Z-form (Figure 1.3). In this secondary structure, the DNA has a left-handed helical twist, rather than the right-handed twist seen in A- or B-form DNA. Z-form DNA also has a far narrower (8.8 Å) major groove compared with B-form DNA whilst having a greater distance between bases (3.7 Å).

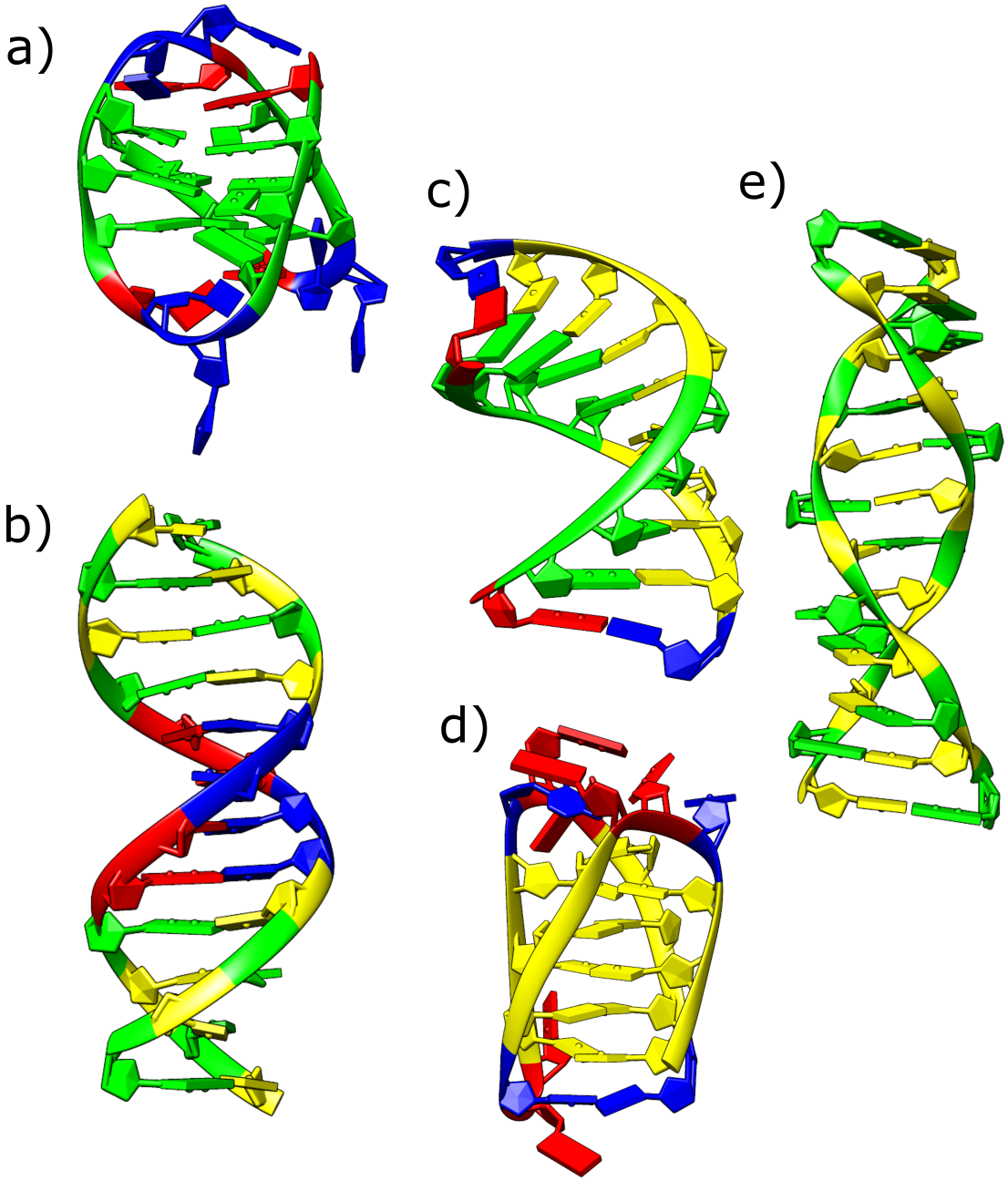

Figure 1.3: Various secondary structures of DNA: a) G-quadruplex (PDB: 143D), b) B-form duplex (PDB: 1BNA), c) A-form duplex (PDB: 440D), d) i-Motif (PDB: 1ELN), and e) Z-form duplex (PDB: 4OCB)

1.1.1 Quadruplex DNA

Following the discovery that guanine bases can form a G-tetrad via Hoogsteen pairing,[10,11] Gilbert and Sen in 1988 presented evidence for a secondary structure now commonly referred to as a G-quadruplex (G4) (Figure 1.4 and Figure 1.3).[12] Composed of stacking guanine quartets, these structures are stabilised by coordination of metal cations, π-stacking between quartets (at least two quartets must be present) and hydrogen bonding within each quartet.[13] Due to the vast array of different topologies that G4 structures can acquire, it is hard to give definitive measurements such as groove widths or degrees of helical twist.[14] Depending upon the orientation of the DNA strands, G4 structures can adopt parallel, antiparallel or hybrid-type structures. The of size the loops and the metal cation present are two factors that can affect the topology of the G4 structure.[2]

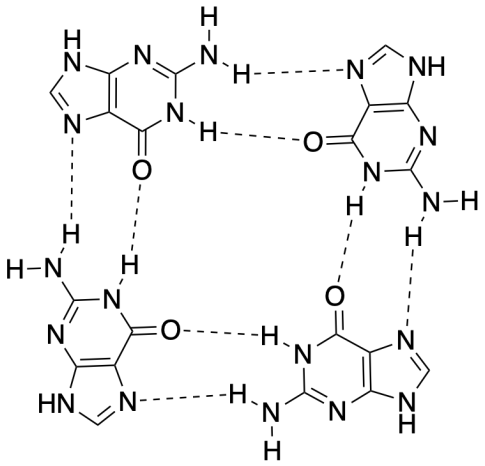

Figure 1.4: Hydrogen bonding between four guanine bases

Many species contain, within their genetic material, a tandem repeat of G_3TTA, although the exact sequence varies between and within each species.[15] These G-rich sequences were discovered to exist at the end of eukaryotic telomeric DNA and the associated G4s were shown to be stable in physiological conditions.[16] Since then, these sequences have been shown to be ubiquitous throughout the human genome, not just in the telomeric region.[17,18]

In 2013, Biffi *et al*. identified a G-quadruplex binding antibody from a phage display library of 2.3×10^{10} different single-chain antibody clones, yielding an antibody named BG4 as the best hit.[19] It was shown that BG4 had a high affinity for G-quadruplex (K_d = 0.5-1.6

nM) with no detectable binding to RNA hairpin, single-stranded or double-stranded DNA forming sequences *in vitro*. The fluorescently-tagged antibody was incubated in human cells and showed distinct foci in the nucleus of the cells, suggestive of G-quadruplex formation. Moreover, a loss of foci was displayed when treated with either DNase or pre-incubation with folded G-quadruplex oligonucleotides, but not when treated with RNase, confirming that it does not bind RNA G-quadruplexes. Treatment of the cells with a G4 stabilising agent, pyridostatin (Figure 1.5), led to a *ca* 2.9-fold increase in nuclear staining, which, again, disappeared with DNase treatment, showing that this compound is able to promote G4 formation *in cellulo*. The limitation to this study is the use of fixed cells, rather than live cells as the environment in which the G4s formed, while this is useful for the study of G4 formation over the various lifetimes of the cell, but is a limitation to the visualisation of G4 in living, unadulterated cells.

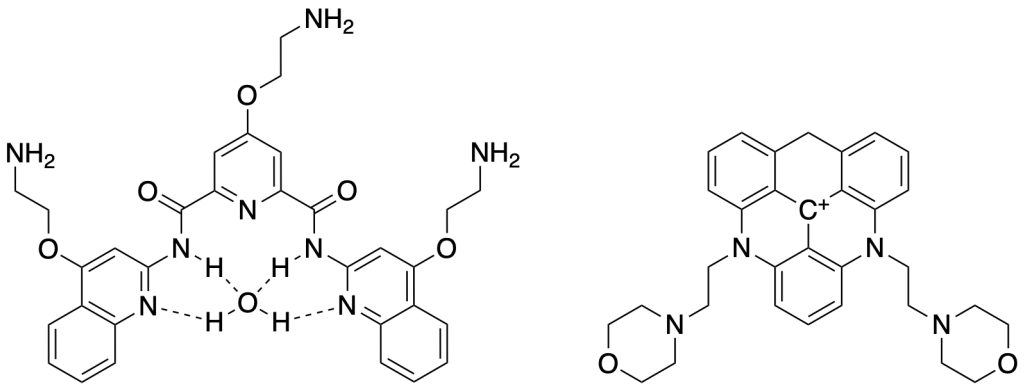

Figure 1.5: Structures of pyridostatin (left) and DAOTA-M2 (right)

This is not the only time that G-quadruplexes have been visualised in cells, work by Shivalingam *et al.*, using the triangulenium DAOTA-M2, was able to visualise G4s using fluorescence lifetime imaging microscopy (Figure 1.5).[20] While the fluorescence intensity enhancements with various DNA secondary structures were not disparate enough to be used to identify G4 (G4 = 3.3-4.9, ssDNA/dsDNA = 2.0-2.8-fold enhancements), using the relationship between the lifetime (τ) and the amplitude (α) of the fluorescence decay components allowed for sufficient discrimination. The longer, second decay component of DAOTA-M2 when in the presence of DNA, varies from 6-16 ns depending upon the nucleic acid topology. Using Eq. 1.1 to fit the fluorescence decay and taking the values of each α and τ, the nucleic acid topologies were able to be identified by the relationship of

τ_2/α_2.

$$I(t) = I_O((1 - \alpha_1 - \alpha_2)e^{-t/\tau_1} + \alpha_1 e^{-t/\tau_2} + \alpha_2 e^{-t/\tau_3}) \tag{1.1}$$

where:

$\alpha =$ the amplitude of each component (normalised to 1)

$\tau =$ the lifetime of each component

$I =$ the intensity of light

$t =$ the timestep

Similar to the work carried out by Biffi *et al.*, the addition of pyridostatin to the cell lead to a decrease in τ_2/α_2, suggestive of the displacement of DAOTA-M2 from G4. This work offers the advantage of visualising G4s in live cells using a cell-permeable small molecule, rather than using an antibody to visualise G4s in fixed cells, and opens the door to further development of small molecules as *in vivo* DNA secondary structure probes.

Gehring *et al.* in 1993 discovered another quadruplex-type secondary structure of DNA.[21] Using the DNA oligomer 5′-d(TCCCCC), it was shown that the single-stranded DNA forms a four-stranded complex stabilised by the intercalating hemiprotonated C-C$^+$ base pairs, now known as an i-motif (Figure 1.6 and Figure 1.3). This structure has been shown to contain a right-handed helical twist with two major and two minor grooves.[22]. Due to the complementarity between G and C, wherever a sequence can form a G-quadruplex, there is the possibility of the complementary strand forming an i-motif.[23]

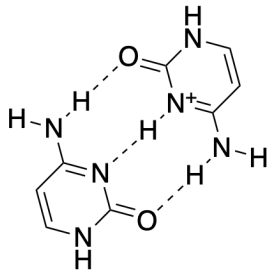

Figure 1.6: Hydrogen bonding between a hemi-protonated cytosine-cytosine$^+$ base pair

The requirement for one cytosine base to be protonated gives the i-motif a dependence upon the pH of its environment.[24] It is at the N3 position that protonation takes place, enabling the C-C^+ pairing. The pK_a at this position is 4.6 for cytosine, and is lower for deoxycytidine (4.25) due to the inductive effect of the sugar.[7] Changing the position of the phosphate residue on the ribose sugar (5′- and 3′-) can have an effect upon the pK_a of the N3 nitrogen; the 3′- position decreases the pK_a (4.16) in comparison to deoxycytidine but the 5′ position increases the pK_a (4.5).[25] When the pH of the environment around the DNA is approximately the same as the pK_a of the N3 nitrogen, half the cytosine bases are protonated, an ideal environment for i-motif formation. When pH $>>$ pK_a too few cytosines are protonated, and at pH $<<$ pK_a too many cytosines are protonated, with both environments leading to a destabilisation of the i-motif structure.[26] Therefore, any effect that will increase the p$K_a$of the N3 nitrogen, may lead to i-motif formation at a less acidic pH.

Cellular environments are crowded by proteins, nucleic acids and complex sugars; whose volume can be up to 40% of the total cellular volume.[27] To elucidate the biological relevance of i-motif DNA, Rajendran *et al.* investigated the affect of molecular crowding upon CCT repeats capable of forming an i-motif structure.[28] Additions of common crowding agents[29] polyethylene glycol (PEG) 200 or 8000 to [5′-CCG$(CCT)_8$CGG-3′] led to the transitional pH, the pH at which 50% of the structure is folded (pH_T), increasing from 6.6 to 7.1 and 7.4, respectively. Similar work has shown that addition of PEG 300 to [5′-TTCCCTACCCTCCCCACCCTAA-3′] increases the pH_T from 6.1 to 7.0.[30] An increase from 0% to 30% w/w of PEG 8000 to the c-MYC promoter sequence was also shown to increase its pH_T from 6.0 to 6.7.[31] It is clear, from these studies, that molecular crowding can affect the pH stability of i-motif DNA, increasing the N3 pK_a.

The loops of the i-motif structure also play an important role on the pH stability of the secondary structure.[32] Gurung *et al.* in 2015, studied the pH stability of the i-motif forming sequence, d$(CCCT_n)_3$CCCT.[33] Moving from a loop length of n = 3 to n = 8, decreases the pH stability, with the pH_T changing from 6.6 to 5.4. Reilly *et al.* corroborated this data using d(CCCTCCCT_nCCCTCCC), where moving from n = 3 to n = 20 led to a decrease in pH stability from 6.66 to 5.98.[34]

It is not just crowding effects or loop length that can influence the pK_a of the cytosines

within an i-motif, the changes in thermal stability brought about by modifying the tract length of i-motif forming sequences have also been investigated. Using sequences of $(C_nT_3)_3C_n$, where n = 2, 3, 4, 5, Mergny *et al*. showed that an increase in the melting temperature (T_m) from 27°C to 59.5°C occurred when increasing n from 2 to 5.[26] By keeping the loops of each sequence the same, this work showed a dependence of thermal stability upon the tract length, but did not sufficiently investigate the effect of tract length upon the pH stability. Wright *et al*. in 2017, did investigate this property using a similar range of sequences, where n varied 1 to 10.[35] However, the sequence where n = 1 did not form an i-motif structure and where n = 10 showed a two-stage melting profile, indicating the presence of two different structures. The pH_T of each sequence was studied and they were shown to range from 6.1 (n = 2) to 7.3 (n = 10), with the highest pH_T being 7.4, where n = 7. Armed with this knowledge, identification of potential genomic i-motif forming sequences that could be stable at physiological pH was carried out. The i-motif identification rule, $C_5(N_{1\text{-}19}C_5)_3$ with N being any base, was fed into a software package designed to find specific DNA sequences in a genome (Quadparser).[17] This yielded 5125 sequences when searching the human genome, which was cut down to 637 by selecting those that overlap with gene promoters. After further selection, 33 were chosen for biophysical characterisation. Of these 33, 17 were shown to have a p$H_T \geq 7.0$, and 12 were shown to have a $T_m \geq 20$°C. This offered a strong evidence for the potential formation of i-motif DNA under physiological conditions, that could lead to the possibility of *in vivo* i-motif formation.

Using in-cell NMR spectroscopy and the transfection of i-motif forming sequences into cells, Dzatko *et al*. showed the first evidence of i-motif stability *in cellulo*.[36] i-Motif DNA shows distinct NMR characteristics with the protonated N3 imino peaks of cytosine appearing at 15-16 ppm.[23] Four sequences from gene promoter regions (DAP, HIF-1α, PDGF-A and JAZF1) were used due to their *in vitro* stability in near-physiological conditions. Appearance of the imino proton peaks between 15 and 16 ppm in cells, showed that i-motif sequences are stable in cellular conditions, with DAP, PDGF-A and JAZF1 all persisting at 35°C. At 40°C only JAZF1 had a detectable i-motif signal, and the intensity of the i-motif signals were restored in all sequences when cooling back down to 20°C, suggesting that i-motif formation is not only possible *in cellulo* but also reversible.

The major breakthrough in this field was in 2018 when Zeraati *et al*. reported that an antibody had been used to visualise i-motif DNA in human cells.[37] Using the Garvan-2 human single-chain variable fragment library, an antibody named iMab was identified as a specific binder to the human telomeric i-motif. No binding was observed to a mutated human telomeric sequence that is incapable of forming an i-motif, or to dsDNA, G4s, hairpin DNA or proteins such as streptavidin or neutravidin. Interestingly, the authors note that the G4 specific antibody (BG4) competes with iMab for binding to several i-motif forming sequences, casting doubt on its specificity to G4. Not only does this work provide evidence for the formation of genomic i-motif DNA but also shows a pH dependency upon its formation. Incubating cells in 2%, 5% and 8% CO_2 altered the pH of the cell with an inverse relationship,[38] and at lower pH levels, an increase in iMab foci was observed, showing the pH dependence of i-motif formation *in vivo*. Similarly to the G4 antibody, this work required the fixing and permeabilisation of the cells. This, together with the in-cell NMR publication, suggests very strongly that i-motif DNA exists in living human cells.

Whilst antibodies that specifically bind to certain secondary structures are incredibly useful tools to study the formation of said structures *in cellulo*, development of membrane permeable small molecule probes will have a number of advantages. The antibodies discussed above both require the cells to be fixed and the membranes to become permeabilised, with the procedures involved in achieving this possibly causing changes to the cellular ultrastructure.[39] The development of cell-permeable, small-molecule probes could allow for the imaging of live cells, and therefore a more accurate reflection of the nature of the DNA secondary structure.

1.2. Ruthenium Polypyridyl Complexes as DNA Probes

Ruthenium polypyridyl complexes are a potential class of small molecules that could be used as *in vivo* probes due to their intense metal-to-ligand charge transfer bands in the visible region,[40] good cellular uptake,[41] and long excited state lifetimes.[42] The photophysical properties of ruthenium polypyridyl complexes can be explained through a promotion of an electron upon absorption of a photon from the *d* metal orbital on the ruthenium to a π^* ligand orbital, giving rise to a metal-to-ligand charge transfer (MLCT)

excited state. Promotion to a σ^* orbital affords a metal centred (MC) excited state.[43] Excitation from the ground state to the ^{1}MLCT state goes through intersystem crossing to form the radiative ^{3}MLCT excited state which can then undergo internal conversion to the ^{3}MC excited state which is short-lived and non-emissive (Figure 1.7).[44,45]

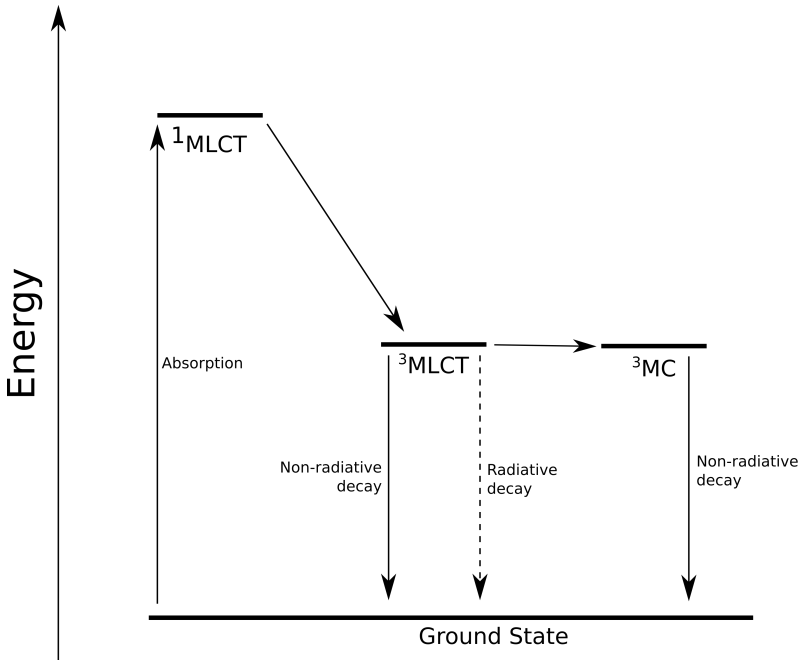

Figure 1.7: Jablonski diagram for typical ruthenium(II)-polypyridyl complexes

Emission of light can occur from either a singlet or triplet excited state.[46] In a singlet excited state, the spin of excited electron does not change from its previous state in the ground state, allowing for fast ($<10^{-9}$ s) radiative decay back to the ground state. Alternatively, this electron could also undergo intersystem crossing to a triplet excited state where a "flip" in the spin of the electron occurs, making its transition back to the ground state "forbidden". The decay from this state, due to its "forbidden" nature, typically occurs on a much longer timescale, up to minutes or even hours but for ruthenium polypyridyl ^{3}MLCT transitions are typically hundreds of nanoseconds to milliseconds.[47]

One of the earliest ruthenium(II) polypyridyl complexes to be studied for its DNA binding properties was $[Ru(phen)_3]^{2+}$ (Figure 1.8, phen = 1,10-phenanthroline).[48] Via recrystallisation with antimony D-tartrate, the two enantiomers, Δ- and Λ-$[Ru(phen)_3]^{2+}$ were isolated. A larger increase in emission intensity was observed for the Δ isomer with calf-thymus DNA, but interestingly, both complexes exhibited the same emission lifetimes even in the presence and absence of DNA as each other, indicating that both bound the

DNA in a similar fashion but that a higher proportion of Δ isomer was bound compared with the Λ isomer. Both enantiomers were believed to bind DNA via intercalation.

In 1984, Barton *et al*. modified the phenanthroline ligand to form $[Ru(DIP)_3]^2$ (DIP = 4,7-diphenyl-1,10-phenanthroline, Figure 1.10).[49] This modification permitted for a greater stereoselective binding of the Λ and Δ isomers of $[Ru(DIP)_3]^{2+}$, compared with the equivalent isomers of $[Ru(phen)_3]^2$.[48] Whilst the Δ enantiomer of $[Ru(DIP)_3]^{2+}$ could, in fact, bind both B-form and Z-form DNA, the Λ enantiomer was unable to bind B-form, a marked improvement in selectivity over the enantiomers of $[Ru(phen)_3]^{2+}$. The binding of the Δ enantiomer to Z-form was attributed to the much wider character of the major groove, eliminating the steric discrimination of the additional phenyl group on the phenanthroline ligands. This was a very early example of secondary structure discrimination by a ruthenium polypyridyl complex.

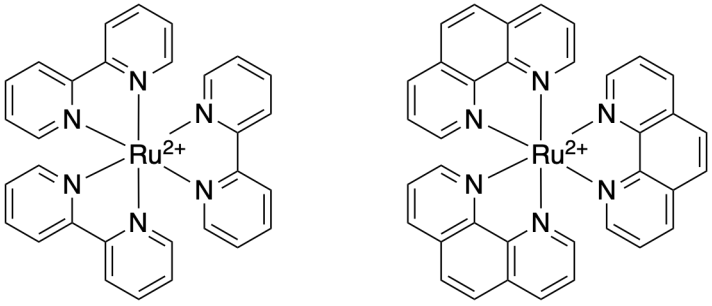

Figure 1.8: Structures of $[Ru(bpy)_3]^{2+}$ (left) and $[Ru(phen)_3]^{2+}$ (right)

In 1990, Barton *et al*. reported the interaction of $[Ru(bpy)_2(dppz)]^{2+}$ (dppz = dipyrido[3,2-a:2′,3′-c]phenazine) as a "molecular light switch" for DNA (Figure 1.9). Non-emissive in aqueous buffer but with a large increase in emission intensity upon intercalation into DNA, this probe rapidly became the focus of Ru-based DNA light switching compounds.[50,51] $[Ru(bpy)_2(dppz)]^{2+}$ possesses two distinct excited states, one emissive and one non-emissive. In an aqueous environment, hydrogen bonding between water and the phenazine nitrogens causes the lowering in energy of the non-emissive state, allowing for its population and subsequent nonradiative decay. Upon intercalation into DNA, and thus protection from water, the complex has similar photophysical properties to when it is in organic media; the emissive state is active and a large increase in quantum yield is observed.[52] Poynton *et al*. proposed, using data from transient infrared red spectroscopy,

that the electron in both the bright and dark state of $[Ru(L)_2(dppz)]^{2+}$ is localised on the dppz ligand, with the characteristic bands for the dark state overlapping with the vibrational states of two D_2O molecules, and therefore the bulk solvent system, when these are hydrogen-bonded to the azanitrogens of the dppz ligand.[53]

By modifying the ancillary ligands of $[Ru(L)_2(dppz)]^{2+}$ to form $[Ru(tpm)(py)(dppz)]^{2+}$ (tmp = tris-(1-pyrazolyl)methane, py = pyridine, Figure 1.10), Metcalfe *et al.* demonstrated that dppz complex derivatives can bind with a higher preference to high GC containing DNA sequences over TA containing sequences.[54] Using poly(dA).poly(dT) and poly(dG).poly(dC) sequences and isothermal titration calorimetry (ITC), $[Ru(tpm)(py)(dppz)]^{2+}$ was shown to have an intrinsic binding constant of 6.3×10^6 M^{-1} with the AT only sequence and 3.0×10^7 M^{-1} with the GC only sequence, a factor of ten greater binding strength for AT sequences.

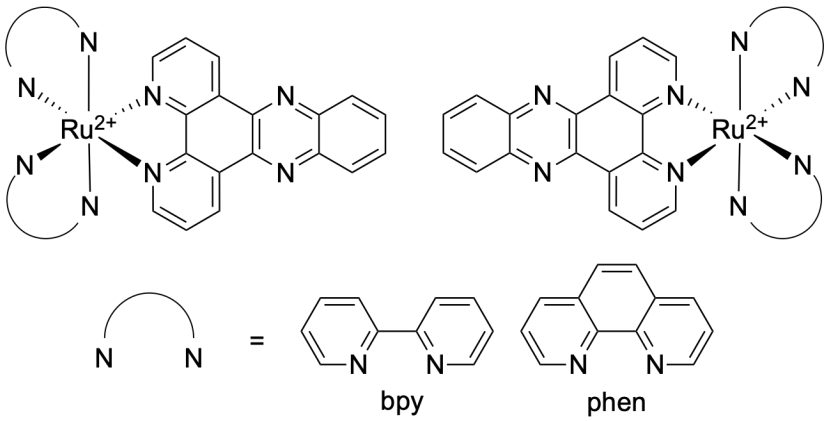

Figure 1.9: Structures of Λ-$[Ru(L)_2(dppz)]^{2+}$ (left) and Δ-$[Ru(L)_2(dppz)]^{2+}$ (right) where L = bpy or phen

Another example of DNA secondary structure discrimination was in the development of $[Ru(Me_4phen)_2(dppz)]^{2+}$, that is able to serve as a "light switch" with single base mismatched DNA (Figure 1.10).[55] Using a 27-mer B-form DNA sequence, one containing a GC match and the other containing a CC mismatch, $[Ru(Me_4phen)_2(dppz)]^{2+}$ showed far greater binding strength to the mismatched (1.8×10^6 M^{-1}) over the well-matched (6.8×10^4 M^{-1}) DNA, as well as a far greater emission intensity enhancement, and a longer emission lifetime. The added steric bulk of the methyl substituted phenanthroline ancillary ligand seemingly acts to discourage intercalation into well-matched DNA but allows for it in mismatched DNA. This has a wider impact on the identification of mismatched DNA, commonly implicated in many forms of cancer.[56,57]

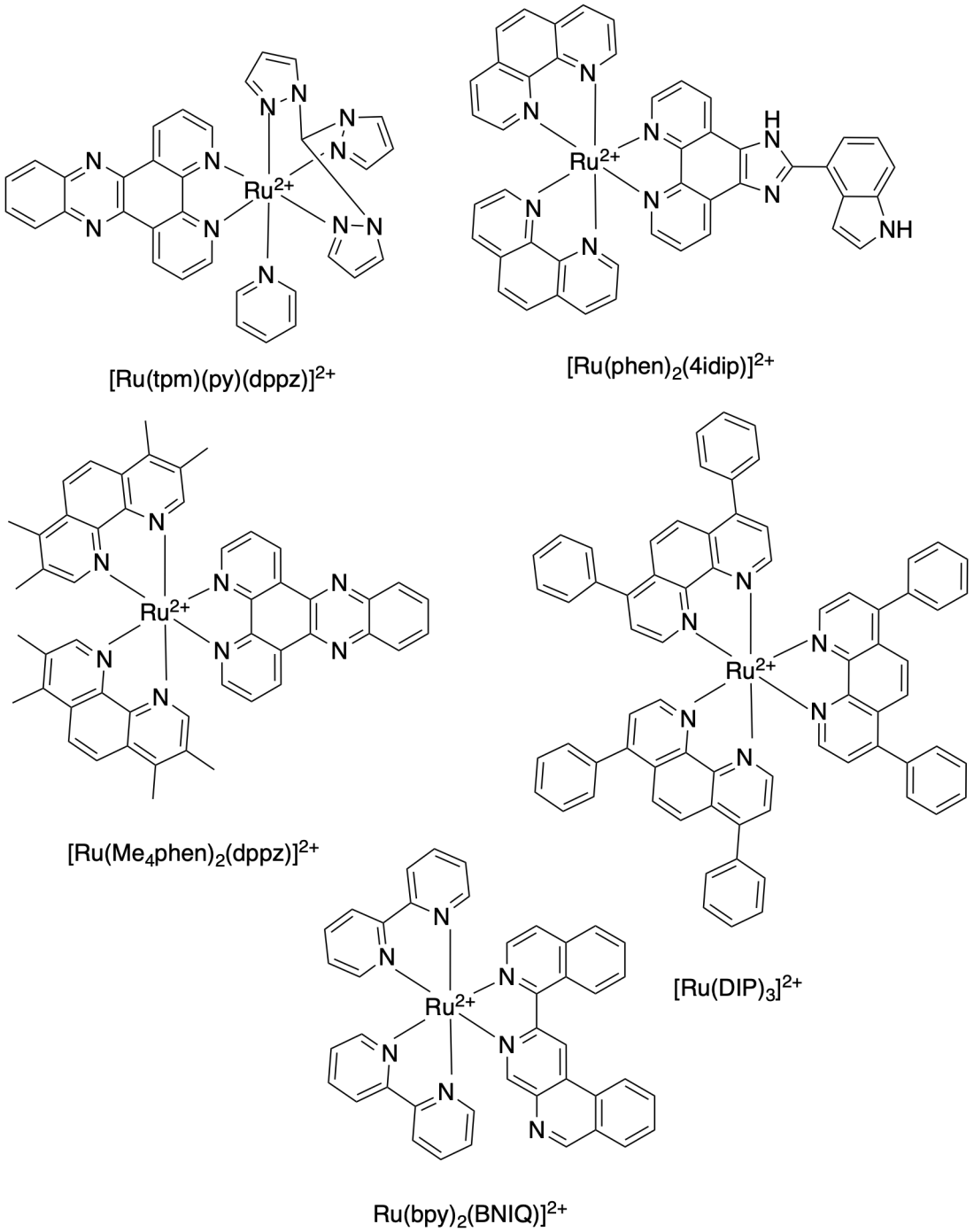

Figure 1.10: Ruthenium complexes that have been used to identify mismatched and Z-form DNA

The same group later published an improvement upon this work with the rational design of $[Ru(bpy)_2(BNIQ)]^{2+}$.[58] This time, instead of a modification to the ancillary ligand, a modification of the intercalating ligand yields a *ca* 500-fold increase in binding affinity for mismatched DNA (3.5×10^6 M^{-1}) over well-matched DNA (7.3×10^3 M^{-1}). The greater steric bulk of the intercalating ligands, much like the increased bulk seen previously in the ancillary ligands, works to prevent intercalation into well-matched DNA but allows for intercalation into mismatched DNA. This serves as another example of Ru-based complexes being used as DNA secondary structure probes.

1.2.1 Ruthenium Complexes as Quadruplex Probes

Many ruthenium polypyridyl complexes have been synthesised with the aim of specifically targeting the G-quadruplex DNA structure (Figure 1.11). In 2006, Rajput *et al*. demonstrated the use of two dinuclear ruthenium-based polypyridyl complexes that could distinguish G4 DNA from B-form DNA using their emission lifetime profiles.[59] Both complexes feature the tetrapyrido[3,2-*a*:2′,3′-*c*:3′′,2′′-*h*:2′′′,3′′′-*j*]phenazine (tppz) ligand, with the first containing two phenanthroline ancillary ligands and the second with bipyridine ancillary ligands (Figure 1.11). The two complexes display a *ca* 2.5 times increase in emission intensity when bound to G4 over duplex DNA, as well as a significant blue shift in emission wavelength. Both complexes display *ca* 30 ns to 40 ns longer lifetime with G4 than with B-form (84 and 92 ns vs 129 and 123 ns, respectively). This is a significant finding, allowing for G4 DNA to be identified using the concentration independent emission lifetime over emission intensity.

In 2012, Shi *et al*. reported the synthesis and DNA interactions of $[Ru(bpy)_2(dppzi)]^{2+}$ with the both anti-parallel and mixed parallel/anti-parallel G-quadruplexes from the human telomeric region (hTeloG).[60] The K_bs displayed were determined to be 9.5×10^5 M^{-1} and 5.1×10^5 M^{-1}, respectively, and are comparable to, but lower than, the initial binding strength of $[Ru(bpy)_2(dppz)]^{2+}$ with B-form DNA ($> 10^6$ M^{-1}). Interestingly, the emission increase upon binding to G4 DNA was switched "off" with additions of $[Fe(CN)_6]^{4-}$, a known quencher, and switched back "on" with addition of more G4 DNA. This is indicative of relatively weak protection from the anionic quencher by the G4 structure, suggestive of an end stacking binding mode, rather than the intercalative mode

observed between dppz complexes and B-form DNA.

Shi *et al.*, reported a dinuclear Ru-based complex containing the obip ligand (2-(2-pyridyl)imidazo[4,5-f][1,10]-phenanthroline) complex, $[Ru_2(obip)(bpy)_4]^{4+}$ (Figure 1.11).[61] Additions of $[Ru_2(obip)(bpy)_4]^{4+}$ to unfolded G4 forming sequences led to the formation of antiparallel G4 and, when in excess, a mixture of parallel/antiparallel G4. This induced formation of G-quadruplex DNA, whilst interesting *in vitro*, would be disadvantageous when trying to detect the natural formation of G4 *in vivo*, as G4 formation will be detected but whether the structure occurs naturally or is induced would be unknown.

The monodentate imidazole containing complexes, $[Ru(L)_2(4\,idip)]^{2+}$ (4idip = 4-indoleimidazo[4,5-f][1,10]phenanthroline, L = bpy or phen, Figure 1.11), have also been shown to induce G4 formation.[62] The binding constants for hTeloG were in the range of 10^6 M^{-1}, while both complexes were emissive with or without DNA, the emission intensity of both increased upon addition of either G4 or B-form DNA, with binding to hTeloG giving the highest intensity. Whilst the authors claim that both complexes bind G4 preferentially over B-form, no binding constants are given for the interaction with B-form DNA and the emission intensity differences would not be strong enough for use *in vivo*. The authors also claim that both complexes inhibit telomerase activity in $HepG_2$ cells at > 10 μM, but no cytotoxicity data was provided so the complexes could in fact be causing cell death, rather than telomerase inhibition.

Porphyrins have been long identified to interact with G4 DNA.[63] As such, the incorporation of a porphyrin moiety into a Ru-complex presented an intriguing development in the search for a G4 interacting probe. Mei *et al.* reported the synthesis and G4 interaction of such a compound, $[Ru(phen)_2(MPyTPP)Cl]^+$, in 2008 (Figure 1.11).[64] With a high binding constant (3.02×10^6 M^{-1}) to hTeloG, the complex showed perturbations of the G4 CD signal, indicating a high disruption of the G4 structure. Other moieties have been tagged onto octahedral Ru-based complexes in order to improve their G4 selectivity, including oligoarginine peptides.[65] Four complexes were compared, two with the oligoarginine, one with a single dppz ligand and one with two dppz ligands ($[Ru(dppz)]-R_8$ and $[Ru(dppz)_2]-R_8$) and two without the oligoarginine moiety ([Ru(dppz)] and $[Ru(dppz)_2]$) (Figure 1.12). All complexes except for $[Ru(dppz)_2]-R_8$ displayed a higher binding affinity for telomeric G4 over other G-quadruplex forming sequences found within the promoter

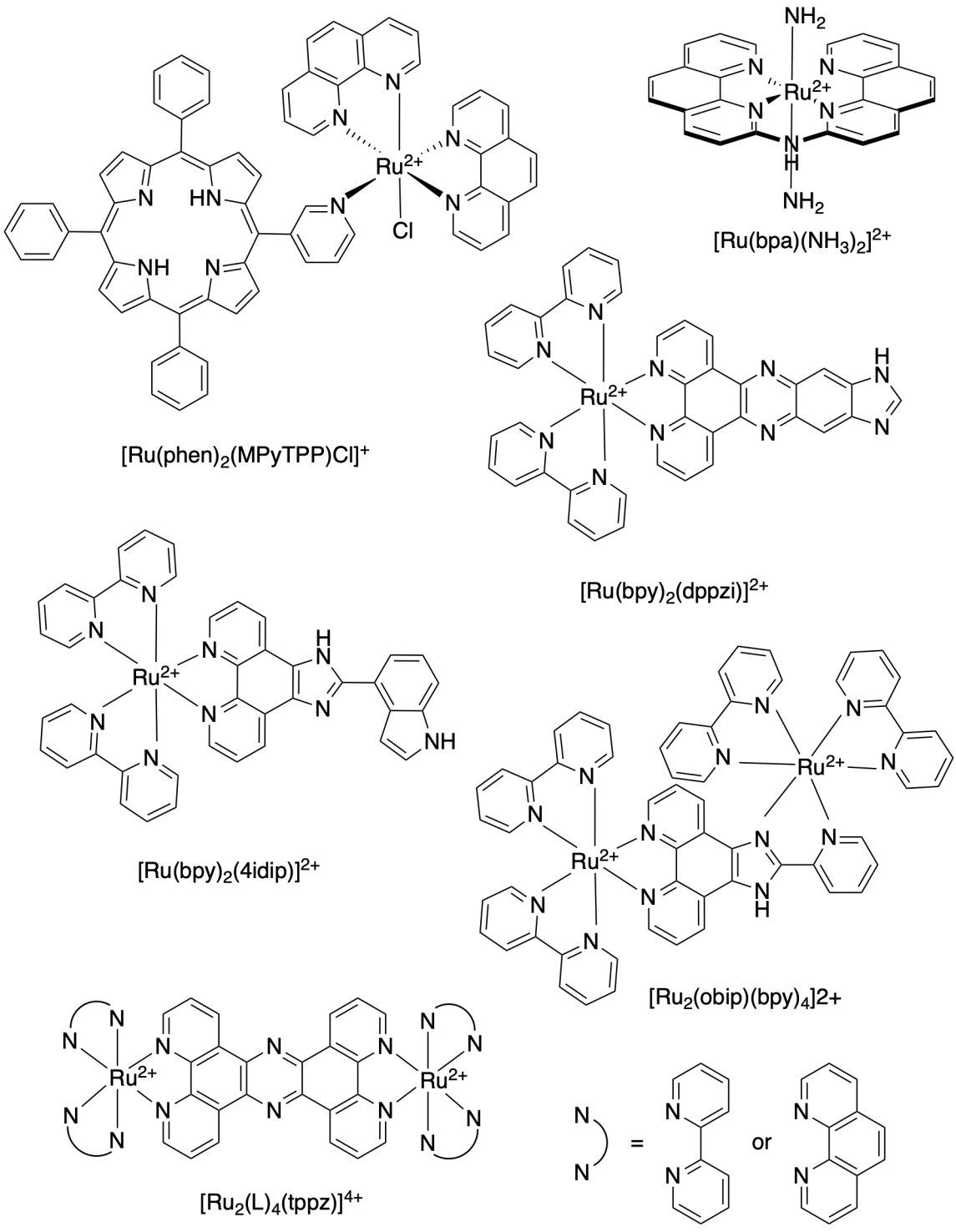

Figure 1.11: Ruthenium based complexes that have been used to target G-quadruplex DNA

regions of c-KIT and c-MYC. AutoDock results suggest that the dppz ligand interacts with the G4 structure via end-stacking or intercalation into the G-tetrads, while the oligoarginine moiety interacts with the backbone of the DNA, aiding stabilisation. *In vivo* studies show that incorporation of the oligoarginine moiety led to internalisation and eventual cell death, complexes lacking this moiety showed no such activity. This study offers a unique, tandem approach for the interaction of Ru-complexes with the G4 secondary structure.

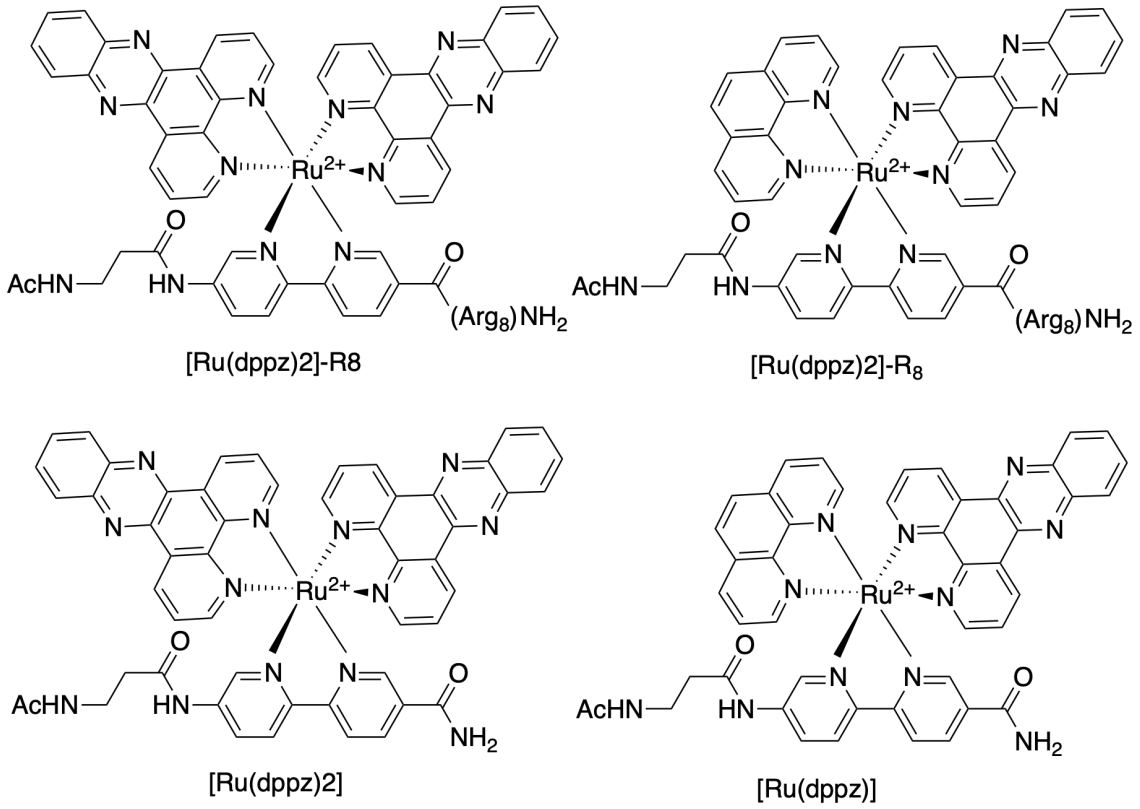

Figure 1.12: Structure of ruthenium-based complexes that target G4 DNA and contain metallopeptides

Another unique approach was the development of $[Ru(bpa)(L)_2]$ (bpa = *N*,*N*-bis-(1,10-phenantholin-2-yl)-amine, L = NH_3, DMSO, or NH_2CH_3) (Figure 1.11).[66] The planar aromatic bpa ligand sits across the x, y-axis of the complex with the two monodentate ligands in the z-axis. This yielded binding constants of *ca* $10^5\,\mathrm{M}^{-1}$ with various G4 structures and large ($> 20°C$) changes in the melting temperature of the DNA with telomeric sequences, at 1:1 DNA:Ru ratios. This unique structure allowed for stacking on top of the G-tetrads, with the ammonia containing complex having the most suitable interactions with G4 whilst blocking the ability to significantly intercalate into B-form DNA.

Published across two separate papers, Shi *et al.* reported on the interaction of both $[Ru(phen)_2(dppz)]^{2+}$ and $[Ru(bpy)_2(dppz)]^{2+}$ with i-motif and G-quadruplex DNA.[67,68] Using the telomeric G-quadruplex forming sequence 5′-AGGGTTAGGGTTAGGGTTAGGG-3′(22AG) and its complementary sequence (22CT), they showed that both complexes have a *ca.* 10-fold higher K_b for G-quadruplex over i-motif DNA (*ca* 10^6 and 10^5 M^{-1}, respectively). It was proposed that this observation was due to the end stacking of the dppz ligand with the G-quartets.[69]

Λ- and Δ-$[Ru(L)_2(dppz)]^{2+}$ (L = bpy or phen) have both been investigated by Pages *et al.*, for their interactions with different i-motif sequences featuring various loop lengths of C_3T_n, where n ranges from 3 to 8.[70] One significant conclusion that can be drawn from the study is that the emission responses of the Λ isomer were more significant than the Δ isomer, the opposite effect to that seen in Λ or Δ- $[Ru(L)_2(dppz)]^{2+}$ and its enantiomers to B-form DNA. This could be due to the possibility of T-T hairpins developing in the longer loops and the dppz ligand intercalating into this substructure. Whilst a significant advancement in the study of dppz containing complexes and i-motif DNA, the specificity shown is reliant upon the loop structures, not the core of the i-motif structure, a limiting factor. As shown so far, i-motif DNA can contain many different lengths in the loop region as well as the loop being composed of different nucleic acids for the numerous i-motif sequences that we know of. Targeting the loop, therefore, may not yield the ability to target all the different i-motif forming sequences.

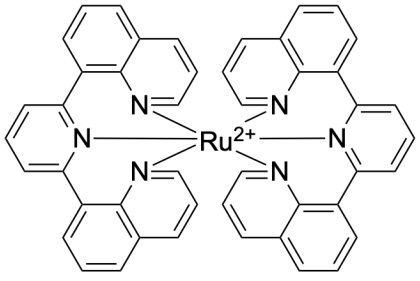

Figure 1.13: Structure of $[Ru(bqp)_2]^{2+}$

While these complexes offer a good starting point for the development of G4 specific probes, their reliance on the end-stacking or intercalative binding are a major pitfall in the development of i-Motif probes. Without the large planar G-tetrad, the i-motif does not allow for an end-stacking mode of binding, and, with the nature of the C-C^+ base pair

stacking, it is reasonable to assume a very limited ability of a ligand to intercalate into the i-motif in between the cytosine bases of the core.[13] This limits the mode of binding to the groove or insertion into the loops. Whilst insertion into the loops offers a great opportunity to target specific i-motif forming sequences, it would heavily detract from the ability of a ligand to target all i-motif forming sequences, rather than specific sequences. This, along with the very small width of the i-motif minor groove, leaves just one single mode of binding that would allow for interaction with only the core, and therefore the probing of all i-motif forming sequences: the major groove.

From the current literature presented here, one can reasonably conclude that $[Ru(L)_2(dppz)]^{2+}$ and its analogues are an unsuitable family of complexes for the development of a Ru-based i-motif specific probe. The inability of the dppz family to target the core of the i-motif limits its usage in identifying all i-motif forming sequences. A new approach is needed, one that does not rely upon intercalation for the switching mechanism and is able to selectively bind the core of the i-motif structure. One must find a suitable Ru-based polypyridyl probe that does not contain an intercalating ligand such as dppz but also possesses good photophysical properties. On that note, *mer*-$[Ru(bqp)_2]^{2+}$ (Figure 1.13)[71] was one of many compounds that were screened in a joint effort between the Waller and Fielden groups prior to this project. This compound showed the ability to bind i-motif and could offer a path towards developing a new Ru-based i-motif probe.

1.2.2 Bis-(2,6-bis(8′-quionlinyl)pyridine) ruthenium (II)

The development of bis-(2,6-bis(8′-quionlinyl)pyridine) ruthenium (II) was the product of years of research towards increasing the emission lifetimes of Ru-based polypyridyl complexes. Typical excited state lifetimes of ruthenium(II) polypyridyl complexes vary considerably, with $[Ru(tpy)_2]^{2+}$ having an excited state lifetime of 0.25 ns, and $[Ru(bpy)_3]^{2+}$ having an excited state lifetime of 850 ns.[72,73] The differences in coordination between tridentate and bidentate complexes results in a reduction of the ligand field strengths, with the tridentate species giving easier thermal access to the ^{3}MC excited state and thus reducing the emission lifetime via vibrational relaxation.[45] To overcome the thermal population of the ^{3}MC excited state in tridentate complexes, attempts have been made to increase the energy gap between the ^{3}MLCT and ^{3}MC states by the addition of electron

donating/accepting groups,[74,75] or altering the π systems of the polypyridyl ligands to stabilise the excited state (Figure 1.14).[76]

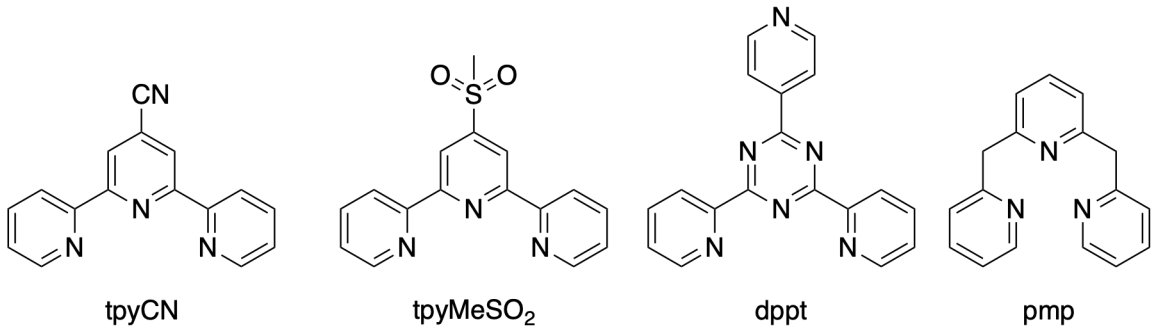

Figure 1.14: Structures of terpyridine derivatives used to form ruthenium polypyridyl complexes

Strongly electron-withdrawing groups, such as the cyano group, have been added to terpyridine based Ru complexes in order to extend their lifetimes. Using 4′-cyano-2,2′:6′,2′′-terpyridine (tpyCN), Wang *et al*., showed that adding this strongly withdrawing group stabilised the ^{3}MLCT state and lead to a life time of 1.2 ns, *ca* five times longer than that of $[Ru(tpy)_2]^{2+}$.[74] As far back as 1992, Constable *et al*., demonstrated the same affect by using a $MeSO_2$ functional group at the 4-position on the central pyridine ($tpyMeSO_2$), giving a lifetime of 25 ns. Polson *et al*., demonstrated that the replacement of the central pyridine with a triazine moiety and addition of another pyridine at the 4-position on this central ring (2,4-di(pyridin-2-yl)-6-(pyridin-4-yl)-1,3,5-triazine (dppt)) led to a lifetime of 15 ns. The electron deficient triazine ring, as well as the addition of further acceptor orbitals of the new pyridine ring, led to a stabilisation of the ^{3}MLCT state by lowering the π^* orbital of the ligand compared to an unfunctionalised terpyridine ligand. Whilst this progress was good and very promising towards the aim of improving the photophysics of **bis**-tridentate Ru complexes, the lifetimes of these complexes still fell far short of the 850 ns lifetime of $[Ru(bpy)_3]^{2+}$.

In 2004, Wolpher *et al*. proposed a new method for increasing the excited-state lifetime of *bis*-ruthenium(II) polypyridyl complexes.[77] To achieve this, it was proposed that the bite angle of the ligands needed to be increased to as close to 180° as possible to achieve near-perfect octahedral geometry around the ruthenium centre. It was suggested that if this were to be achieved then the rate of population of the nonemissive states would decrease, without decreasing the energy of the ^{3}MLCT state. 6-(2-picolyl)-2,2′-bipyridine (pbpy)

and its ruthenium complex (Figure 1.15) were synthesised as an attempt at achieving this with the resulting lifetime being *ca* 70 times longer than the lifetime of $[Ru(tpy)_2]^{2+}$, a promising start.[77,78]

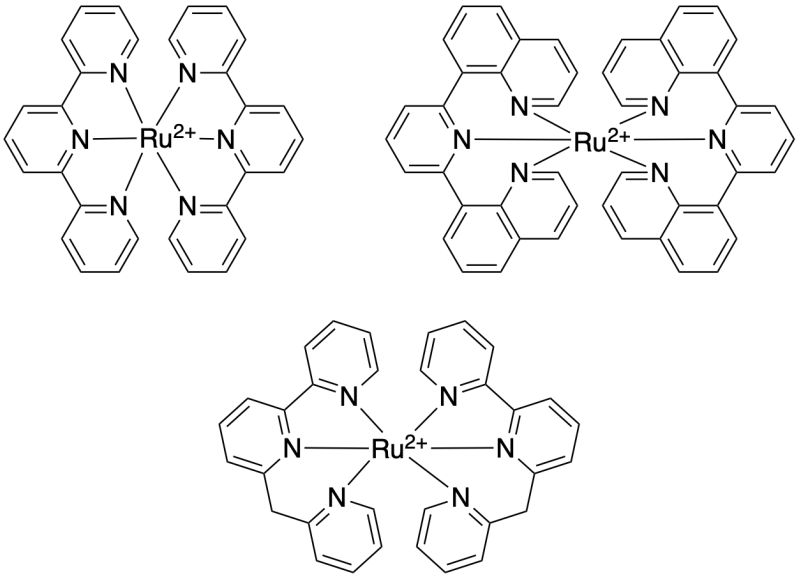

Figure 1.15: Structures of $[Ru(tpy)_2]^{2+}$ (top left) and $[Ru(bqp)_2]^{2+}$ (top right) and $[Ru(pbpy)_2]^{2+}$ (bottom)

In 2006, the same group, this time led by the work of Abrahamsson, published the synthesis of the 2,6-bis(8'-quinolinyl)-pyridine ligand (bqp, **1**) and its meridional ruthenium complex *mer*-$[Ru(\mathbf{1})_2]^{2+}$ (*mer*-**1a**), which has an excited state lifetime of 3.0 µs, significantly larger than traditional bidentate ruthenium(II) complexes (Figure 1.15).[71] DFT calculations suggested the bite angle between the two pyridyl nitrogen atoms to be 179.6°, with X-ray crystallographic data showing the angle to be 177.6°. Further work by Borg *et al*., investigated the ^{3}MLCT and ^{3}MC states in more detail and found that one must go further than the ligand-field splitting hypothesis when dealing with the extended lifetimes of this family of complexes.[79] By comparing DFT data obtained from $[Ru(pmp)_2]^{2+}$ and $[Ru(\mathbf{1})_2]^{2+}$, they found that in order to move from the ^{3}MLCT to the ^{3}MC state, the complex must undergo geometric distortions that in the more flexible pmp containing complex is more favoured than in the bqp complex. The methane bridges in $[Ru(pmp)_2]^{2+}$ allow for this increased flexibility in the ligand where as the more rigid bqp ligand does not, creating a barrier to the population of the ^{3}MC from the ^{3}MLCT.

Further work by Jäger *et al*. showed that $[Ru(\mathbf{1})_2]^{2+}$ can form three different isomers that can be isolated from each other (Figure 1.16).[80] As well as the meridional complex

reported by Abrahammson *et al.*,[71] two facial isomers, *cis*-**1a** and *trans*-**1a**, were also isolated and both ^{1}H NMR and crystal structures were published for all three. *mer*-**1a** is the most thermodynamically favourable so lowering the temperature and reaction time results in a higher yield of both *fac* isomers, with *cis*-**1a** becoming the major product. It was reported that the facial isomers exhibited significantly red shifted MLCT absorption bands compared to *mer* but that their photophysical properties were complex and needed further investigation. The change in the geometry of the ligand around the Ru centre could shift the ability of the complex to undergo the geometric distortion necessary for the population the ^{3}MC state.

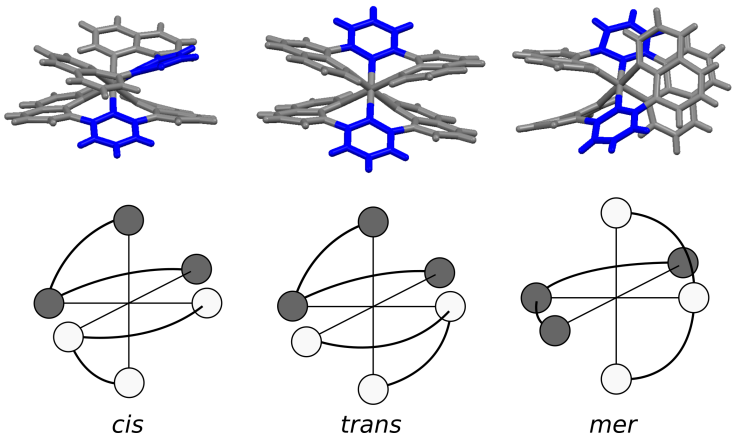

*Figure 1.16: Crystal structure of cis-**1a** (left), trans-**1a** (centre), and mer-**1a** (right) with central pyridine rings coloured blue and a 3D depiction of geometry below*

The aim of this project was to investigate the use of $[Ru(\mathbf{1})_2]^{2+}$ and its analogues as an i-motif specific probe. The long excited-state lifetimes, facile synthesis and narrow width (*ca* 9 Å), could be utilised in the design of an i-motif binding complex. The ability to functionalise the 4-position of the pyridine ring[81] gives good scope for changing the properties of the complex to increase its interaction with i-motif DNA via different interactions. An increase in fluorescence upon binding would be desirable, especially during *in vivo* experimentation. This may be possible by investigating the geometric changes between the three isomers and how interaction with a macromolecule that could be capable of restricting such changes could influence the emission of the facial isomers.

1.3. Methods

To fully investigate the interactions between Ru-based complexes and DNA, many techniques can be used.[40,82] Below, each technique used in this project is discussed.

1.3.1 UV-vis Absorption Measurements

Absorption titration of DNA into a solution containing ruthenium complexes is routinely used to measure the strength and type of binding interaction by observing the change in the electronic transitions of the complex upon DNA binding.[82] Generally, ruthenium-based polypyridyl complexes exhibit absorption properties outside of region in which DNA absorbs light. This allows for the measurement of the absorbance of a Ru complex whilst titrating in DNA, leading to chromatic shifts. Intercalation is usually identified by the hypochromic and bathochromic shifts in the $\pi - \pi^*$ transition of the ligand, caused by the π stacking of the aromatic ligand and the DNA base pairs.[83]

To calculate the strength of binding of the Ru complex to DNA, the intrinsic binding constant (K_b) is calculated. Two commonly used methods of doing so are shown in Eq. 1.2 and 1.3.

$$\frac{(\epsilon_a - \epsilon_f)}{(\epsilon_b - \epsilon_f)} = (b - (b^2 - 2K_b^2 C_t[\text{DNA}]/n)^{1/2})/(2K_b C_t) \tag{1.2a}$$

$$b = 1 + K_b C_t + K_b[\text{DNA}]/2n \tag{1.2b}$$

$$[\text{DNA}]/(\epsilon_a - \epsilon_f) = [\text{DNA}]/(\epsilon_b - \epsilon_f) + 1/[K_b(\epsilon_b - \epsilon_f)] \tag{1.3}$$

where C_t is the total concentration of the Ru complex, [DNA] is the concentration of DNA in base pairs for B-form DNA, G-tetrads for G4s and C-C^+ pairs for i-motif DNA,[84] $\epsilon_a = A_{obs}/[\text{compound}]$, and ϵ_b, and ϵ_f are the extinction coefficients of the bound and free complex, respectively. When using known lengths of B-form DNA, it is possible to use the molarity of the DNA instead of the base pairs as the concentration in these calculations.

1.3.2 Emission Intensity

For most ruthenium polypyridyl complexes, emission intensity is a strong indicator of binding strength between the Ru-complex and DNA.[50,85] As the complex binds to the DNA, where through intercalation or electrostatic interactions, it is protected somewhat from the solvent, which typically acts an emission quencher, and the emission of the complex increases. There is generally a positive relationship between binding strength and emission intensity increases, the tighter a complex binds DNA, the larger the emission intensity increase. In some circumstances, looking at the normalised emission increase is useful to see the changes that are occurring between different complexes, this can be done using Eq. 1.4.

$$I_N = \frac{I_a}{I_0} \tag{1.4}$$

where:

I_a = the emission at given DNA concentration

I_0 = the emission in the absence of DNA

1.3.3 Emission Lifetime

Emission lifetime measurements can also be informative as to the binding interactions between Ru-complexes and DNA.[86] Intercalation of ethidium bromide into DNA can cause an increase in its emission lifetime,[87] and the same is true of Ru complexes, with shorter emission lifetimes arising from the free or ionically bound states and elongation of the lifetime arising from the intercalative form.[88]

To measure the lifetime of a Ru complex, excitation via a timed laser pulse is achieved and the emission of photons is measured, with the precise time of its arrival at the detector calculated, and the decay profile is fitted to Eq. 1.5.

$$I(t) = \alpha_1 e^{-t/\tau_1} + \alpha_2 e^{-t/\tau_2} + ... \alpha_n e^{-t/\tau_n} \tag{1.5}$$

where:

$n =$ the number of components

$\alpha =$ the amplitude of each component normalised to 1

$\tau =$ the lifetime of each component

$I =$ the intensity of light

$t =$ the timestep

The fractional contribution of each component can then be calculated using Eq. 1.6.

$$f_i = \alpha_i \tau_i / \Sigma_j \alpha_j \tau_j \tag{1.6}$$

1.3.4 Emission Polarisation

When a Ru complex binds DNA through electrostatic interactions, its rotational freedom is not as restricted as when it is bound through intercalation.[40] As the intercalated complex's rotation is fixed to that of the DNA, which has a much slower rotation compared with the free Ru complex, an increase in emission polarisation is therefore observed upon intercalation.[40] Emission polarisation can be calculated from Eq. 1.7.

$$P = \frac{I_{\parallel} - I_{\perp}}{I_{\parallel} + I_{\perp}} \tag{1.7}$$

where:

$I_{\parallel} =$ the emission intensity of light parallel to the source

$I_{\perp} =$ the emission intensity of light perpendicular to the source

Higher polarisation is indicative of intercalative binding, while lower, or even zero, polarisation indicates weak, electrostatic type interactions.[86]

1.3.5 Circular Dichroism

Circular dichroism (CD) is a technique used to measure the optical polarisation of molecules and is routinely used for probing the secondary structures of DNA.[89] By measuring the asymmetry in the sugar backbones and the helical twists of DNA structures, CD can be used to show which secondary structure is present. Not only this, but due to interactions between ligands and the DNA, induced CD (ICD) signals can be measured.[90]

Typical wavelengths of absorption of various DNA secondary structures are known.[89] For example, B-form DNA typically shows a positive band at *ca* 280 nm and a negative band at *ca* 245 nm. Parallel G4s display a positive band at *ca* 260 nm, with antiparallel forms showing a negative band at *ca* 260 nm and a positive band at *ca* 295 nm. i-Motif DNA shows a positive band at *ca* 290 nm and a negative band at *ca* 265 nm. By heating a sample and monitoring a particular wavelength, the thermal stability of the DNA structure can be monitored. i-Motif DNA, for example, displays a decrease in the signal at *ca* 290 nm as the temperature is increased, indicating an unfolding of the structure.

1.3.6 Fluorescent Indicator Displacement (FID)

Thiazole orange (TO) has been shown to fluoresce in the presence of DNA but not in aqueous media.[91] Using this property, small molecules can be screened to measure the level of displacement of TO from DNA using Eq. 1.8. Despite that fact that TO may have different binding constants to different DNA structures, and the displacing ligands may also bind in multiple binding pockets within the DNA, this is still a useful technique to screen large libraries of small molecules for their ability to bind to DNA.[92]

$$\text{TO Displacement (\%)} = 1 - \left(\frac{I_{TO+DNA+L} - I_{TO}}{I_{TO+DNA} - I_{TO}}\right) \times 100 \tag{1.8}$$

where:

$$I_{TO} = \text{the fluorescence of TO}$$

$$I_{TO+DNA} = \text{the fluorescence of TO with DNA}$$

$$I_{TO+DNA+L} = \text{the fluorescence of TO with DNA and ligand}$$

1.3.7 Förster Resonance Energy Transfer (FRET)

FRET is a phenomenon in which the energy of an excited fluorophore (the donor) transfers its energy across to a separate ground-state fluorophore (the acceptor), given that the excited-state of the donor overlaps the ground-state of the acceptor. This rate of transfer is given as $E = 1/(1 + (r/R_0))^{-6}$ where r and R_0 are the separation distance between the two fluorophores and Förster distance (the distance at which the energy transfer efficiency is 50%), respectively. The 10^{-6} dependence upon distance gives this technique a high level of precision. While studying the folding of quadruplex DNA structures, labelling of the DNA sequences at the 5′ and 3′ end with 6-carboxyfluorescein (FAM) and 6-carboxytetramethylrhodamine (TAMRA), respectively, can lead to the occurrence of FRET. By monitoring the emission of the acceptor fluorophore, as the donor is brought into close proximity, for example due to the folding of the DNA, the emission of the acceptor increases leading to a rise in its emission intensity. If the variable of temperature is added to the experiment, the emission of the acceptor, and thus the folding of the DNA, can be monitored across a range of temperatures and the transitional temperature, the point at which 50% of the DNA is folded (T_{m}), can be obtained. By the additions of a ligand or changes in pH the thermal stability of the DNA quadruplex can therefore be observed.

1.3.8 AutoDock and AutoDock Vina

AutoDock 4.2[93] and AutoDock Vina[94] are two widely used docking software packages for probing ligand-macromolecule interactions.[95,96] Whilst AutoDock Vina has largely superseded AutoDock 4.2, Vina does not contain parameters for transition metal elements outside of the first row, or the ability to add these manually. AutoDock 4.2, however, does allow for manual additions of various parameters, including that of ruthenium.

Vina, unlike AutoDock 4.2, also does not require manual preparation of grid maps, the choosing of search parameters, or the clustering of results after docking, as all of these are performed by Vina automatically, vastly speeding up the process of high-throughput screening. Therefore, for the screening of organic molecules from the NCI library, Vina was used due its increased speed, but for the evaluation of Ru complexes, AutoDock 4.2 was used.

2. Studying the DNA Binding Properties of the Three Isomers of $[Ru(bqp)_2]^{2+}$

2.1. Introduction

The discovery by Jäger *et al*., that a tridentate polypyridyl ligand could form a facial complex was significant as other common tridentate Ru-based complexes, such as $[Ru(tpy)_2]^{2+}$, were not reported to form with facial geometries due to the restricted bite angles of the ligand.[80] The increased bite-angle of the bqp ligand allow for the coordinated ligand to sit in a facial geometry, as well as the meridional geometry. The reportedly complex photophysical properties of the facial isomers indicated that the change in geometry around the ruthenium caused a substantial change in the electronic properties of the complex. Previously reported facial geometries of tridentate Ru complexes is extremely limited. In 2000, Romero *et al*. published the synthesis of *cis*,*fac*-$[Ru(bpea)_2]^{2+}$, which showed low wavelength ^{3}MLCT absorption bands (380 nm), with a low intensity band (ϵ =167 M cm^{-1}) at 566 nm (Figure 2.1).[97] The emission properties of this complex and analogues is sparsely reported, only one such report has been found that states the lifetime of this complex is 17 ns, far shorter than that of *mer*-**1a** but still an improvement upon $[Ru(tpy)_2]^{2+}$.

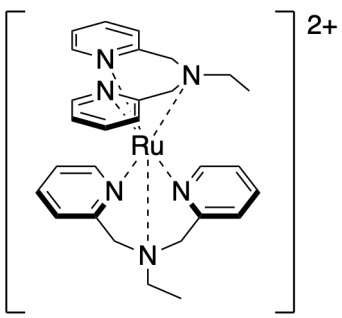

Figure 2.1: Structure of cis,fac-$[Ru(bpea)_2]^{2+}$

From the crystal structures, one can observe how the geometries of the three isomers differ (Figure 2.2). Taking the N-Ru-N angle of the pyridine rings in each complex demonstrates one of the key differences between *cis*-**1a** compared to the other isomers. *cis*-**1a** has an angle of *ca* 90° with *mer*-**1a** and *trans*-**1a** having angles of *ca* 180° between the pyridine rings (Table 2.1). This causes the size of *cis*-**1a** to be much smaller across one axis. If one were to take the furthest distances across the x, y and z axes of each isomer and form a 3D box of those dimensions, one would find *cis*-**1a** to not only form the smallest grid in terms of volume but also to form the most elongated grid - *cis*-**1a** contains a short z axis and relatively long x and y axes (Table 2.1).

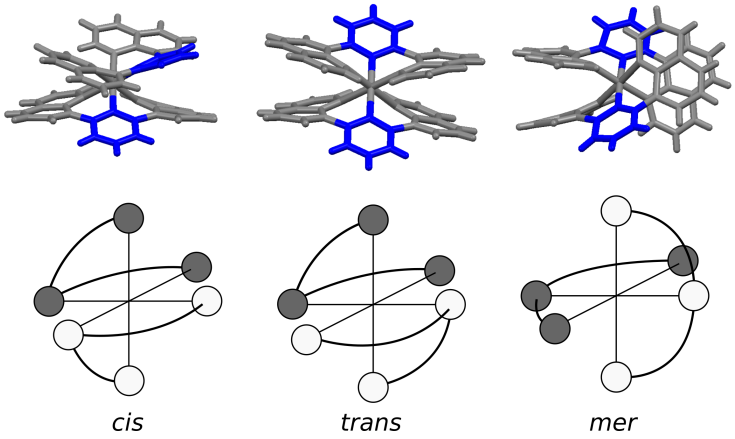

*Figure 2.2: Crystal structure of cis-**1a** (left), trans-**1a** (centre), and mer-**1a** (right) with central pyridine rings coloured blue and a 3D depiction of geometry below*

The symmetric nature of *mer*-**1a** and *trans*-**1a** yield seven environments in the ^{1}H-NMR spectra.[80] *cis*-**1a**, however, being asymmetrical in nature, gives a complex NMR spectrum with twice as many environments (Figure 2.5). This asymmetry in the geometry of *cis*-**1a** could influence its MLCT energies, as one could envisage two MLCT transitions, where the electron can transfer from the Ru centre to either of the two ligands. Similar properties are found in $[Ru(L)_2(dppz)]^{2+}$ complex, where the auxiliary ligands contribute towards the dark and bright states within its electronic properties. In 2004, Ortmans *et al.*, published the DNA binding interactions of $[Ru(TAP)_2(dppz)]^{2+}$ (TAP = 1,4,5,8-tetraazaphenanthrene) which displays a bright excited state in water without the presence of DNA.[98] It is understood that this bright state arises from the MLCT transition in which the charge is localised to the TAP ligand rather than the dppz ligand, causing the bright emission properties.

*Table 2.1: Geometrical properties of mer-**1a**, cis-**1a**, and trans-**1a** obtained from their published crystal structures*

	N-Ru-N Angle (°)	x (Å)	y (Å)	z (Å)	Volume (Å^3)
mer-**1a**	176.3	10	8	12	1033
cis-**1a**	92.0	12	11	6	799
trans-**1a**	180.0	9	12	11	1101

Both *mer*-**1a** and *cis*-**1a** are chiral and therefore exist as two enantiomers (Δ and Λ). Enantiomeric separation of ruthenium complexes has been accomplished through a few different techniques. In the 1980s, Barton *et al*. routinely separated Ru-based polypyridyls via recrystallisation with antimony D-tartrate,[48,49] where successive recrystallisations would be performed until no change in the $[\alpha]_D$ values were observed. Optical purities of ≥ 0.92 were achieved by using this method. However, this technique was unable to resolve the enantiomers of $[Ru(L)_2(dppz)]^{2+}$ and instead the enantiomeric separation was achieved by separating out the enantiomerically pure intermediate $[Ru(phen)_2(phen-dione)]^{2+}$ (phen-dione = 1,10-phenanthroline-5,6-dione).[83] The enantiomerically pure intermediates were able to undergo recrystallisation with antimony-tartrate salts before reaction with 1,2-diaminobenzene to yield Δ- and Λ-$[Ru(phen)_2(dppz)]^{2+}$.

More recent development in this area has led to the use of chiral HPLC as a way to separate enantiomers. McQuaid *et al*., separated a cyano-functionalised dppz derivative ($[Ru(TAP)_2(11\text{-}CN-dppz)]^{2+}$, 11-CN-dppz = dipyrido[3,2-a:2′,3′-c]phenazine-11-carbonitrile) on a cyclofructan based chiral column with a mobile phase of 70:30:2:0.8 MeOH:ACN:TEA:AA.[99] Whilst this circumvents issues around the removal of antimony containing salts and the apparent difficulty of recrystallising dppz derivatives, it does pose its own drawbacks. Using a flow rate of 5 mL min^{-1} and a 200 µL injection of a 3 mg L^{-1} analyte, the enantiomers were separated. Each run at these volumes and concentrations yields a maximum of 0.3 mg of a pure enantiomer, assuming no loss during anion metathesis. Multiple injections are required to yield a reasonable quantity of each enantiomer for characterisation and biophysical testing. With modern autosample injections and automatic collections, this process can be largely circumvented but the time necessary to find the correct conditions for separation is laborious.

In this study, the racemic mixtures of both *mer*-**1a** and *cis*-**1a** were initially investigated for their DNA binding properties. Separation of Ru enantiomers is not straight forward

and unless significant discoveries are elucidated with the racemic mixtures, laborious separation of enantiomers is not favoured. The enantiomers of *cis*-**1a** were, however, separated due to the DNA binding properties of the racemic mixture, which will be discussed later.

2.2. Results and Discussion

2.2.1 Synthesis and Separation

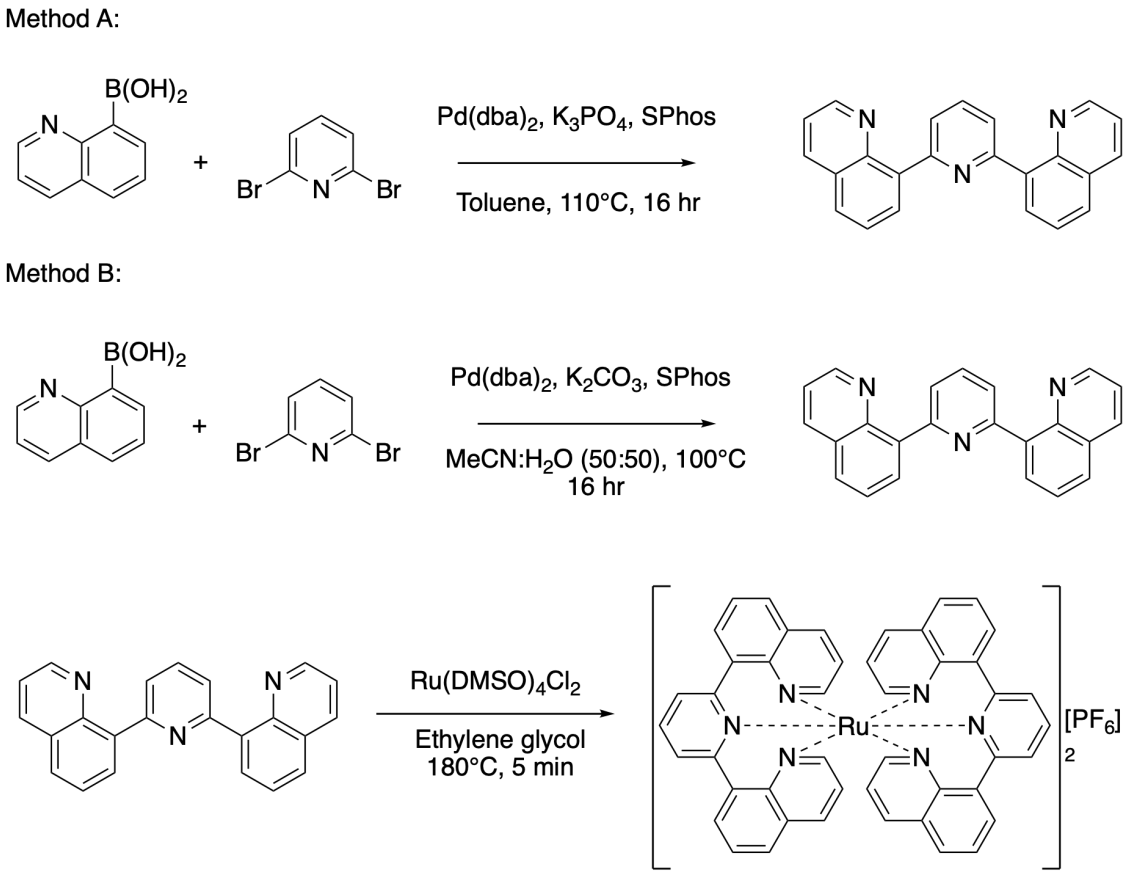

Figure 2.3: Synthetic pathway for the synthesis of ***1a***

The synthesis of these complexes initially followed the literature method from Abrahamsson *et al*. (Figure 2.3, Method A).[71] A Suzuki coupling of the two equivalents of the 8-quinolineboronic acid to 2,6-dibromo-pyridine in anhydrous toluene yielded high amounts ($>$ 80%) of the bqp ligand at the scale originally published (*ca* 300 mg bqp). However, it was found that this method did not scale well to larger quantities, so a new procedure was developed. Following similarly published methods of Suzuki couplings,[100]

the solvent system was changed to a 50:50 mix of MeCN:H_2O, and the dihalide was swapped from the bromo derivative to the far cheaper chloro (Figure 2.3, Method B). The addition of water to the solvent system has been shown to offer increased homogeneity with the inorganic base.[101,102] It was also found that addition of DCM to the cooled reaction mixture, the subsequent separation to remove H_2O, followed by the concentration of the organic layer and precipitation of the product with diethyl ether led to pure product in >80% yield at scales of >5 g. The additional purification step of precipitation from diethyl ether removed the need for chromatography whilst preserving the high yield and high purity of the product (Figure 2.4).

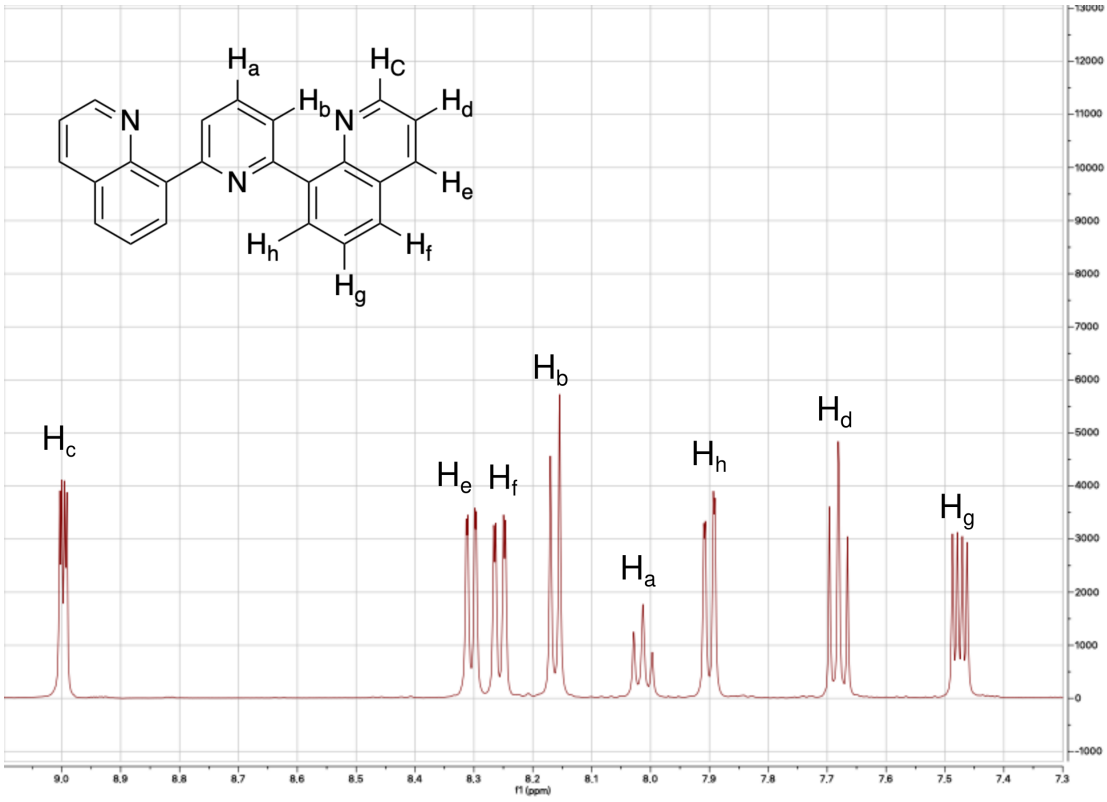

*Figure 2.4: ^{1}H-NMR of the aromatic region of **1** in $CDCl_3$ performed at 400 MHz*

The synthesis of the three isomers from $Ru(DMSO)_4Cl_2$ and **1**, was not changed as this generally yielded the optimum ratio of the three isomers. Attempts were made to lower the temperature of the reaction to investigate whether this would yield higher ratios of *trans*-**1a** but to no avail. This action only led to a lowering of the overall yield of the reaction whilst maintaining the same ratio of the three isomers. Reactions performed at >180 °C led to an increase in the yield of *mer*-**1a**, so the originally reported conditions

were used going forward.

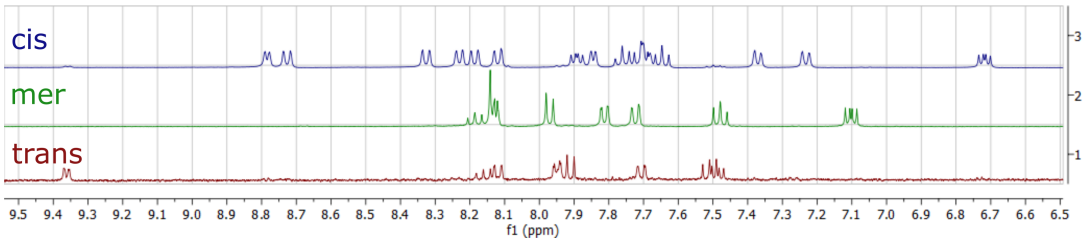

Figure 2.5: Aromatic region of the three isomers as $[Cl]^-$ salts in d_4-MeOD performed at 400 MHz

The separation of the isomers was reported to have been achieved via HPLC with a gradient of MeCN:H_2O (12-17%) with 0.1% HCO_2H over 70 mins. This was replicated using a C18 RP-HPLC column, but under different conditions to those originally reported. It was found that dissolving the mixture of isomers in MeCN as a PF_6^- salt and using MeCN / H_2O as eluents did not yield sufficient separation. Instead MeOH was used in place of MeCN and having the compounds as Cl^- salts (Figure 2.6). *mer*-**1a** separated out from the two facial isomers very well, but the separation of the two facial isomers proved more difficult. The low yield of *trans*-**1a** and its difficult separation from *cis*-**1a** required multiple runs to obtain a useable quantity.

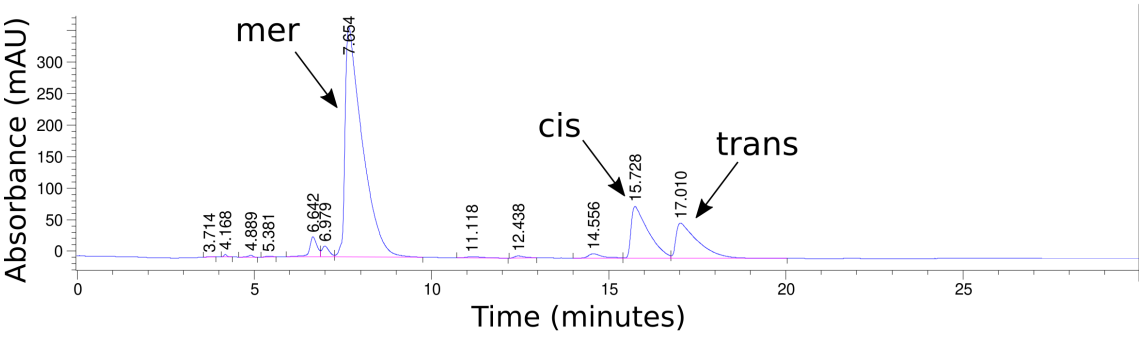

*Figure 2.6: HPLC trace showing the separation of mer-**1a**, cis-**1a**, and trans-**1a** using 40-60% MeOH:H_2O and 0.1% CF_3CO_2H over 30 mins*

Having successfully synthesised and separated the isomers, the next stage was to investigate the biophysical properties that they possess in the presence of DNA. This study was conducted using two i-motif forming sequences, the i-motif forming sequence from the human telomeric region that forms a stable i-motif in acidic conditions (hTeloC = 5′-d[(TAA-CCC)$_4$]-3′)[23] and the i-motif from the death associated protein (DAP) promotor region that forms under neutral conditions (DAP = 5′-d[(CCC-CCG)$_4$-CCC-CC]-3′).[35] The

complementary G-rich strand of the human telomeric sequence (hTeloG = 5′-d[(GGG-TTA)$_4$]-3′) was used to test against G-quadruplex DNA and a custom double-stranded sequence (DS = 5′-d[GGC-ATA-GTG- CGT-GGG-CGT-TAG-C]-3′), and it's complementary sequence (5′-d[GCT-AAC-GCC-CAC-GCA-CTA- TGC-C]-3′), were used for testing against dsDNA. All aqueous experiments were performed in buffers containing 100 mM potassium chloride and 10 mM sodium cacodylate at either pH 6.8 (DAP, hTeloG or DS) or pH 5.5 (hTeloC). Potassium chloride was chosen to mimic *in cellulo* conditions and sodium cacodylate chosen due its pHbeing almost temperature independent.[103]

2.2.2 Emission Intensity and Intrinsic Binding Constants

The first step towards developing a new probe is to test the strength of DNA binding and changes in emission upon DNA binding to an array of different DNA secondary structures.

In the absence of DNA, *mer*-**1a** shows intense emission, ascribed to phosphorescence from a ^{3}MLCT excited state (Figure 2.7). The two facial isomers, however, do not display such an intense excited state and are considered to be in an "off" state. Whilst some emission is measured, with *trans*-**1a** displaying a slightly higher level of emission than *cis*-**1a**, the geometrical arrangement of the ligand into the facial isomer clearly alters the accessibility of the non-emissive ^{3}MC state. Further investigation into this process is discussed later in this chapter.

Upon addition of DNA, *mer*-**1a** shows an increase in emission (see Table 2.2 and Figure 2.8). Upon addition of hTeloC, the emission does increase initially but as more DNA is added, this emission returns to its starting point. *trans*-**1a**, initially in an "off" state, undergoes a larger increase in its emission upon addition of DNA (Figure 2.9). The largest increase is seen with DAP (a 5.42-fold increase), whilst DS, hTeloC and hTeloG undergo a similar "switch on" amount to each other (*ca* 3-fold), once error is taken into consideration. This switch on effect is more dramatic when observing *cis*-**1a** (Figure 2.10). The racemic mixture of enantiomers was the first to be studied with a large increase in its emission profile in the presence of all DNA (minimum of *ca* 15-fold up to 55-fold increase) with the largest increase being observed with DS, a *ca* 10-fold increase in the response seen with *trans*-**1a** and DAP.

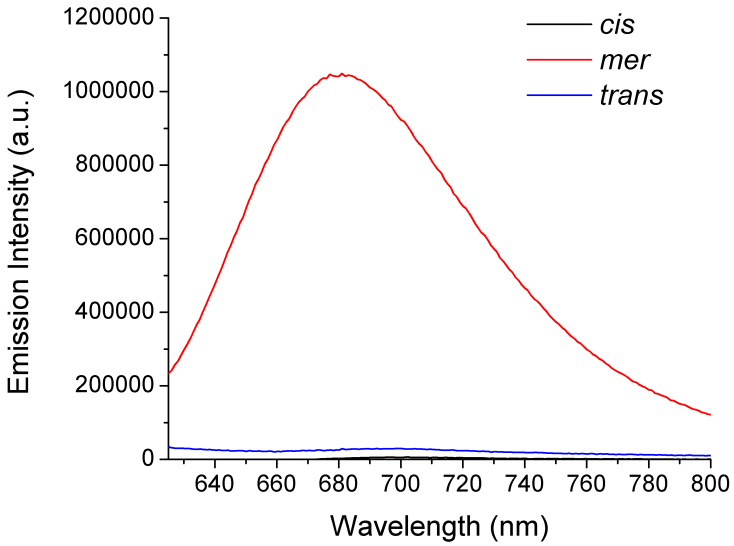

Figure 2.7: Emission Intensity of 5 µM *cis-**1a*** ($\lambda_{ex} = 590$ nm)*, trans-**1a*** ($\lambda_{ex} = 490$ nm)*, and mer-**1a*** ($\lambda_{ex} = 550$ nm) *in* 100 mM *potassium chloride and* 10 mM *sodium cacodylate at* pH *6.8*

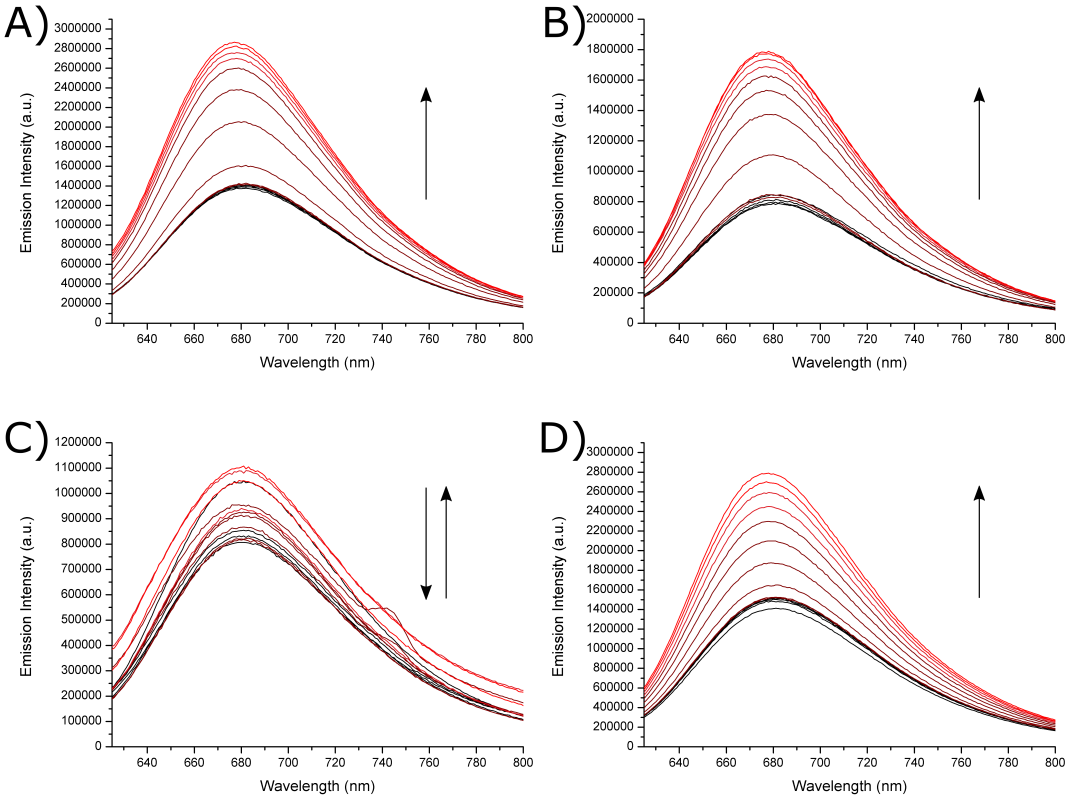

Figure 2.8: Emission titrations of 5 µM *mer-**1a*** *and* 0 µM *to* 7.7 µM *(black to red) of A) DAP, B) DS, C) hTeloC* (pH *5.5), and D) hTeloG in* 100 mM *potassium chloride and* 10 mM *sodium cacodylate at* pH *6.8 unless stated otherwise.* $\lambda_{ex} = 550$ nm

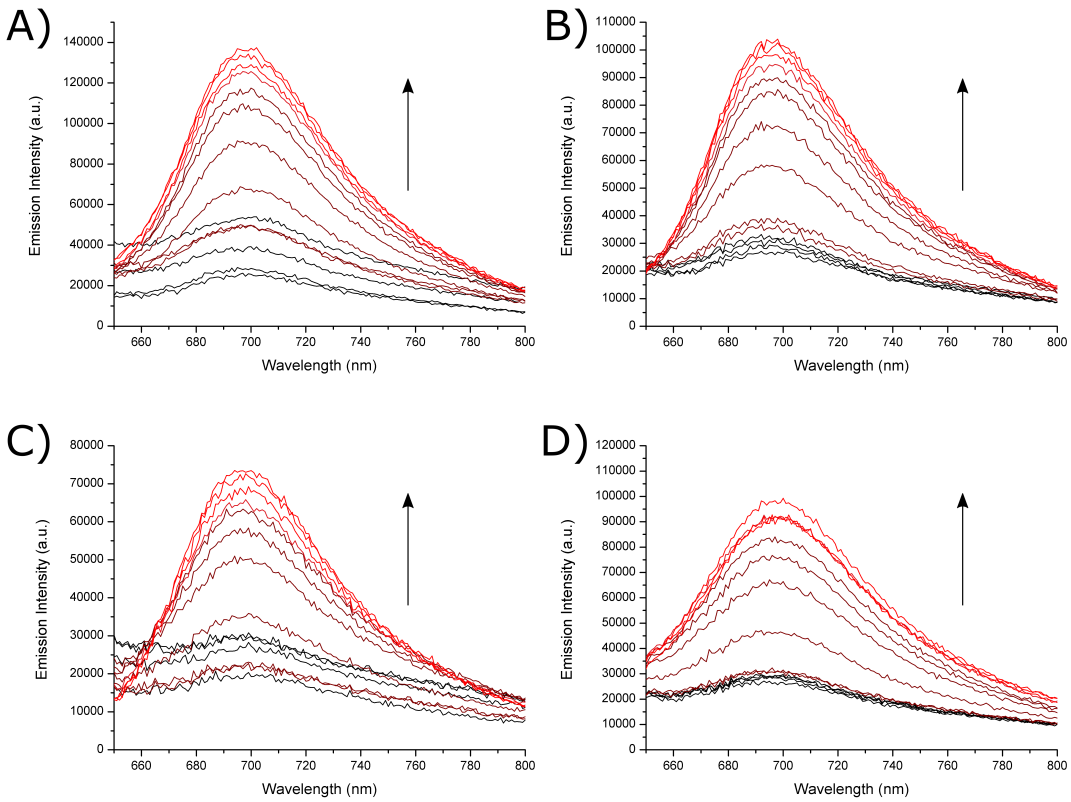

Figure 2.9: Emission titrations of 5 µM *trans-**1a** and* 0 µM *to* 7.7 µM *(black to red) of A) DAP, B) DS, C) hTeloC (*pH *5.5), and D) hTeloG in* 100 mM *potassium chloride and* 10 mM *sodium cacodylate at* pH *6.8 unless stated otherwise.* $\lambda_{ex} = 490\,\text{nm}$

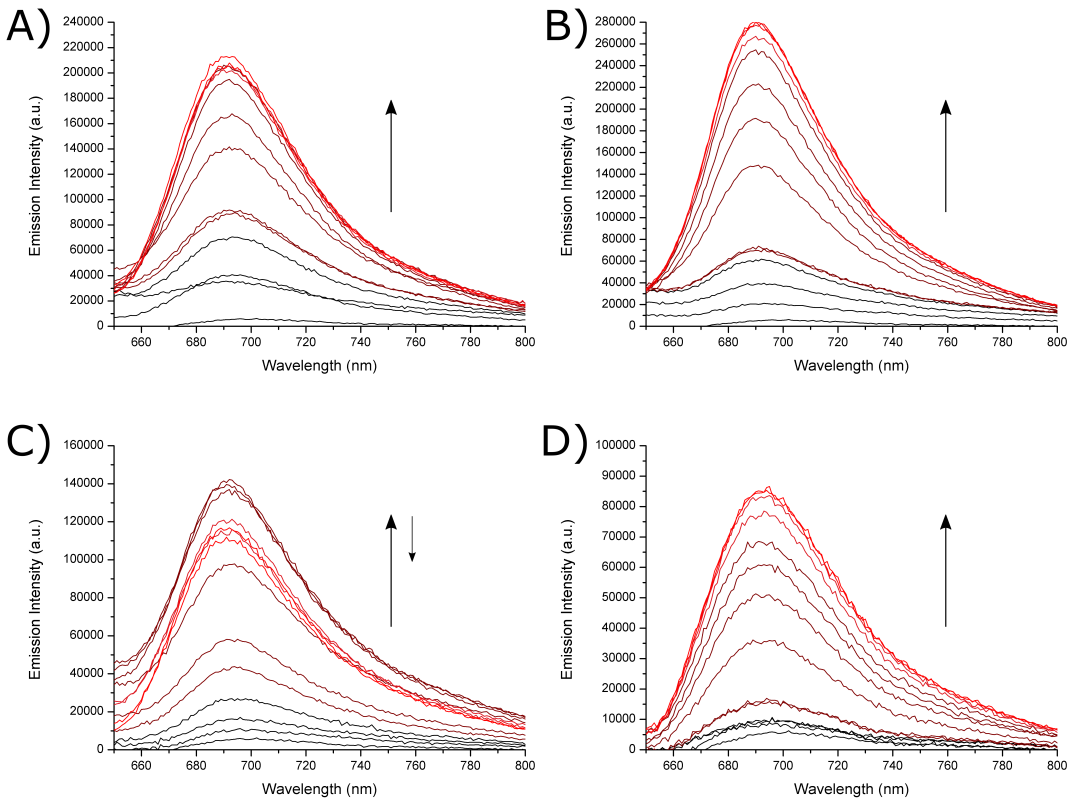

Figure 2.10: Emission titrations of 5 µM *cis-**1a** and* 0 µM *to* 7.7 µM *(black to red) of A) DAP, B) DS, C) hTeloC* (pH *5.5), and D) hTeloG in* 100 mM *potassium chloride and* 10 mM *sodium cacodylate at* pH *6.8 unless stated otherwise.* $\lambda_{ex} = 590\,\text{nm}$

From absorption titrations of increasing amount of DNA into a constant concentration of Ru complex, the intrinsic binding constant (K_b) was obtained from the ratio of the slope to the intercept in a plot of $[DNA]/(\epsilon_a - \epsilon_f)$ against [DNA], where ϵ_a and ϵ_f are the molar extinction coefficients for the apparent and free complex, respectively, and [DNA] is the molar concentration of DNA.

mer-**1a** displays K_b values on the order of 10^5 M^{-1}, while both facial isomers exhibit K_b values on the order of 10^6 M^{-1}. This suggests a much weaker binding interaction between the meridional complex and DNA than that exhibit by the two facial complexes. The largest K_b was found to be from *cis*-**1a** in the presence of DS DNA ($8.40 \pm 1.01 \times 10^6$ M^{-1}), followed by the same complex with DAP ($6.94 \pm 0.26 \times 10^6$ M^{-1}). This was significantly higher than the binding constants exhibited with hTeloC or hTeloG (1.15 ± 0.15 and $0.63 \pm 0.02 \times 10^6$ M^{-1}, respectively). *trans*-**1a** was found to exhibit lower binding constants with DS and DAP than *cis*-**1a** and are almost on par with the binding constants displayed with hTeloC or hTeloG - *trans*-**1a** shows little discrimination between the strength of binding to any of the DNA sequences.

*Table 2.2: Emission Intensity and Intrinsic Binding Constants of cis-**1a**, mer-**1a**, and trans-**1a**. [a] 5 μM Ru complex with 20 μM DNA, λ_{ex} = 490 nm (mer), 550 nm (trans), 590 nm (cis), and λ_{em} = 690 nm (mer), 700 nm (trans), 700 nm (cis). [b] Obtained from absorption titration of 0 μM to 20 μM DNA into 5 μM Ru complex. Error bars represent the standard deviation from multiple repeats.*

		Normalised Emission Increase[a]	Intrinsic Binding Constant (K_b) 10^6 M^{-1}[b]
cis-**1a**	DAP	41.19 ± 0.24	6.94 ± 0.26
	DS	54.67 ± 2.83	8.40 ± 1.01
	hTeloC	21.95 ± 0.10	1.13 ± 0.15
	hTeloG	15.85 ± 0.66	0.63 ± 0.02
mer-**1a**	DAP	1.02 ± 0.04	0.60 ± 0.01
	DS	1.03 ± 0.02	0.78 ± 0.13
	hTeloC	0.00 ± 0.01	0.63 ± 0.00
	hTeloG	0.93 ± 0.43	0.30 ± 0.13
trans-**1a**	DAP	5.42 ± 0.30	3.39 ± 1.40
	DS	3.40 ± 0.28	3.33 ± 0.24
	hTeloC	2.90 ± 0.71	2.27 ± 0.43
	hTeloG	3.26 ± 0.79	2.24 ± 0.73

There seems to be a direct correlation between binding constant and the emission intensity increases. *cis*-**1a** displays the greatest "switch on" effect in the order of DS > DAP > hTeloC > hTeloG and also displays the same order for the intrinsic binding constants. *cis*-**1a** has a clear preference for DS and DAP with hTeloC and hTeloG causing a much

smaller photophysical response. *mer*-**1a** does not show the same level of discrimination and the binding constants largely match with the emission response. *trans*-**1a**, however, exhibits much tighter binding to hTeloC and hTeloG than *cis*-**1a** but does not exhibit the same level of switch on effect. Both facial isomers display different levels of switch on effect, but the response from *cis*-**1a** is far greater than that of *trans*-**1a** and cannot be simply explained by an increased binding strength to the DNA.

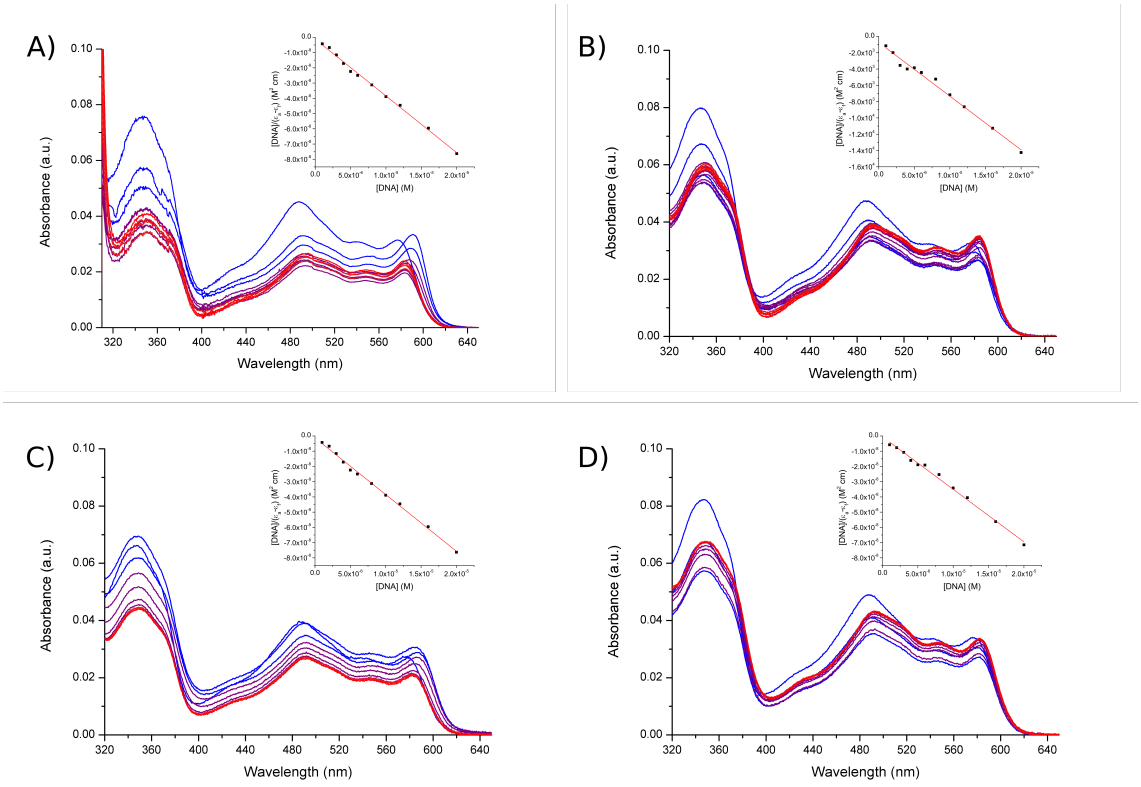

Figure 2.11: Absorption titrations of 4.5 µM *cis-**1a** and* 0 µM *to* 20 µM *(blue to red) of A) DAP, B) DS, C) hTeloC, and D) hTeloG with [DNA] vs [DNA]/($\epsilon_a - \epsilon_f$) inset*

Bathochromic shifts in the ^{3}MLCT bands in a absorption titration indicate a lowering of the ^{3}MLCT transition energy, whereas hypochromism is associated with the strength of intercalation into the DNA bases, resulting from $\pi - \pi$ stacking interactions between the Ru complex and the DNA bases.[104] The strength of intercalation is found to correlate with increasing chromatic shifts. This could unveil more information surrounding the mystery of the switch on effect in *cis*-**1a** and the lack of switch on effect in *trans*-**1a**.

Both bathochromic and hypochromic changes are observed upon addition of all DNA sequences to all Ru complexes (Table 2.3). The largest hypochromic shift observed is of *cis*-**1a** when bound to the DAP i-motif. *mer*-**1a** generally exhibits the lowest amount of

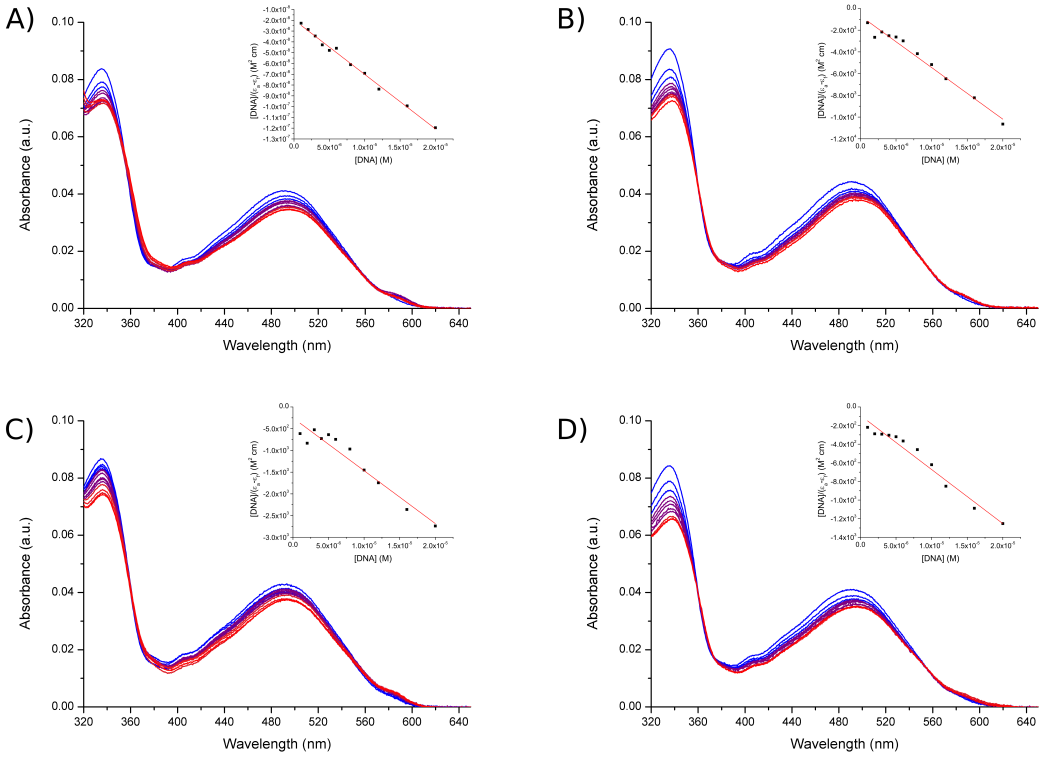

Figure 2.12: Absorption titrations of 4.5 µM *mer-**1a** and* 0 µM *to* 20 µM *(blue to red) of A) DAP, B) DS, C) hTeloC, and D) hTeloG with [DNA] vs [DNA]/($\epsilon_a - \epsilon_f$) inset*

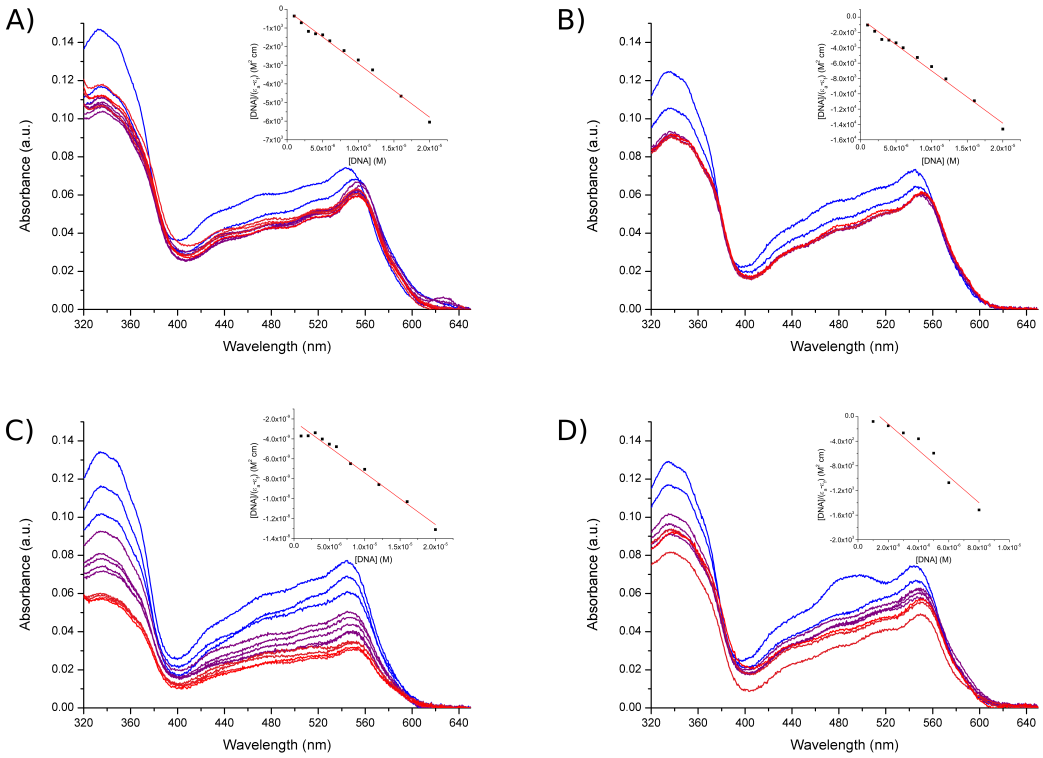

Figure 2.13: Absorption titrations of 4.5 µM *trans-**1a** and* 0 µM *to* 20 µM *(blue to red) of A) DAP, B) DS, C) hTeloC, and D) hTeloG with [DNA] vs [DNA]/($\epsilon_a - \epsilon_f$) inset*

bathochromic shift in the presence of DNA. Despite the large bathochromic shifts observed with *trans*-**1a**, it generally exhibits low amounts of hypochromicity.

Table 2.3: Absorption titration data obtained from the end point of a titration of 0 µM *to* 20 µM *DNA into* 5 µM *Ru complex. Error bars represent the standard deviation from multiple repeats.*

		Bathochromicity (nm)	Hypochromicity (%)
cis-**1a**	DAP	7 ± 0	48 ± 2
	DS	7 ± 0	21 ± 0
	hTeloC	9 ± 1	30 ± 2
	hTeloG	7 ± 1	48 ± 0
mer-**1a**	DAP	6 ± 2	26 ± 2
	DS	3 ± 1	27 ± 1
	hTeloC	4 ± 1	27 ± 2
	hTeloG	4 ± 0	37 ± 1
trans-**1a**	DAP	7 ± 1	18 ± 1
	DS	8 ± 1	13 ± 5
	hTeloC	6 ± 1	42 ± 1
	hTeloG	8 ± 1	25 ± 0

One of the largest hypochromic shifts is between *cis*-**1a** and hTeloG, this is contrary to what one would expect given the binding strengths and switch on effects. When bound to this DNA sequence *mer*-**1a** shows its largest amount of hypochromism (37 ± 1 %) and a moderate amount of hypochromism will all types of DNA . *trans*-**1a** exhibits its largest hypochromic shift with hTeloC, which conversely has the lowest amount of binding and emission increase. The highest amount of hypochromism is displayed when interacting with DAP or DS, with which it also displays the highest strength of binding and switch on effects. This inverse relationship between switch on effect or binding strength, with the percentage of hypochromism continues with *cis*-**1a** and DS. The exception to this is with DAP which displays a high level of switch on, binding strength, and hypochromism. There seems to be very little relationship between bathochromicity and any of the other photophysical properties.

It seems at this point that greater chromatic shifts (except for *cis*-**1a** and DAP) are equated with a lower binding strength and lower emission intensity increases. This seems counter intuitive when compared with dppz-based probes where increased chromatic shifts lead to a greater switch on effect. This, however, is not the case in this class of complex; a greater chromatic shift does not necessitate a greater emission switch on, and, as already established, a strong binding strength also does not necessitate a greater switch

on. There is no indication that a lowering of the ^{3}MLCT band in the absorption correlates with the emission intensity increases observed and the binding mode is still difficult to ascertain from this data alone. Increased interaction between the aromatic ligands of $[Ru(bqp)_2]^{2+}$ and the DNA base pairs may not be the cause of the observed light switch.

2.2.3 Fluorescent Indicator Displacement Assay

To understand more about the strength and character of the Ru-DNA interaction, the ability of the Ru complexes to displace a known DNA binder, such as ethidium bromide,[105] was investigated. In our own group, such an assay has been developed with the less toxic thiazole orange (TO).[106] TO shows no fluorescence in the absence of DNA but once in the presence of DNA, undergoes a conformational change that leads to a high level of fluorescence., which then can be switched off by displacing TO with another compound and observing the fluorescence of TO decreasing.[107]

Table 2.4: % TO displacement and DC_{50} results of 0 µM *to* 4.5 µM *cis-**1a**, mer-**1a**, and trans-**1a** with* 1 µM *DAP, DS, hTeloC and hTeloG. Error bars represent the standard deviation from multiple repeats.*

		D_{TO} (%)	DC_{50} (µM)
cis-**1a**	DAP	87 ± 1	1.61 ± 0.01
	DS	69 ± 1	2.02 ± 0.01
	hTeloC	43 ± 2	>4.50
	hTeloG	66 ± 1	2.32 ± 0.00
mer-**1a**	DAP	66 ± 1	2.52 ± 0.00
	DS	53 ± 1	3.64 ± 0.01
	hTeloC	21 ± 2	>4.50
	hTeloG	30 ± 2	>4.50
trans-**1a**	DAP	45 ± 3	>4.50
	DS	40 ± 2	>4.50
	hTeloC	32 ± 2	>4.50
	hTeloG	48 ± 2	>4.50

Using 1 µM of DNA and additions of Ru complex from 0.5 µM to 4.5 µM, the amount of TO displacement and the corresponding DC_{50} values were obtained (Table 2.4). None of the *trans*-**1a** titrations displaced more than 50% of the TO so no DC_{50} values were obtained, as were some of the other titrations with *mer*-**1a** and *cis*-**1a**. The highest displacement and lowest DC_{50} were observed with *cis*-**1a** and DAP, followed by the same complex and DS and hTeloG. In general, *cis*-**1a** displaced TO more effectively from all types of DNA than either *mer*-**1a** or *trans*-**1a**.

There seems to be little correlation between the K_bs and the D_{TO} values found here. This could be down to a number of reasons: the binding location of TO is unknown, the Ru complex could bind in a different location to that of TO, the binding strength of TO is unknown in some the DNA sequences used, and quenching effects between the Ru complexes and TO could be occurring.

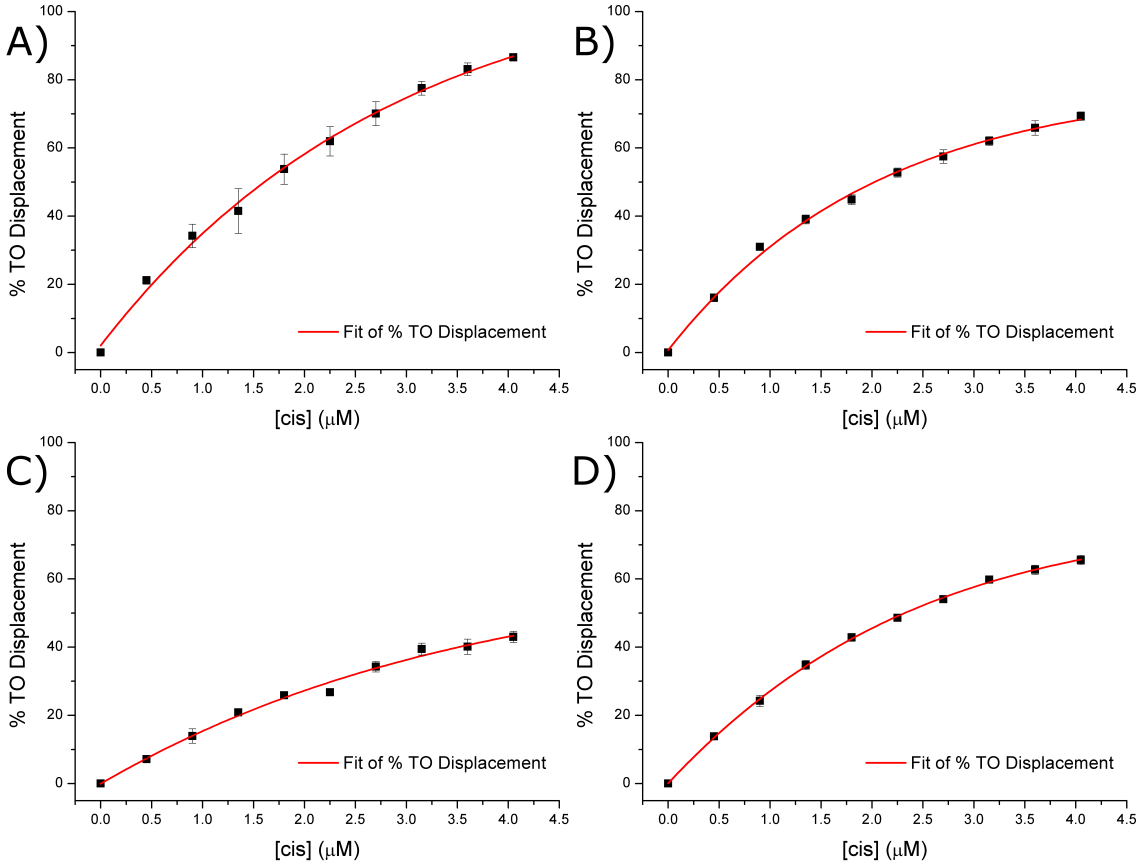

Figure 2.14: % TO displacement of 0 μM *to* 4.5 μM *cis-**1a** with* 1 μM *A) DAP, B) DS, C) hTeloC and D) hTeloG. Error bars represent the standard deviation from multiple repeats.*

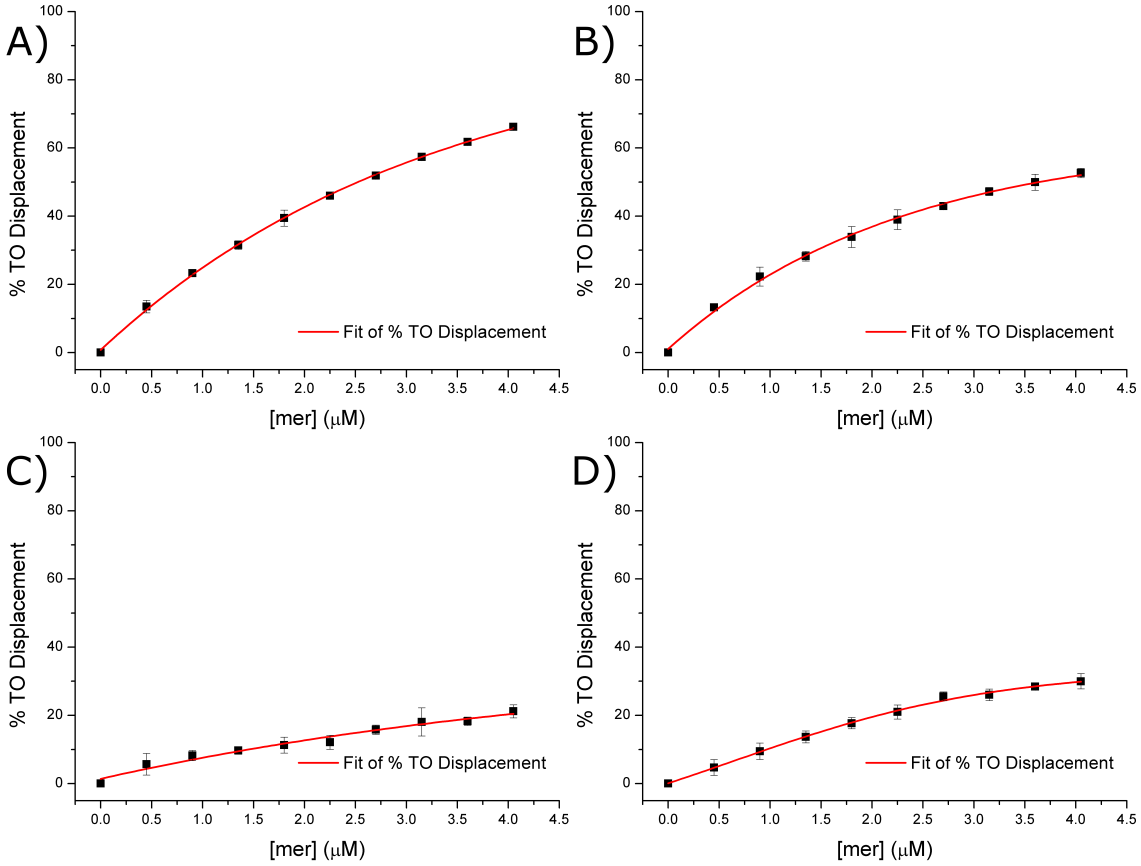

Figure 2.15: % TO displacement of 0 μM *to* 4.5 μM *mer-**1a** with* 1 μM *A) DAP, B) DS, C) hTeloC and D) hTeloG. Error bars represent the standard deviation from multiple repeats.*

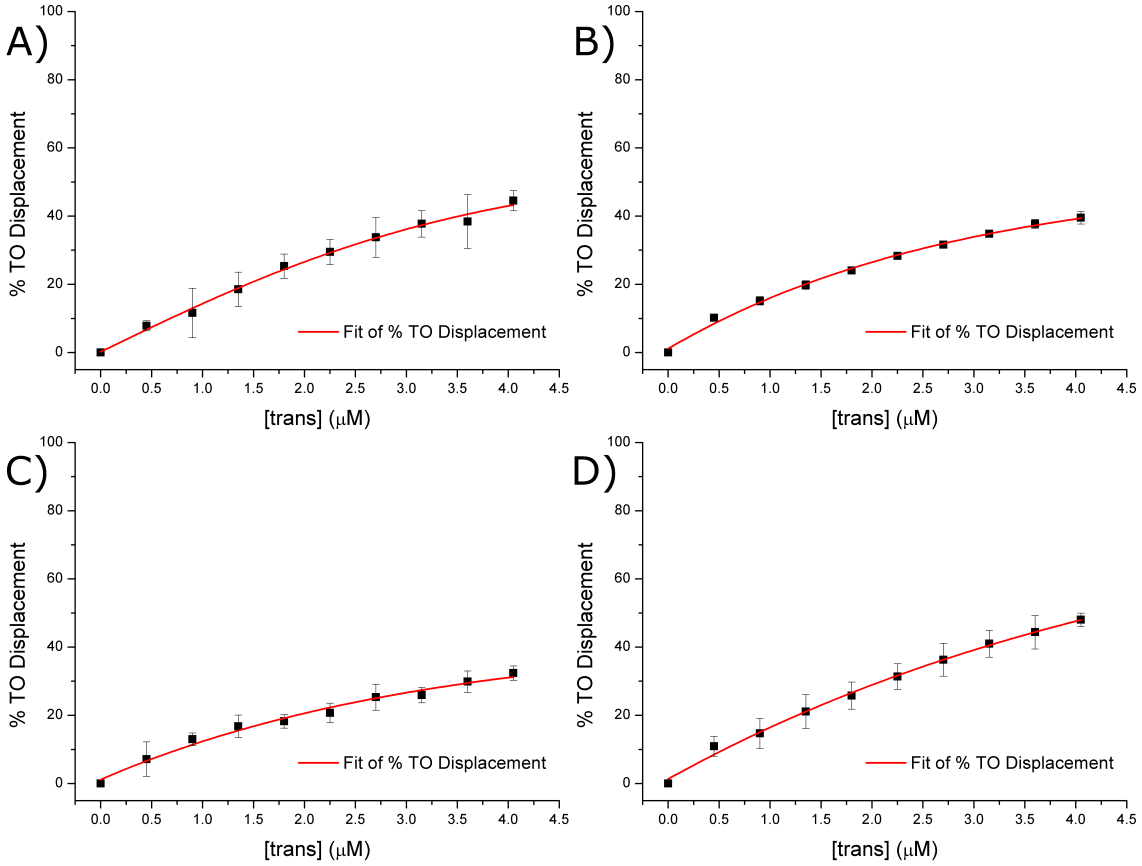

Figure 2.16: % TO displacement of 0 μM *to* 4.5 μM *trans-**1a** with* 1 μM *A) DAP, B) DS, C) hTeloC and D) hTeloG. Error bars represent the standard deviation from multiple repeats.*

The interactions between the TO, DNA and the Ru probe combined is too complex to decipher what is occurring in reality. Instead, attention was turned to investigate the the source of the light switching mechanism in *cis*-**1a**.

2.2.4 Finding the Source of the Light Switching Mechanism

The most common switch on effect in Ru-DNA probes is that caused by a change in the interaction between the fluorophore and the solvent, such as in $[Ru(L)_2(dppz)]^{2+}$, which displays a bright fluorescence in aprotic organic solvents, such as MeCN, but is in an "off" state in aqueous media.[108] Intercalation into DNA protects the dppz ligand from water and leads to a large increase in emission. The three isomers of $[Ru(bqp)_2]^{2+}$ do not possess the phenazine nitrogens present in the dppz complex, the only nitrogen atoms in bqp are coordinated to the central Ru atom. Solvent interactions were, however, still investigated to see if this was in fact the source of the light switching mechanism. *cis*-**1a**, however, displays no switch on effect in either ethanol, isopropanol, or acetonitrile (Figure 2.17).

This, as well as the lack of external nitrogens, pointed away from the possibility of solvent interactions causing the switch on effect in this isomer.

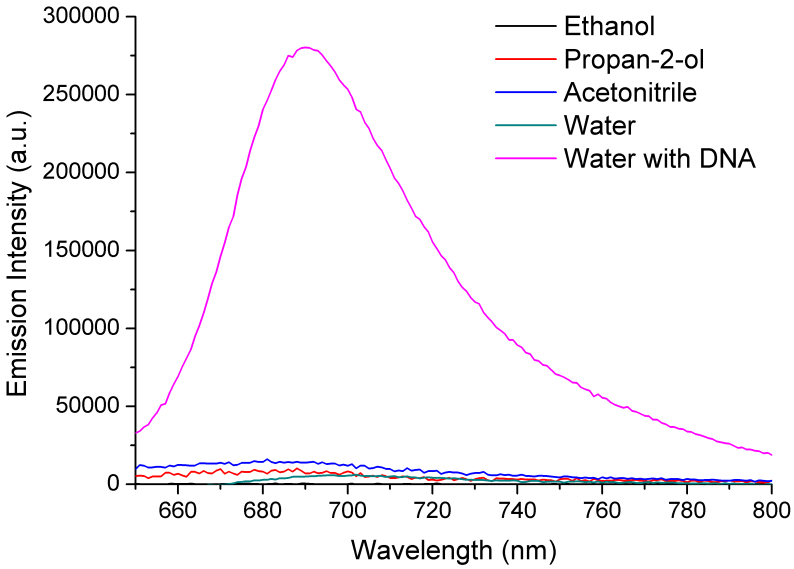

*Figure 2.17: Emission intensity of cis-**1a**$[PF_6]_2$ in ethanol (black), isopropanol (red), acetonitrile (blue), and cis-**1a** in water (green) and in the presence of DNA (pink)*

Next, to probe this mechanism further, aggregation-induced emission (AIE) was investigated as a possible cause. Most AIE probes feature functional groups that either interact intermolecularly, e.g. via halogen bonding, or possess freely rotating functional groups that rotate in solution. When aggregated due to concentration an enhancement in the emissive properties of the complexes is observed due to these inter or intramolecular interactions.[109–111]

Sheet *et al.*, reported the synthesis and AIE properties of $[Ru(phen)_2(diCl-phen)]^{2+}$ (diCl-phen = 4,7-dichlorophenanthroline, Figure 2.18) where increasing fractions of H_2O:MeCN (0:10 to 9:1) solutions containing the organically soluble PF_6^- salt led to increasing emission intensities, visible by the naked eye.[109] Increased π stacking interactions, stabilised by increased halogen bonding led to decreased intramolecular motion which can inhibit the radiative decay of the ^{3}MLCT. Work from Tang and co-workers have shown that restriction of intramolecular rotation in hexaphenylsilole (HPS) and arylbenzene compounds (Figure 2.18) leads to a switching on of their emissive properties in much the same way.[112,113]

Whilst $[Ru(bqp)_2]^{2+}$ does not contain any rotating functional groups, a decrease in intramolecular motion due to DNA binding cannot be ruled out. With this in mind

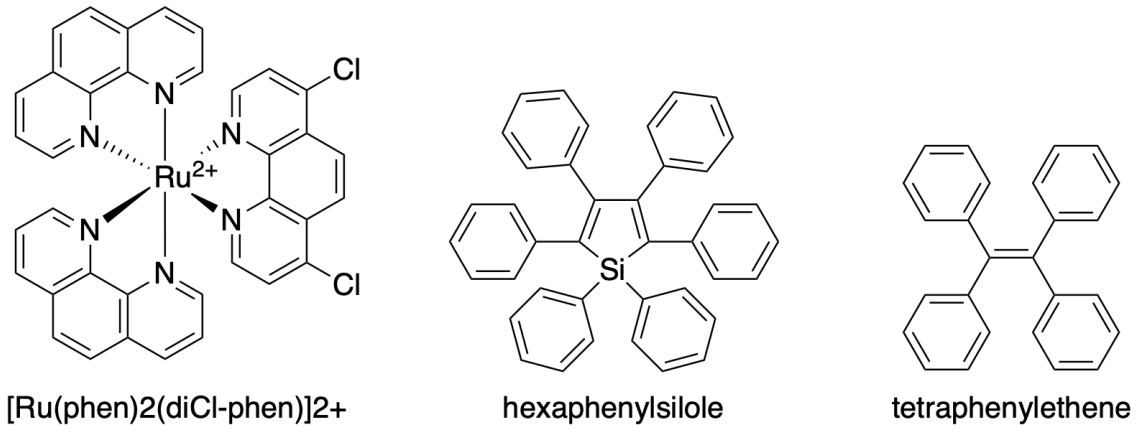

Figure 2.18: One inorganic ($[Ru(phen)_2(diCl-phen)]^{2+}$ (left))[109] and two organic (hexaphenylsilole (centre) and tetraphenylethene (right))[112] examples of aggregation-induced emission probes

the PF_6^- salt of *cis*-**1a** in acetonitrile solutions with increasing quantities of water (0 - 90%) were prepared. The insolubility of the PF_6^- salt in water would cause a higher concentration of the Ru complex in the MeCN, and thus aggregation, as the quantity of water increased. Similarly, increasing amounts of PEG-300 solution in water - a common crowding agent - were prepared using the Cl^- salt of *cis*-**1a**. Neither of these experiments yielded any switch on effect in *cis*-**1a** (Figure 2.19).

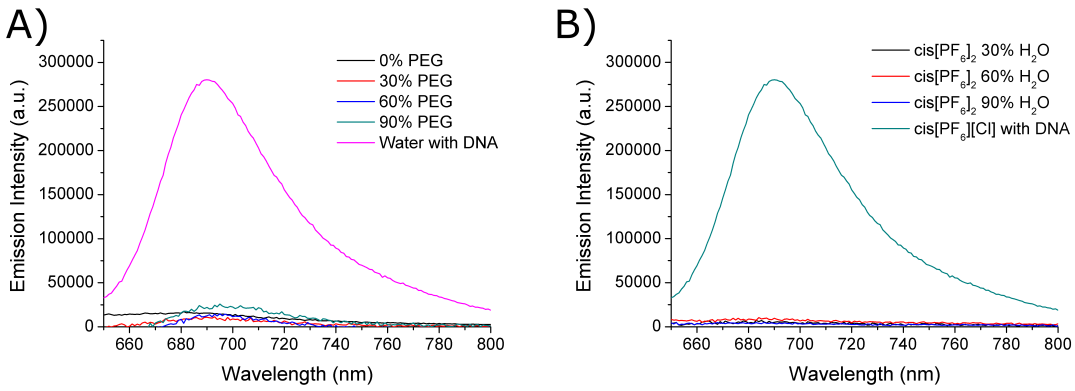

Figure 2.19: Emission intensity of A) 9 μM *cis-**1a** in water with increasing amount of PEG-300, and B)* 9 μM *cis-**1a**$[PF_6]_2$ in MeCN with increasing amount of water*

At this stage, it seemed as though neither solvent exclusion nor AIE are causing the emission switch on effects observed when *cis*-**1a** is bound to DNA. It was proposed that perhaps time-resolved emission may lead to a greater understanding of the Ru-DNA interactions, but may also offer a way to identify specific DNA sequences, such as in the previous discussed case presented by Shivalingham *et al.*[20]

Time-resolved Emission

Using multi-channel scaling (MCS) the time-resolved emission of the complexes in the absence and presence of DNA were measured. The decay curves were fitted using $I(t) = \alpha_1 e^{-t/\tau_1} + \alpha_2 e^{-t/\tau_2} + ... + \alpha_n e^{-t/\tau_n}$ where α and τ are the amplitude and lifetime of each component. The average lifetime was also calculated using $\bar{\tau} = \Sigma \alpha_i \tau_i$. All three isomers displayed nanosecond emission lifetimes (Table 2.5). *mer*-**1a** displays very long, microsecond phosphorescence in the presence and absence of DNA with the $\bar{\tau}$ of free complex being 758 ± 11 ns. The reported literature value for the complex is 3.0 µs and this discrepancy can be attributed to the literature studies being conducted in deaerated acetonitrile and these studies being in aerated aqueous buffer. The lifetime of *mer*-**1a** is far longer than those of two facial isomers with or without DNA and possesses a two component decay. The first, which contributes very little to the overall decay is much shorter than the second (166 ± 8 ns vs 768 ± 12 ns, respectively). When bound to DNA the amplitude of the longer second component drops significantly, in the case of hTeloC there is a 47% decrease, but the lifetime of the component increase significantly, *ca* 2-fold. The increase of the amplitude of the short component upon DNA is curious, the presence of the DNA must be enhancing the population of that excited state via electronic, steric or solvent related processes.

The decays of *cis*-**1a** and *trans*-**1a** consist of two components in the absence of DNA and yield very low levels of emission, with decay to a nonradiative ^{3}MC a possible cause. The amplitude of this second component is greater in *trans*-**1a** than *cis*-**1a**, which is reflected in their levels of emission intensity. In the presence of DNA, a third component arises in *cis*-**1a**. The new additional component could be explained in a number of ways, this could arise from a portion of the population of Ru complex binding DNA and the presence of the first and second component representing the portion of the population that is unbound. It could also represent radiative decay from a second ^{3}MLCT excited state that, prior to binding to DNA, decayed via vibrational nonradiative pathways, with the bound species exhibiting all three components in its decay. There is a direct correlation between the amplitude of this third component and emission intensity increases observed upon binding all types of DNA. The emergence of the third lifetime component in *cis*-**1a** is

Table 2.5: Time-resolved emission data of 5 μM Δ-, Λ-, *and cis-***1a** *with* 20 μM *DAP, DS, hTeloC and hTeloG using a* 485 nm *LED source and measuring at* 700 nm *with multi-channel scaling. Error bars represent the standard deviation from multiple repeats.*

		α_1	τ_1 (ns)	α_2	τ_2 (ns)	α_3	τ_3 (ns)	$\bar{\tau}$ (ns)	Change in $\bar{\tau}$ vs no DNA
cis-**1a**	No DNA	0.96 ± 0.02	23 ± 1	0.04 ± 0.02	338 ± 1			37 ± 6	
	DAP	0.40 ± 0.01	62 ± 14	0.39 ± 0.02	261 ± 14	0.21 ± 0.03	1049 ± 40	352 ± 27	9.61 ± 0.75
	DS	0.43 ± 0.02	62 ± 3	0.32 ± 0.02	181 ± 0	0.26 ± 0	746 ± 17	275 ± 0	7.51 ± 0.00
	hTeloC	0.36 ± 0.10	57 ± 15	0.47 ± 0.09	192 ± 23	0.17 ± 0.01	783 ± 48	239 ± 3	6.53 ± 0.08
	hTeloG	0.45 ± 0.04	37 ± 6	0.41 ± 0.03	177 ± 13	0.14 ± 0.01	757 ± 49	197 ± 4	5.38 ± 0.11
mer-**1a**	No DNA	0.07 ± 0.00	166 ± 8	0.93 ± 0.00	768 ± 12			758 ± 11	
	DAP	0.23 ± 0.05	341 ± 29	0.77 ± 0.05	1,714 ± 51			1,634 ± 77	2.15 ± 0.10
	DS	0.15 ± 0.05	191 ± 17	0.85 ± 0.05	2,080 ± 42			2,048 ± 56	1.25 ± 0.03
	hTeloC	0.56 ± 0.07	610 ± 26	0.44 ± 0.07	1,498 ± 81			1,187 ± 4	0.69 ± 0.00
	hTeloG	0.18 ± 0.04	318 ± 95	0.82 ± 0.04	1,764 ± 36			1,720 ± 58	0.84 ± 0.03
trans-**1a**	No DNA	0.81 ± 0.01	43 ± 2	0.19 ± 0.01	524 ± 25			136 ± 2	
	DAP	0.60 ± 0.01	213 ± 6	0.40 ± 0.01	849 ± 17			468 ± 3	3.44 ± 0.02
	DS	0.71 ± 0.01	176 ± 5	0.29 ± 0.01	628 ± 18			308 ± 3	2.26 ± 0.02
	hTeloC	0.55 ± 0.01	216 ± 7	0.45 ± 0.01	907 ± 17			527 ± 3	3.87 ± 0.02
	hTeloG	0.65 ± 0.01	153 ± 4	0.35 ± 0.01	713 ± 14			350 ± 2	2.57 ± 0.01

therefore clearly playing a major role in the emission intensity increases that are observed when bound to DNA.

Table 2.6: 5 µM *Ru complex with a total concentration of* 15 µM *DNA using* 485 nm *LED source and measuring at* 700 nm *with multi-channel scaling. Error bars represent the standard deviation from multiple repeats.*

	DS + hTG	DS + hTG + DAP
α_1	0.39 ± 0.03	0.41 ± 0.02
τ_1	44 ± 5	50 ± 4
α_2	0.36 ± 0.03	0.40 ± 0.02
τ_2	171 ± 13	231 ± 13
α_3	0.25 ± 0.01	0.19 ± 0.01
τ_3	736 ± 15	969 ± 33
$\bar{\tau}$	562 ± 14	679 ± 25

This third component of *cis*-**1a** when bound to DAP is far longer than when bound to other types of DNA. To investigate whether this could be used to identify the presence of DAP in the presence of other DNA sequences, the lifetime of *cis*-**1a** was measured in the presence of both DS and hTeloG by the addition of the Ru complex to the combined solution of DNA sequences to act as a control measurement (Table 2.6). Both the amplitude and lifetime of each component gave an almost identical value to that of *cis*-**1a** bound to DS, confirming that *cis*-**1a** binds DS far better than the human telomeric G-quadruplex. *cis*-**1a** was then also added to a separate solution containing DS, hTeloG and DAP, with the lifetime being obtained. In this case, the amplitudes and lifetimes became more reflective of that when bound to DAP, but not perfectly reflective. There was still some subpopulation of the total that was bound to DS. A good example of this is in the lifetime of the second component; when bound to DS only this is 181 ns and to DAP only is 261 ns, compare these values to when *cis*-**1a** is bound to the mixture of DS, hTeloG and DAP (231 ns) and one will find the value is below that of DAP but still above the statistical mean of the two values, implying that more of the Ru complex population is bound to DAP than DS.

The lifetime of the third component is far longer (*ca* 200 ns) with DAP present than without. This discovery means that not only does *cis*-**1a** bind DAP more favourably than DS but it can also identify when DAP is present in a mixture of other DNA sequences. It was at this point that the separation of the enantiomers of *cis*-**1a** seemed more pertinent that ever - could the enantiomeric discrimination of DNA yield even better results? Could

the study of the enantiomers shine more light on the switch on mechanism in emission intensity?

2.2.5 Δ and Λ Enantiomers of *cis,fac*-[Ru(bqp)$_2$]$^{2+}$

Attempts to separate the two enantiomers by recrystallisation with antimony D-tartrate or L-tartaric acid were unsuccessful, with the $[\alpha]_D$ values showing no change. Instead HPLC separation techniques were employed. Initial separation attempts were made using MeOH with 0.05% TFA and the racemic mixture as a Cl^- salt on a Chiralpak IC column, which did not yield sufficient separation (Figure 2.20). To lower the solubility of the complex in order to try to slow down their separation along the column, increasing percentages of EtOH were used. This yielded some better separation and ultimately using 90% EtOH gave enough separation to see changes in the circular dichroism (CD) signals of the solutions.

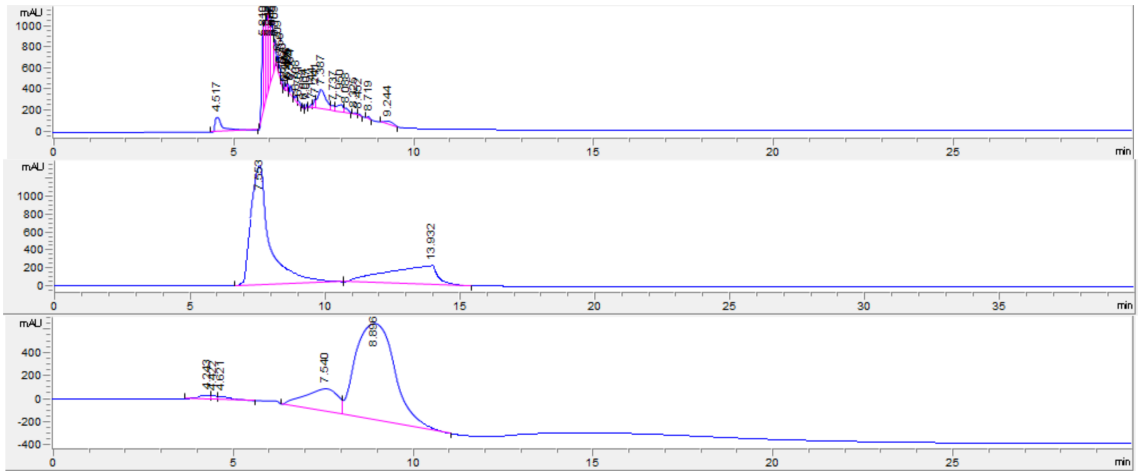

*Figure 2.20: HPLC trace from the separation of Δ- and Λ,cis-**1a** in 100% MeOH (top), 10% MeOH in EtOH (middle), and 100% IPA (bottom), all with 0.05% TFA over 30 mins*

To see if these results could be improved any further, IPA was used. No sufficient separation was achieved under these conditions so it was decided that 90% EtOH and 10% MeOH would be used to separate the compounds. Whilst further attempts to optimise the conditions could have been made, the current separation was sufficient and the quantities that could be passed down the column were in line with those discussed earlier, so the conditions were not changed further. Both the chemical purity and enantiopurity of the enantiomers were checked using the extinction coefficients in comparison to the racemic

mixture and their CD spectra, respectively (Figure 2.21 and Figure 2.22).

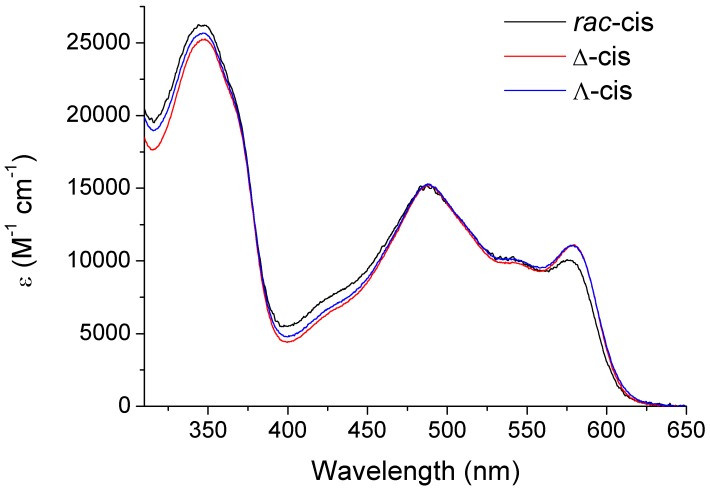

*Figure 2.21: Extinction coefficients of rac-, Δ and Λ,cis-**1a** in H_2O*

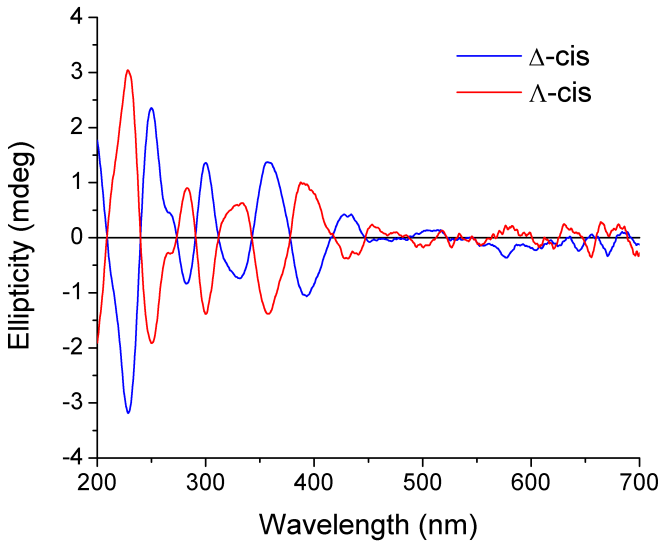

Figure 2.22: CD spectra of 10 µM Δ *and* Λ,*cis-**1a** in water*

To assign the two enantiomers as either Δ or Λ, a crystal structure of at least one enantiomer must be obtained. Crystals of both enantiomers were grown from slow diffusion of diethyl ether into a methanolic solution of each enantiomer. This yielded red/purple crystals for both enantiomers. Only one enantiomer, however, yielded X-ray diffraction quality crystals (). Despite multiple batches of crystal growth and multiple screening of crystals per growth batch, Λ,*cis*-**1a** did not grow crystals of high enough

quality to obtain a structure. After multiple attempts, it was concluded that the crystal structure of Δ enantiomer, the HPLC trace, and the CD spectra of the two separated enantiomers were enough to be confident in their configurations.

Figure 2.23 shows a graphical depiction of how these two enantiomers were assigned their absolute configurations. Setting the central pyridine of the bottom bqp ligand (red) to 0°, the pyridine of the top bqp (blue) will be at an either −90° or 90° angle, i.e. a clockwise or anticlockwise position. The complex at 90° (anticlockwise) is right handed and is therefore assigned as Δ with the clockwise enantiomer assigned as Λ, in the same way that bidentate complexes are assigned. The CD spectra of the enantiomers shows that, not only are they pure, as the signals are almost perfectly opposite and equal to each other, but that they have a complex "undulating" characteristic. It is from this crystal structure and the CD spectra that both enantiomers were assigned their absolute configuration, despite the lack of crystal structure of Λ.

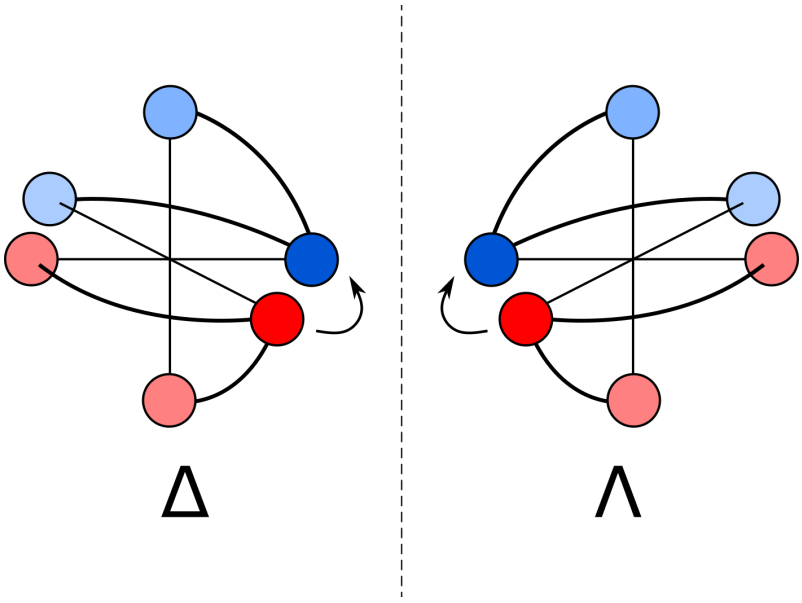

*Figure 2.23: 3D depiction of Δ (left) and Λ,cis-**1a** (right) with arrows indicating the chirality of the complexes*

The emission of the Λ enantiomer with DS displays a lower emission increase when compared to that of the racemic mixture - from 55-fold to 21-fold - and the Δ enantiomer displays an approximate equal and opposite effect to 79-fold (Table 2.7). The enantiomeric discrimination for the quadruplex structures is less dramatic, with hTeloC and hTeloG staying largely the same. The biggest change here was the interaction with DAP, which sees an increase of 41-fold in the racemic mixture and either 60-fold or 47-fold with the

*Table 2.7: Biophysical properties of Δ-, Λ-, and rac,cis-**1a**. [a] 5 μM Ru complex with 20 μM DNA using a 485 nm LED source and measuring at 700 nm with multi-channel scaling. [b] 5 μM Ru complex with 20 μM DNA, $\lambda_{ex} = 590\,\text{nm}, \lambda_{em} = 700\,\text{nm}$. [c] Obtained from absorption titration of 0 μM to 20 μM DNA into 5 μM Ru complex. Error bars represent the standard deviation from multiple repeats.*

		$\bar{\tau}$ (nm)[a]	Increase of $\bar{\tau}$ vs no DNA[a]	Normalised Emission Increase[b]	Intrinsic Binding Constant (K_b) $10^6\ \text{M}^{-1}$[c]	Bathochromicity (nm)[c]	Hypochromicity (%)[c]
Δ,*cis*-**1a**	No DNA	36.6 ± 6					
	DAP	238 ± 13	6.5 ± 0.6	59.76 ± 0.70	3.88 ± 0.60	7 ± 1	30 ± 3
	DS	312 ± 7	8.5 ± 0.2	78.78 ± 2.60	4.62 ± 0.93	7 ± 1	36 ± 3
	hTeloC	222 ± 1	6.1 ± 0.0	28.92 ± 0.07	0.58 ± 0.13	5 ± 1	33 ± 2
	hTeloG	135 ± 12	3.7 ± 0.3	20.09 ± 4.27	0.53 ± 0.20	5 ± 1	37 ± 3
Λ,*cis*-**1a**	No DNA	33.1 ± 4					
	DAP	225 ± 57	6.8 ± 1.7	46.53 ± 2.37	3.13 ± 0.06	6 ± 1	35 ± 3
	DS	121 ± 14	3.6 ± 0.4	21.37 ± 4.97	1.21 ± 0.20	4 ± 1	26 ± 1
	hTeloC	199 ± 11	6.0 ± 0.3	29.18 ± 2.52	2.73 ± 0.76	5 ± 1	33 ± 2
	hTeloG	198 ± 0	6.0 ± 0.0	23.89 ± 1.19	0.57 ± 0.11	1 ± 1	37 ± 3
rac,*cis*-**1a**	No DNA	36.6 ± 6					
	DAP	753 ± 85	9.6 ± 0.7	41.19 ± 0.24	6.94 ± 0.26	7 ± 0	48 ± 2
	DS	555 ± 3	7.5 ± 0.0	54.67 ± 2.83	8.40 ± 1.01	7 ± 0	21 ± 0
	hTeloC	481 ± 5	6.5 ± 0.1	21.95 ± 0.10	1.13 ± 0.15	9 ± 1	30 ± 2
	hTeloG	473 ± 8	5.4 ± 0.1	15.85 ± 0.66	0.63 ± 0.02	7 ± 1	48 ± 0

Δ and Λ isomers, respectively. This change shows that the Λ isomer has the ability to discriminate between the DNA sequences, with its emission intensity increases with DAP being approximately double that of the other DNA sequences, mainly due to the fall in emission observed with this enantiomer over the racemic mixture when in the presence of DS DNA.

The increases of $\bar{\tau}$ in the Δ and Λ enantiomers in the presence of DAP are less than that of the racemic mixture, 6.5 ± 0.6 and 6.8 ± 1.7 ns vs 9.6 ± 0.8 ns, respectively (Table 2.8). Akin to changes in emission intensity, the $\bar{\tau}$ of Λ,*cis*-**1a** is shorter in relation to the racemate in the presence of DS, whilst Δ,*cis*-**1a** increases (3.6 ± 0.4 and 8.5 ± 0.2 ns vs 7.5 ± 0.0 ns, respectively). The enantiomers seem to show very little difference in their binding to hTeloC, with both showing similar levels of emission intensity and lifetime increases. Interestingly, despite the vast emission intensity responses, the τ_3 of the enantiomers in the presence of DS are not significantly different to each other, however, the amplitude of these components do differ dramatically and it is this amplitude that has the most direct correlation to the emission intensity.

The K_b values for the enantiomers shows the complexity of their interactions with DNA. Whilst the emission intensity with DAP shows an increase for the Δ enantiomer compared with the racemate, the K_b shows a decrease. In fact, the racemic mixture has a K_b approximately double that of either of the enantiomers. Either cooperative binding is occurring here or a complex interaction that skews the absorption profile of the racemic mixture so much that an accurate binding constant cannot be determined. This phenomenon also plays out with DS, whilst the Δ enantiomer displays a higher K_b value and emission intensity increase over Λ, the racemate displays a larger K_b than either. The emission intensity increase of the racemate, however, does follow the pattern of the enantiomers as it is an approximate average of the two.

The K_b values obtained for hTeloC and hTeloG do not display such a phenomenon, perhaps this is expected as the two enantiomers show far less favourable interactions with these two DNA sequences. The K_b values of hTeloC for the racemate is an approximate average of the two separated enantiomers and for hTeloG there is no significant change between the enantiomers or the racemate. For both sequences, however, there is a slight quenching of emission in the racemate compared to the two enantiomers.

Table 2.8: Time-resolved emission data of 5 μM Δ-, Λ-, *and rac,cis-**1a** with* 20 μM *DAP, DS, hTeloC and hTeloG using a* 485 nm *LED source and measuring at* 700 nm *with multi-channel scaling. Error bars represent the standard deviation from multiple repeats.*

		α_1	τ_1 (ns)	α_2	τ_2 (ns)	α_3	τ_3 (ns)	$\bar{\tau}$ (ns)	Change in $\bar{\tau}$ vs no DNA
Δ,*cis*-**1a**	No DNA	0.96 ± 0.02	23 ± 1	0.04 ± 0.02	338 ± 1			37 ± 6	
	DAP	0.38 ± 0.07	24 ± 15	0.43 ± 0.06	187 ± 15	0.18 ± 0.01	802 ± 21	238 ± 23	6.49 ± 0.64
	DS	0.35 ± 0.10	59 ± 15	0.32 ± 0.06	229 ± 79	0.33 ± 0.04	673 ± 29	312 ± 7	8.51 ± 0.18
	hTeloC	0.49 ± 0.03	57 ± 2	0.37 ± 0.02	200 ± 11	0.14 ± 0.01	865 ± 26	222 ± 1	6.07 ± 0.04
	hTeloG	0.50 ± 0.01	19 ± 3	0.37 ± 0.00	121 ± 12	0.13 ± 0.01	621 ± 8	135 ± 12	3.69 ± 0.32
Λ,*cis*-**1a**	No DNA	0.97 ± 0.02	23 ± 1	0.03 ± 0.02	340 ± 44			33 ± 4	
	DAP	0.38 ± 0.10	28 ± 14	0.44 ± 0.06	186 ± 25	0.17 ± 0.04	751 ± 26	225 ± 57	6.79 ± 1.71
	DS	0.46 ± 0.09	39 ± 18	0.48 ± 0.08	130 ± 27	0.06 ± 0.00	702 ± 62	121 ± 14	3.64 ± 0.43
	hTeloC	0.35 ± 0.01	45 ± 3	0.50 ± 0.01	162 ± 2	0.14 ± 0.00	702 ± 48	199 ± 11	6.00 ± 0.33
	hTeloG	0.43 ± 0.00	28 ± 2	0.43 ± 0.00	159 ± 3	0.15 ± 0.01	799 ± 14	198 ± 0	5.97 ± 0.00
rac,cis-**1a**	No DNA	0.96 ± 0.02	23 ± 1	0.04 ± 0.02	338 ± 1			37 ± 6	
	DAP	0.40 ± 0.01	62 ± 14	0.39 ± 0.02	261 ± 14	0.21 ± 0.03	1049 ± 40	352 ± 27	9.61 ± 0.75
	DS	0.43 ± 0.02	62 ± 3	0.32 ± 0.02	181 ± 0	0.26 ± 0	746 ± 17	275 ± 0	7.51 ± 0.00
	hTeloC	0.36 ± 0.10	57 ± 15	0.47 ± 0.09	192 ± 23	0.17 ± 0.01	783 ± 48	239 ± 3	6.53 ± 0.08
	hTeloG	0.45 ± 0.04	37 ± 6	0.41 ± 0.03	177 ± 13	0.14 ± 0.01	757 ± 49	197 ± 4	5.38 ± 0.11

Traditional Ru-DNA binding calculations mainly involve extrapolating data from absorption titrations.[40] These calculations involve the assumption that the DNA is one contiguous chain of identical binding sites, where end-chain interactions are completely outnumbered by the interactions between base pairs and are as such treated as negligible.[114] In the case of this study, where DNA sequences are made up of 22 to 24-mer oligonucleotides, this is certainly not the case. i-Motif DNA contains three loop regions as do G-quadruplexes that also present the opportunity for end-stacking onto the G-tetrad. This poses many issues in the determination of binding constants between Ru complexes when comparing the data that could be obtained from a 22-mer DS sequence and a 24-mer hTeloC that contains six C-C^+ base pairs at its core, three loop regions and one trailing single-stranded region.

Some attempts have been made to calculate binding constants using either base pairs, G-tetrads or C-C^+ pairs as the unit of DNA concentration, but these omit the loop region and end-stacking ability of the quadruplex structures. All of these issues are also present without even discussing the ability of the already intercalated i-motif C-C^+ core to incorporate an intercalating ligand. It seems that one major flaw in the current approach is in the determination of binding constants where the DNA structures contain vastly different types and locations of binding interactions.

Whilst the relationship between emission intensity and the amplitude of the third decay component are strong, there seems to be a great disparity between the binding strength of the Ru complexes to the DNA. Cooperative binding and a complex switch-on mechanism make discerning what is happening to the Ru complexes upon binding and/or excitation challenging. Computational studies could reveal insights into the switch-on mechanism and by studying the electronic transitions of the complexes in the presence and absence of DNA, a reasonable explanation as to the cause of the emission changes could be possible.

2.2.6 DFT and Docking Calculations

To begin with, *mer*-**1a**, *trans*-**1a**, Δ and Λ,*cis*-**1a** were all docked against all DNA types in AutoDock 4.2[115] using their crystal structures[71,80] with their geometries set as flexible. This enabled us to see how these complexes interact with DNA and the possible locations in

which they bind. The DNA structures used here were the human telomeric i-motif (PDB: 1ELN),[116] the human telomeric G-quadruplex (PDB: 1KF1)[117] and the same experimental double-stranded sequence used in this study which was generated in Chimera 1.10.2[118] and minimised using the Amber ff99bsc0 force field. The Ru parameters were added as "atom_par Ru 2.96 0.056 12.000 -0.00110 0.0 0.0 0 -1 -1 1 # Non H- bonding". The lack of a crystal or NMR structure of DAP limited this work to studying only the hTeloC i-motif. In fact, the sequence used is a modified hTeloC structure solved by NMR, a crystal structure of an intramolecular i-motif is yet to be obtained.

*Table 2.9: Docking results of mer-**1a**, trans-**1a**, Δ- and Λ,cis-**1a** against hTeloC, DS and hTeloG with the complexes set to a flexible geometry*

		hTeloC	DS	hTeloG
mer-**1a**	Inhibition Constant (μM)	1.80	1.33	2.41
	Binding Affinity (kcal mol)	-7.36	-7.47	-7.87
	DNA Contacts	27	65	42
trans-**1a**	Inhibition Constant (μM)	1.18	2.22	0.24
	Binding Affinity (kcal mol)	-8.18	-7.81	-9
	DNA Contacts	34	65	65
Δ,*cis*-**1a**	Inhibition Constant (μM)	0.99	1.69	0.17
	Binding Affinity (kcal mol)	-8.19	-7.87	-9.22
	DNA Contacts	93	82	65
Λ,*cis*-**1a**	Inhibition Constant (μM)	0.40	2.23	0.20
	Binding Affinity (kcal mol)	-8.73	-7.71	-9.11
	DNA Contacts	117	69	66

In these docking studies, end-stacking onto the G-quadruplex structure seems to be favoured by all the complexes, displaying both lower binding affinities and inhibition constants than other DNA types (Table 2.9 and Figure 2.24). This results in lower DNA contacts as generally only one ligand is interacting with the DNA, compare this to the i-motif structure hTeloC that has the highest number of DNA contacts with all complexes. More in-depth calculations were also necessary to elucidate the processes associated with the DNA light switching behaviour. For this, density functional theory (DFT) was employed. This was originally carried out in parallel between myself and Dr. John Fielden using Gaussian[119] and ADF,[120] respectively. It was found that ADF more easily allowed for the addition of DNA partial charges into the calculations, so ADF2018 was used and the calculations were performed by Dr. John Fielden.

The ^{3}MC states of Ru polypyridyl complexes can lie at an energy that is thermally

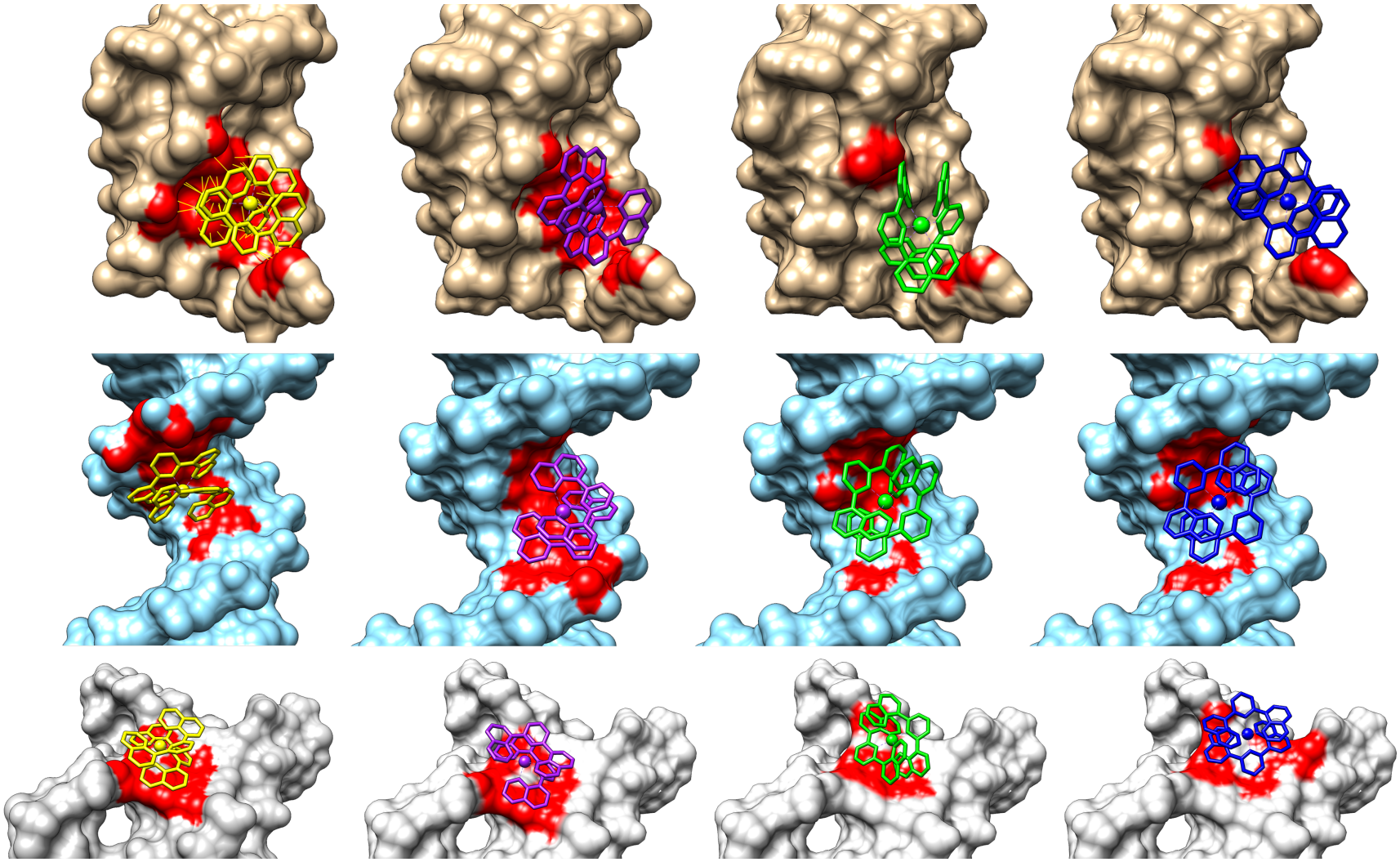

*Figure 2.24: Binding locations of the flexible geometries of Λ,cis-**1a** (yellow, left), Δ,cis-**1a** (purple, centre-right) mer-**1a** (green, centre-right), and trans-**1a** (blue, right) against hTeloC (top), DS (centre) and hTeloG (bottom), with DNA contacts coloured red, calculated with AutoDock 4.2*[115]

accessible from the emissive ^{3}MLCT excited state, as previous discussed. Previous studies into the computed electronic states of $[Ru(tpy)_2]^{2+}$ and *mer*-**1a**, have shown that the ^{3}MLCT and ^{3}MC states lie close in energy in *mer*-**1a**, but the ^{3}MLCT is elevated up to 0.28 eV above the ^{3}MC.[121–125] There is also a larger transition state barrier in *mer*-**1a** for the conversion of ^{3}MLCT to ^{3}MC, whilst for $[Ru(tpy)_2]^{2+}$, this is not as large (0.08 eV against 0.28 eV in *mer*).[124,125]

To investigate the electronic properties of the two facial isomers DFT calculations were performed. Using PBE0-dDsc functional and TZP basis set, the geometries of *mer*-**1a**, Δ,*cis*-**1a**, Λ,*cis*-**1a** and *trans*-**1a** were calculated. Single-point electronic structure calculations were then performed on these geometries using the B3LYP functional, yielding a 0.26 eV gap from the lower ^{3}MC state and the higher ^{3}MLCT for *cis*-**1a**, and 0.86 eV for *trans*-**1a**. This is consistent with the experimentally determined emission of *cis*-**1a** and *trans*-**1a** in the absence of DNA as well as the literature studies of $[Ru(tpy)_2]^{2+}$ and *mer*-**1a**. This suggests that the ^{3}MC is more favourably populated over the ^{3}MLCT leading to the lower emission intensity and lifetimes observed with both facial complexes. The similarity of these results to $[Ru(tpy)_2]^{2+}$, indicate the pathways for nonradiative decay in these complexes are most likely similar to those of the facial isomers, i.e. a smaller transition state barrier for ^{3}MLCT to ^{3}MC conversion compared with *mer*-**1a**, and also a low entropy of the ^{3}MLCT state.

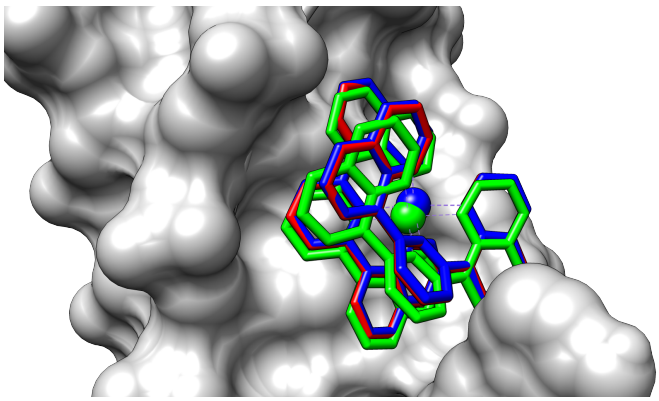

*Figure 2.25: Docked locations of the Δ,cis-**1a** GS (blue), ^{3}MLCT (red), and ^{3}MC (green) to hTeloC (grey)*

The ^{3}MC state of *mer*-**1a** features a lengthening of the N(q)-Ru-N(q) (q = quinoline) bonds that are *trans* to each other. In *mer*-**1a** these are on the same bqp ligand, but in the facial isomers these would be on the different ligands and so it is logically more favourable for this transition to occur in the facial isomers. This stretch could be dis-

favoured when bound to the sterically imposing DNA. These geometries were docked to the DNA structures using AutoDock 4.2 and three properties were extracted from these calculations, an estimated dissociation constant, the free energy of binding and the number of contacts between the Ru complex and the DNA. In order to determine how the binding location changed, the distances that the Ru atoms move in reference to the GS docking calculations were also calculated. The contacts between the Ru complex and the DNA atoms were calculated using Chimera 1.10.2 and looking for a Van der Waals overlap of -0.4 Å. AutoDock calculations of the triplet states of *cis*-**1a** suggest that the ^{3}MC state is disfavoured upon binding to DNA over that of the ^{3}MLCT state. The estimated dissociation constant, free energy of binding and the binding site location of the GS is more similar to the ^{3}MLCT state than the ^{3}MC, which in some cases move substantially in location compared to the GS (Table 2.10, Figure 2.25). This would suggest that the ^{3}MC state of *cis*-**1a** is harder to form once the complex is bound to DNA than when not.

*Table 2.10: Docking results for Δ- and Λ,cis-**1a** with DS, hTeloC and hTeloG*

		Ground-state			^{3}MC				^{3}MLCT			
		Dissociation Constant (μM)	Binding Affinity (kcal mol^{-1})	DNA Contacts	Dissociation Constant (μM)	Binding Affinity (kcal mol^{-1})	DNA Contacts	Distance from GS (Å)	Dissociation Constant (μM)	Binding Affinity (kcal mol^{-1})	DNA Contacts	Distance from GS (Å)
Δ,*cis*-**1a**	DS	1.71	-7.87	64	4.44	-7.30	65	0.69	1.66	-7.89	63	0.15
	hTeloC	0.98	-8.19	66	2.45	-7.65	77	0.54	0.9	-8.24	66	0.05
	hTeloG	0.17	-9.23	65	0.31	-8.88	58	4.91	0.16	-9.27	67	0.00
Λ,*cis*-**1a**	DS	2.23	-7.71	60	4.90	-7.24	58	3.43	1.94	-7.79	65	0.03
	hTeloC	0.4	-8.73	79	2.90	-7.56	67	0.54	0.42	-8.70	80	0.05
	hTeloG	0.2	-9.13	66	0.36	-8.79	64	4.68	0.18	-9.19	65	0.08

The partial charges of the DS and hTeloC DNA atoms surrounding the binding site of the GS of both enantiomers of *cis*-**1a** were extracted and put back into the DFT calculations. This probes the effect of the electronic influence of the DNA upon the Ru complexes. For the Δ-cis enantiomer with hTeloC, this resulted in a 0.594 eV reduction in the HOMO-LUMO gap - consistent with the bathochromic shifts seen in the absorption titrations. In the presence of either DS or hTeloC the ^{3}MLCT state of Δ becomes more stable - a 0.04 eV and 0.29 eV decrease is observed vs the ^{3}MC state, respectively. Whilst these exact numbers may not accurately reflect the experimental observations, the general trend of similar energies in the ^{3}MLCT and ^{3}MC states in the absence of DNA moving toward a more stabilised ^{3}MLCT state vs the ^{3}MC in the presence of DNA give a clearer understanding of the type of processes occurring upon DNA binding.

From the experimental and computational data presented here, it is suggested that the steric restriction imposed upon *cis*-**1a** by the DNA disfavours the population of the ^{3}MC state, and thus reduces the level of nonradiative decay occurring upon DNA binding. In the case of *trans*-**1a** this process is not as disfavoured, leading to a less extreme switch on effect than that observed in *cis*-**1a**. This combination of the steric restriction and the electronic influence of DNA upon the Ru complexes results in the switch on/off states that are observed experimentally. The influence of the electronic effects of DNA binding is assumed to play a larger part in the switch on mechanism over pure steric restriction. If steric restriction alone were to favour the emissive state then a switch on similar to, or in some cases larger than, *cis*-**1a** would be seen in *trans*-**1a** especially with the hTeloC and hTeloG sequences. The lower electronic barrier to the nonradiative decay in *trans*-**1a** must be having a larger influence on the emissive properties of this complex compared to *cis*-**1a**.

The work presented in this chapter is a large step towards to the development of an i-motif specific Ru-based light switching complex. The ability of *cis*-**1a** to distinguish DAP even in the presence hTeloG or DS DNA is remarkable. This, twinned with the discovery of, to the best of our knowledge, a new light switching mechanism that does not rely upon solvent exclusion will have ramifications in the fields of both ruthenium-based polypyridyl complexes and DNA secondary structures.

2.3. Conclusions

The study of the three isomers of $[Ru(bqp)_2]^{2+}$, as well as the two enantiomers of *cis*-**1a**, offers great promise in the development of an i-motif specific small molecule probe. *rac*,*cis*-**1a** was able to detect the presence of DAP even in the presence of the DS DNA sequences, despite having a lower binding affinity for it according to the traditional binding constant calculations. These calculations rely upon assumptions that are not suitable when dealing with DNA secondary structures that contain more complex environments and more possible binding sites than a contiguous strand of base pairs.

The promise offered by *rac*,*cis*-**1a** and its ability to identify i-motif forming DNA sequences using lifetime measurements is an important discovery for the field. Very few Ru complexes have been investigated for their i-motif affinity and all those that have did not show any affinity above those of G-quadruplex or B-form DNA. The dppz containing complexes strongly favour binding to G-quadruplex over i-motif, possibly due to the necessity of the DNA to protect the complex from water, something that is possibly not as favourable in i-motif structures as it is G-quadruplex structures.

Whilst there are still questions surrounding the light switching mechanism of *cis*-**1a**, and the limited switch on of *trans*-**1a**, a working hypothesis has been presented. A mixture of steric restriction imposed by the DNA as well as the electronic interaction with DNA may be causing *cis*-**1a** to favour the formation of the ^{3}MLCT state more in the presence of DNA than in its absence. The discovery of a new switching mechanism that does not rely upon solvent exclusion or AIE is an important step in the development of an i-motif specific probe, as well as a general DNA probe. More in-depth computational analysis could yield a better or deeper explanation but is unfortunately not possible at this time due to limitations in the parametrisation of i-motif DNA in molecular dynamics simulations.[126]

The racemic mixture in many regards outperforms either of the separated enantiomers in its preference for binding DNA. The Λ,*cis*-**1a** enantiomer, however, does pose a good starting point for the further development of an i-motif specific probe. Whilst Δ,*cis*-**1a** bound DAP better than the Λ enantiomer, the enantiomeric discrimination offered by DAP was far less than that of DS. The Λ enantiomer saw a significant drop off in emission

intensity, compared with the racemic mixture, in the presence of DS but only a moderate change with DAP, which remained almost double that of the other DNA sequences.

The following chapters are built upon this work and will show the steps taken to synthesise different analogues and discover new synthetic pathways in the further development of this project.

3. A New Synthetic Route to *cis*-$[Ru(bqp)_2]^{2+}$ and its Analogues

3.1. Introduction

In previous chapters of this work the modifications of the ancillary ligands in $[Ru(L)_2(dppz)]^{2+}$ have been discussed, here it would be apt to discuss the modification to the dppz ligand with the application of how modifications to the bqp ligand could influence the photophysical and DNA binding properties of bqp containing complexes. The possible modifications that can be made to a metal polypyridyl complex are virtually endless when incorporating both ligand and metal modifications. Changing the metal can dramatically change the photophysical properties and modifying a ligand can hinder or improve both the photophysical and DNA binding properties. Over the following pages, a small subset of both metal and ligand modifications relevant to this work will be discussed.

Many modifications have been made at the 10, 11, 12, and 13-positions of the dppz ligand (Figure 3.1). Sun *et al*., showed how addition of methyl groups at either the 10 (dppm2) or 11 and 12 (dppx) positions leads to a lower relative viscosity of the bound complex, indicating that methylation at these position hinder intercalation (Figure 3.1).[127] The same publication also shows how the addition of another azanitrogen atom at the 10-position leads to the loss of light switching properties but retains the high intercalation into DNA base pairs, suggesting that this adaption stabilises the bright state of the free complex but does not hinder the intercalative properties.

In 2016, Poulsen *et al*., published a series of analogues with additional heterocyclic moieties at the 10:11 position of the dppz ligand (pdppz and mpdppz, Figure 3.1).[128] Both

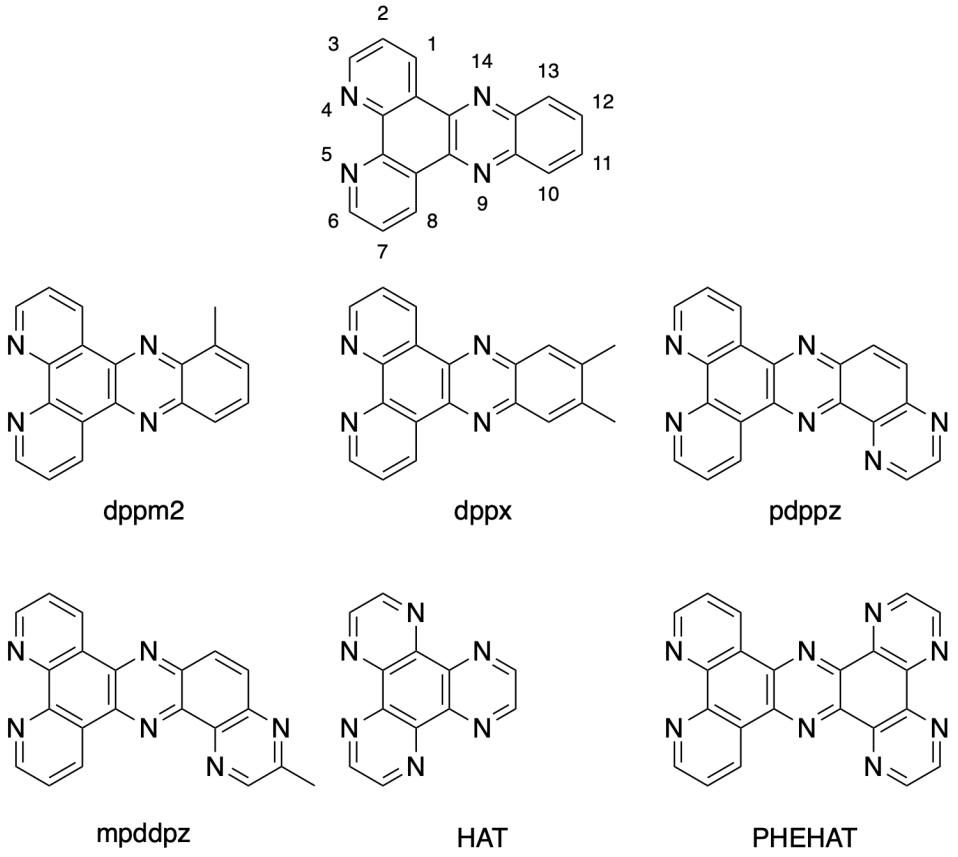

Figure 3.1: Numbering of the dppz ligand atoms and some analogues of the dppz structure

analogues when coordinated to form their respective $[Ru(phen)_2(L)]^{2+}$ complex, yielded $K_b$values in the range of 10^6 M^{-1}, with pdppz exhibiting double the binding strength of mpdppz. Both complexes retained the light switching ability that is associated with the dppz family of complexes, indicating that such a change did not substantially change the environment around the azanitrogen atoms of the phenazine moiety, as the work by Sun *et al*. did.

Other modifications of the dppz ligand can lead to very interesting and useful properties. For example, the ligands PHEHAT and HAT (PHEHAT = 1,20-phenanthrolino[5,6-**b**]1,4,5,8,9,12,-hexaazatriphenylene), HAT = 1,4,5,8,9,12-hexaazatriphenylene) display $K_b$values on par with that of the equivalent dppz containing complex (10^6 M^{-1}) and retain the light switching properties but generally exhibit higher oxidising abilities when bound to DNA.[129–132] This leads to electron transfer from the guanine of DNA to the excited complex resulting in the photocleavage of the DNA, making this family of complexes potential photodynamic therapeutic drugs.

Modifications such as these highlight how finely tuned the electronic properties of the $[Ru(L)_2(dppz)]^{2+}$ family are, and how structural modifications can change these properties.[133,134] Such changes lead to new applications, expanding our knowledge as to how these complexes interact with DNA, and their electronic properties.

3.1.1 Modification of the bqp Ligand

In 2007, Jäger *et al.*, published a selection of bqp derivatives containing different functional groups (Figure 3.2).[81] Using Suzuki-Miyaura palladium catalysed carbon coupling reactions, good yields, up to 90%, were reported. A range of electron withdrawing and donating functional groups were used, showing the versatility allowed within their reaction conditions. In refluxing toluene with $Pd(dba)_2$ and SPhos (2-dicyclohexylphosphino-2′,6′-dimethoxybiphenyl) as catalysts, various 2,6-dihalopyridine with different functional groups at the 4-position were used. Using other common reaction conditions, the nitro functionalised analogue was reduced to form an amine, which was subsequently reacted to form the bromo derivative.

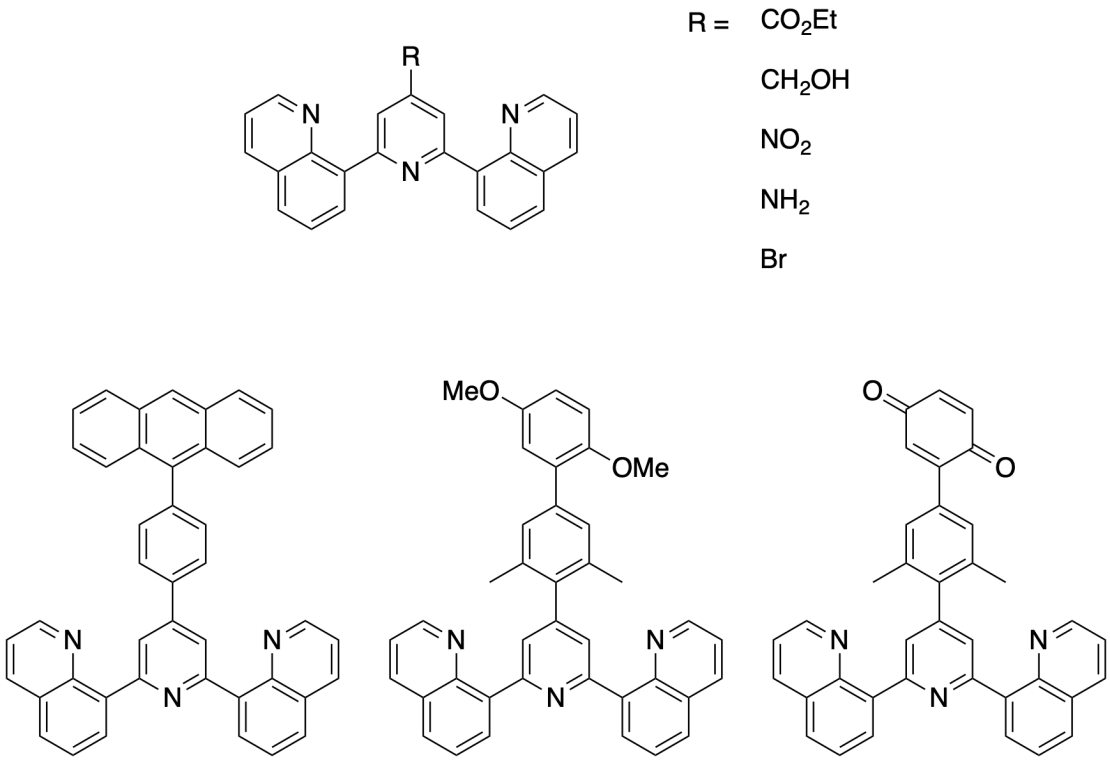

Figure 3.2: Previously published bqp analogues

This work also presented the synthesis of aryl containing bqp analogues via a Kröhnke reaction (Figure 3.3). The application of these complexes was to develop better chromophores in artificial photosynthesis, where longer lifetimes and better photophysical properties are required. The development of the aryl substituted ligands allowed for a greater donor-acceptor disparity in heteroleptic Ru complexes. This work set the foundation for the development of many different functionalised bqp ligands.[122,135,136]

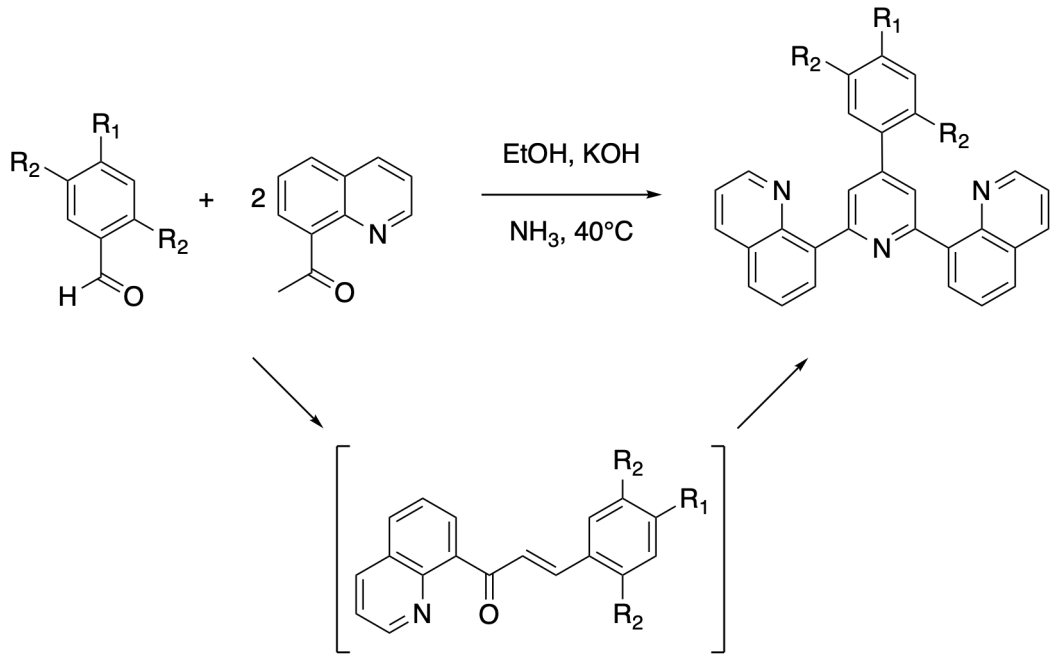

Figure 3.3: Kröhnke-type coupling reaction used to form bqp analogues

Of the ligands reported by Jäger in 2007, the corresponding *mer* ruthenium complexes were reported in 2010, with some showing stark improvements upon the photophysical properties of *mer*-$[Ru(bqp_2)]^{2+}$.[137] The homoleptic complex *mer*-$[Ru(bqpCO_2Et)_2]^{2+}$, for example, displayed a 5.5 µs lifetime, 2.5 µs longer than that of the unfunctionalised complex. The electron withdrawing effect of the ester group stabilises the ^{3}MLCT state, leading to a longer lifetime. Conversely, the electron donating methoxy group led to a decrease in the emission lifetime of $[Ru(bqpOMe)_2]^{2+}$ to 1.2 µs. The heteroleptic complex, synthesised via the $[Ru(bqpR)(MeCN)_3]^{2+}$ intermediate, $[Ru(bqpCO_2Et)(bqpNH_2)]^{2+}$, composed of one withdrawing and one donating group, led to a slight reduction in lifetime to 2.0 µs, albeit with a significantly red shifted (41 nm) emission peak.

Kumar *et al.* in 2010, reported the synthesis of many different bqp derivatives, including the ability to perform Suzuki-Miyaura reactions on the ligands whilst coordinated to

ruthenium.[136] Included in this work were a few complexes that displayed interesting photophysical changes upon modification of the electron configuration of the ligand. A bqp ligand containing a 4-substituted *m*-xylene moiety that had either a dimethoxy- or dione-substituted benzene in the 4-position (Figure 3.2) The modification of the electron withdrawing/donating effects of the two groups leads to a *ca* 3000-fold increase in lifetime from 0.91 ns to 2700 ns, respectively. A bichromophoric complex, $[Ru(bqp)(bqp-Ph-anth)]^{2+}$, was reported by Ragazzon *et al*. in 2013 and displayed an emission lifetime of 42 µs (Figure 3.2).[138] It was proposed that the anthracene appendage offered a slightly lower lying ^{3}MLCT state to that of the bqp ligand, and the rapid energy exchange to this moiety led to the unprecedented lifetime of the complex. These studies show how relatively simple chemical modifications can have significant impact on the photophysical properties of these complexes, but DNA binding was not the focus of $[Ru(bqp)_2]^{2+}$ systems. The lessons learnt in these studies can help guide future development of bqp containing complexes.

3.1.2 Other Metal Systems

Other modifications to the $[Ru(L)_2(dppz)]^{2+}$ complex involve using different metals. Complexes containing the dppz ligand have been synthesised with many different metals: Cu,[139] Co,[140] Re,[141,142] Rh,[143] Pt,[144] Os,[145,146] and Ir.[147–149] Barton and co-workers published an osmium containing complex $[Os(phen)_2(dppz)]^{2+}$ in 1995 and showed that it retains the light switching ability of its Ru-based cousin, albeit with a much lower quantum yield.[145]

Herebian *et al*. showed that increasing the overall charge of the $[(Cp^*)Ir(dppz)(L)]^{n+}$ (where n = 1 and L = AccysOH, n = 2 and L = HcysOMe, n =3 and L = H_2metOMe) complex leads to increasing $K_b$values (Figure 3.4).[147] The increasing charge led to $K_b$values of $8.80 \pm 0.06 \times 10^4\,\mathrm{M}^{-1}$ where n = 1, $2.30 \pm 0.04 \times 10^5\,\mathrm{M}^{-1}$ where n = 2 and $2.62 \pm 0.03 \times 10^6\,\mathrm{M}^{-1}$ where n = 3, indicating that stronger electrostatic interactions of the positive metal complexes and negative DNA backbone lead to increased DNA binding. However, DFT studies of common DNA intercalators suggest that the electrostatic contribution to binding is lower than one would expect and contributes much less to the ligand-DNA interaction than other factors.[150,151] Perhaps it is the changing of the ancillary ligand rather than the overall charge of the Ir complexes that drives the differences observed in the $K_b$values, with the electrostatic contribution being minor.

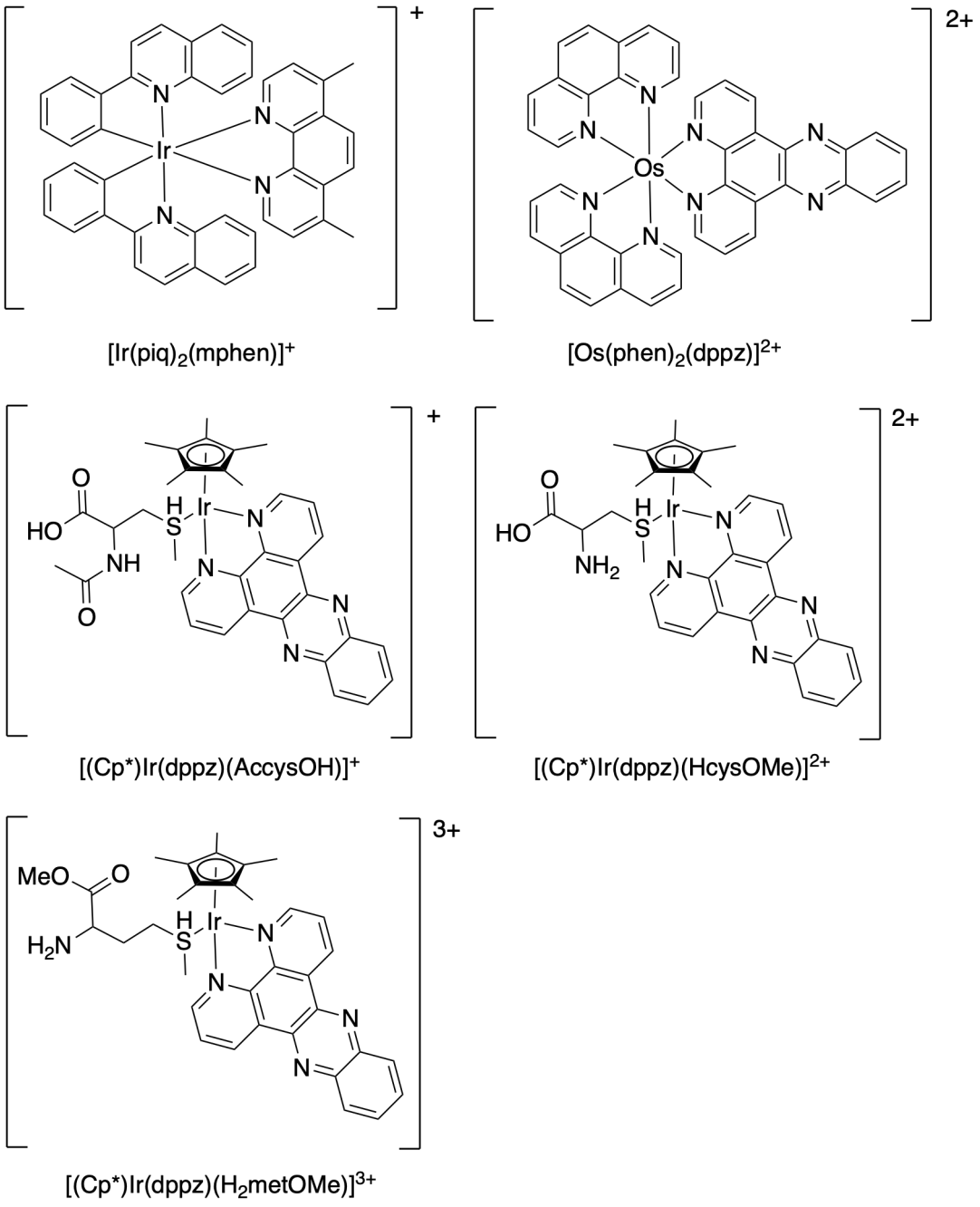

Figure 3.4: DNA binding compounds that feature metals other than Ru

Lu *et al*. in 2016 published a series of Ir-based complexes that have good G-quadruplex binding properties.[152] In particular $[Ir(piq)_2(mphen)]^+$ (piq = 1,10-phenylisoquinoline, mphen = 4,7-dimethylphenanthroline) that showed good G-quadruplex selectivity over dsDNA or ssDNA, as well as an increased fluorescence intensity upon binding. Increased loop length of the G-quadruplex sequence led to an enhanced fluorescence response from the complex, indicating that the loop contributed highly to the binding interaction. The complex showed this type of enhancement with a number of different G-quadruplexes.

3.1.3 Tridentate *fac*-Ru Complexes

As the work of the previous chapter developed, it started to become clear that the facial isomers of $[Ru(bqp)_2]^{2+}$ had more interesting DNA binding interactions that the meridional isomer. Among the many *mer* analogues that exist in the literature, there are only a handful of polypyridyl complexes that have a facial geometry. One such complex contains the ligand diguanidylpyridine (dgpy) (Figure 3.5).[153] From a refluxing solution containing $[Ru(DMSO)_4Cl_2]$ and dgpy, the coordinated facial complex *fac*-$[Ru(dgpy)_2]^{3+}$ was made in an 80% yield, with the authors reporting that the microwave heated reaction improves the yield of the single product over conventional heating, suggesting that other isomers may also form during the course of the reaction. The ligand is capable of forming a meridional geometry as it complexes along with 4′-phenyl-2,2′:6′,2′′-terpyridine (tpy-Ph) to form *mer*-$[Ru(dgpy)(tpy-Ph)]^{2+}$. The dgpy ligand displays substantial σ donation, leading to a lower energy band in the absorption spectrum. Due to the ruthenium in the homoleptic complex being in oxidation state of +3, it was reported that the facial ligand shows no emissive properties upon excitation due to the nature of its low lying LMCT state, ascertained via TD-DFT calculation. With such an electron rich ligand, σ donation to the metal would be expected, any MLCT transitions would be very limited due to the oxidation state of the ruthenium atom. Despite our work indicating that emission from facial isomers is short lived, in this case, the electron donating effect of the dgpy ligand is assumed to play a larger role in the lack of emission rather than just the geometry alone.

As discussed in the previous chapter, the complexes *fac*-$[Ru(bpea)_2]^{2+}$ and *fac*-$[Ru(bpea-pyr)_2]^{2+}$ were published in 2000 by Romero *et al*.[97] Despite the aliphatic linker between the two pyridine units, the complexes displayed lifetimes of 17.0 and 4.6 ns,

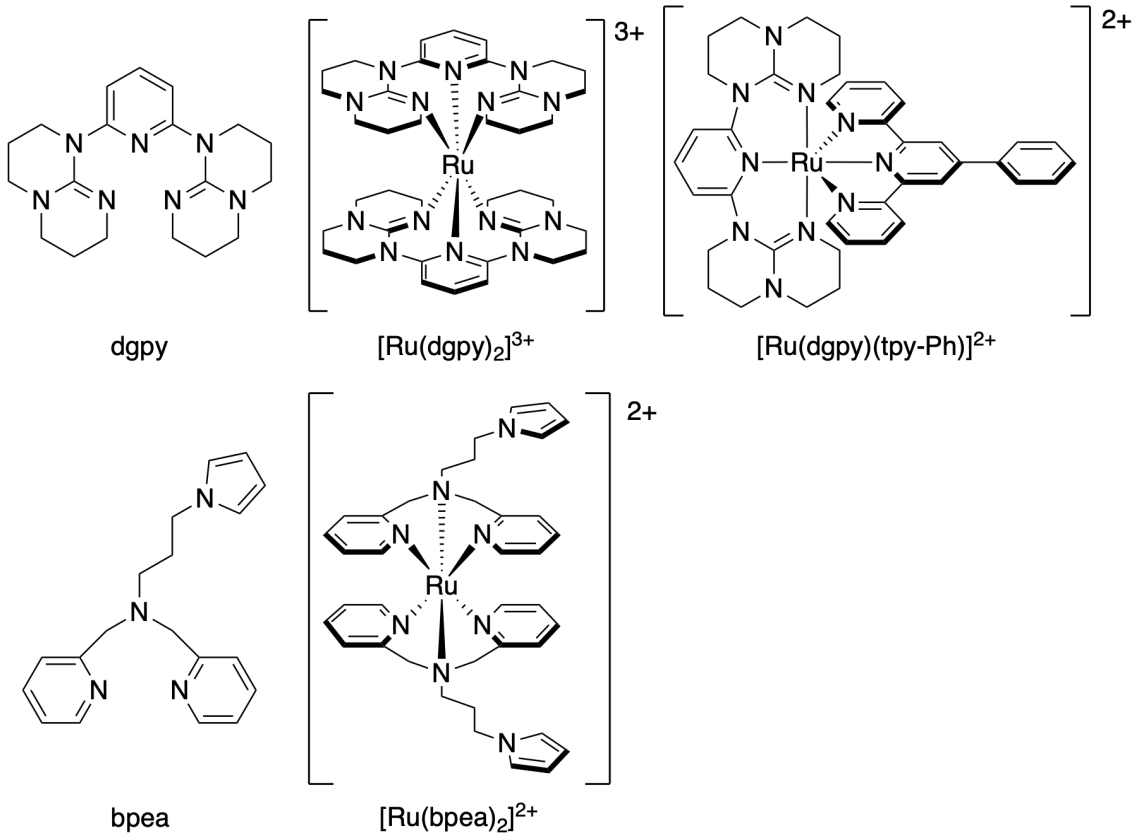

Figure 3.5: Facial ruthenium polypyridyl complexes

remarkably longer than that of $[Ru(tpy)_2]^{2+}$ (0.25 ns). The lack of π delocalisation between the pyridine rings seems to not play such an important role, with dπ-π^* transitions occurring on localised pyridine rings. The lowest lying transitions of *fac*-$[Ru(bpea)_2]^{2+}$ and *fac*-$[Ru(bpea-pyr)_2]^{2+}$ displayed low extinction coefficients (167 and 975 $M^{-1}\,cm^{-1}$, respectively) and were assigned to be metal-centred in character.

Whilst these are interesting cases of Ru complexes forming facial isomers, they do not offer much in terms of a unique facial-only synthetic pathway for the bqp ligand and derivatives. The unique case of the flexible aliphatic linkers or very strong σ donating ligands would not apply to the bqp structure. Instead, to find potentially novel synthetic pathways, other facial complexes were sought after. One such class of complex is the long researched piano-stool type complex.[154,155] Also known as the half-sandwich arene complex, this class of complex display DNA binding in their own right and are the focus of photodynamic therapies.[112,156,157] In these complexes, the arene "blocks" the face on one side of the Ru atom, forcing the other ligands to sit in what would be considered a facial

configuration. Typically these complexes do not use tridentate ligands, as displacement of a monodentate ligand in aqueous solution leads to the formation of an reactive aqua ligand containing complex.[158,159] One could envisage how using such an arene containing complex as an intermediate, facial-only isomers of Ru complexes could be synthesised.

Synthesis of such a complex would involve the displacement of the arene substituent with that of a tridentate polypyridyl. Work by Muetterties showed that the stability of an η^6-arene coordinated to a metal is higher if it has more electron donating character to the arene.[160] For example, it would be easier to displace η^6-C_6H_6 with $C_6(CH_3)_6$ than vice versa. The η^6-arenes were also shown to displace at very high temperature and in a step-wise fashion, moving from η^6- to η^4- to η^2- before being full displaced. It would be logical to assume the removal of an η^6-arene by a tridentate polypyridyl ligand would follow a similar displacement mechanism with the arene moving from η^6- to η^2- and the polypyridyl from monodentate to tridentate. Substitution of this kind would most likely need to be fast to prevent isomerisation of an intermediate complex to the more thermodynamically favourable meridional geometry but equally, if not heated enough the arene would not be displaced - a "Goldilocks principle" would be needed.

With this is mind, this chapter focusses on the development of both the analogues of the bqp ligand, and their corresponding Ru complexes, as well as the development of a facial-only synthetic route. Following on from the work of the previous chapter, the development of these complexes initially focussed on the synthesis of various functionalised bqp ligands but, as much of this work was done in parallel with the previous chapter, this development shifted into a synthetic pathway that would yield the *cis,fac*-$[Ru(bqp)_2]^{2+}$ isomer without the formation of either *trans* or *mer*.

3.2. Results and Discussion

3.2.1 Analogues of bqp

Synthesis began with some simple analogues of bqp, made using 2,6-dihalo-4-R-pyridine (Figure 3.6). Initial conditions used in this synthesis were similar to those of previously bqp analogues, a microwave assisted reaction in $MeCN/H_2O$ with K_2CO_3, SPhos and $Pd(dba)_2$.[136] However, it was found that due to the poor stirring offered by the microwave

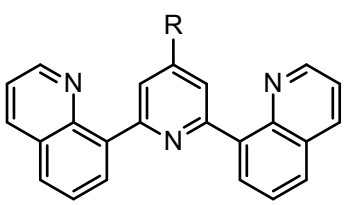

1, **2**, **3**, **4**, **5** and **6**

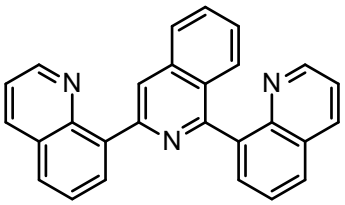

7

	–R
1	–H
2	$-NO_2$
3	$-NH_2$
4	$-CF_3$
5	$-CH_3$
6	$-OCH_3$

Figure 3.6: Structure and numbering of the derivatives of the bqp ligand

reactor and the limited vial sizes, heating via conventional methods with the same solvent mixture and catalysts led to higher yields (Table 3.1), so these conditions were used going forward.

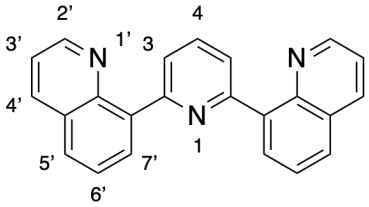

Figure 3.7: Atom numbering of the bqp ligand

Table 3.1: Yields of the Suzuki-Miyuara coupling of different bqp analogues under either conventional or microwave assisted heating conditions

Compound	Microwave Heating Yield (%)	Conventional Heating Yield (%)
2	49	77
5	22	54
4	32	34

The electron withdrawing/donating effects of the different functional groups can be seen when monitoring the H_b NMR shift (Table 3.2 and Figure 3.8) As one would expect, the least shielded proton is on **2** ranging to the most shielded on **3**. Whilst this may have implications of the photophysical properties, with **2** expected to stabilise the ^{3}MLCT state, these groups will also have implications on the DNA binding potential. Those compounds with the potential to H-bond to the DNA bases, e.g. **3**, would be expected to have better binding properties than those that can not, such as **5**.

The complexation to ruthenium of some of these compounds was achieved using the methods previously reported by Jäger *et al.* in 2009.[80] Heating the ligand and $Ru(DMSO)_2Cl_2$ at 180°C in ethylene glycol using microwave heating yielded moderate results. Interestingly $[Ru(\mathbf{5})_2]^{2+}$ did not form the *trans* isomer during synthesis, only

Table 3.2: ^{1}H-NMR shift of the H_b proton with yields of different bqp analogues

Compound	H_b ^{1}H-NMR shift (ppm)	Yield (%)
2	8.97	77
3	7.32	88
4	8.40	34
5	7.94	54
6	7.69	85
7	7.81	75

producing the *cis* and *mer* isomers. Presumably the weak electron donating effect of the methyl group has some *cis* directing effect upon the coordination of the second ligand to the ruthenium.

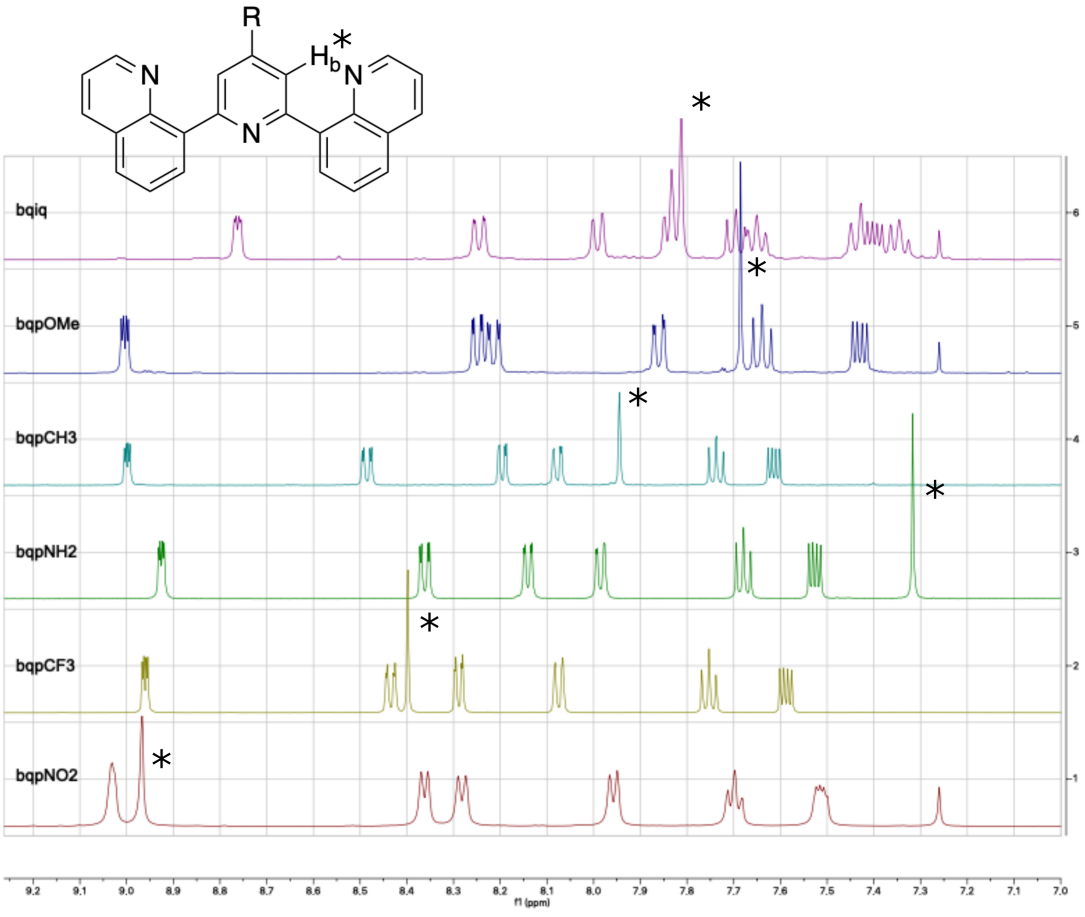

*Figure 3.8: ^{1}H-NMR spectra of (top - bottom) **7** $CDCl_3$, **6** ($CDCl_3$), **5** (d_6-DMSO), **3** (CD_3CN), **4** (CD_3OD), and **2** ($CDCl_3$), where ∗ signifies the H_b proton peak, performed at 400 MHz*

The overall low yield of these complexes and the higher ratio of *mer* formed during the reaction, led onto development of a synthetic system that favoured the formation of the facial isomers. It became increasingly important that the synthesis of the facial isomers should take a more prominent role in the development of new analogues as the results of

the previous chapter were collected. Due to this, the research presented in this chapter moved away from the synthesis using the analogues of the bqp ligand and moved closer towards to a new synthetic pathway for the formation of only the facial isomers, and preferably the *cis* isomer.

3.2.2 Cyclisation of the bqp Ligand

Having studied the crystal structure of the *cis* and *trans* isomers of $[Ru(bqp)_2]^{2+}$, one idea focussed on the modification of the bqp ligand to prevent formation of the *mer* isomer. The carbon atoms at position 15 and 25 in the bqp ligand are 3.40 Å apart, a reasonable distance for a methylene linker to span (Figure 3.9). One method to add a methyl bridge to two quinoline units is via the use of a Grignard reagent and tetramethylethylenediamine (TMEDA) in a one step reaction (Figure 3.10).[161]

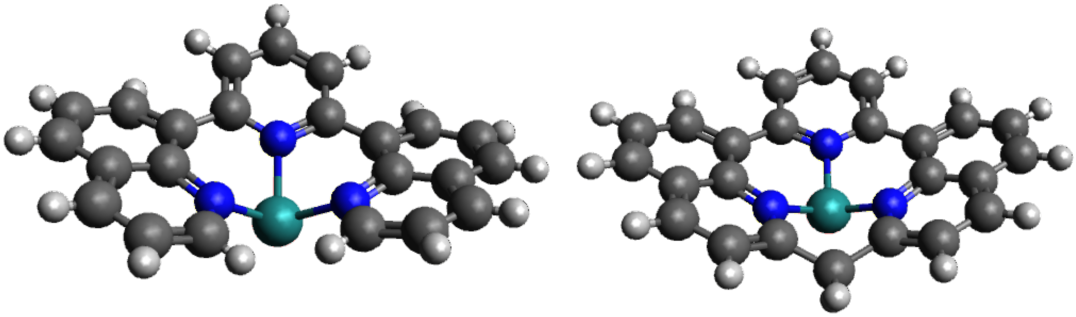

Figure 3.9: Graphical depiction of (left) bqp when bound in the facial geometry and (right) the same structure with a methylene bridge added using the Avogadro software suite[162]

With this in mind, synthetic Scheme A was drawn up as a possible synthetic route to the synthesis of *fac*-$[Ru(mqp)_2]^{2+}$ via the ligand 2,6-(8′-(2′,2′′-methyl)quinolinyl)pyridine (mqp) (Figure 3.11). The addition of the methylene bridge between the quinoline units would prevent the formation of the meridional complex as a sufficient N(q)-Ru-N(q) bite-angle of approximately 180° would be impossible. This would force the complex into either a *cis,fac* or *trans,fac* geometry. This could even lead to heteroleptic complexes, of one mqp ligand and one analogue of bqp, as the addition of the second bqp could only be in a facial arrangement.

In refluxing toluene with TMEDA and MeMgCl, bqp was stirred for 2 h, following

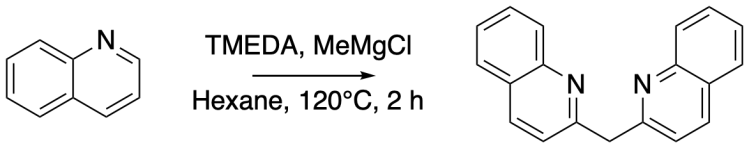

Figure 3.10: Synthetic route of di(quinolin-2-yl)methane

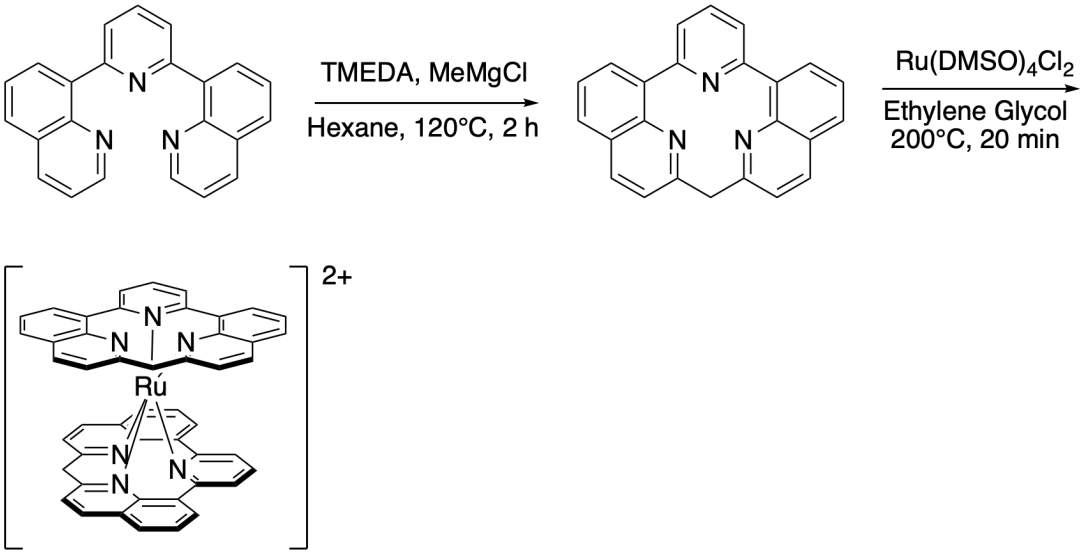

Figure 3.11: Proposed synthetic Scheme A for the synthesis fac-[Ru(mqp)$_2$]$^{2+}$

an adapted method from literature procedure of di(quinolin-2-yl)methane.[161] This initial attempt at forming mqp was, however, unsuccessful. Despite numerous changes to the procedure, such as changing the solvent system, the ratio of starting materials and temperatures, evidence for the formation of the desired product was absent. Even though the disappearance of the 2′-proton peaks in the ^{1}H-NMR spectrum of the product from these reactions was observed, the newly emerging methyl peaks were in a 1:3 ratio of aromatic peak to methylene peak. It would be expected for this to be a 1:1 ratio if only two methylene protons were added (Figure 3.13 and Figure 3.14).

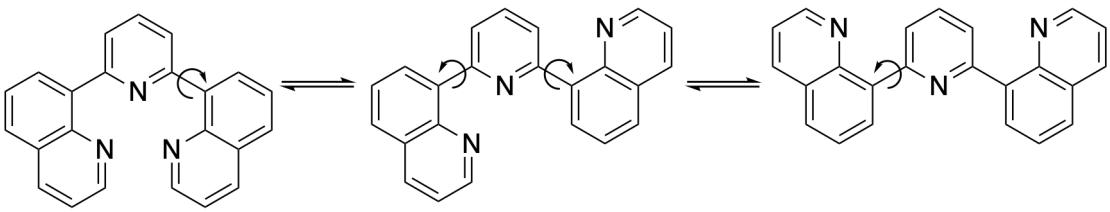

Figure 3.12: Rotation of the pyridine-quinoline bond in bqp

From the disappearance of the 2′-proton from the quinoline unit and the emergence of the 6H peak at 2.76 ppm it became obvious that in fact both carbons were being methylated,

forming two CH_3 groups rather than one bridging CH_2 group. This was confirmed by mass spectrometry where an *m/z* value of 362.1659 was found for the $[M+H]^+$ ion that would be expected to be 362.1652 for compound **8**. When one looks at the bqp ligand, it seems reasonable that the two quinoline units may face "down" and therefore allow for a bridging methyl to be formed, but in solution it seems that this constrained geometry is not favoured (Figure 3.12). Rotation of the quionline-pyridine bond would lead to a geometry that would not favour the formation of a bridging methylene group between the two quinoline units.

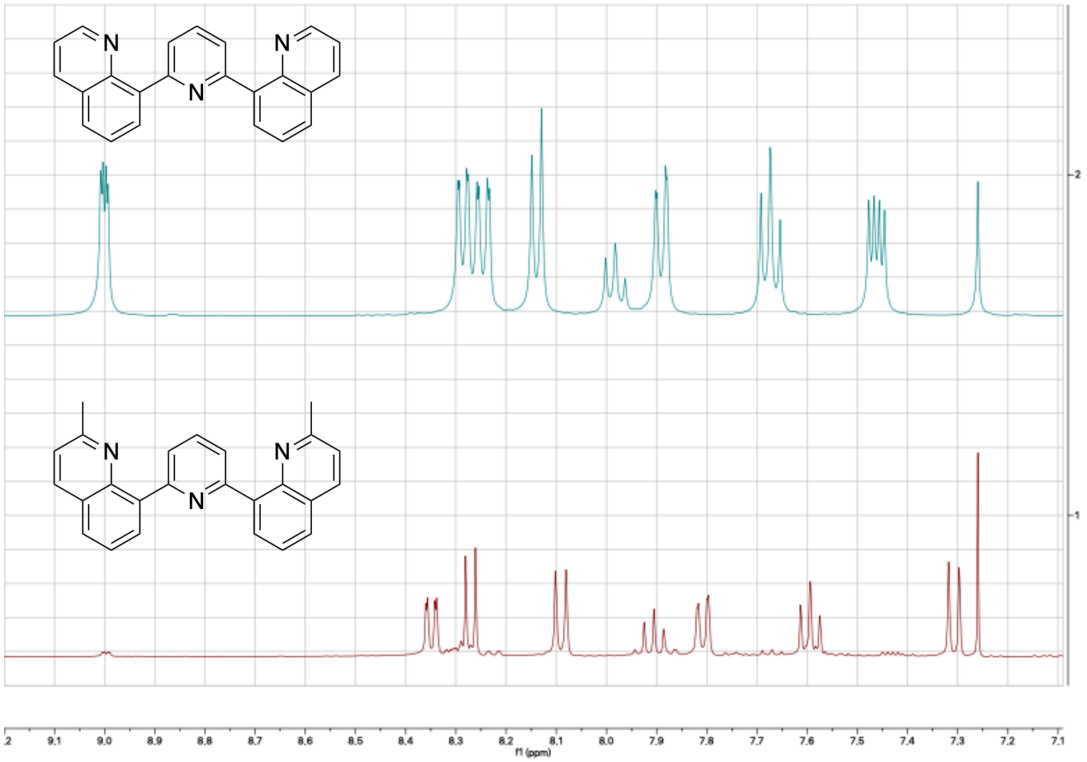

*Figure 3.13: Overlaid ^{1}H-NMR spectra of bqp (top) and **8** (bottom), both performed with $CDCl_3$ at 400 MHz*

It was proposed that templating the bqp onto a metal such as Zn may aid the geometrical arrangement necessary for a bridging quinoline to form but the conditions required for the addition of a methylene group involve the use of aprotic hydrocarbon solvents such as toluene or hexane. Attempts at this synthesis in more polar solvents that may allow for the solubility of a Zn containing complex were unsuccessful so instead, a new idea was pursued that could allow for the formation of the facial isomers without modification to the bqp ligand.

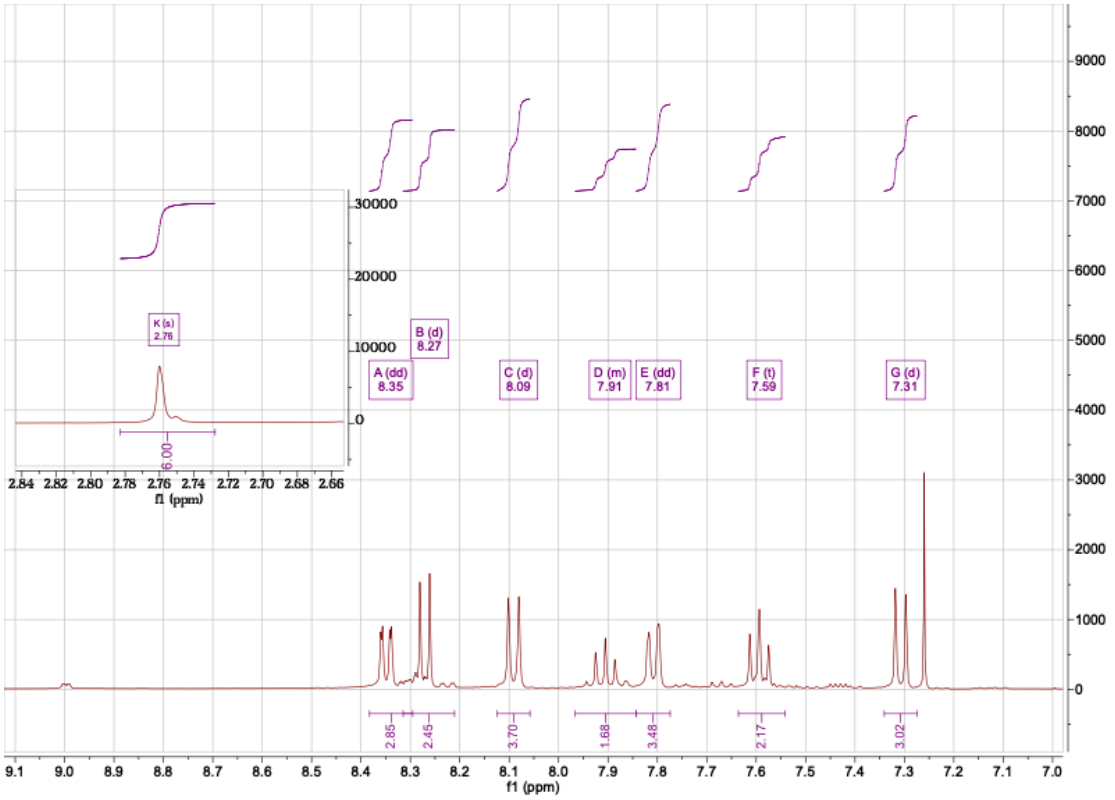

*Figure 3.14: Aromatic region of the ^{1}H-NMR spectrum of **8** in $CDCl_3$ with aliphatic region inset, performed at 400 MHz*

3.2.3 Synthesis of a [Ru(arene)(bqp)]$^{2+}$ Intermediate

Whilst "piano stool" Ru arene complexes are interesting in their own right, it was proposed that their use as an intermediate could lead to a facial only complex with the arene "blocking" one face of the ruthenium coordination environment. To pursue this, the starting material [Ru(*p*−cymene)Cl_2]$_2$ (**9**) was synthesised by the oxidative addition of α-phellandrene to $RuCl_3 \cdot n\,H_2O$. Stirring this dimer with one equivalent of bqp in MeOH overnight led to the formation of [Ru(*p*−cymene)(bqp)]$^{2+}$ **10** which was precipitated from solution as a PF_6^- salt in a 52% yield. The ^{1}H-NMR confirmed the formation of the complex as it shows a ratio of one equivalent of bqp (15 aromatic protons) to one cymene (two doublets of two protons at 5.36 and 5.13 ppm) (Figure 3.15). To try and improve this yield further stirring with $AgCF_3SO_2$ to aid in the removal of Cl^- ions from the ruthenium atoms led to a negligible improvement in yield of 3%. The initial synthetic conditions, were therefore chosen to avoid the extra step of the removal of AgCl from the reaction mixture.

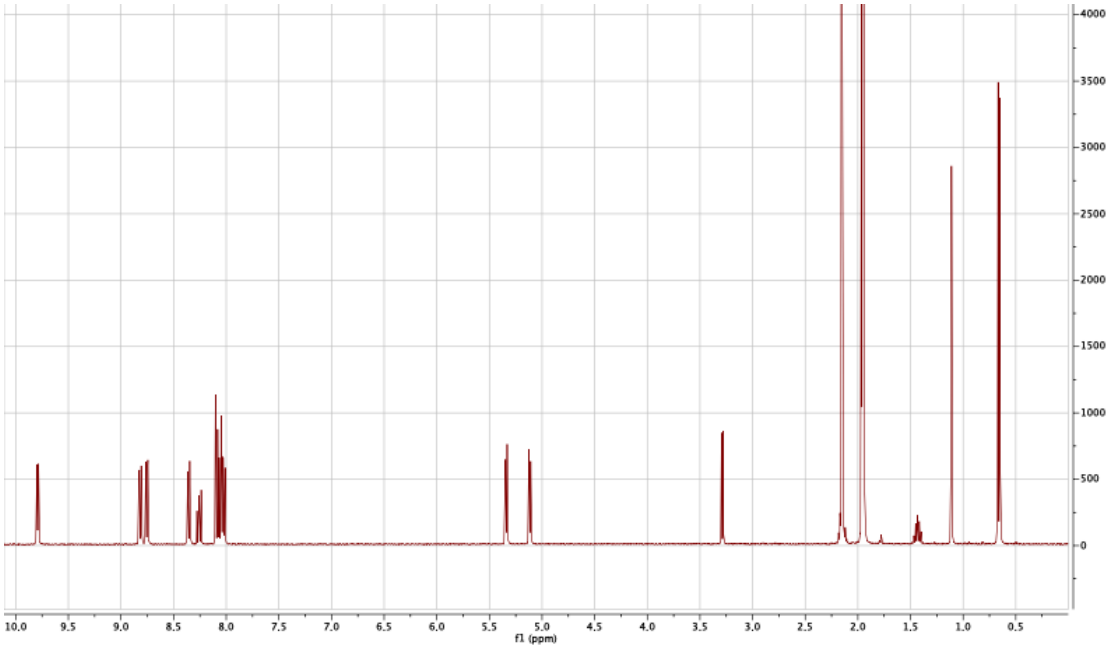

Figure 3.15: ^{1}H-NMR spectra of [Ru(p−cymene)(bqp)]$^{2+}$ in CD_3CN, performed at 400 MHz

X-ray crystallography confirmed the structure and geometry of the complex, with one bqp ligand sitting in a facial geometry and the *p*-cymene ligand occupying the other face (Figure 3.16). Whilst some disorder remains in the PF_6^- counter anions, the Ru complex diffracted well and shows the cymene in a η^6- coordination. The average Ru-C_{arene} bond length was measured at 2.22 ± 0.03 Å and the distance to the centre of the arene ring is *ca* 1.97 Å, slightly longer than seen with other Ru-cymene complexes.[158,163–165] The length of the Ru-C_{arene} bonds that are *trans* to the central pyridine (*trans*$_{py}$, see Figure 3.16) or each quinoline (*trans*$_{q}$) are slightly shorter than that of the bonds that are *cis* to both the quinoline and pyridine (Table 3.3). This seems to be opposite effect of the *trans*-bond weakening observed in phosphine containing Ru-cymene complexes,[166,167] as, in this case, the *trans*$_{py}$ and *trans*$_{q}$ bonds become stronger rather than weaker. Considering the stepwise displacement mechanism of the arene proposed by Muetterties[160] and discussed previously, it is likely that the strength of the Ru-C_{arene} bonds, along with any preference of bqp to associate via a quinoline or pyridine first mechanism, may determine the ratio of *cis* or *trans*. If the second bqp ligand coordinates via a quinoline-first mechanism *trans* to the first central pyridine, then one could envisage the formation of the *cis* isomer being more favoured than the *trans* isomer due to these disparate bond lengths. Equally, if the mechanism initiates *trans* to the quinoline, then the *trans* isomer would become more

favoured. It could also be that displacement initiates with the coordination of the pyridyl nitrogen of the second bqp ligand. The ratios of the two isomers upon displacement of the arene will inform as to the mechanism involved in the coordination of the second bqp, and, modification of the arene substituent could lead to higher yields of either isomers, as one chooses.

Table 3.3: Ru-C_{arene} bond lengths of [Ru(p−cymene)(bqp)]$^{2+}$

	Bond Length Å
$trans_{py}$	2.20(2)
$trans_{q}$	2.21(1)
cis	2.26(1)
All	2.22(3)

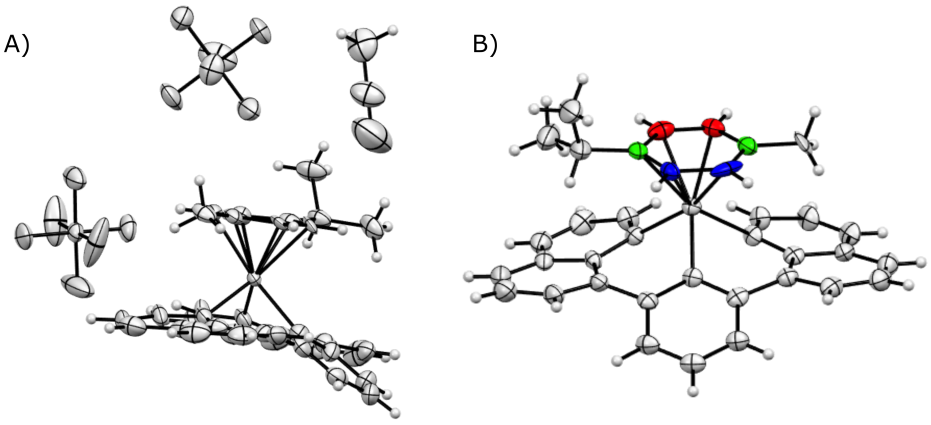

Figure 3.16: A) Thermal ellipsoid plot of [Ru(cymene)(bqp)][PF_6]$_2$ with counter anions included, and B) thermal ellipsoid plot of [Ru(p−cymene)(bqp)]$^{2+}$, where the coloured atoms represent the $trans_q$ (green), $trans_{py}$ (red) and cis (blue) atom pairs in the arene ring

Addition of this second bqp ligand that would afford only the facial isomers, preferably the *cis* isomer in a high yield, and allow for the addition of different analogues of the bqp ligand in a facile manner, proved more difficult than first anticipated. To begin with, however, the isomerism of the two facial complexes was tested. Taking a few milligrams of a mixture of *cis*- and *trans*-[Ru(bqp)$_2$]$^{2+}$, obtained via their conventional synthesis, and heating this mixture at 180°C in ethylene glycol overnight led to no change in the ratio of isomers and no formation of the *mer* isomer. To determine the ratio of each isomer in a mixture of products, ^{1}H-NMR spectroscopy was used. Each isomer gives a unique peak outside of the range of the others, in the case of *cis* this is found at 6.65 ppm, *trans* at 9.15 ppm, and *mer* at 7.05 ppm (Figure 3.17). These peaks all arise from quinoline protons,

so functionalisation of the central pyridine should not significantly change the ^{1}H-NMR of these peaks, allowing them to be used as key markers of each isomer. By confirming that the facial isomers do not form the meridional isomer in these conditions, any ratio of the three isomers that could be formed during synthesis would be due the step-wise displacement of the arene and any rearrangement of intermediate complexes rather than one isomer forming and then later thermally rearranging into another.

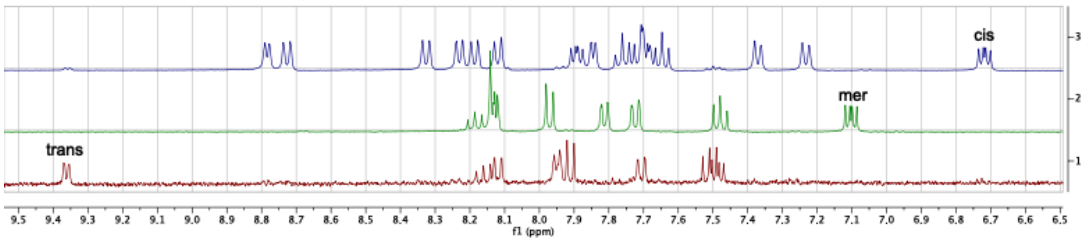

Figure 3.17: ^{1}H-NMR spectra of the aromatic region of cis (top), mer (middle) and trans (bottom) in CD_3OD at 400 MHz. Labels show the distinct ^{1}H-NMR signals that can be used to distinguish the isomers from each other

Displacement of an arene from ruthenium by a polypyridyl ligand has be shown to occur via excitation with UV light.[159] Photoirradiation of an arene complex ($[Ru(arene)(L)_2Cl]^+$) in MeCN has been shown to lead to the displacement of the arene and coordination of the acetonitrile ($[Ru(L)_2Cl(MeCN)_3]^+$), which can be readily displaced by another ligand.[168,169] To try this, equimolar amounts of bqp and $[Ru(p-cymene)(bqp)][PF_6]_2$ were stirred in MeCN using a 125 W Hg immersion UV light source. After 72 h of stirring, no change in the composition of the solution was observed, only the starting materials were found in the ^{1}H-NMR (Table 3.4). Both MeOH and DCM, weakly coordinating solvents, were also used but no displacement of the arene was observed. Stirring the same mixture overnight in refluxing MeCN also showed no formation of the desired product, only the unreacted starting materials were observed.

Efforts were then turned to using the microwave assisted conditions used to form the facial isomers from $Ru(DMSO)_4Cl_2$. Heating the equimolar solution at 180°C in ethylene glycol in a microwave reactor for 2 min led to the formation of a red solution that, by observing the ^{1}H-NMR spectrum, seemed to contain a very small amount of the desired complex alongside plenty of starting material (Figure 3.18). Putting this mixture back into the microwave reactor for a further 1 h led to formation of a ratio of *cis*:*trans*:*mer* of 10:1:8. Whilst this was promising, only *ca* 50% of the desired isomer was formed, with the total

yield of *ca* 50% for the synthesis of the combined isomers making the total yield of *cis* from the reaction only *ca* 25%.

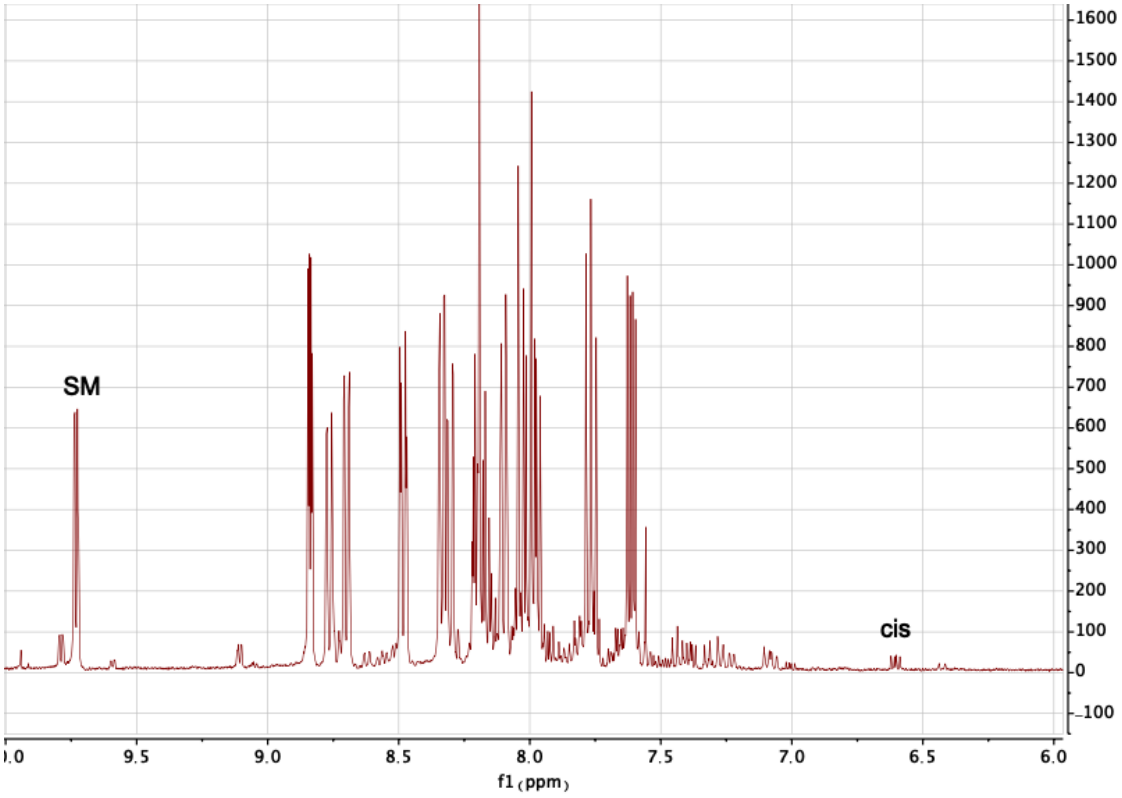

Figure 3.18: ^{1}H-NMR spectra obtain from the crude product of $Ru(DMSO)_4Cl_2$ and bqp in a 1:1 ratio heated at 180°C in ethylene glycol for 2 min *with microwave assisted heating. Performed in CD_3CN at 400 MHz*

To improve upon this further, timescales between 5 min to 20 min were used. After 5 minutes, both *cis*- and *trans*-$[Ru(bqp)_2]^{2+}$ were formed with a total yield of 24% and a ratio of 4:1, *cis*:*trans*. A slight improvement was achieved after 10 minutes with a total yield of 29% and a ratio of 7:1, *cis*:*trans*. However, if heated for longer than 10 minutes, the thermodynamically favourable *mer* isomer would begin to form. Whilst some isomer control was achieved in these conditions, the addition of a functionalised bqp derivative as the second ligand led to very different results. With the addition of **4** as the second ligand and heating for 5 minutes under the conditions used previously led to formation of the *mer* isomer. Finding the ideal temperature and time for each addition, whilst possible, would be laborious so the low yielding and time sensitive nature of this procedure force the investigation back towards the use of conventional heating.

Heating an equimolar mixture of bqp and $[Ru(p-cymene)(bqp)][PF_6]_2$ in ethylene glycol at 180°C overnight led to the successful formation of $[Ru(bqp)_2]^{2+}$, at a 49% yield.

This mixture of isomers contained a ratio of *cis*:*trans*:*mer* of 10:3:4, an improvement upon the microwave reaction, as the yield of *cis* from this reaction would be 28%, but the formation of *mer* was still occurring. Lowering the temperature of this reaction could garner more control over the formation of the isomers, with lower temperatures possibly favouring the less thermodynamically stable facial isomers. However, reacting equimolar amounts of [Ru(*p*−cymene)(bqp)][PF_6]$_2$ and bqp in refluxing isopropanol yielded only starting materials, as was the case when the solvent used was MeCN. The solubility of ruthenium hexafluorophosphate complexes in alcohols is low, so anion metathesis from [Ru(*p*−cymene)(bqp)][PF_6]$_2$ to [Ru(*p*−cymene)(bqp)][Cl]$_2$ yielded better results. Heating this chloride salt and bqp in isopropanol at 80°C led to the formation of only the facial isomers, *cis* and *trans*, in a 4:1 ratio, respectively, and a yield of 44%. This was a step in the right direction, lowering the temperature allowed for a greater control of the isomer formation but the yield of *trans* was still significant. The higher *cis* ratio indicates that the coordination of the second bqp ligand either stems from the coordination of the quinolyl nitrogen *trans* to the central pyridine, or from the pyridyl nitrogen *trans* to either of the quinolines. Changing the arene and therefore possibly changing the *trans*-bond strengthening effect could yield a better product ratio.

As previously discussed, the arene is displaced from the metal complex in a step-wise fashion, moving from η^6- to η^4- to η^2- before being fully displaced.[155] The stabilities, or the displacement series, of different arenes has also been reported with more electron rich arenes being more difficult to displace.[160] With this in mind, it was hypothesised that using benzene instead of the more electron rich *p*-cymene may give even more control over the formation of the isomers, possibly influencing the ratio of *cis*:*trans* formation.

Synthesis of the [Ru(benzene)Cl_2]$_2$ dimer (**11**)was achieved in similar conditions to that of *p*-cymene dimer. Refluxing $RuCl_3 \cdot n\,H_2O$ and 1,3-cyclohexadiene in 96% EtOH led to the formation of the dimer in 92% yield. Stirring the dimer with two equivalents of bqp (1:1, Ru:bqp) and four equivalents of silver trifluoromethanesulfonate at room temperature led to the formation of [Ru(benzene)(bqp)]$^{2+}$ **12** in a 60% yield.

Similar to the cymene containing complex, [Ru(benzene)(bqp)][PF_6]$_2$ crystals were grown by slow addition of diethyl ether into acetonitrile and the small yellow crystals were diffracted with a Mo source (Figure 3.19). Interestingly, the benzene containing complexes

Table 3.4: Reaction conditions used in the multiple attempts at synthesising fac-$[Ru(bqp)_2]^{2+}$. [a] obtained from the ^{1}H-NMR spectra

Ru source	Ligand	Solvent	Heating Type	Temperature (°C)	Time (h)	Total $[Ru(bqp)_2]^{2+}$ Yield (%)	*cis*:*trans*:*mer*Ratio[a]
$[Ru(p-cymene)(bqp)][PF_6]_2$	bqp	MeCN	UV	RT	16	-	-
$[Ru(p-cymene)(bqp)][PF_6]_2$	bqp	DCM	UV	RT	16	-	-
$[Ru(p-cymene)(bqp)][PF_6]_2$	bqp	MeOH	UV	RT	16	-	-
$[Ru(p-cymene)(bqp)][PF_6]_2$	bqp	MeCN	Conventional	82	16	-	-
$[Ru(p-cymene)(bqp)][PF_6]_2$	bqp	Ethylene Glycol	Microwave	180	1	50	10:1:8
$[Ru(p-cymene)(bqp)][PF_6]_2$	bqp	Ethylene Glycol	Microwave	180	5 min	24	4:1:0
$[Ru(p-cymene)(bqp)][PF_6]_2$	bqp	Ethylene Glycol	Microwave	180	10 min	29	7:1:0
$[Ru(p-cymene)(bqp)][PF_6]_2$	bqp	Ethylene Glycol	Microwave	180	20 min	46	10:2:3
$[Ru(p-cymene)(bqp)][PF_6]_2$	bqpNO2	Ethylene Glycol	Microwave	180	5 min	-	-
$[Ru(p-cymene)(bqp)][PF_6]_2$	bqp	Ethylene Glycol	Conventional	180	16	49	10:3:4
$[Ru(p-cymene)(bqp)][PF_6]_2$	bqp	Isopropanol	Conventional	80	16	-	-
$[Ru(p-cymene)(bqp)][Cl]_2$	bqp	Isopropanol	Conventional	80	16	44	4:1:0
$[Ru(benzene)(bqp)][Cl]_2$	bqp	Isopropanol	Conventional	80	16	12	9:1:0
$[Ru(benzene)(bqp)][Cl]_2$	bqp	*n*-Butanol	Conventional	100	16	40	9:1:0
$[Ru(benzene)(bqp)][Cl]_2$	bqp	*n*-Butanol	Conventional	125	16	82	18:1:1

feature a greater *trans*-bond strengthening than the cymene equivalent. The $trans_{py}$ bonds are shorter when the arene is benzene rather than cymene (2.15 ± 0.01 and 2.20 ± 0.02 Å, respectively). As stated in the case with cymene, if the second bqp equivalent displaced the arene by first coordinating from the nitrogen of the pyridine, this would favour a higher proportion of the *cis* isomer over the *trans* isomer, this mechanism was also proposed by Jäger *et al*. in 2010.[137] Although the $trans_{q}$ and *cis* bond lengths of the arenes do not differ significantly, the *trans* bonds do. If the second addition of bqp leads to a higher ratio of the *cis* isomer then it would indicate that the pyridine coordinates first at the $trans_{q}$ position followed by the coordination the flanking quinolines. The increased strength of the $trans_{py}$ bond would therefore disfavour the formation of the *trans* isomer, if the second bqp coordinates via the pyridyl nitrogen first. If, however, a higher ratio of the *trans* isomer forms, then the opposite could be true; coordination of the quinoline first at the $trans_{q}$ position. One can also not ignore the increased steric bulk of the *p*-cymene over the benzene. Although the crystal structure of $[Ru(p-cymene)(bqp)]^{2+}$ shows no disorder in the positioning of the arene ring, the NMR shows two uniform doublets indicating free movement of the arene, suggesting that the bulky isopropyl group is not *cis*/*trans* directing, but the increased steric bulk of the arene could still influence the accessibility of the ruthenium atom to the incoming bqp ligand. This could have a kinetic influence of the formation of one isomer or the other, with less bulky benzene potentially favouring one over the other.

Table 3.5: Ru-C_{arene} bond lengths of both $[Ru(p-cymene)(bqp)]^{2+}$ and $[Ru(benzene)(bqp)]^{2+}$

	Bond Length Å	
	cymene	benzene
$trans_{py}$	2.20(2)	2.15(1)
$trans_{q}$	2.21(1)	2.21(1)
cis	2.26(1)	2.25(1)
All	2.22(3)	2.20(3)

Heating, at 80°C overnight, an equimolar mixture of $[Ru(benzene)(bqp)][Cl]_2$ and bqp in a 50:50 mixture of isopropanol and water led to a *cis*:*trans* ratio of 9:1, a vast improvement over the *p*-cymene equivalent, however, the overall yield was low (12%). This result suggests that coordination of the second bqp ligand occurs from the pyridine unit at $trans_{q}$ position, followed by the flanking quinoline units. Increased strength of the

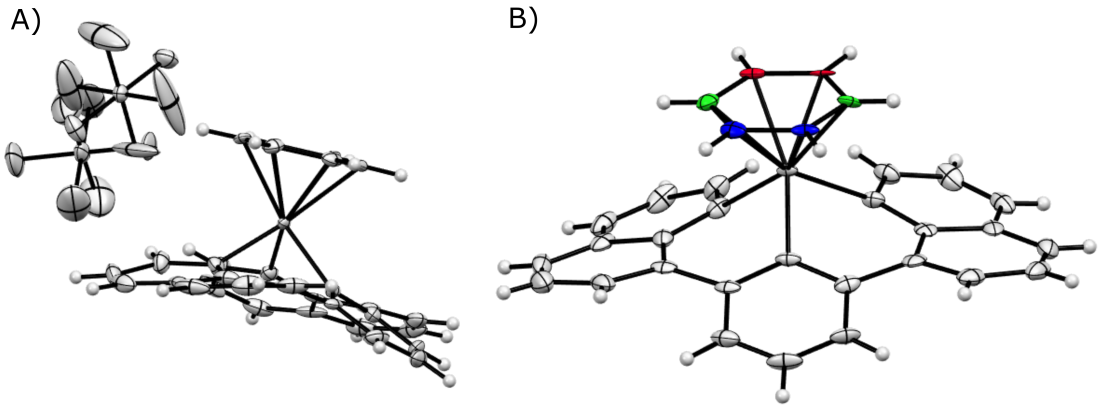

Figure 3.19: A) Thermal ellipsoid plot of [Ru(benzene)(bqp)][PF_6]$_2$ with counter anions included, and B) thermal ellipsoid plot of [Ru(benzene)(bqp)]$^{2+}$, coloured atoms represent the trans$_q$ (green), trans$_{py}$ (red) and cis (blue) atom pairs in the arene ring

trans$_{py}$ Ru-C$_{arene}$ bonds disfavours coordination in a *trans* geometry, leading to a higher ratio of the *cis* isomer. It was found that using *n*-BuOH as the solvent and heating at 100°C overnight led to a much higher overall yield (40%) whilst maintaining the same *cis*:*trans* ratio. Increasing this temperature again to 125°C led to an even higher yield (82%), with a small amount of *mer*, giving an overall 18:1:1 ratio of *cis*:*trans*:*mer* (Figure 3.20). This high overall yield of [Ru(bqp)$_2$]$^{2+}$ and high *cis* formation allows for a total yield of *cis* of >70%.

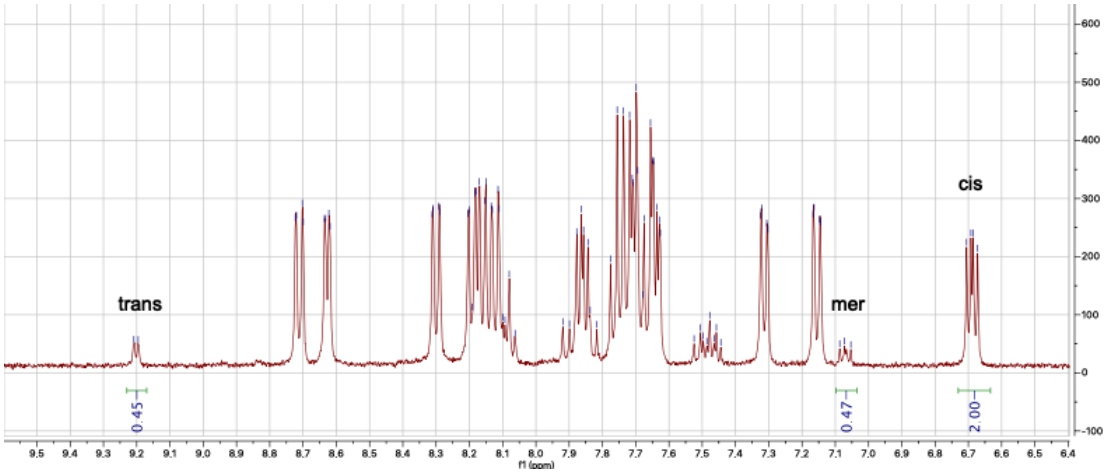

Figure 3.20: Aromatic region of the ^{1}H-NMR spectrum of the crude product from the synthesis of cis-[Ru(bqp)$_2$]$^{2+}$ in CD_3CN at 400 MHz

It could be envisaged that lowering the temperature further and using a less labile arene could offer higher yields of *trans*, although it would also most likely result in a lowering of the total [Ru(bqp)$_2$]$^{2+}$ yield, whilst control over *mer* has already been established

in the literature. This synthetic route allows for a high control over isomer formation and also allows for the synthesis of heteroleptic facial isomers of $[Ru(bqp_2)]^{2+}$ without structural modification of the bqp ligand, as was attempted in the synthesis of mqp . Separation of these isomers can be achieved via HPLC or due to the high overall yield of *cis*, recrystallisation may yield only *cis*. However, restricted time did not permit exploration of this second option.

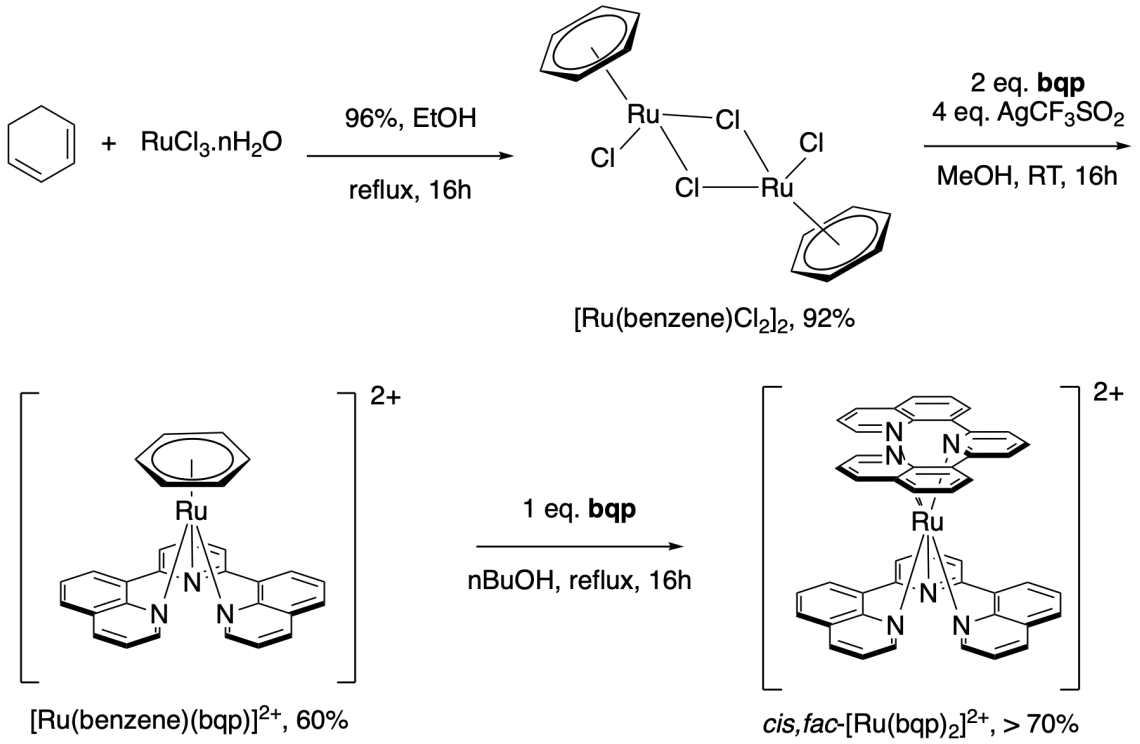

Figure 3.21: Final synthetic route for the synthesis of cis-$[Ru(bqp)_2]^{2+}$ in high yields

3.2.4 Heteroleptic facial isomers of $[Ru(bqp)_2]^{2+}$

The development of the above synthetic pathway (Figure 3.21) allows for the possibility of heteroleptic facial isomers of $[Ru(bqp)_2]^{2+}$ by adapting the second addition of bqp. Using some of the bqp ligand analogues described earlier in this chapter, this was explored.

Addition of the CF_3 containing ligand (**4**) at this step led to the formation of *cis*- and *trans*-$[Ru(bqp)(\mathbf{4})]^{2+}$ (Figure 3.22). The ratio of *cis*:*trans* for this analogue was 8:1 at an overall yield of 26%. Despite a lower total yield of all isomers, the high *cis* ratio is promising. The addition of the inductively electron withdrawing trifluoromethyl group seems to disfavour complexation over the unfunctionalised bqp ligand as large

quantities of the [Ru(benzene)(bqp)]$^{2+}$ starting material were present. Raising the reaction temperature or time may lead to a higher overall yield whilst maintaining the isomer ratios, as was seen previously.

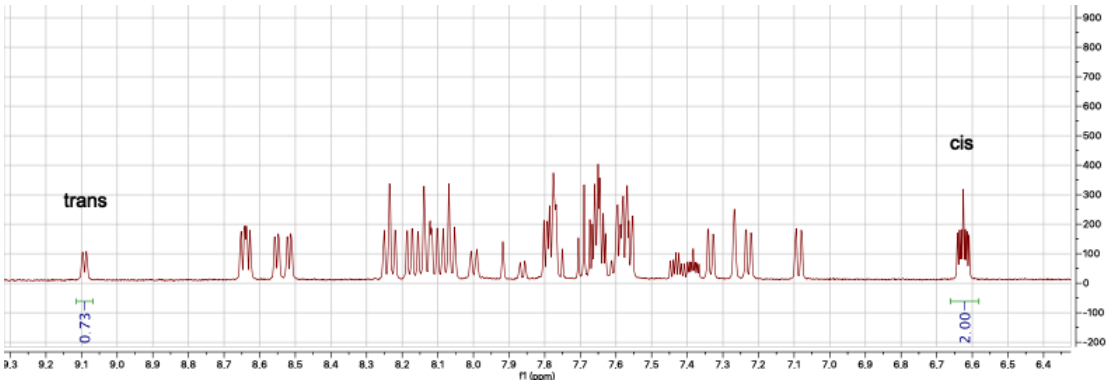

*Figure 3.22: ^{1}H-NMR spectrum of the crude product from the synthesis of cis-[Ru(bqp)(**4**)]$^{2+}$ in CD_3CN performed at 400 MHz*

A series of other bqp ligands were also used, with all showing high proportions of *cis* formation whilst limiting the amount of *trans* or *mer* (Figure 3.23). This shows the predominant factor in the *cis*:*trans*:*mer* ratio is the Ru-containing precursor and not the electronic properties of the ligand, allowing for the synthesis of many different types of bqp analogues. The electronic properties do, however, influence the overall amount of reacted starting material, with the more electron rich bqp ligands displaying better displacement of the arene than the more electron deficient.

In the case of **2**, large amounts of unreacted starting material were present despite the reaction being performed on the 16 h timescale. In contrast, addition of **3** led to lower amounts of starting material remaining. It could be possible to overcome this by increasing the timescale or temperature of the reaction depending upon the type of ligand that was added. Time did not permit for the purification of these remaining complexes, future work would focus on the synthesis, purification and biophysical analysis of these types of complexes. However, the presence of the peak at *ca* 6.60 ppm is indicative of the formation of the *cis* isomer, and, whilst this isn't conclusive proof, it does strongly suggest that formation of these heteroleptic complexes is possible.

This synthetic route provides not the only the opportunity to make the *cis* isomer in high yields (>70%) whilst keeping the yields of the other two isomers low, it also presents the opportunity to synthesise novel, homoleptic, facial, tridentate ruthenium polypyridyl

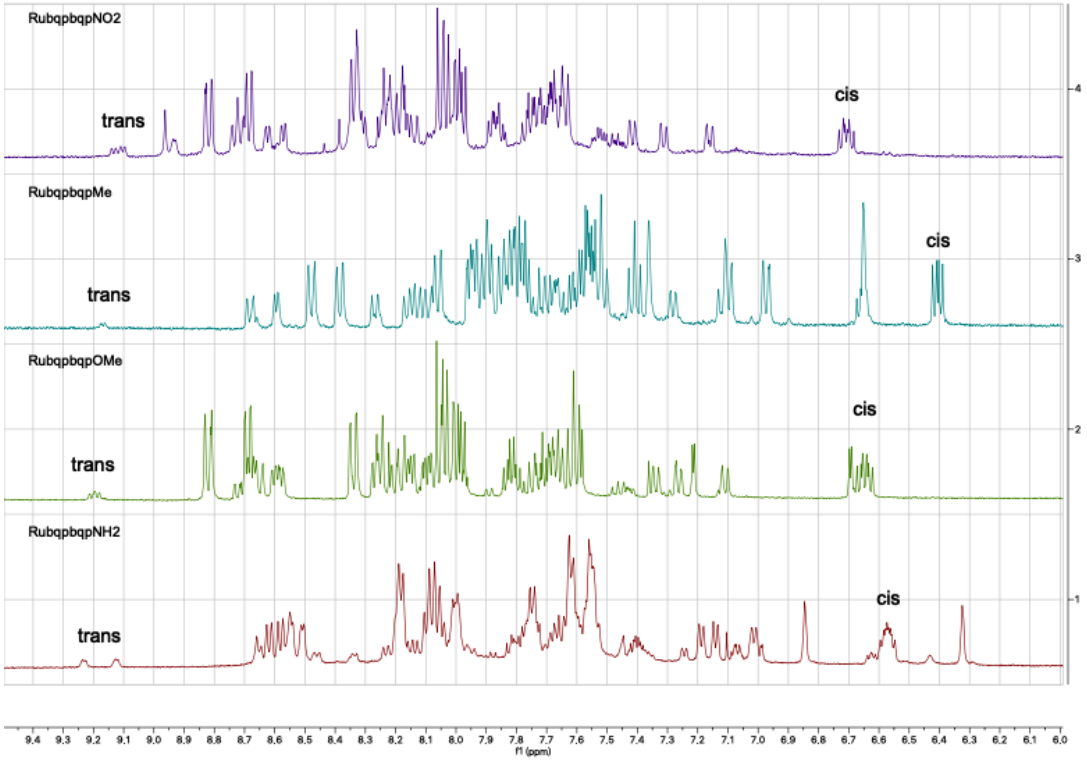

*Figure 3.23: ^{1}H-NMR aromatic region of the crude products for the synthesis of (top - bottom) cis-[Ru(bqp)(**2**)]$^{2+}$, cis-[Ru(bqp)(**5**)]$^{2+}$, cis-[Ru(bqp)(**6**)]$^{2+}$, and cis-[Ru(bqp)(**3**)]$^{2+}$, all performed using CD_3CN at 400 MHz*

complexes. Prior to this research, such complexes have not been reported, the only facial bqp containing complexes to be reported were that of the heteroleptic $[Ru(bqp)_2]^{2+}$.[80] For the future development of i-motif targeting Ru-based probes, this is a significant achievement.

3.2.5 $[M(bqp)_2]^{n+}$ Analogues

As was the case in the synthesis of the $[Ru(bqp)(bqpR)]^{2+}$ complexes, the $[M(bqp)_2]^{n+}$ complexes were synthesised initially as *mer* complexes before the discovery of the biophysical properties of the *cis* isomer. Alcock *et al*. published a series of bis-terpyridine complexes with a series of different metals.[170] Refluxing the terpyridine derivative with a metal-acetate salt in MeOH led to high yields of $[M(bitpy)_2][PF_6]_2$ (where M = Fe, Ni, Cu, Zn, Cd or Co) where addition of KPF_6 precipitated the complexes from MeOH. This showed that *bis* tridentate polypyridyl complexes are facilely obtainable from common starting materials. To test this with bqp, Ni(II) acetate was refluxed with 2 equivalents of bqp overnight and a yellow solid was precipitated by addition of KPF_6. Crystals of

$[Ni(bqp)_2][PF_6]_2$ complex were grown by dissolving the complex in a 50:50 mixture of acetone and water and cooling overnight at 4°C. As expected due to the conditions used in the synthesis, only the meridional isomer was formed, no evidence of either facial isomer was observed. Due to the *d*-8 configuration of the complex, and therefore in an octahedral ligand field, its paramagnetism, ^{1}H-NMR spectra were not obtained but elemental analysis shows the purity of the complex, and along with the crystal structure (Figure 3.24), confirms the formula to be $[Ni(bqp)_2][PF_6]_2$. Similarly, the cobalt complex was also synthesised using the same conditions but X-ray diffraction quality crystal were not obtained. However, elemental analysis was obtained for the pure PF_6^- salt.

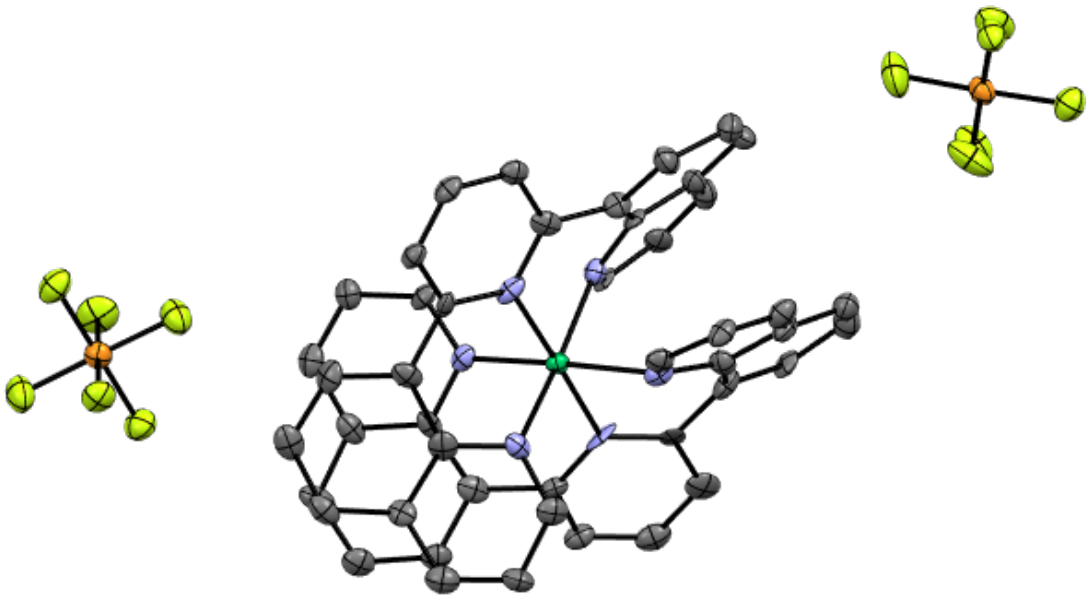

Figure 3.24: Thermal ellipsoid plot of the crystal structure of mer-$[Ni(bqp)_2]^{2+}$ with atoms coloured by element

This synthetic route demonstrates the facile nature of the formation of meridional complexes of bqp. Future work would focus on the DNA interactions of these complexes and the addition of functionalised bqp ligands to change both the photophysical and DNA binding properties of the complexes. However, due to the increasing evidence that the facial isomers of $[Ru(bqp)_2]^{2+}$ provided a better platform for the development of an i-motif DNA specific light switch, focus was turned towards the possibility of the synthesis of other facial complexes containing different metals.

After successfully obtaining a synthetic route to form the *cis* isomer of $[Ru(bqp)_2]^{2+}$ in

high yields, attempts were made with other transition metals. Stirring $IrCl_3 \cdot H_2O$ and cyclopentadiene in MeOH at RT led to the formation of the $[Ir(Cp)Cl_2]_2$ dimer. This was subsequently stirred with bqp overnight in MeOH at RT but did not yield the desired $[Ir(Cp)(bqp)]^{2+}$ product. Instead the $[Ir(Cp^*)Cl_2]_2$ (**13**) dimer was formed in a similar reaction using pentamethylcyclopentadiene and $IrCl_3 \cdot H_2O$. The addition of bqp to this dimer was successful as shown in the ^{1}H-NMR spectrum of $[Ir(Cp^*)(bqp)]^{2+}$ (**14**) (Figure 3.25). The peak environments are very similar to the Ru complex containing the same ligands. One interesting feature of the ^{1}H-NMR spectrum is the shift of the most deshielded proton, likely the 2′ proton of the quinoline unit. Increased donation from the quinolinyl nitrogen to the iridium would result in a higher chemical shift of the adjacent proton when compared with the ruthenium-based complex with the same ligands. This would suggest that this complex could be more stable, possibly allowing for higher temperature conditions in the final synthetic step.

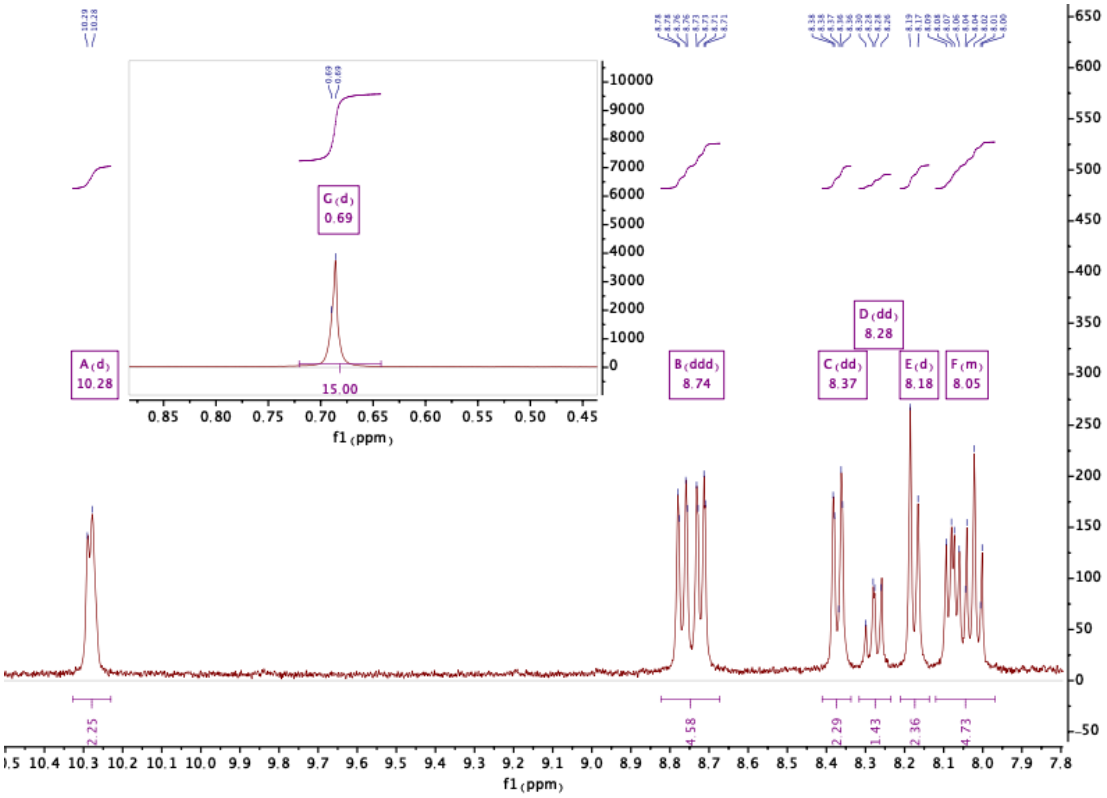

Figure 3.25: ^{1}H-NMR spectrum of $[Ir(Cp^*)(bqp)]^{2+}$ in CD_3CN at 400 MHz

Heating $[Ir(Cp^*)(bqp)]^{2+}$ in ethylene glycol at 180°C with one equivalent of bqp and 1 mL of a saturated KCl solution led to the formation of an orange solution to which

addition of KPF_6 led to the precipitation of an orange solid in 39% yield. The ^{1}H-NMR spectrum of this orange solid suggests that this could be a facial bis-bqp iridium complex. However, more evidence will need to be obtained to support this, for example, mass spectrometry and a solved X-ray crystal structure.

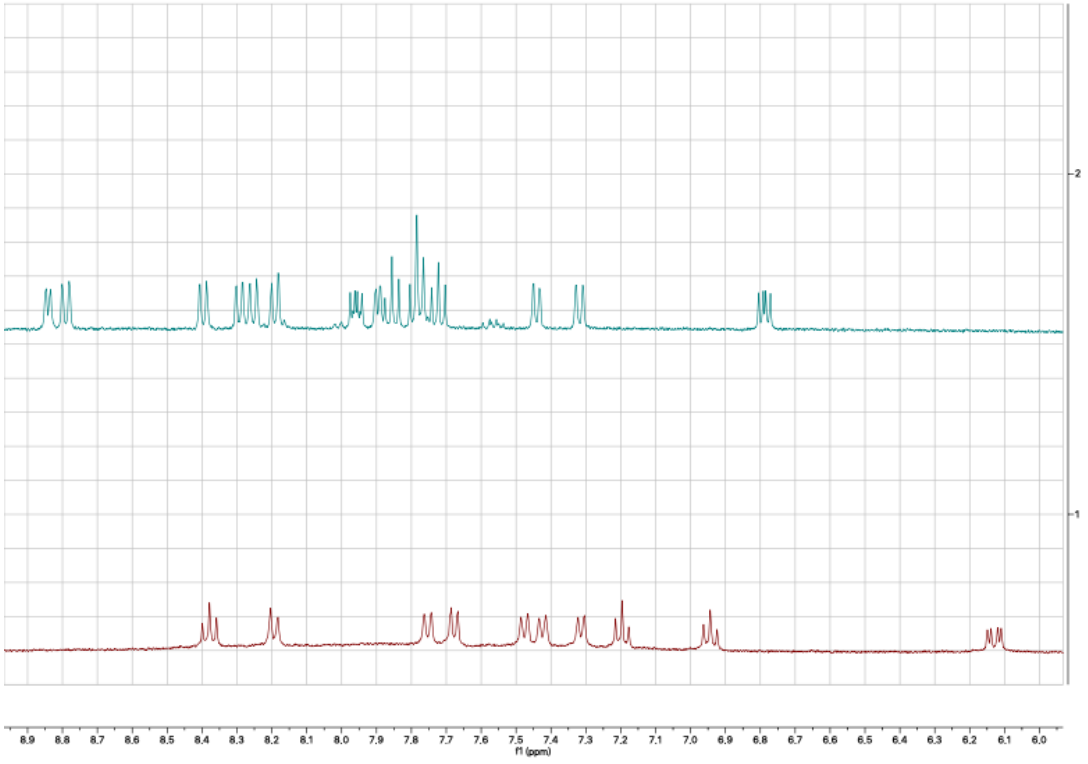

Figure 3.26: ^{1}H-NMR spectra of cis-$[Ru(bqp)_2]^{2+}$ (top) and $[Ir(bqp)_2]^{3+}$ (bottom) in CD_3CN at 400 MHz

This showed that it may be possible to form facial isomers of other transition metal complexes containing the bqp ligand. With the formation on an arene-bqp Ir intermediate, the same could well be possible for other transition metals. Displacement of this arene could be achievable and lead to many different heteroleptic, facial transition metal complexes, some of which may possess favourable DNA binding interactions.

3.3. Conclusions

This chapter has outlined the steps taken towards the synthesis of high yielding heteroleptic facial isomers of $[Ru(bqp)_2]^{2+}$. After initial attempts at this synthesis via modification of the bqp ligand by the addition of a methylene bridge between the two quinoline units, focus was turned onto the synthesis via an arene containing intermediate. This led to

high yields of predominantly the *cis* isomer (*cis*:*trans*:*mer*, 18:1:1). Moreover, the addition of different functionalised bqp ligands demonstrated the possibility for the formation of heteroleptic complexes that still yielded high levels of the *cis* isomer. The coordination mechanism of the second bqp ligand was also suggested to occur via the coordination of the pyridyl nitrogen before the quinolinyl nitrogens, as evidenced by the Ru-C_{arene} bond lengths of the cymene and benzene containing complexes.

Additionally, progress was made towards the synthesis of facial $[M(bqp)_2]^{n+}$ complexes. Formation of $[Ir(Cp^*)(bqp)]^{2+}$ from the $[Ir(Cp^*)Cl_2]_2$ dimer was achieved and steps were taken towards the synthesis of the facial $[Ir(bqp)_2]^{3+}$ complex. Formation of other *mer* isomers of a selection of first row transition metals was also achieved and, although the aim of this chapter moved away from this work, future work could include the photophysical and biophysical properties of these.

The DNA binding and photophysical properties of these complexes is to be investigated and the future work of this project will focus on both of these analyses. The DNA interactions of the *cis*-$[Ru(bqp)(bqpR))]^{2+}$ complexes will provide further evidence for the switching mechanism and how these modifications change the biophysical properties of them. The other transition metal complexes may also provide more insight into the switching mechanism and whether it is maintained across a series of different metals.

Future work should focus on the continued development of the *cis*-only synthetic route and its applications to forming facial derivatives of $[Ru(bqp)_2]^{2+}$ as well as the development of facial $[M(bqp)_2]^{n+}$ complexes. Facial heteroleptic Ru-based complexes will help to elucidate more detail on the type of interactions that occur between this family of complex and DNA, as well as potentially improving the photophysical responses of the complexes in the presence of DNA.

4. Computational and Experimental Identification of i-Motif Binding Ligands

4.1. Introduction

In order to design better i-motif probes, more must be learnt about ligand-i-motif interactions. Many research groups have published ligands that can bind the i-motif but many do not exhibit i-motif specific binding.[171,172] With the aim of this project to discover a Ru-based i-motif probe for cellular imaging purposes, learning more about the i-motif's ability to accommodate ligands is key. This chapter will focus on the computational and experimental high-throughput screening of a library of organic compounds. The aim of this was to learn how different shapes and functional groups impact upon the binding ability of ligands to the i-motif. This information can then be taken and applied to the rational design of a Ru-based probe that can selectively identify the i-motif structure *in vivo*.

A prime example of this concept was shown by the work of Wang *et al.* whereby linking a benzo[*d*,*e*]isoquinoline to an Ir(III) polypyridyl unit, led to an enhanced recognition of G-quadruplex over dsDNA ($[Ir(bpy)_2(mbpb)]^+$, Figure 4.1).[173] The incorporation of the G-quadruplex specific isoquinolinyl unit on to a phenanthroline ligand enabled the compound to selectively target the G-quadruplex structure with the Ir(III) unit acting as a signalling probe. In 2016, Lin *et al.* synthesised a similar complex but using a benzofuran derivative as the G-quadruplex targeting moiety that also showing good G-quadruplex selectivity using a similar strategy ($[Ir(ppy)_2(edpahombc)]^+$, Figure 4.1).[174] Although these studies did not include i-motif DNA when testing for selectivity, they do demonstrate the possibility of tuning the binding affinity of a complex towards a certain secondary

structure by the addition of organic moieties.

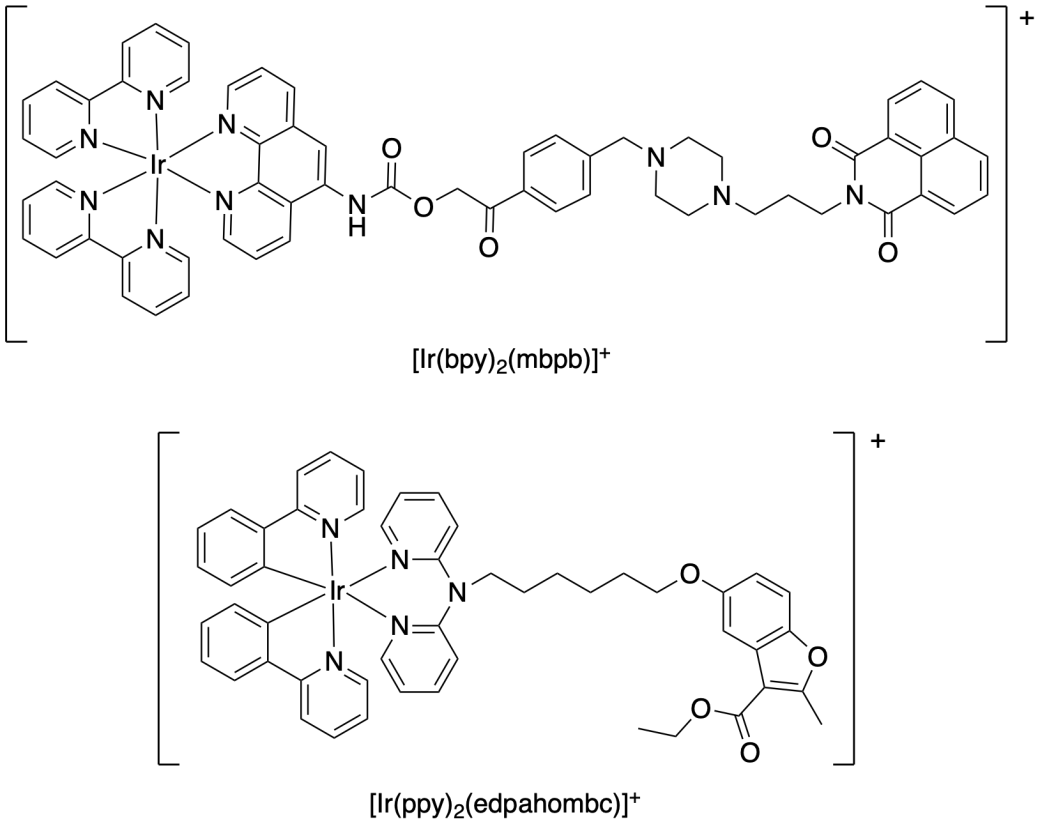

Figure 4.1: Two G-quadruplex binding Ir-based compounds

In order to discover organic compounds that bind a certain secondary structure, one must investigate the ligand-DNA interaction, a process that is incredibly important in modern drug discovery.[175] Virtual high-throughput screening is often far quicker than experimental equivalents and can aid in narrowing a search field to a group of molecules that often contain similar chemical properties.[176,177] Many tools have been developed to aid in the virtual high-throughput screening, such as DOCK,[178] GOLD,[179] AutoDock,[93] and FlexX[180] To compare the performance of these different tools, ten docking programs were evaluated by Wang *et al*. in 2016.[181] Of these tools, AutoDock Vina (Vina) was rated as one of the best performers. Developed by researchers at the Scripps Institute, Vina was a significant improvement over its predecessor AutoDock 4.2.[94,115] Previous AutoDock versions had utilised a genetic algorithm (GA) that explored the best docking pose of a series of different conformations before"breeding" the best poses and, after many iterations, arriving at the most optimised binding pose.[182] Vina moved away from this to use an iterative local search method, improving both performance and accuracy.[94] Due to

this increased performance, speed and ease of use, this tool was chosen for the *in silico* screening of a library of organic compounds.

When using these screening techniques, it is common to use X-ray crystallographic information to evaluate the binding location of a ligand. This involves removing the bound ligand from the ligand-receptor crystallographic data and searching the binding location with virtual compounds. There are of course many assumptions made in this and in some cases, as with i-motif DNA, no X-ray crystallographic data containing a ligand exist. In these cases, evaluating the receptor for potential ligand binding sites is often necessary and less computationally expensive.[181] One such software package developed to tackle this problem is Fpocket.[183]

Fpocket searches a receptor surface for what is known as an alpha sphere, an area on the surface that is surrounded by atoms but does not contain an atom itself, i.e. a pocket. It then identifies those pockets that are close to each other and then scores each one by calculating the properties of the atoms that form the pocket. This leads to the identification of regions upon a receptor surface that contain pockets which can favourably accommodate a ligand. Whilst this can lead to the identification of "ligandable" regions on a receptor, to treat a receptor as such a rigid body in this way is undesirable. However, treating the receptor as flexible is computationally expensive. Given the instability of the i-motif structure in molecular mechanical calculations,[126] treating the i-motif as rigid is the best way forward. To validate these techniques further, however, they must be backed by experimental data.

In an attempt to validate the theoretical *in silico* DNA binding properties that this chapter explores, two experimental techniques were also performed. In 2017, work published by our group explored the possibility of creating a fluorescent indicator displacement (FID) assay.[91] Ethidium bromide, thiazole orange, acridine orange, crystal violet, and a pyrene derivative were all investigated, with thiazole orange (TO) displaying the largest fluorescence increase upon binding the human telomeric i-motif (hTeloC) and low fluorescence when bound to the same unfolded sequence. A two-binding site model was assigned due to the 2:1 binding ratio of TO to hTeloC, the binding constants of which are 3.7 ± 0.7 and $78 \pm 13\,\mu M$. The locations of these binding sites is unknown, but there are few binding locations that an i-motif could accommodate. The already intercalated

core may accommodate an intercalating ligand but binding to the loop region has been shown to occur in other studies,[184] whilst groove binding on dsDNA is very common and the i-motif features similar grooves.[185] Displacement of TO from the DNA was shown to occur from a number of ligands with mitoxantrone and tilorone showing high ($> 70\%$) TO displacements (D_{TO}). This technique was developed into a high-throughput screen allowing for thousands of molecules to be screened for their TO displacement, and therefore their DNA binding properties.

The second technique used was a Förster resonance energy transfer (FRET) melting assay. In this assay, the DNA is labelled at each terminus with a fluorophore (5′ and 3′ end with 6-carboxyfluorescein (FAM, donor) and 6-carboxytetramethylrhodamine (TAMRA, acceptor), respectively). When the DNA is folded, the emission of the donor is quenched by that of the acceptor which in turn will fluoresce at a longer wavelength. In this work, the fluorescence of the donor is monitored so that as the temperature increases, the DNA unfolds leading to an increase in fluorescence. This assay was performed by Dr Abdelhamid from within the Waller group and will be discussed here.

For this project, the NCI Diversity Set VI library was chosen due to the ease of which it can be obtained but more importantly, an SDF file can be obtained that contains the same molecules that are physically supplied by the NCI. This, therefore, allows for both the *in silico* and *in vitro* screening of over 1500 molecules. The diversity set VI selected for molecule with hydrogen bond donors/acceptors, positive charge, aromatic units and acid/base groups.[186] After narrowing down to 1 million compounds, diversity was then encouraged by only accepting molecules that had 5 new pharmacophores when compared to any molecule already in the set. Molecules that were relatively flexible and contained fewer than one chiral centres or contained undesirable features, e.g. obvious leaving groups or weakly bonded heteroatoms, were also removed, yielding 1584 molecules. These properties could also make for good DNA binders and the increased diversity could help identify certain chemical features that aid in DNA binding. The full NCI library, containing over 250,000 compounds, and the ChEMBL library,[187] containing 2 million compounds, were also used for *in silico* searching of potential i-motif binding compounds.

The DNA sequence used in this chapter is the i-motif forming sequence hTeloC (5′-[TAA-CCC]$_4$-3′). There are currently no published crystal structures of this, or any, in-

tramolecular i-motif sequence, but there are structures which have been solved by NMR. Using modified bases, PDB 1ELN and 1EL2 were solved using NMR spectroscopy but for *in silico* screening, the addition of extra functional groups onto the i-motif structure could yield misleading results. Instead, a manually edited 1EL2 sequence to match the hTeloC experimental sequence, and equilibrated using molecular dynamics simulations to account for minor conformational changes, which has been previously published by our group, was used.[188] This removes the modifications necessary for solving the NMR structure, allowing for more accurate results to be acquired. Due to the acidic requirements for forming the hTeloC i-motif,[23] a pH 5.5 buffer containing 10 mM sodium cacodylate was used.

Statistical analysis between the different techniques shown here could yield more insight into the DNA binding properties of the library investigated over looking at any technique in isolation. To do this, a Pearson correlation coefficient was calculated according to Eq. 4.1.[189] Any correlation could provide interesting insights, for example, if TO displacement was higher from those compounds that gave better free energies of binding to the loop than the groove, it could suggest that TO binds in the loop or that displacement of TO from this location was more favourable than from the groove. However, a very strong correlation would be required to make such a claim.

$$\rho = \frac{c(x,y)}{\sigma_x \sigma_y} \tag{4.1}$$

where:

$x, y =$ the two subsets of data that are being compared

$c =$ covariance

$\sigma =$ standard deviation

Other analyses can also yield a better insight into the types of molecules that bind well to DNA. To find similar features, or chemical similarities, within a group of molecules, one can calculate the Tanimoto similarities between each of the molecules. The Tanimoto

similarity, first outlined in 1960,[190] and defines the similarity between two bit vectors using Eq. 4.2. In 1965, Morgan proposed a method for obtaining a *fingerprint* for a molecule by assigning each atom an identifier and then updating each atoms identifier based on the neighbouring atoms, which can be turned into a bit vector - a long series of zeroes and ones.[191] Using the Tanimoto similarity equation, one can arrive at a value between 0 and 1, with 1 being achieved when comparing two identical molecules. It has becoming commonly assumed that a Tanimoto similarity between two molecules of > 0.85 would give a high probability of that they would share the same bioactivity.[192] Recently, however, doubt has been cast upon this by investigating the multitude of different fingerprint analyses and also selecting molecules with a specific activity level and then retroactively comparing their similarities, to discover that in some circumstances, the similarity scoring can be as low as 0.3.[193] One limitation to the Morgan fingerprint analysis is that this compares the 2D similarity rather than the 3D similarity, which for discovery of how 3D ligands interact with a 3D receptor is a clear limitation, however, 3D similarities are far more complicated to calculate and the tools available to do so are limited.

$$f(A,B) = \frac{A \times B}{A^2 + B^2 - A \times B} \tag{4.2}$$

Using the tools and techniques described here, this chapter focusses on the search for i-motif binding DNA compounds using a mixture of *in silico* and *in vitro* techniques, as well as any correlations that can be drawn from the different techniques.

4.2. Results and Discussion

4.2.1 Computational Screening

In the absence of crystallographic data showing the ligand-DNA binding sites i-motif DNA, Fpocket was used to identify potential ligand binding sites on an i-motif structure.[183] The human telomeric i-motif was initially passed through Fpocket, which identified two possible ligand binding locations. The first was located in the loop region and the second along one of the major grooves (Figure 4.2). From this, three grids were created for Vina

to search, the first (loop) and second (groove) were 24 $Å^3$ and centred upon the locations of the binding pockets identified by Fpocket. The third encapsulated the i-motif in its entirety in order to probe whether binding locations one and two were in fact the best binding locations.

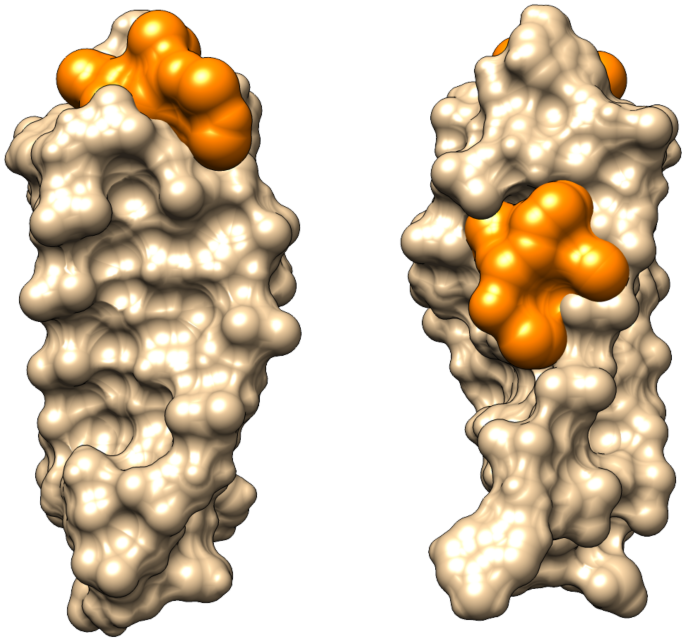

Figure 4.2: The pocket regions (orange) of the loop (left) and groove (right) identified by Fpocket on the hTeloC i-motif (beige)

There were thirty two compounds within the library that could not be screened using Vina as they contained an As atom, which Vina does not contain parameters for. This left 1552 compounds that were to be screened against each receptor. A script using the programming language Python was created to iterate over each binding site and each molecule with the free energies of binding exported into a CSV file and the binding locations saved as PDB files.[194] From these docking calculations, the top 100 compounds for each receptor were also identified and of these, 59 molecules were found to appear in the top 100 for all three pockets (see Appendix A1). The compound NCI 3391 is in the top three compounds regardless of the chosen pocket, with the search over the whole i-motif structure finding the opposite groove to the one identified by Fpocket as the lowest energy binding site (Figure 4.3). It is quite likely, therefore, that such a compound would bind the i-motif in multiple places. Of the locations analysed for the top ligands, the search over

the whole structure returns a binding location that is either in the same or opposite major groove to that predicted by Fpocket.

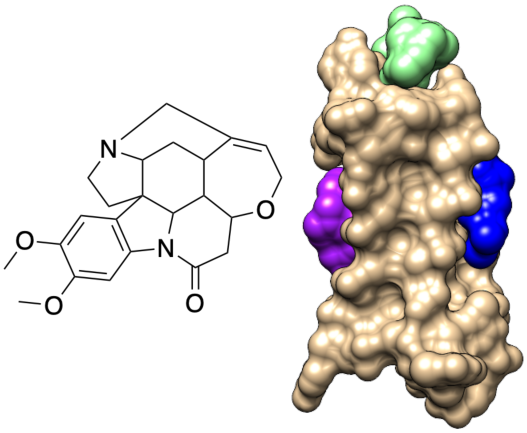

Figure 4.3: 2D structure of NSC 3391 (left) and binding locations when searching the loop (green), groove (purple) and the whole structure (blue) (right)

One can learn a lot not only from examining the top hits but also by examining the bottom hits (Figure 4.4, Figure 4.5 and Figure 4.6). Looking at the bottom hits for each of the binding pockets, they tend to be small, non-linear, aliphatic molecules. This is in stark contrast to the top hits which tend to feature longer, more linear heteroaromatic molecules. Common DNA binding ligands, like ethidium bromide or polyamides, tend to either have multiple heteroaromatic rings or a more linear backbone, or both, leading to the increased hydrogen bonding ability of the ligand, as well as, in some cases, base specificity.[87,185,195]

Of course, the type of molecule that could bind the loop may differ from one that could bind a groove so to quantify the differences in binding pockets, Pearson correlation coefficients were calculated using the free energies of binding of the ligands in each dataset. When correlating the free energy of binding of the different binding pockets on the DNA, the relationships were strong. They all gave Pearson coefficients $\geq$0.90, with the correlation between binding pockets two and three yielding 0.98 (Figure 4.7). This indicates that the binding location that was found when searching the whole DNA structure (pocket 3), was almost identical to that of the groove (pocket 2). In the case of loop vs groove or loop vs the whole structure, the relationship was not as strong, although still significant, suggesting that ligands that can bind well to one pocket of the DNA also bind well to another but will still differ to some degree. Whilst these correlations are

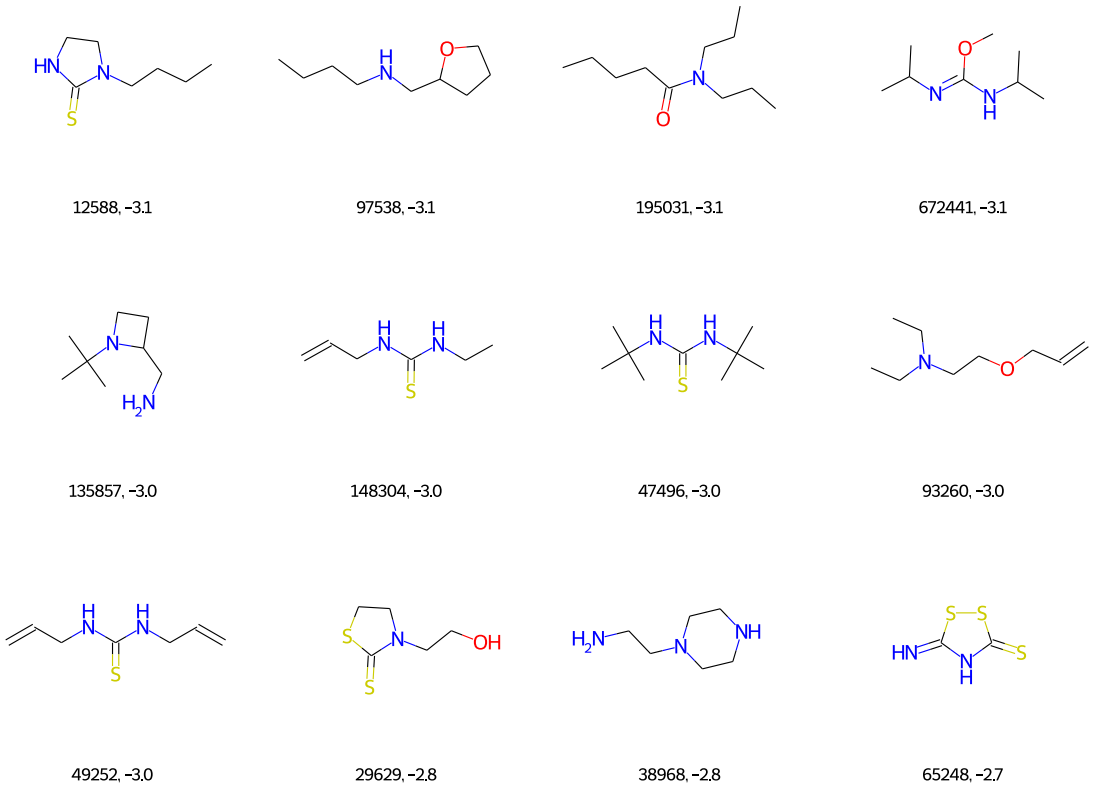

Figure 4.4: The weakest binding 12 molecules identified by searching the loop

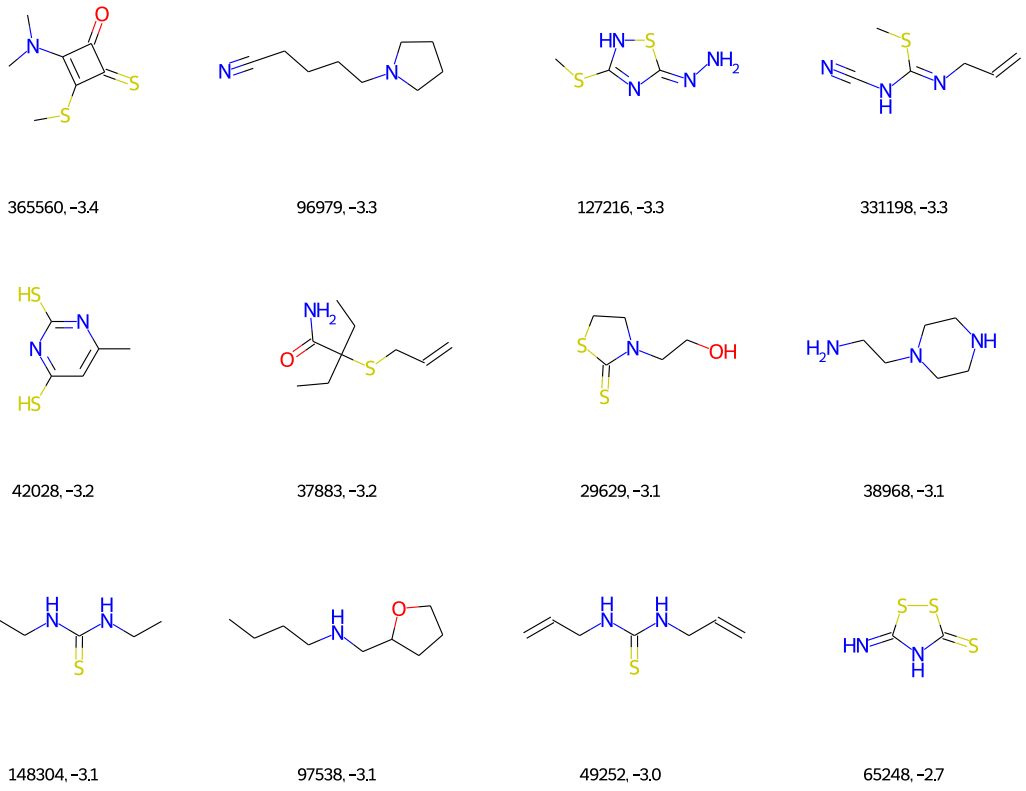

Figure 4.5: The weakest binding 12 molecules identified by searching the groove

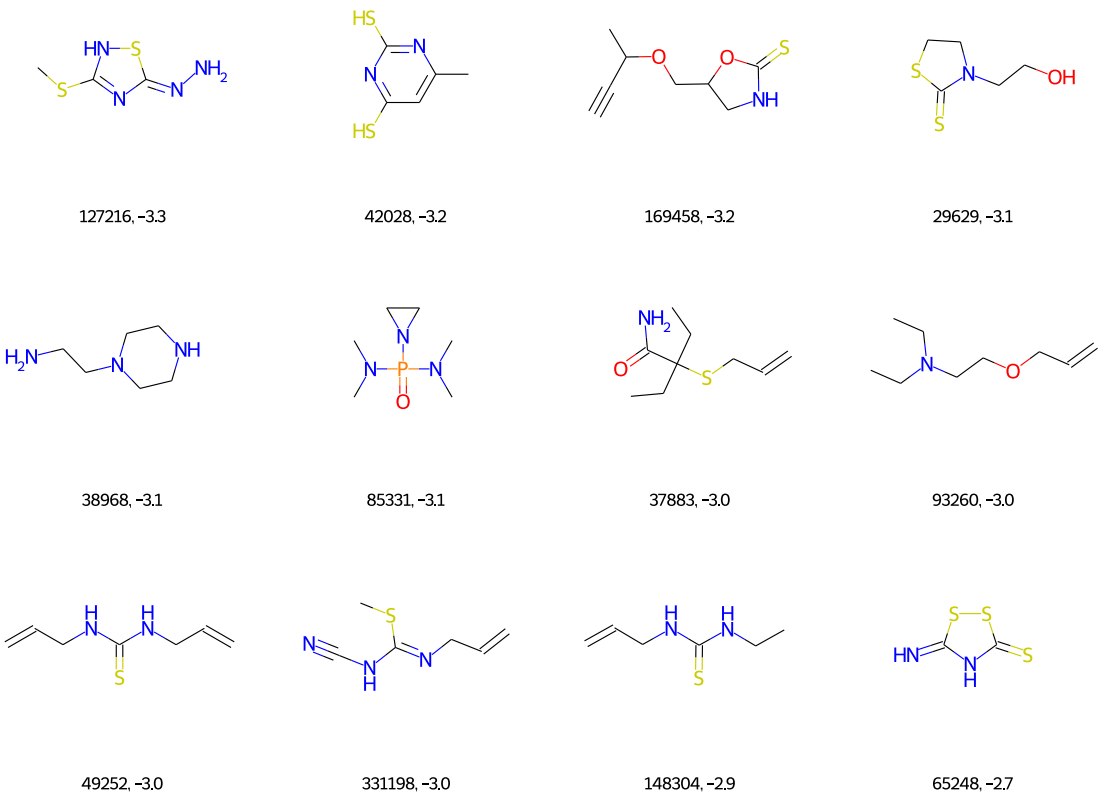

Figure 4.6: The weakest binding 12 molecules identified by searching the whole DNA structure

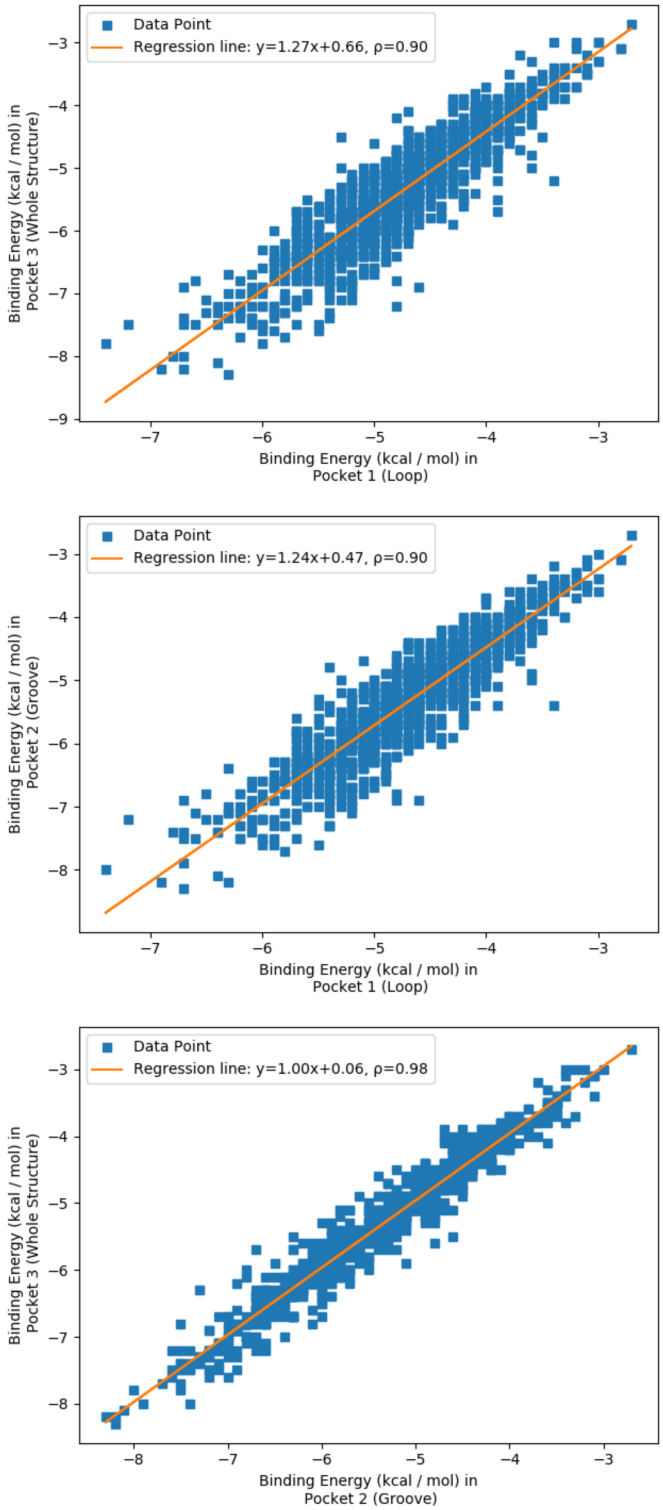

Figure 4.7: Correlations between pocket 3 and 1 (top), 2 and 1 (middle), and 2 and 3 (bottom), with their linear regression fits in orange

largely unsurprising, it does suggest that the groove is a more favourable binding location when the DNA is treated as a rigid body.

When comparing groove vs loop, taking the top 100 ligands for each gives 136 unique ligands, with 64 being shared across both pockets. There are 36 ligands that feature in one pocket but not in the other (see Appendix A2 and A3). The average mass of a ligand that binds the loop but not the groove is 359 $\pm$ 56 and vice versa is 354 $\pm$ 61 with the average number of atoms being 25.7 $\pm$ 3.9 and 25.6 $\pm$ 3.8, respectively. These numbers do not show a significant difference in the make up of the ligands but, when comparing what elements make up each ligand there is quite a difference. The average number of N and O atoms in a molecule that binds the loop is 2.8 (11% of the atoms) and 3.7 (14%), respectively, whereas for those that bind the groove that changes to 2.1 (8%) and 2.6 (10%). There is one more oxygen and nearly one more nitrogen atom on each molecule that binds the loop over that that binds the groove, suggesting that hydrogen bonding has a much greater effect when binding the residues in the loop over those in the groove. Of these heteroatoms, if one only counts the aromatic ones then the percentages are 5.3% and 3.8% for loop and groove respectively. This tells us that the type of molecule that binds the loop over the groove tends be slightly heavier, with more atoms and, more hetero and heteroaromatic atoms than those that bind in the groove. Moreover, plugging these ligands back into the NCI database, one can pull out extra information. For example, there are on average 1.8 hydrogen bond donors and 4.8 acceptors in each ligand that binds the loop over the groove, with that becoming 1.4 and 4.4, respectively, in the opposite scenario. Not only does this show that there is more hydrogen bonding ability in the ligands that bind the loop over the groove but that there are more hydrogen bond acceptors over donors per ligand in both circumstances. This knowledge could guide someone who was investigating the type of molecule to design to target the i-motif structure.

From here it was interesting to find out if there were common features or structures that determined the free energy of binding of the compounds. Clustering all the compounds with a Tanimoto similarity of 0.6 yielded 85 clusters containing a total of 207 molecules (Figure 4.8). The other molecules did not find any similar partners and were placed in clusters that contained just one molecule, these were therefore not included in this analysis. Putting back in the free energies of binding to each molecule and calculating the average

of each cluster identified seven clusters, clusters 25, 26, 28, 29, 32, 34 and 39 (Figure 4.9). There are some common features that are shared across these clusters; 25, 26, 29 and 32 are composed of linear molecules containing multiple aromatic rings with lots of hydrogen bonding potential. This type of molecule has been identified on many occasions to bind DNA grooves, particularly the minor groove of dsDNA.[196] Encouragingly, unpublished data from within our group has also identified molecules from clusters 25 and 29 as being good i-motif binders, who appear frequently using different experimental techniques with different i-motif forming sequences. However, in order to fully quantify the results presented here, they must be compared to experimental data. Theoretical data alone is not enough to make firm conclusions about the types of molecules that can bind i-motif DNA.

4.2.2 Fluorescent Indicator Displacement Assay

Two techniques were used to experimentally explore the *in silico* results obtained so far: the first was an FID assay, and the second a FRET melting assay. The FID assay was performed with all molecules in the library against the hTeloC i-motif at pH 5.5. Of the 1584 molecules, 32 showed a TO displacement (D_{TO}) of over 50% (Figure 4.10). These compounds are considered hits and, due to the high percentage of TO that they displaced, will have lower dissociation constants for hTeloC than TO. This calculates to a 2% hit-rate for this assay, where typical high throughput screens yield hit rates of 0.01 % to 0.14 %,[197,198] displaying how this particular library contains molecules that can act as strong DNA binders. As was the case with docking calculations, the best non-hits were also examined (Figure 4.11). In the case of the docking, the weakest binders tended to be aliphatic, non-linear molecules but this was not quite the case with the FID assay. There was a general lack of heteroaromatic rings, bar a couple of exceptions, amongst the 12 lowest TO displacing compounds, which tend to be non-linear and feature many unfunctionalised phenyl rings. However, it is interesting to note that NSC 60659, a compound that shares some similar features with dppz (Tanimoto similarity = 0.43) is one of the weakest TO displacers within this library. With evidence mounting that dppz containing complexes when bound to i-motif DNA have a higher affinity for longer looped sequences,[70] it seems like intercalation into the core of the i-motif is unfavourable Perhaps that is why the top hits identified here have a shape more similar to that of classical groove binders rather

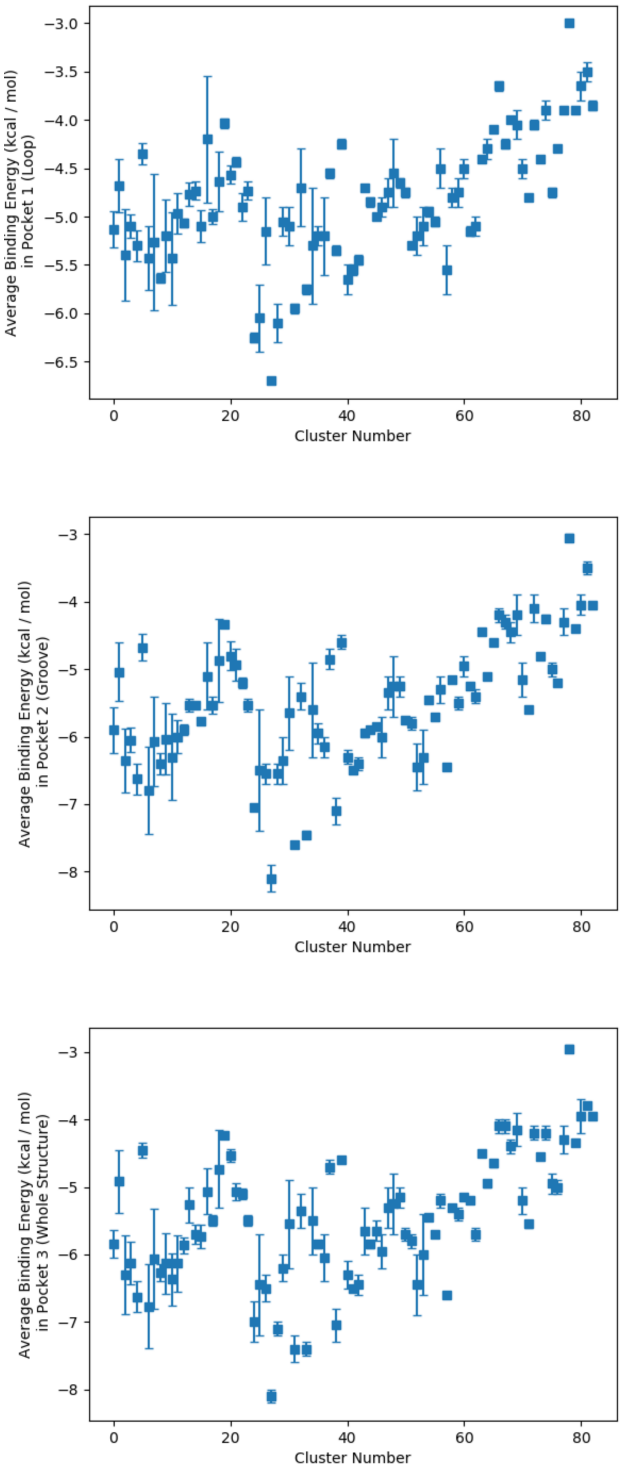

Figure 4.8: Average free energy of binding of each cluster identified using a Tanimoto similarity of 0.80. Error bars represent standard deviation of the free energy of binding from the molecules within each cluster.

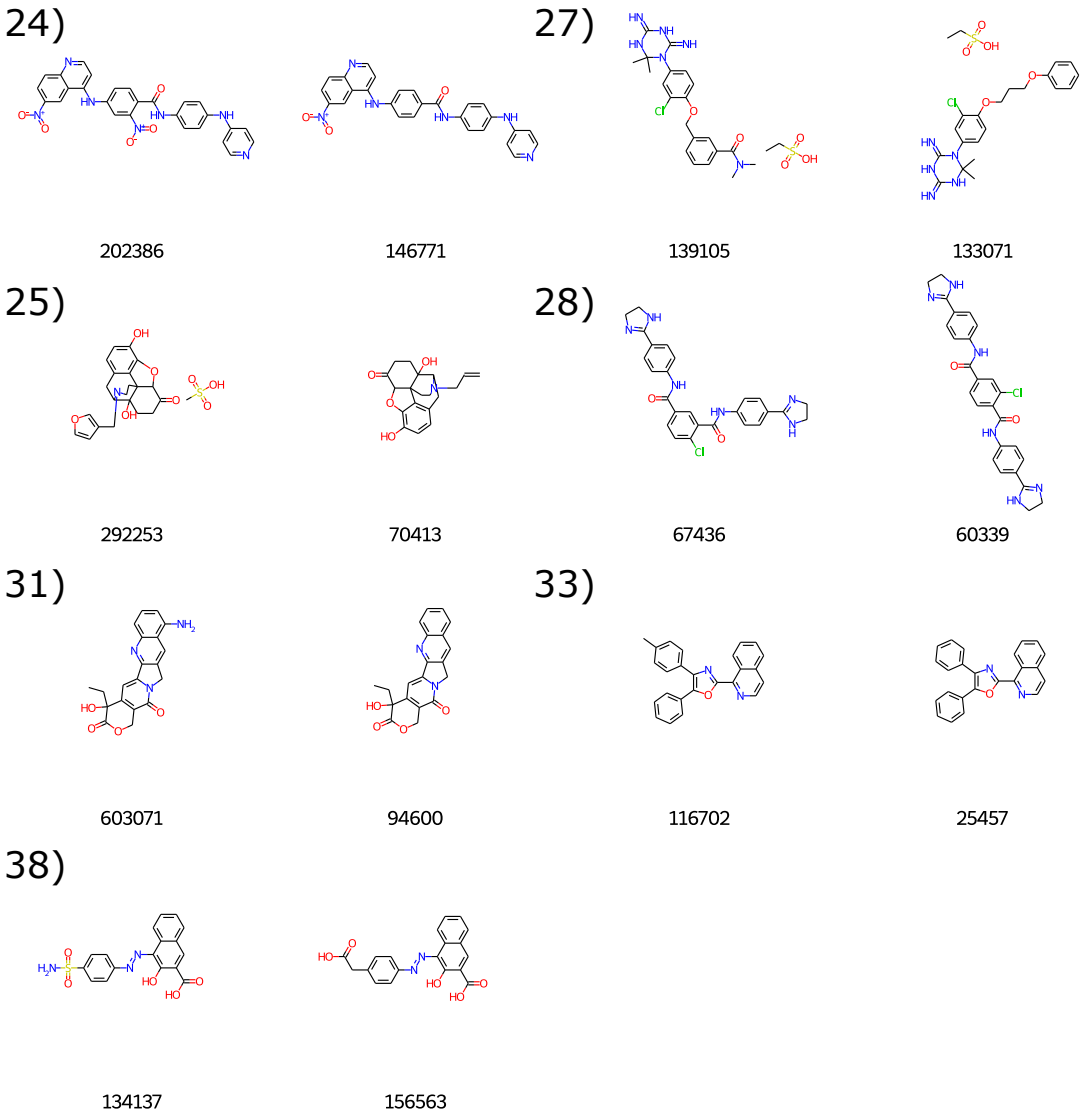

Figure 4.9: The top seven clusters identified using the free energy of binding of each cluster where each molecule is labelled with its corresponding NSC code

than classical base pair intercalators.

To further validate the data collected in the FID assay and the docking calculations, Pearson correlation coefficients were calculated and a plot of TO displacement vs the free energy of binding for each binding pocket were created (Figure 4.12). With all three binding pockets, the Pearson coefficient indicated a slight negative correlation between the free energy of binding and the TO displacement, i.e. the stronger the binding, the better the TO displacement. While this correlation isn't considered a statistically strong one, it does show that there is at least a weak-moderate correlation between the FID assay and the computational screening. The weakest correlation of the three is against the loop binding pocket (-0.33), with the groove and whole structure search being approximately the same (-0.37 and -0.36, respectively). Whilst the differences between the correlations of the FID assay and each binding pocket are small, it is interesting to note that when the Vina grid included the entire i-motif structure, all analysed ligand-receptor complexes had the ligand in one of the major grooves, and the correlation of TO displacement was stronger with this and the groove binding pocket when compared with the loop. The shape, size and features of the molecules, along with the correlations of the different techniques, suggests that the ligands identified here could well be binding in the groove of the i-motif and future work should focus upon this hypothesis. The run of six C-C^+ base pairs along the groove of the i-motif could offer the potential of sequence specific identification of i-motif DNA, similar to what has been achieved with polyamide ligands that target the minor groove of dsDNA.[199]

It is interesting to note that no compound that exhibited a TO displacement of $<$50% also exhibited a free energy of binding of $<$-5.0 when bound to either the loop or groove. This feature of the correlation could be used to eliminate compounds from the more time consuming experimental screening by first performing an *in silico* screen, if a molecule exhibits a free energy of binding $>$-5.0, that one should not include it in the experimental screen.

Of the top 100 compounds identified for each of the four datasets (the three docking locations and the FID assay), there were 16 compounds that were present in all four (Figure 4.13). Searching these molecules on SciFinder and refining the references that contain them by either "i-motif" or "G-quadruplex" yields only one reference. NSC 319990

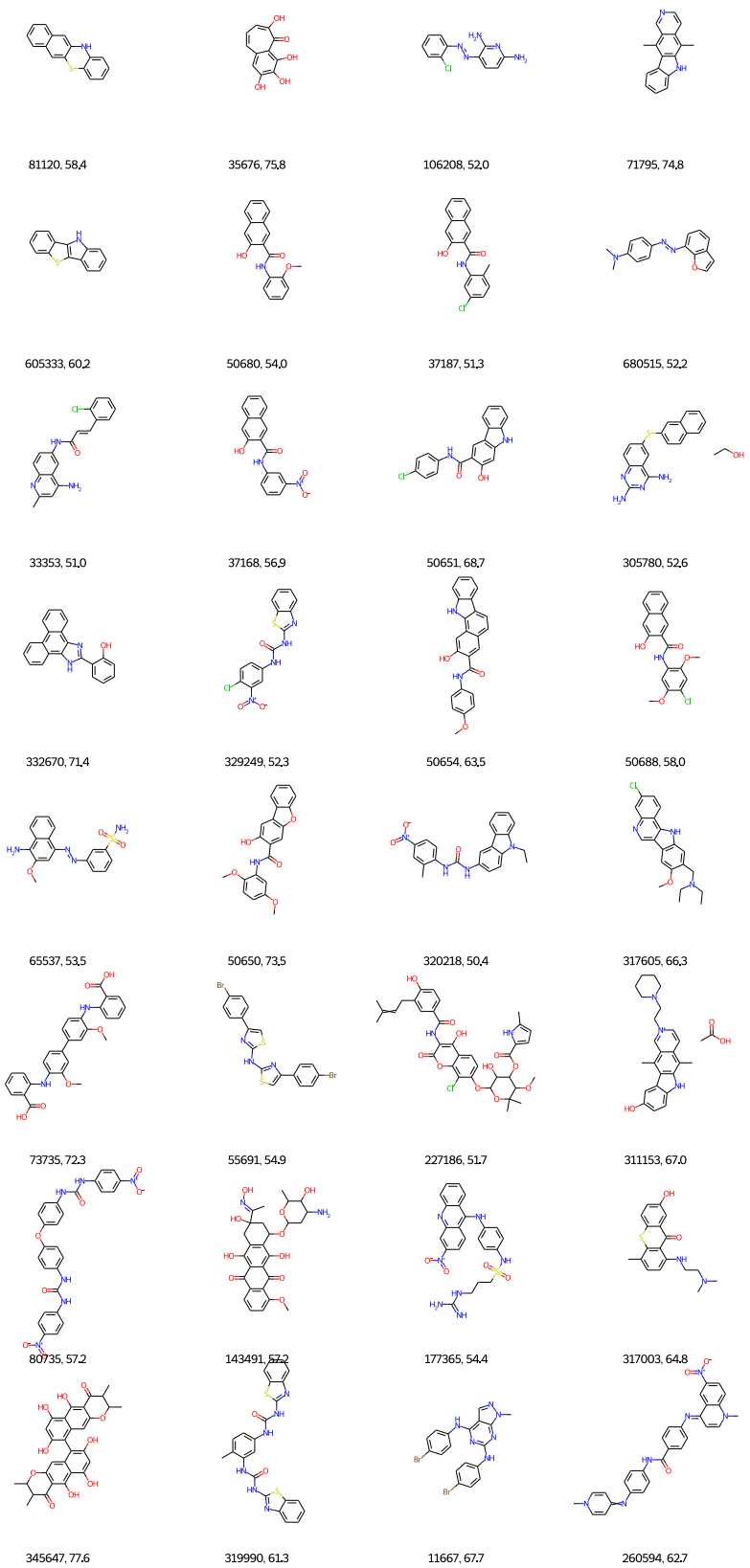

Figure 4.10: The compounds that gave $D_{TO} \geq 50\%$, labelled with NSC codes followed by their D_{TO} values (%)

38743, 0.2

88349, 0.2

17362, 0.2

371178, 0.2

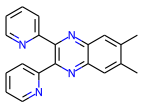

60659, 0.2

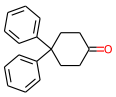

117554, 0.1

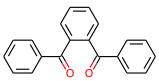

6145, 0.1

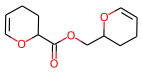

38983, 0.0

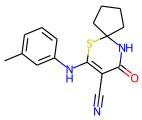

319436, 0.0

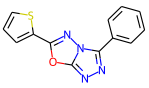

166596, 0.0

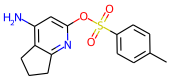

3753, 0.0

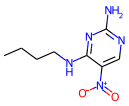

85326, 0.0

Figure 4.11: The compounds that gave the lowest D_{TO} values, labelled with NSC codes followed by their D_{TO} values

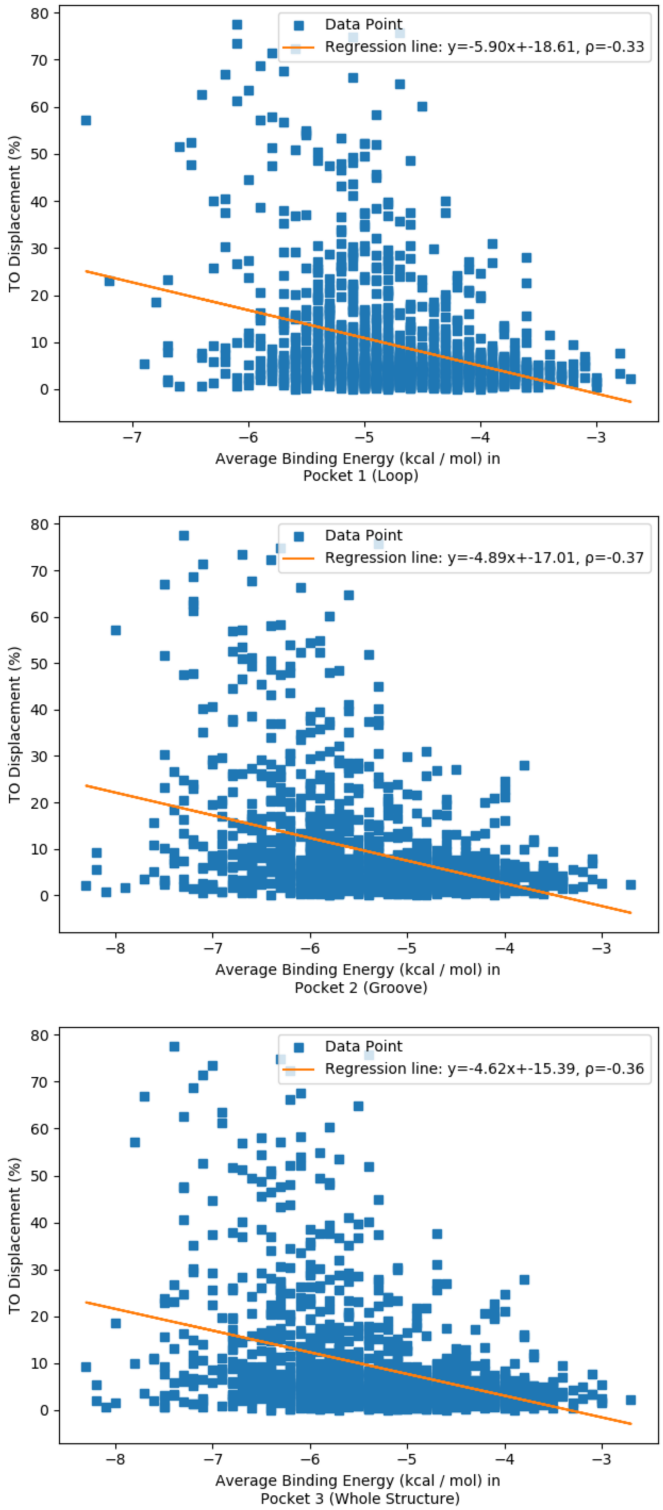

Figure 4.12: Correlations between the TO displacement (%) and docking search 1 (top), 2 (middle), 3 (bottom), with their linear regression fits in orange

was previously identified in a screen of NCI libraries against G-quadruplex DNA.[200] None of these molecules have been reported for their i-motif interaction and could offer a strong platform for the development of i-motif binding ligands and/or inorganic complexes containing i-motif directing moieties. To identify similar compounds that may also bind i-motif and widen the library of potential hits, each molecule of this group of 16 was searched in the larger NCI library, containing over 250,000 molecules and all compounds with a Tanimoto similarity of 0.8 were returned. Surprisingly this yielded no molecules, and even when lowering the similarity to 0.5 there were still no similar molecules returned. It was concluded that the search library was too small and that the diversity within it must be limited. Instead the same search was performed with the ChEMBL library of *ca* 2 million compounds for structures with a Tanimoto similarity of 0.80, yielding 67 hits (see Appendix A4).

Not all compounds found molecules similar to themselves, such as NSC 50651, 50654, 260594, and 33575. Some found many similar compounds, such as 143491 that had 16 matches. This opens up the number of potential ligands dramatically. One common feature through out this is the high number of hydrogen bond acceptors/donors featured in all of the identified ligands, along with the linearity of many of them. These features could be driving the groove binding abilities of the ligands, leading to the high binding properties observed. In contrast, the G-quadruplex tends to favour larger ligands that can cover the G-tetrad as end-stacking upon this is highly favourable.[201] To explore this library further, and to investigate the effect of them on the thermal stability of the DNA, a FRET melting assay was performed.

4.2.3 FRET Melting Assay

The FRET melting assay was performed on all ligands within the library using 5′-FAM-[TAA-CCC]$_4$-TAMRA-3′ by Dr. Mahmoud Abdelhamid from the Waller group. The FAM moiety was excited at 470 nm and the emission was monitored at 510 nm with the temperature increasing by 1°C per minute from 25°C to 70°C. During the course of the melt, the DNA unfolds, creating a larger distance between the two fluorophores and thus decreasing the FRET to the TAMRA moiety. The ratio of ligand:DNA was kept the same as that used for the FID assay (5:1), but the absolute concentrations were changed. The

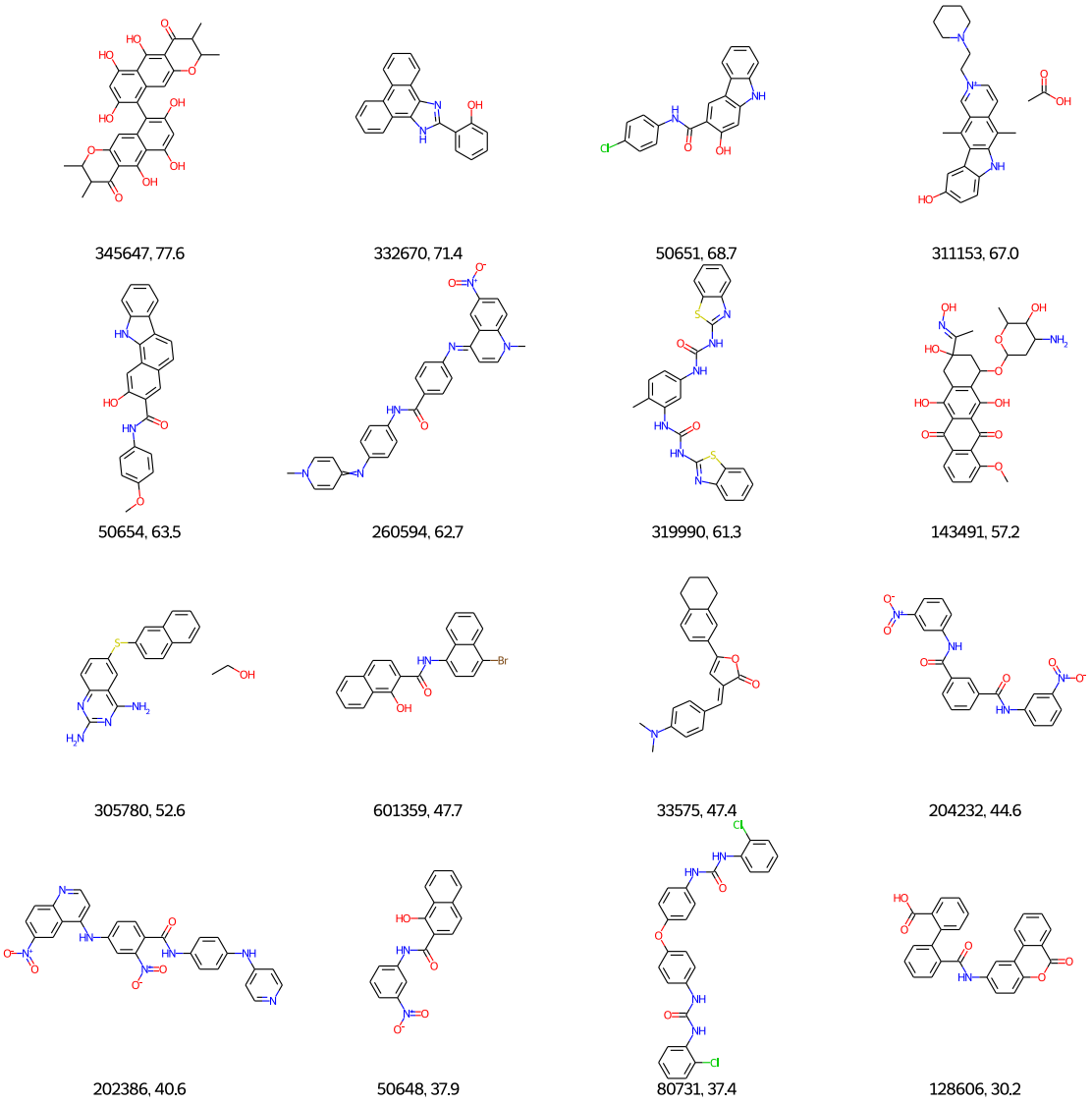

Figure 4.13: The 16 compounds identified in the top 100 ligands for each of the docking searches and the FID assay, labelled by their NSC code

concentration of DNA used was 0.2 µM with five equivalents of ligand at 1 µM. Due to equipment failings, two QIAgen Rotor-Gene Q-Series PCR machines were used over the course of the screen. Interestingly, the two machines, despite being the same models, gave varying results. Both machines recorded the same melting temperatures for the control samples, where only DMSO was added to the DNA, but gave very different melting temperatures for the samples containing the ligands. In the second machine used, the melting temperatures were almost always 2-4°C higher than the control samples, for every ligand (Figure 4.14).

$$z = \frac{x - \mu}{\sigma} \tag{4.3}$$

where:

μ = mean

σ = standard deviation

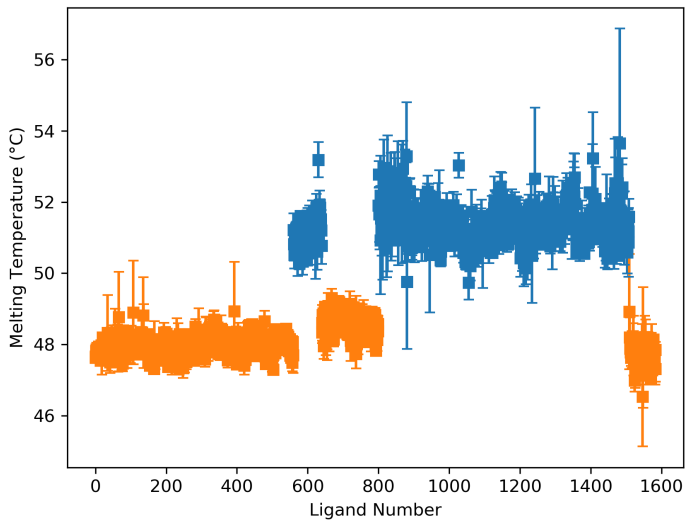

Figure 4.14: Plot of the melting temperatures obtained for each ligand from the two machines, machine one (blue) and machine two (orange)

Due to this disparity between the different machines, the raw scores of each melt were converted to a z-score using Eq. 4.3 (Figure 4.15), where the two populations used

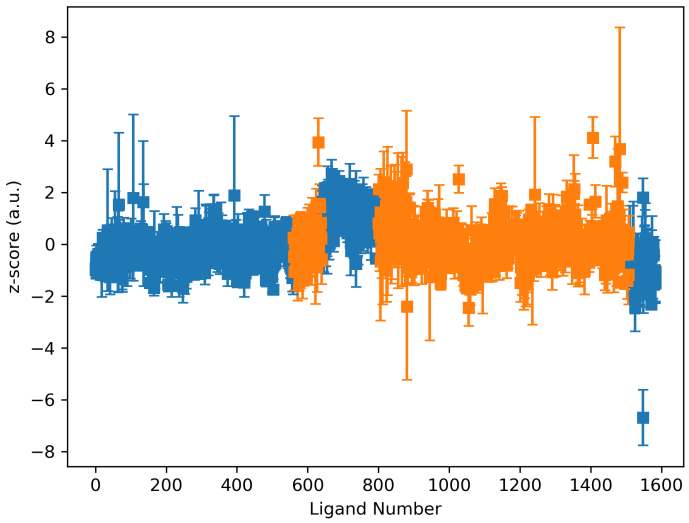

Figure 4.15: Plot of the z-score obtained for each ligand from the two machines, machine one (blue) and machine two (orange)

were from each machine, allowing for comparisons across the whole library. Correlations between this assay and the other assays yielded Pearson correlation coefficients of 0.01 with the docking assay and -0.01 with the FID assay (Figure 4.16), indicating that there is no correlation between FRET and the other assays.

A z-score outside of the -1.96 to 1.96 range indicates a significant result with a 95% confidence (Figure 4.18).[202] Searching for ligands that, when including their triplicate error, are outside of this range yields only 10 ligands, a hit rate of 0.6%. The ligand furthest outside of this range is NSC 143491, with a z-score of -6.69. This compound also appears in the top hits for the other techniques with a TO displacement of 57 ± 2 % at 5 equivalents and docking energies of -7.4, -8.0 and $-7.8\,\mathrm{kcal\,mol^{-1}}$ for the binding pockets on the loop, groove and whole structure, respectively. Interestingly, this compound also delivered the highest amount of matches (16) when searching the ChEMBL library for similar molecules to the hits obtained in this study. Going back to the docking calculations performed with this ligand, highlight its groove binding ability. The binding affinity for the loop was measured at $-7.4\,\mathrm{kcal\,mol^{-1}}$ and 36 contacts (an overlap of less than 0.4 Å) were measured between the ligand the DNA. Five hydrogen bonds were also found between the ligand and DNA, with four arising from the hydroxylimine group to three of the bases contained in the loop (Figure 4.17). In a solution state, this loop would be flexible

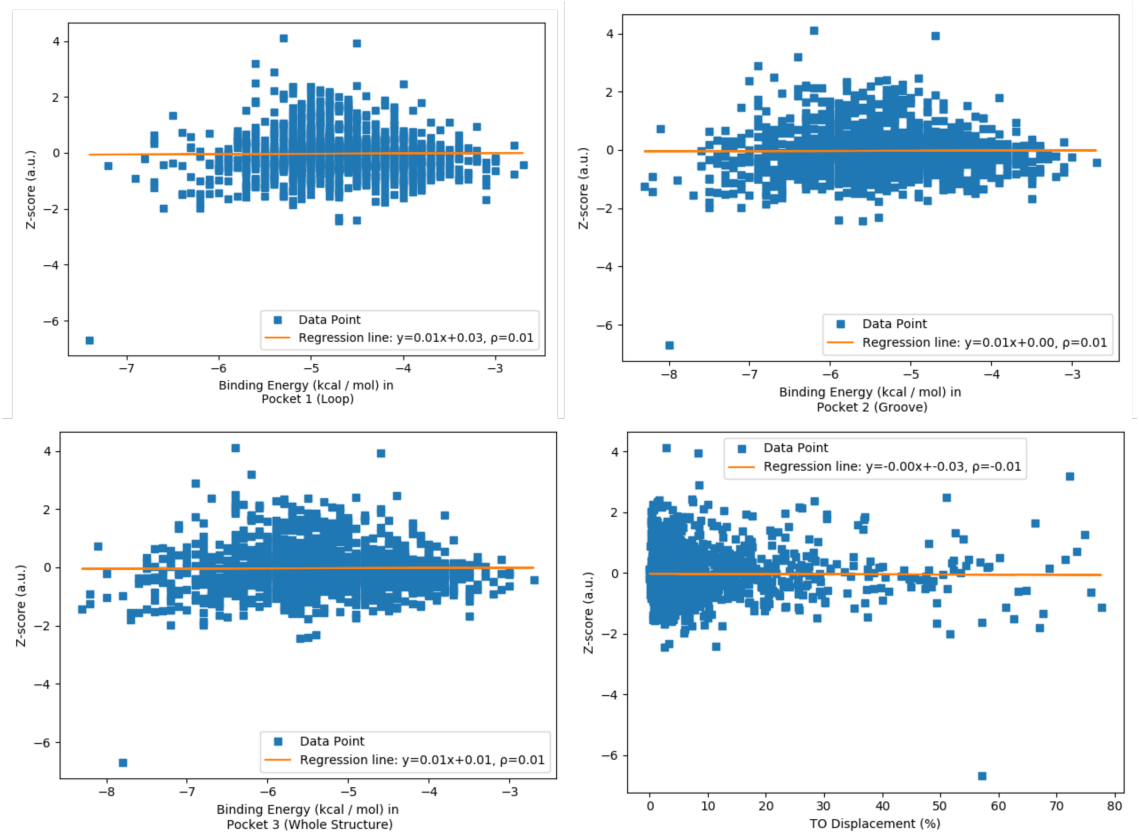

Figure 4.16: Correlation between the FRET melting z-scores and (left-right) docking search 1, 2, 3, and the FID assay, with their linear regression fits in orange

and the protrusion of the hydroxylimine group into this cavity would be less favourable as the shape of the cavity could well be changing. In the case of the groove, a binding affinity of $-8.0\,\mathrm{kcal\,mol^{-1}}$ was found and 26 contacts between ligand and DNA. While the number of contacts is fewer in the groove, the overall strength of each contact is higher, leading to the better affinity. Four hydrogen bonds were identified with one significant bond between the hydroxylimine of 143491 and the amine group of a cytosine. The others arise from the carboxyl groups of 143491 interacting with the phosphate backbone along the groove. Significantly, the search across the whole structure found the same location for the ligand as that of the just the groove search.

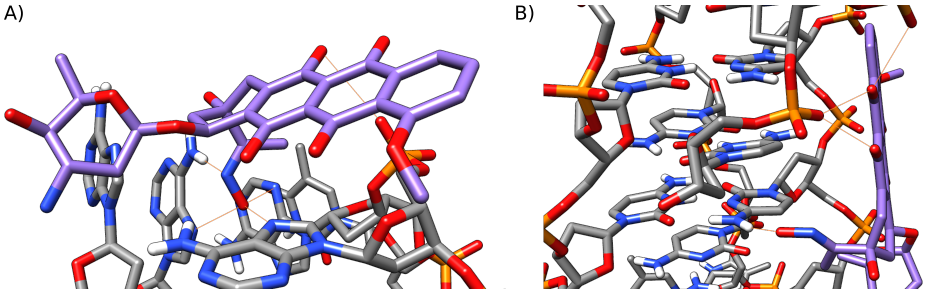

Figure 4.17: Docking locations of 143491 (purple) in the loop (left) and in the groove (right) with hydrogen bonds coloured orange

It is no surprise then, that 143491 shows a negative z-score, indicating a destabilisation of the i-motif structure. Interactions directly with the cytosine bases in the structure could likely lead to a destabilising effect on the i-motif which is sensitive to any disruption to the pK_a environment of the cytosines.[26,28,35] This could possibly explain the high D_{TO} value obtained for this ligand; if it has a destabilising effect upon i-motif DNA and the fluorescence of TO is dependent upon binding a folded structure, any source of unfolding will appear as though the TO is being displaced, when in reality, the DNA is unfolding.

Whilst this technique offered poor correlations with the other techniques explored here, it has identified a number of molecules that could be having an effect on the thermal stability of the i-motif DNA. Through exploring the interactions of over 1500 molecules with i-motif DNA using three different techniques, a number of molecules have been identified. These could be used going forward to rationally design i-motif targeting inorganic complexes. There are lessons that can be learnt from the type of molecules identified through using these three techniques. Designing a molecule that is linear, has

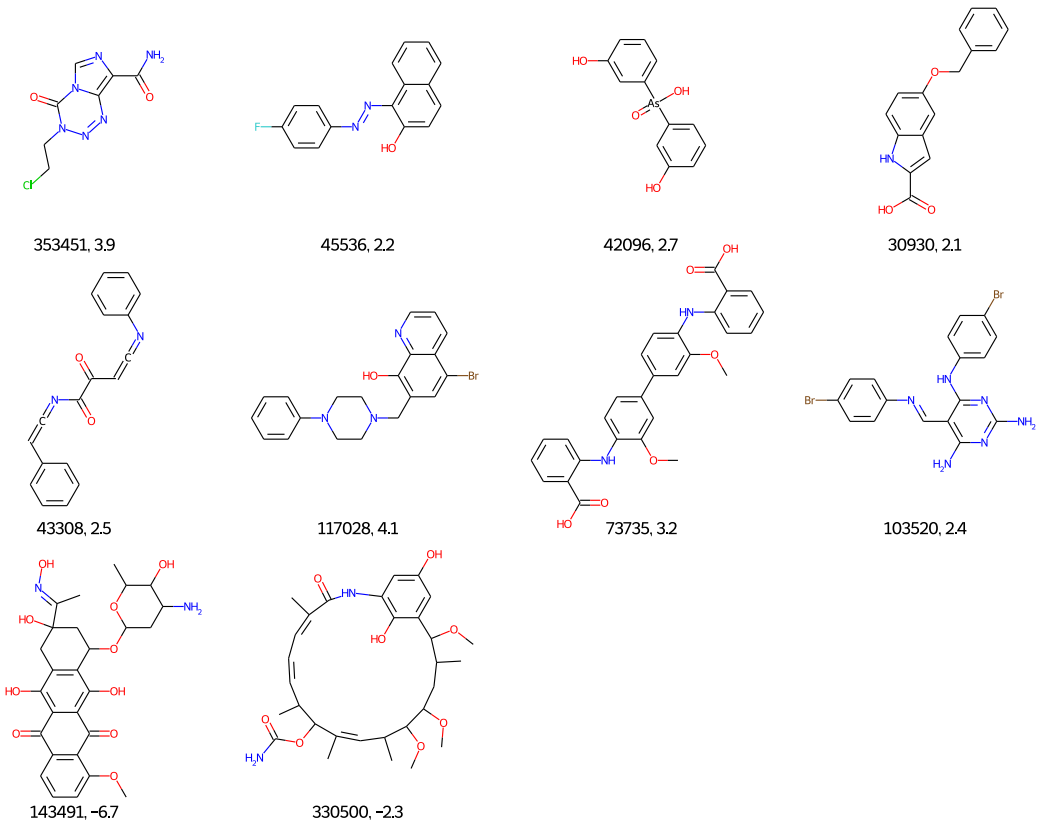

Figure 4.18: Ligands with a z-score greater than 2 or less than -2 labelled by their NSC number followed by their respective z-score

good hydrogen bond donor/acceptor groups - preferably more acceptors than donors - could lead to the design of an i-motif targeting ligand. Whilst specificity towards the i-motif was not explored in this study, further work could focus on this to then be able to distinguish molecules that target the i-motif over other DNA secondary structures.

4.3. Conclusions

Through the use of three different techniques, one *in silico* and two biophysical, a number of i-motif binding ligands have been identified. Docking the ligands in the NCI Diversity Set VI, a library of 1584 compounds, using AutoDock Vina showed a stronger binding affinity for the groove of the i-motif over the loop region. A stronger correlation was found between a search of the whole structure vs the groove rather than vs the loop. Of the top 100 ligands for each search, 59 were found to occur in all three searches, and when also comparing the FID assay, 16 were found to appear in all four. A high hit-rate (2%) was found for the FID assay, showing not just the capability of the i-motif to accommodate a ligand but also the usefulness of this library when finding DNA binding ligands. Additionally, this high hit rate could occur due to a high level of false positives, destabilisation of the i-motif structure would lead to a decrease in TO fluorescence and a ligand that was thought to be binding well to the i-motif is in fact unfolding the structure, although the FRET melting assay should indicate when this is occurring. Searching the 16 hits for similar compounds in the ChEMBL library yielded 67 analogues, which could offer a platform for the development of many i-motif binding ligands. Of these ligands, it was found that most of them were linear in structure and feature multiple heteroaromatic rings in their structure, adding to the argument that these ligands could indeed be binding the groove of the i-motif.

Correlations between the FID assay and the docking assays were shown to be weak-moderate, with Pearson correlation coefficients of *ca* -0.30 for the TO displacement and the free energy of binding of each docking search. Whilst the FRET analysis did not yield any significant correlations with the other two techniques, it did identify 10 ligands with significant effect on the thermal stability of the DNA and helped to identify NSC 143491 as a potential i-motif destabilising ligand. Further, *in silico* binding suggests this ligand

binds along the major groove of the DNA structure, interacting with the cytosine residues of the i-motif core. Future work will focus, in tandem with the previous chapters, on the design of i-motif binding metal based complexes. The properties of which can be increasingly tuned towards the i-motif as the binding properties of other compounds is explored further. Screening of this library against G-quadruplex and dsDNA using these techniques could also help to identify i-motif specific ligands. Synthesis of an NSC 143491 containing metal complex would be interesting to explore further the effects it has on the i-motif stability, and any of the 16 compounds identified to have good *in silico* and TO displacement properties could offer the potential to identify i-motif DNA *in vivo*.

5. Conclusions

It was the aim of the project to develop an i-motif specific Ru-based complex for the use of *in vivo* imaging of i-motif DNA. Whilst that has not been directly achieved, a significant step towards that goal has been taken. The discovery that *cis*,*fac*-$[Ru(bqp)_2]^{2+}$ can act as a light switch in the presence of DNA and does not rely upon solvent exclusion, as dppz containing complexes do, is a new phenomenon for Ru-based DNA probes and will have ramifications for the field. The evidence presented here suggests that this photophysical phenomenon occurs due to the electronic and steric interactions between the complex and DNA, rather than protection from the bulk solvent. This opens up a new class of light switches that could be used to identify specific DNA sequences. The work presented here shows how using time-resolved emission techniques, the DAP i-motif was identified even in the presence of both DS and G4 DNA. Moreover, the Λ isomer of *cis* was shown to have *ca.* double the emission intensity with the DAP i-motif over DS or G4 DNA, a promising improvement over the racemic mixture.

A new synthetic route for the formation of this isomer in high yields with <10% formation of the two other isomers was also presented. This route not only offers the formation of heteroleptic facial isomers but could also be used in the formation of facial isomers of complexes containing metals other than ruthenium. This synthetic route can be tuned by controlling the temperature and by careful selection of the arene used in the $[Ru(arene)(bqp)]^{2+}$ precursor. Synthesis of $[Ir(Cp^*)(bqp)]^{2+}$ was achieved and could be used in the formation of a bis-tridentate facial iridum complex. Application of this to other metals, such as Os, could also yield similar results.

High-throughput screening of three different techniques and 1584 ligands from the NCI Diversity Set VI library was shown to identify many ligands that can bind i-motif DNA. The FID assay yielded a hit rate of 2% for ligands that can displace thiazole orange

$\geq$50% from the human telomeric i-motif. This data was corroborated by *in silico* screening using AutoDock Vina. There were 16 ligands identified as being in the top 100 hits for both the *in silico* and FID screens. Searching the ChEMBL library for similar compounds yielded 67 molecules that could also offer good i-motif binding abilities. Future work will focus on screening this library against DS and G4 DNA to identify i-motif specific ligands as well as incorporation of these ligands into Ru-based complexes to improve the i-motif binding ability of the $[Ru(bqp)_2]^{2+}$ family of complexes.

This work has shown significant progress towards the goal of developing an i-motif specific emissive Ru-based probe and will hopefully lead to many projects being pursued off the back of it.

5.1. Future Work

The future work building off of the back of this project should firstly focus on completing the synthesis and biophysical characterisation of the $[Ru(bqp)(bqp-R)]^{2+}$ complexes that were explored in Chapter 3. This will lead to the application of the new synthetic route presented in that chapter as well as the exploration of the light switching mechanism presented in Chapter 2. Changing the chemical, and therefore photophysical, properties of this class of complex could confirm the hypothesis presented thus far regarding the light switching mechanism. Addition of hydrogen bonding groups on the bqp ligand may also lead to increased DNA binding properties.

Secondly, work should also focus on development of facial bqp complexes containing metals other than ruthenium. Not only will this also contribute towards understanding the light switching mechanism, it may also lead to an increased DNA interaction. Applying the knowledge garnered in Chapter 4 to synthesise i-motif targeting organic molecules or inorganic molecules containing the organic moieties may lead to increased i-motif specific binding.

There are many directions that future work could follow, but it is imperative that a complete understanding of the light switching mechanism and binding interactions of the $[Ru(bqp)_2]^{2+}$ to i-motif DNA should be attempted. This greater understanding could lead to the development of an i-motif DNA specific *in vivo* probe.

6. Experimental

6.1. Materials and Methods

General Methods

Microwave heating was performed using a Biotage Initiator+ microwave synthesizer in a 5 mL sealed microwave vial. HPLC analysis was carried out using an Agilent 1260 infinity with a reverse-phase C18 column. ^{1}H-NMR spectra were recorded using either a Bruker 400 MHz or Bruker 500 MHz spectrometer and chemical shifts are reported in parts per million (ppm) relative to the residual solvent. All reagents were obtained as ACS grade from Sigma Aldrich, Fisher Scientific or FluoroChem and used as supplied. $Ru(DMSO)_4Cl_2$,[203] $[Ru(benzene)Cl_2]_2$,[204] $[Ru(p-cymene)Cl_2]_2$,[204] and $[Ir(C_6(CH_3)_6)Cl_2]_2$[205] were synthesised according to the published methods.

DNA Sequences

Sequences were bought from Eurogentec with RP-HPLC purification and made up to a 1 mM stock solution using MilliQ water. The concentrations were then checked using a nanodrop to read the absorbance at 260 nm and the extinction coefficient supplied from the manufacturer used to calculate the concentration. The sequences used are hTeloC = (5′-d[$(TAA-CCC)_4$]-3′), hTeloG = (5′-d[$(GGG-TTA)_4$]-3′), DS = (5′-d[GGC-ATA-GTG-CGT-GGG-CGT-TAG-C]-3′) and its complementary sequence (5′-d[GCT-AAC-GCC-CAC-GCA-CTA-TGC-C]-3′), DAP = (5′-d[$(CCC-CCG)_4$-CCC-CC]-3′). All buffers used were 100 mM potassium chloride and 10 mM sodium cacodylate that were pH corrected to pH 5.5 (hTeloC) or pH 6.8 (hTeloG, DS, and DAP). All DNA samples were thermally annealed in a heat block at 95°C for 5 minutes and left overnight to return to room temperature.

X-ray Crystallography

Data were collected by Dr. Kevin Vincent on a Rigaku XtalLab Synergy S diffractometer equipped with a PhotonJet Cu micro-focus source and a Hypix hybrid photon counting detector. Data reduction, cell refinement and absorption collection were carried out by Dr. John Fielden using Rigaku CrysAlisPro[206] software and solved using SHELXT-2018[207] via Olex2-1.3.[208] Refinement was achieved by full-matrix least-squares on all F043 data using SHELXL-2018[209] and molecular graphics were prepared using Ortep-3.[210] Full crystallographic data can be found in the Appendices.

6.1.1 Separation of Δ and Λ-*cis,fac*-$[Ru(bqp)_2]^{2+}$

Separation was achieved on a Chiralpak IC00CG-MA002 HPLC column with 10% MeOH in EtOH and 0.05% TFA over 30 mins. Multiple runs were performed with a 100 µL injection of a 5 mg mL^{-1} solution of the racemic mixture in MeOH. The fractions were combined and collected for each enantiomer and solvent removed via rotary evaporation. The solids were then dissolved in MeOH and stirred overnight in thoroughly washed Amberlite IRA-400, which was then filtered to remove the resin. After removal of the solvent, the solid was then dissolved in water to form a 10 mM stock solution. The circular dichroism spectra were collected for each enantiomer and the extinction coefficient obtained from their absorbance trace to ensure purity. X-ray diffraction quality samples were also obtained of the Δ enantiomer by slow diffusion of diethyl ether into a MeOH solution.

Emission Intensity Experiments

Emission titration experiments were carried out using a Horiba Jobin Yvon Fluorolog spectrofluorometer and an open-top 10 mm quartz cuvette. 4.5 µM of a Ru complex was prepared in the appropriate buffer and spectra obtained using an excitation wavelength of 490 nm (*mer*), 550 nm (*trans*) or 575 nm (*cis*), a 10 nm slit width over a range of 625 – 800 nm (*mer*) or 650 – 800 nm (*cis* and *trans*), an averaging time of 0.1 s, a data interval of 1 nm and a scan rate of 600 nm min^{-1}. DNA was then titrated into the cuvette at intervals between 0 and 20 µM and spectra obtained after each addition. All emission intensity experiments

were carried out in triplicate with the error calculated using the standard error and plotted using Origin. The normalised emission increase results were calculated from Eq. 6.1:

$$I_N = \frac{I}{I_a} \tag{6.1}$$

where I_N is the normalised emission, I is the emission in the absence of DNA and I_a is the emission at a given DNA concentration. For the solvent-based experiments, the same procedure was carried out using the parameters above for 4.5 µM in either ethanol, propan-2-ol or acetonitrile.

Absorption Spectroscopy Experiments

Absorption spectra were obtained using a JASCO V-730 Spectrometer. The values reported are calculated from the averages of independent repeats, with error reported as the standard error. 4.5 µM solution of the corresponding ruthenium complex in the appropriate buffer was made and measured over 310-650 nm, a data interval of 0.5 nm, bandwidth of 1 nm and a scan speed of 400 nm min^{-1}. Varying amounts of DNA were added (up to 20 µM) to this solution at RT and absorption spectra were taken after each addition until no further change was observed. The data was then fitted to a linear regression model (Eq. 6.2).

$$\frac{[DNA]}{\epsilon_a - \epsilon_f} = \frac{[DNA]}{\epsilon_b - \epsilon_f} + \frac{1}{(\epsilon_a - \epsilon_f)K_b} \tag{6.2}$$

where $[DNA]$ is the concentration of DNA, ϵ_a, ϵ_f and ϵ_b are the extinction coefficients of a given concentration ($\mathrm{A_{abs}}$/[Ru]), the extinction coefficient of the free metal complex and the extinction coefficient of the bound complex, respectively. In a plot of $[DNA]/(\epsilon_a - \epsilon_f)$ as a function of $[DNA]$, K_b is given as the ratio of the slope to the intercept. Hypochromicity (H%) was calculated using Eq. 6.3:

$$H\% = 100 \times (\frac{\epsilon_f - \epsilon_b}{\epsilon_f}) \tag{6.3}$$

Multi-Channel Scaling (MSC) Phosphorescence Lifetimes

A 4.5 µM soltuion of the corresponding ruthenium complex in the appropriate buffer was made and the lifetime was obtained using an Edinburgh Instruments FS5 with a 485 nm LED source. To this solution was added 20 µM DNA and the lifetime measured again. All decays were recorded until at least 10 000 counts at an emission wavelength of 690 ± 15 nm (*mer*) or 700 ± 15 nm (*cis* or *trans*). Traces were fitted with an exponential tail fitting equation (Eq. 6.4) where $\Sigma\alpha_i$ is normalised to unity. All traces were fitted with a χ^2 value of between 0.90 and 1.30. All traces were processed using the Fluoracle software package. The values reported are calculated from the averages of independent repeats, with error reported as the standard error.

$$I(t) = \alpha_1 e^{-t/\tau_1} + \alpha_2 e^{-t/\tau_2} + ... \alpha_n e^{-t/\tau_n} \tag{6.4}$$

where:

$n =$ the number of components

$\alpha =$ the amplitude of each component normalised to 1

$\tau =$ the lifetime of each component

The fractional contribution of each component can then be calculated using Eq. 6.5.

$$f_i = \alpha_i \tau_i / \Sigma_j \alpha_j \tau_j \tag{6.5}$$

Fluorescence Indicator Displacement (FID) Assay

The FID assay was carried out on a BMG CLARIOstar plate reader using an excitation of 430 nm and emission was measured at 450 nm which was normalised to 0%. 96-well plates (Corning 96 well solid black flat bottom plates) were used for this assay.

For experiments with Ru complexes, 90 µL of thiazole orange (TO) at a concentration of 2 µM in 10 mM sodium cacodylate and 100 mM potassium chloride that was pH corrected to pH 5.5 (hTeloC) or pH 6.8 (DAP, hTeloG and DS) was added to each well. The fluorescence was then measured. DNA was added to a 1 µM concentration, shaken at 700 rpm in the plate reader for 30s and left to equilibrate for 20 min. After equilibration the fluorescence was measured again. Additions in to each well (in triplicate) of 0.45 µM Ru complex were added over a range of 0.45 µM to 4.05 µM. The fluorescence was measured after each addition and the percentage displacement of TO value (D_{TO}) was calculated using Eq. 6.6. The concentration at which 50% of the TO was displaced (DC_{50}) was calculated using Origin software to plot the percentage TO displacement which were then fitted with a dose-response curve and the DC_{50} obtained from solving the equation for y = 50%.

$$\text{TO Displacement (\%)} = 1 - \left(\frac{I_{TO+DNA+L} - I_{TO}}{I_{TO+DNA} - I_{TO}}\right) \times 100 \tag{6.6}$$

where I_{TO}, I_{TO+DNA} and $I_{TO+DNA+L}$ are the fluorescence of the TO, TO with DNA, and TO with DNA and ligand, respectively.

For experiments with the NCI Diversity Set VI library, a solution of 2.4 µM TO was made up in a 100 mM sodium cacodylate, pH 5.5 buffer and 90 µL was added to each well of a 96 well plate, which was then measured for its fluorescence. Addition of 1 µL of a 108 µM hTeloC DNA was added to each well to give a concentration of 1.2 µM DNA. This was shaken at 700 rpm in the plate reader for 30s and left to equilibrate for 10 min before the fluorescence of well was measured. From a plate containing a 1 mM stock of each NCI ligand, 0.54 µL was added to the plate containing TO and DNA to give a concentration of 6 µM. The fluorescence of each well was then measured and the TO displacement calculated using Eq. 6.6.

Förster Resonance Energy Transfer (FRET) Melting Assay

This work was performed by Dr. Mahmoud Abdelhamid on a QIAgen Rotor-Gene Q-Series PCR using the labelled oligonucleotide hTeloC$_{FRET}$ (5′-FAM-d[TAA- CCC-TAA-CCC-TAA-CCC-TAA-CCC]-TAMRA-3′(FAM = 6-carboxyfluorescein, TAMRA = 6-carboxytetramethyl-rhodamine). Strip-tubes were prepared containing a buffered solution (10 mM sodium cacodylate, pH 5.5) of 19 µL hTeloC$_{FRET}$ and 1 µL ligand in DMSO (or just DMSO for controls) with final concentrations of 0.2 and 1 µM hTeloC$_{FRET}$ and ligand, respectively. Samples were heated from 25 °C to 70 °C at increments of 1°C, holding each temperature for 1 min. The fluorescence of each sample was measured using an excitation of 470 nm and the emission was detected at 510 nm. The melting temperature (T_m) was calculated by normalising the melting curve for each ligand from 0 to 1 and then plotting this against the temperature with the T_m being the temperature where y = 0.5. The z-score for each ligand was calculated as $z = (x - \mu)/\sigma$ where μ and σ are the mean and standard deviation of the population, respectively.

Emission Polarisation Measurements

Experiments were performed on an Edinburgh Instruments FS5. A 4.5 µM solution of Ru was taken and its emission polarization was measured with the emission polarizer at both 0 and then 90°. To this, a known concentration of DNA was added, and the emission polarization was measured again, repeating from 1 µL to 20 µL DNA. The polarization was calculated using Eq. 6.7.

$$P = \frac{I_{\parallel} - I_{\perp}}{I_{\parallel} + I_{\perp}} \tag{6.7}$$

where, $I_{\parallel}$ and $I_{\perp}$ are the emission intensity parallel and perpendicular to the excitation plane, respectively.

Aggregation-induced Emission

200 µL mixtures of acetonitrile in water (0% - 90% water) and PEG-300 in water (0% PEG-300 to 90% PEG-300) were made up. For each fraction, two samples were made, one

containing 2 µL *cis* (from a 1 mM stock of *cis*$[PF_6]_2$ or *cis*$[PF_6][Cl]$) and one containing 2 µL acetonitrile or water as a control. The sample without *cis* was scanned using an excitation wavelength of 575 nm (*cis*), a 10 nm slit width over a range of 650 – 800 nm, an averaging time of 0.1 s, a data interval of 1 nm and a scan rate of 600 nm min^{-1} and then subtracted from the samples containing *cis*. The solvent based experiments were conducted similarly to the above experiments using a 10 µM solution of *cis*$[PF_6]_2$ in acetonitrile. All data were plotted using Origin.

Density Function Theory (DFT) Calculations

DFT calculations were carried out using the ADF suite and performed by Dr. John Fielden.[120,211] All calculations were carried out using the ADF triple-ζ TZP basis set with the zero-order regular approximation (ZORA) to account for relativitstic effects.[212] The dispersion corrected hybrid functional PBE0-dDsc[213,214] was used for all geometry optimisations, as this was found to give the closest match to ground state geometries (also tested were the dispersion corrected hybrid B3LYP-D3[215,216] and the range separated hybrid ωB97X[217]). Other recent work[121,122] has also found inclusion of dispersion important for obtaining correct geometries for bqp complexes. Geometries of triplet states were calculated using unrestricted DFT (uDFT), starting from the ground state geometry for ^{3}MLCT, and from a geometry stretched along an N(quinoline)-Ru-N(quinoline) axis for ^{3}MC. uDFT was used rather than TD-DFT because it is considered to perform better for charge-separated states, such as MLCT states. For single-point calculations of electronic structure and energy the B3LYP[56] functional was used, as this best reproduced experimentally measured electronic absorption spectra (by TD-DFT). To estimate the electronic influence of DNA, single-point calculations for selected isomer/sequence combinations were carried out in the presence of partial charges extracted from AutoDock calculated DNA binding sites. Solvent (water) was introduced using COSMO[59-61] with Allinger atomic radii in geometry optimisations and TD-DFT calculations of electronic spectra. In single-point energy calculations solvent was introduced using SM12[62,63] instead, as COSMO is incompatible with application of the external electric field used to model the electronic effect of DNA.

AutoDock 4.2

Docking simulations were carried out with AutoDock 4.2[115] and either the telomeric i-motif (PDB: 1ELN),[116] the telomeric G-quadruplex stabilised by K^+ (PDB: 1KF1)[117] or the same double-stranded DNA sequence as that used experimentally (5′-GGC-ATA-GTG-CGT-GGG-CGT-TAG-C-3′) and its complementary sequence built using Chimera 1.10.2[118] and minimized using the AMBER ff99bsc0 force field. Ground state structures of the three ruthenium complexes were obtained from their previously published crystal structures,[71,80] and triplet excited states were computed via DFT. Ligands and receptors were prepared using the provided python scripts in the MGLTools package and docking was accomplished using a Lamarckian Genetic Algorithm. This was done allowing flexibility in the Ru complexes for the binding study, but for the combination with DFT rigid Ru complexes were used to ensure different excited state geometries were preserved. Ruthenium atom parameters used for AutoDock 4.2 were "atom_par Ru 2.96 0.056 12.000 -0.00110 0.0 0.0 0 -1 -1 1 # Non H-bonding". Contacts between Ru complexes and DNA were calculated using Chimera 1.10.249 with a Van der Waals overlap of -0.4 Å.

AutoDock Vina

Using the hTeloC PDB file obtained from Abdelhamid *et al.*,[188] the grid parameters in Table 6.1 were used to define the search area on the receptor. A python script was written[194] open the SDF file of the library and then each molecule in the library was converted to a PDB file, subsequently converted to a PDBQT file, docked to each of the pockets, after which the docking results, the NSC number and SMILES string for each molecules were extracted and exported into a CSV file. This script iterated over each of the 1584 compounds in the NCI Diversity Set VI library.

Table 6.1: Grid parameters used for AutoDock Vina calculations

		Pocket 1 (Loop)	Pocket 2 (Groove)	Pocket 3 (Whole Structure)
Centre	x	69.474	61.561	56.333
	y	29.685	35.063	29.596
	z	15.872	6.016	5.577
Size	x	24	24	120
	y	24	24	62
	z	24	24	76

Tanimoto Similarity Searching and Clustering

Using the python module RDKit,[218] each molecule was converted to a Morgan fingerprint bit vector and each molecule was compared to each other for their Tanimoto similarity, generating a distance matrix of similarities. This matrix was then used to generate clusters with each molecules position in the array being returned. From this, the molecules structure was obtained from its position and fed back into the clusters to put each molecule into each clusters. The docking, TO displacement and z-score for molecule were stored in the identity of each molecule allowing one to calculate the average of each of these properties for each cluster, these were then plotted against the clusters assigned number with the error reported as the standard deviation.

For the Tanimoto similarity search, the 16 chosen compounds were each converted to a Morgan fingerprint bit vector. Each molecule in either the NCI full library or the ChEMBL library were then also converted to Morgan fingerprint bit vectors and their similarity compared to each of the 16 chosen molecules. If this similarity was ≥ 0.80 then the SMILES string of each molecule was exported.

6.2. Synthesis

6.2.1 General Procedures

General procedure for the Suzuki coupling in the synthesis of bqp and derivatives

8-quinolineboronic acid (2 eq.), functionalised 2,6-dihalogenated-pyridine (1 eq.), SPhos (0.05 eq.), $Pd(dba)_2$ (0.05 eq.) and dried K_2CO_3 (5 eq.) were added to a 50:50 mixture of acetonitrile and water. This suspension was then heated at 100°C under an N_2 atmosphere and overnight. The suspension was allowed to cool to room temperature and filtered. To the filtrate was added DCM and the organic layers separated, dried over $MgSO_4$ and the solvent removed via rotary evaporation. The remaining solid was purified with flash column chromatography (0-10% methanol in DCM).

General synthesis of [Ru(bqp)(η^6 – arene)]$^{2+}$ and derivatives

A suspension of **bqp** (1 eq.) and dichloro(η^6-arene)ruthenium(II) dimer (0.55 eq.) in methanol (10 mL) was stirred at temperature. NH_4PF_6 (2.5 eq.) was then added to the solution before being stirred for a further 30 mins. The solid was then filtered and washed with methanol. To obtain the chloride salt, the PF_6 containing salt was dissolved in acetone and excess NBu_4Cl was added before the solid was removed via filtration and washed with excess acetone.

$Ru(DMSO)_4Cl_2$

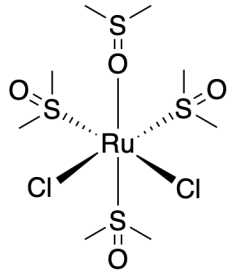

This complex was prepared according to the published literature procedure.[203] DMSO (10 mL) was heated to reflux under an N_2 atmosphere for 30 mins after which $RuCl_3 \cdot 2\,H_2O$ (1.00 g, 2.06 mmol) was added and the reflux continued for a further 5 mins. The solution was allowed to cool to room temperature before the product was precipitated by adding 30 mL acetone. The yellow product was refridgerated for 4 hrs and then filtered and washed with excess acetone to afford a yellow powder (1.13 g, 50% yield). IR (FTIR) 3008, 2920, 1400, 1310, 1112, 1018, 922, 676, 604 Anal. Calcd for $C_8H_{24}Cl_2O_4RuS_4$: C, 19.83; H, 5.00; found: C, 19.94; H, 5.06.

2,6-Bis(8′-quinolinyl)-pyridine (1)

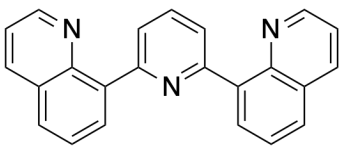

Synthesised according to the general procedure for bqp ligands using 2,6-dibromopyridine (1606 mg, 9.28 mmol) to yield an off-white powder (912 mg, 65% yield). ^{1}H-NMR (500 MHz, $CDCl_3$): δ 9.00 (dd, J = 4.2, 1.9 Hz, 2H), 8.30 (dd, J = 7.2, 1.5 Hz, 2H), 8.26 (dd, J = 8.3, 1.8 Hz, 2H), 8.16 (d, J = 7.8 Hz, 2H), 8.01 (t, J = 7.8 Hz, 1H), 7.90 (dd, J = 8.2, 1.5 Hz, 2H), 7.68 (dd, J = 8.1, 7.2 Hz, 2H), 7.47 (dd, J = 8.3, 4.2 Hz, 2H). ^{13}C-NMR (101 MHz, $CDCl_3$): δ 156.69, 150.22, 145.98, 139.24, 136.46, 135.03, 131.59, 128.68, 128.57, 126.64, 125.52, 120.99. FTMS: Expected [M+H$^+$]: 334.1339, Observed: 334.1340. Anal. Calcd for $C_{23}H_{15}N_3$: C, 82.85; H, 4.54; N, 12.61; found: C, 82.61; H, 4.68; N, 12.49.

***mer*-[Ru(1)$_2$][PF$_6$][Cl] (*mer*-1a)**

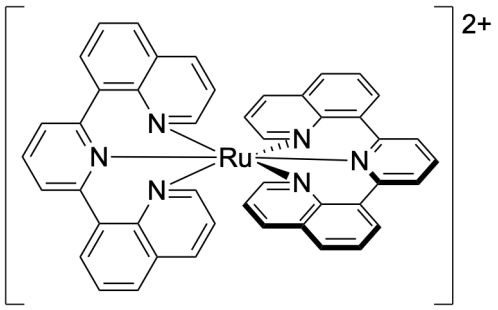

A crude mixture of all three isomers were prepared according to the literature procedure.[80] This crude mixture of *mer*-, *cis*-, and *trans*-**1a** (200 mg, 0.189 mmol) was dissolved in acetonitrile and to it excess tetrabutylammonium chloride was added and left to stir for 30 min. The red solid was filtered and washed with acetone and the *mer* isomer was then separated by preparative HPLC (40-60% MeOH/H_2O plus 0.1% CF_3CO_2H over 40 min). ^{1}H-NMR (400 MHz, CD_3OD): δ 8.13 (t, J = 8.0 Hz, 2 H), 8.08 (s, 4 H), 8.06 (dd, J = 4.5, 1.4 Hz, 4 H), 7.91 (d, J = 8.2 Hz, 4 H), 7.75 (dd, J = 7.5, 1.1 Hz, 4 H), 7.66 (dd, J = 8.2, 1.0 Hz, 4 H), 7.42 (t, J = 7.8 Hz, 4 H), 7.04 ppm (dd, J = 8.0, 5.3 Hz, 4 H). ^{13}C-NMR (101 MHz, CD_3OD): δ 159.69, 158.31, 148.03, 139.60, 138.95, 134.35, 133.29, 132.06, 129.20, 128.26, 128.12, 123.33. FTMS ([$C_{46}H_{30}N_6Ru$]$^{2+}$) m/z: calc: 384.0787 found: 384.0785. Anal. Calcd for $C_{46}H_{30}N_6RuClPF_6 \cdot 4\,H_2O$: C, 54.13; H, 3.76; N, 8.24; found: C, 54.14; H, 3.34; N, 8.50.

***cis,fac*-[Ru(1)$_2$][PF$_6$][Cl] (*cis,fac*-1a)**

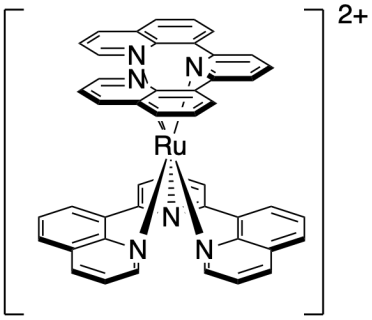

The complex was isolated as a fraction from the synthesis of *mer*-**1a** to yield a purple solid. ^{1}H-NMR (400 MHz, CD_3OD): δ 8.83 (dd, J = 5.3, 1.1 Hz, 2 H), 8.78 (dd, J = 8.2, 0.9 Hz, 2 H), 8.38 (dd, J = 8.1, 0.9 Hz, 2 H), 8.29 (dd, J = 7.3, 1.2 Hz, 2 H), 8.24 (dd, J = 8.2, 1.0 Hz, 2 H), 8.17 (dd, J = 8.1, 0.9 Hz, 2 H), 7.93 (dd, J = 8.2, 5.3 Hz, 2 H), 7.89 (dd, J = 5.4, 1.3 Hz, 1 H), 7.83 (t, J = 8.0 Hz, 2 H), 7.74 - 7.79 (m, J = 4.0, 4.0, 3.1 Hz, 3 H), 7.70 (t, J = 7.8 Hz, 2 H), 7.43 (dd, J = 7.5, 1.2 Hz, 2 H), 7.31 (dd, J = 8.1, 1.2 Hz, 2 H), 6.77 ppm (dd, J = 8.2, 5.3 Hz, 2 H). ^{13}C-NMR (101 MHz, CD_3OD): δ 159.52, 158.88, 138.86, 137.61, 132.32, 132.24, 131.44, 130.59, 130.14, 129.66, 129.18, 127.84, 127.58, 126.90, 125.63, 122.45, 121.67. FTMS ($[C_{46}H_{30}N_6Ru]^{2+}$) *m/z*: calc: 384.0787 found: 384.0785. Anal. Calcd for $C_{46}H_{30}N_6RuClPF_6 \cdot 4\,H_2O$: C, 54.13; H, 3.76; N, 8.24; found: C, 53.70; H, 3.93; N, 7.91.

***trans,fac*-[Ru(1)$_2$][PF$_6$][Cl] (*trans,fac*-1a)**

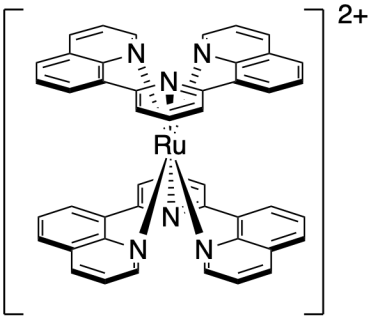

The complex was isolated as a fraction from the synthesis of *mer*-**1a** to yield a purple solid. ^{1}H-NMR (400 MHz, CD_3OD): δ 9.19 (dd, J= 5.2, 1.3 Hz, 4H), 8.14 (t, J = 8.0, 2H), 8.06 (dd, J = 8.1, 0.7 Hz, 4 H), 7.86 (dd, J = 7.5, 1.1 Hz, 4H), 7.81 (d, J = 8.2 Hz, 4H), 7.68 (dd, J = 8.0, 0.8 Hz, 4H), 7.47 (m, 8 H). ^{13}C-NMR (101 MHz, CD_3OD): δ 160.64, 160.00,

139.98, 138.76, 138.73, 133.44, 133.36, 132.56, 131.26, 128.96, 128.70, 128.02, 126.75, 123.57, 122.79. FTMS ($[C_{46}H_{30}N_6Ru]^{2+}$) *m/z*: calc: 384.0788 found: 384.0788. Anal. Calcd for $C_{46}H_{30}N_6RuClPF_6 \cdot 4\,H_2O$: C, 54.13; H, 3.76; N, 8.24; found: C, 54.11; H, 3.96; N, 8.44.

2,6-bis(8′-quinolinyl)-4-nitropyridine (2)

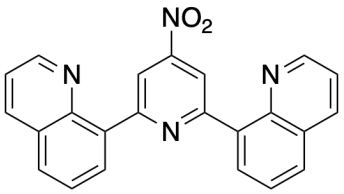

Synthesised according to the general procedure using 2,6-dichloro-4-nitropyridine (1000 mg, 5.18 mmol) to yield a yellow solid (1499 mg, 77% yield). ^{1}H-NMR (500 MHz, $CDCl_3$): δ 8.97 (dd, J = 4.2, 1.8 Hz, 1H), 8.95 (s, 1H), 8.32 (dd, J = 7.2, 1.5 Hz, 1H), 8.21 (dd, J = 8.3, 1.8 Hz, 1H), 7.90 (dd, J = 8.2, 1.4 Hz, 1H), 7.64 (dd, J = 8.1, 7.2 Hz, 1H), 7.44 (dd, J = 8.3, 4.1 Hz, 1H). ^{13}C-NMR (126 MHz, $CDCl_3$): δ 159.04, 153.52, 150.76, 145.69, 137.10, 136.84, 131.87, 129.92, 128.81, 126.70, 121.55, 118.32. FTMS ($[C_{23}H_{14}N_4O_2]$) *m/z*: calc: 378.1117 found: 378.1301 Anal. Calcd for $C_{23}H_{14}N_4O_2$: C, 73.01; H, 3.73; N, 14.81; found: C, 72.68; H, 3.49; N, 14.66.

2,6-bis(8′-quinolinyl)-4-aminopyridine (3)

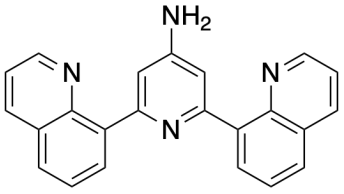

To a suspension of bqpNO2 (194 mg, 0.45 mmol) and 10% Pd/C (26 mg) in 50 mL EtOH was added 0.5 mL hydrazine hydrate. This solution was then heated to reflux for 1 h at which point a further 0.5 mL hydrazine hydrate was added. After refluxing overnight, the solution was cooled, filtered through a Celite plug and the filtrate was concentrated. To the concentrated filtrate was added 100 mL chloroform and the solution was heated to reflux for 5 min before being allowed to cool to RT. The off-white solid (348 mg, 88%) was

then removed via filtration and washed with chloroform. ^{1}H-NMR (400 MHz, CD_3CN): δ 8.92 (dd, J = 4.1, 1.9 Hz, 2H), 8.35 (dd, J = 8.3, 1.9 Hz, 2H), 8.13 (dd, J = 7.2, 1.5 Hz, 2H), 7.97 (dd, J = 8.2, 1.5 Hz, 2H), 7.67 (dd, J = 8.1, 7.2 Hz, 2H), 7.52 (dd, J = 8.3, 4.1 Hz, 2H), 7.31 (s, 2H), 5.07 (s, 2H). FTMS ([$C_{23}H_{14}N_4O_2$]) *m/z*: calc: 378.1117 found: 378.1301. Anal. Calcd for $C_{23}H_{14}N_4O_2$: C, 73.01; H, 3.73; N, 14.81; found: C, 72.68; H, 3.49; N, 14.66.

2,6-bis(8′-quinolinyl)-4-trifluoromethylpyridine (4)

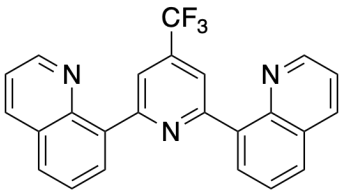

Synthesised according to the general procedure using 2,6-dichloro-4-(trifluoromethyl)pyridine (864 mg, 4.00 mmol) to yield a yellow solid (541 mg, 34% yield). ^{1}H-NMR (500 MHz, CD_3OD): δ 8.99 (dd, J = 4.2, 1.8 Hz, 2H), 8.46 (dd, J = 8.4, 1.8 Hz, 2H), 8.43 (d, J = 0.7 Hz, 2H), 8.32 (dd, J = 7.2, 1.5 Hz, 2H), 8.10 (dd, J = 8.2, 1.5 Hz, 2H), 7.78 (dd, J = 8.2, 7.2 Hz, 2H), 7.62 (dd, J = 8.3, 4.2 Hz, 2H). ^{13}C-NMR (126 MHz, CD_3OD): δ 158.05, 150.42, 145.40, 137.10, 136.86, 131.46, 129.60, 128.86, 126.24, 121.37, 120.86, 120.83. FTMS ($C_{24}H_{14}F_3N_3$) *m/z*: calc: 401.1140 found: 401.1396 Anal. Calcd for $C_{24}H_{14}F_3N_3 \cdot (H_2O)_{0.5}$: C, 70.22; H, 3.69; N, 10.24; found: C, 69.91; H, 4.07; N, 10.35.

2,6-bis(8′-quinolinyl)-4-methylpyridine (5)

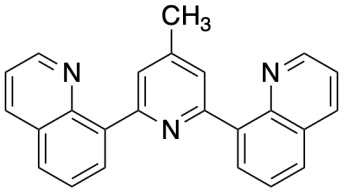

Synthesised according to the general procedure using 2,6-dichloro-4-methylpyridine (648 mg, 4.00 mmol) to yield a yellow solid (750 mg, 54% yield). ^{1}H-NMR (500 MHz, CD_3OD): δ 8.77 (dd, J = 4.4, 1.8 Hz, 2H), 8.68 (dd, J = 7.4, 1.3 Hz, 2H), 8.66 (dd, J = 8.4, 1.8 Hz, 2H), 8.51 (d, J = 0.8 Hz, 2H), 8.33 (dd, J = 8.3, 1.3 Hz, 2H), 7.94 (dd, J = 8.2, 7.4 Hz,

2H), 7.76 (dd, *J* = 8.3, 4.3 Hz, 2H), 2.84 (d, *J* = 0.8 Hz, 3H). ^{13}C-NMR (126 MHz, CD_3OD): δ 158.16, 150.31, 149.96, 144.30, 138.74, 132.80, 132.19, 129.26, 127.01, 126.40, 124.86, 122.46, 21.13. Anal Calcd for $C_{24}H_{17}N_3 \cdot H_2O$: C, 78.87; H, 5.24; N, 11.50; found: C, 78.89; H, 5.29; N, 11.40 a

2,6-bis(8′-quinolinyl)-4-methoxypyridine (6)

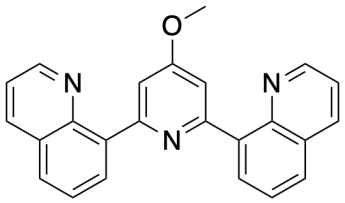

Synthesised according to the general procedure using 2,6-dichloro-4-methoxypyridine (500 mg, 2.81 mmol) to yield a yellow solid (864 mg, 85% yield). ^{1}H-NMR (400 MHz, $CDCl_3$): δ 9.00 (dd, *J* = 4.1, 1.9 Hz, 2H), 8.23 (ddd, *J* = 14.7, 7.8, 1.7 Hz, 4H), 7.86 (dd, *J* = 8.1, 1.5 Hz, 2H), 7.69 (s, 2H), 7.64 (dd, *J* = 8.1, 7.2 Hz, 2H), 7.43 (dd, *J* = 8.3, 4.2 Hz, 2H), 3.98 (s, 3H). ^{13}C-NMR (101 MHz, $CDCl_3$): δ 165.18, 158.49, 150.64, 146.43, 139.90, 136.82, 131.88, 129.08, 128.92, 126.95, 121.35, 112.34, 55.68.

2,6-bis(8′-quinolinyl)-4-isoquinoline (7)

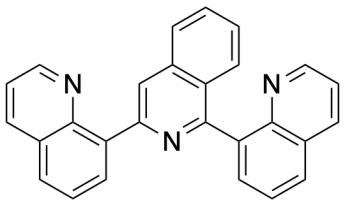

Synthesised according to the general procedure using 1,3-dichloroisoquinoline (1000 mg, 5.05 mmol) to yield a yellow solid (1458 mg, 75% yield). ^{1}H-NMR (400 MHz, $CDCl_3$): δ 8.76 (dd, J = 4.2, 1.8 Hz, 2H), 8.24 (dd, J = 8.3, 1.8 Hz, 2H), 7.99 (dd, J = 8.2, 1.5 Hz, 2H), 7.87 – 7.78 (m, 6H), 7.73 – 7.62 (m, 5H), 7.49 – 7.30 (m, 7H) ^{13}C-NMR (101 MHz, $CDCl_3$): δ 150.68, 146.87, 144.79, 137.72, 136.12, 131.26, 130.83, 129.22, 128.41, 128.31, 127.38, 127.00, 126.28, 126.09, 121.35, 119.60.

2,6-bis(2-methylquinolin-8-yl)pyridine (8)

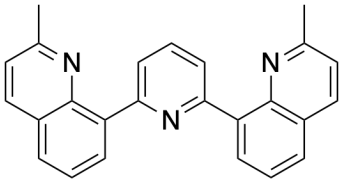

2,6-bis(8′-quinolinyl)-pyridine (100 mg, 0.30 mmol) was added to an oven-dried flask and dissolved in anhydrous toluene. To this solution was added TMEDA (90 µL, 0.60 mmol) and MeMgCl (0.30 mL, 0.90 mmol, 3M solution in THF). The reaction was heated to 120°C for 2 hr before allowing to cool to RT. The solvent was removed under vacuum and DCM (150 mL) was added to the solids. This was subsequently filtered and washed with more DCM before further purification via column chromatography (7.5% MeOH/DCM, silica gel) to yield a yellow/brown solid (25 mg, 23% yield) ^{1}H-NMR (400 MHz, $CDCl_3$): δ 8.36 (dd, J = 7.3, 1.5 Hz, 2H), 8.28 (d, J = 7.8 Hz, 2H), 8.11 (d, J = 8.4 Hz, 2H), 7.93 (t, J = 7.7 Hz, 1H), 7.82 (dd, J = 8, 1.5 Hz, 2H), 7.62 (t, J = 7.5 Hz, 2H), 7.33 (d, J = 8.3 Hz, 2H), 2.77 (s, 6H). TODO FTMS ($C_{25}H_{19}N_3{}^+H^+$) *m/z*: calc: 362.1652 found: 362.1652

$[Ru(8)_2][PF_6]_2$ (8a)

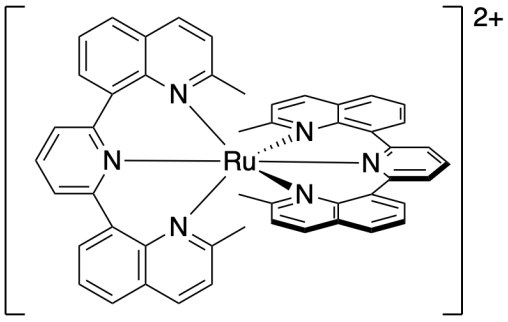

In a 2 mL microwave vial, 2,6-bis(2-methylquinolin-8-yl)-pyridine (**8**) (40.7 mg, 0.113 mmol) and $Ru(DMSO)_4Cl_2$ (26.7 mg, 0.055 mmol) were added. A stirrer bar was added before sealing the tube. The contents were vacuum dried and were purged with nitrogen. Ethylene glycol (1.5 mL) was added using a syringe and the solution was heated for 20 min at 200°C using microwave heating. The dark red solution was stirred in DCM (20 mL) and a saturated aqueous solution of NH_4PF_6 (20 mL). The organic layers were separated

and combined and the solvent removed via rotary evaporation. The crude material was then purified via preparative TLC using a mixture of [40:4:1 CH_3CN/H_2O/sat. KNO_3] as the eluent. The orange band was collected, and the counteranion exchanged with NH_4PF_6 to give a red solid (2.5 mg, 4.1% yield). ^{1}H-NMR (500 MHz, CD_3OD): δ 8.20 (t, J = 8.0 Hz, 2H), 7.87 (d, J = 8.2 Hz, 4H), 7.74 (m, 8H), 7.64 (t, J = 1.4 Hz, 4H), 7.48 (t, J = 7.7 Hz, 4H), 6.94 (d, J = 8.2 Hz, 4H), 2.09 (s, 12H). FTMS ($RuC_{50}H_{38}N_6$) *m/z*: calc: 412.1098 found: 412.1099

[Ru(*p*−cymene)Cl_2]$_2$ (9)

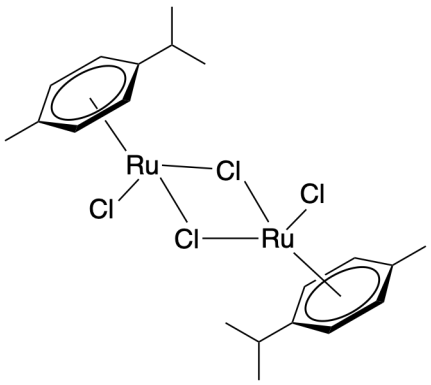

$RuCl_3 \cdot nH_2O$ (1.00 g, 4.10 mmol) and α-phellandrene (1 mL) were refluxed in 96% ethanol overnight. The solution was allowed to cool, forming a red-brown precipitate. This solid was filtered from the solution, washed with ethanol and diethyl ether to yield a red solid (2.13 g, 85 %). ^{1}H-NMR (400 MHz, CD_3OD): δ 5.90 (d, J = 6.3 Hz, 2H), 5.68 (d, J = 6.3 Hz, 2H), 2.80 (hept, J = 6.9 Hz, 1H), 2.22 (s, 3H), 1.32 (d, J = 6.9 Hz, 7H). ^{13}C-NMR (101 MHz, $CDCl_3$): δ 101.25, 96.76, 81.31, 80.55, 30.64, 22.16, 18.94.

[Ru(*p*-cymene)(1)][PF_6]$_2$ (10)

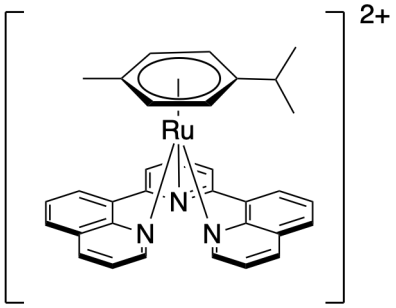

Synthesised according to the general procedure using **bqp** (50 mg, 0.15 mmol) and dichloro(*p*-cymene)ruthenium(II) dimer (49 mg, 0.08 mmol) to yield a yellow solid (71 mg, 55%) ^{1}H-NMR (400 MHz, CD_3CN): δ 9.78 (dd, J = 5.2, 1.4 Hz, 2H), 8.80 (dd, J = 8.3, 1.4 Hz, 2H), 8.74 (dd, J = 7.4, 1.4 Hz, 2H), 8.34 (dd, J = 8.2, 1.3 Hz, 2H), 8.25 (dd, J = 8.5, 7.6 Hz, 1H), 8.10 – 7.98 (m, 6H), 5.33 (d, J = 6.4 Hz, 2H), 5.10 (d, J = 6.4 Hz, 2H), 1.42 (p, J = 6.9 Hz, 1H), 1.10 (s, 3H), 0.65 (d, J = 6.9 Hz, 6H). ^{13}C-NMR (101 MHz, CD_3CN): δ 159.47, 157.14, 147.75, 142.60, 141.85, 135.19, 134.11, 130.69, 129.95, 128.48, 124.71, 88.72, 88.42, 22.02, 1.88, 1.68.

[Ru(benzene)Cl_2]$_2$ (11)

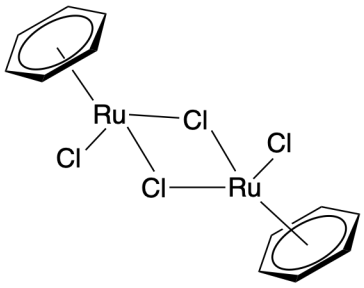

$RuCl_3 \cdot n_2H_2O$ (1.00 g, 4.10 mmol) and 1,3-cyclohexadiene (1 mL) were refluxed in 96% ethanol overnight under N_2. The solution was allowed to cool, forming a red-brown precipitate. The solid was filtered from the solution, washed with ethanol and diethyl ether to yield a red solid (1.89 mg, 92 %). ^{1}H-NMR (400 MHz, $CDCl_3$): δ 5.71 (s, 6H). Anal Calcd for $C_{12}H_{12}Cl_4Ru_2$: C, 28.85; H, 2.13; found: C, 28.82; H, 2.42.

[Ru(benzene)(1)][PF_6]$_2$ (12)

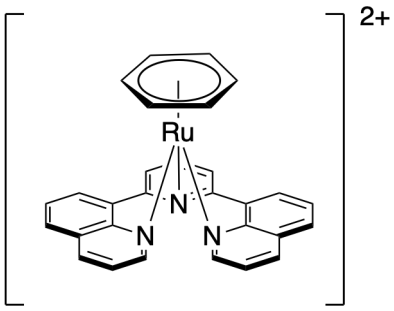

Synthesised according to the general procedure using **bqp** (100 mg, 0.30 mmol) and **11** (150 mg, 0.30 mmol) with additional $AgPF_6$ (303 mg, 1.2 mmol) and stirred overnight to

yield a yellow solid (92 mg, 60%). ^{1}H-NMR (400 MHz, CD_3CN): δ 9.82 (dd, J = 5.2, 1.5 Hz, 2H), 8.82 (dd, J = 8.3, 1.4 Hz, 2H), 8.69 (dd, J = 7.5, 1.4 Hz, 2H), 8.34 (dd, J = 8.3, 1.3 Hz, 2H), 8.25 (dd, J = 8.5, 7.6 Hz, 1H), 8.09 – 7.96 (m, 6H), 5.31 (s, 6H). ^{13}C-NMR (101 MHz, CD_3CN): δ 159.91, 157.29, 148.39, 142.81, 141.98, 135.28, 134.05, 130.24, 129.90, 128.35, 124.31, 91.10.

$[Ir(C_5(CH_3)_5)]Cl_2]_2$ (13)

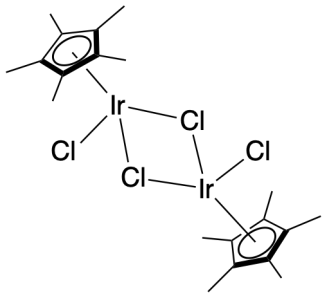

$IrCl_3 \cdot 3\,H_2O$ (200 mg, 0.57 mmol) and $C_5(CH_3)_5$ (1 mL) were added to 10 mL MeOH and refluxed overnight under N_2. The red solution was allowed to cool to RT forming a red solid. The solution was concentrated to yield more solid before being filtered to yield a red solid (99 mg, 22% yield). ^{1}H-NMR (400 MHz, $CDCl_3$): δ 1.59 (s, 15H). ^{13}C-NMR (101 MHz, $CDCl_3$): δ 86.24, 9.38.

$[Ir(C_5(CH_3)_5)(bqp)][Cl]_2$ (14)

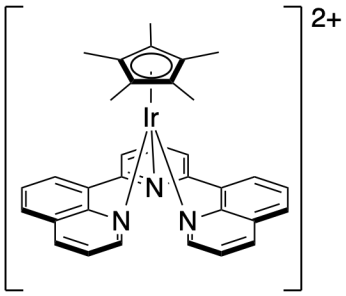

$[Ir(Cp^*)Cl_2]_2$ (50 mg, 0.06 mmol) and $AgPF_6$ (62 mg, 0.25 mmol) were stirred in DCM for 10 min before bqp (40 mg, 0.12 mg) in 4 mL DCM was added and stirred for a further 48 hr at RT. The solution was then filtered through a Celite plug and the solid was washed with DCM. The product was then precipitated by adding excess NH_4Clbefore being filtered and washed with DCM to yield a peach solid (33 mg, 38% yield). ^{1}H-NMR (400 MHz,

CD_3CN): δ 10.28 (d, J = 5.1 Hz, 2H), 8.77 (dd, J = 8.2, 1.5 Hz, 2H), 8.72 (dd, J = 7.5, 1.5 Hz, 2H), 8.37 (dd, J = 8.2, 1.5 Hz, 2H), 8.28 (dd, J = 8.7, 7.2 Hz, 1H), 8.18 (d, J = 8.0 Hz, 2H), 8.11 – 7.98 (m, 5H), 0.69 (d, J = 1.5 Hz, 15H). ^{13}C-NMR (101 MHz, CD_3OD): δ 157.15, 154.06, 145.71, 142.24, 142.08, 134.47, 133.20, 132.86, 130.49, 129.11, 127.87, 124.92, 91.35, 6.57.

References

(1) J. D. Watson and F. H. C. Crick, "Molecular structure of nucleic acids", *Nature*, 1953, **171**, 737–738.

(2) M. L. Bochman, K. Paeschke and V. A. Zakian, "DNA secondary structures: stability and function of G-quadruplex structures", *Nature Reviews Genetics*, 2012, **13**, 770–780.

(3) J. Amato, N. Iaccarino, A. Randazzo, E. Novellino and B. Pagano, "Noncanonical DNA Secondary Structures as Drug Targets: the Prospect of the i-Motif", *ChemMedChem*, 2014, **9**, 2026–2030.

(4) M. Vorlíčková, I. Kejnovská, K. Bednářová, D. Renčiuk and J. Kypr, "Circular Dichroism Spectroscopy of DNA: From Duplexes to Quadruplexes", *Chirality*, 2012, **24**, 691–698.

(5) R. E. Franklin and R. G. Gosling, "Molecular Configuration in Sodium Thymonucleate", *Nature*, 1953, **171**, 740–741.

(6) M. H. F. Wilkins, A. R. Stokes and H. R. Wilson, "Molecular Structure of Nucleic Acids: Molecular Structure of Deoxypentose Nucleic Acids", *Nature*, 1953, **171**, 738–740.

(7) C. Meier, *Advanced Organic Chemistry of Nucleic Acids*, VCH, 1994.

(8) E. Chargaff, S. Zamenhof and C. Green, "Human Desoxypentose Nucleic Acid: Composition of Human Desoxypentose Nucleic Acid", *Nature*, 1950, **165**, 756–757.

(9) D. W. Ussery, in *Encyclopedia of Life Sciences*, John Wiley & Sons, Ltd, Chichester, UK, 2002.

(10) M. Gellert, M. N. Lipsett and D. R. Davies, "Helix Formation By Guanylic Acid", *Proceedings of the National Academy of Sciences*, 1962, **48**, 2013–2018.

(11) K. Hoogsteen, "The crystal and molecular structure of a hydrogen-bonded complex between 1-methylthymine and 9-methyladenine", *Acta Crystallographica*, 1963, **16**, 907–916.

(12) D. Sen and W. Gilbert, "Formation of parallel four-stranded complexes by guanine-rich motifs in DNA and its implications for meiosis", *Nature*, 1988, **334**, 364–366.

(13) J.-L. Mergny and D. Sen, "DNA Quadruple Helices in Nanotechnology", *Chemical Reviews*, 2019, **119**, 6290–6325.

(14) A. I. Karsisiotis, C. O'Kane and M. Webba da Silva, "DNA quadruplex folding formalism – A tutorial on quadruplex topologies", *Methods*, 2013, **64**, 28–35.

(15) P. L. T. Tran, J.-L. Mergny and P. Alberti, "Stability of telomeric G-quadruplexes", *Nucleic Acids Research*, 2011, **39**, 3282–3294.

(16) W. I. Sundquist and A. Klug, "Telomeric DNA dimerizes by formation of guanine tetrads between hairpin loops", *Nature*, 1989, **342**, 825–829.

(17) J. L. Huppert and S. Balasubramanian, "Prevalence of quadruplexes in the human genome", *Nucleic Acids Research*, 2005, **33**, 2908–2916.

(18) A. Bedrat, L. Lacroix and J.-L. Mergny, "Re-evaluation of G-quadruplex propensity with G4Hunter", *Nucleic Acids Research*, 2016, **44**, 1746–1759.

(19) G. Biffi, D. Tannahill, J. McCafferty and S. Balasubramanian, "Quantitative visualization of DNA G-quadruplex structures in human cells", *Nature Chemistry*, 2013, **5**, 182–186.

(20) A. Shivalingam, M. A. Izquierdo, A. L. Marois, A. Vyšniauskas, K. Suhling, M. K. Kuimova and R. Vilar, "The interactions between a small molecule and G-quadruplexes are visualized by fluorescence lifetime imaging microscopy", *Nature Communications*, 2015, **6**, 8178.

(21) K. Gehring, J.-L. Leroy and M. Guéron, "A tetrameric DNA structure with protonated cytosine-cytosine base pairs", *Nature*, 1993, **363**, 561–565.

(22) I. Berger, M. Egli and A. Rich, "Inter-strand C-H...O hydrogen bonds stabilizing four-stranded intercalated molecules: stereoelectronic effects of O4' in cytosine-rich DNA.", *Proceedings of the National Academy of Sciences*, 1996, **93**, 12116–12121.

(23) J.-L. Leroy, M. Guéron, J.-L. Mergny and C. Hélène, "Intramolecular folding of a fragment of the cytosine-rich strand of telomeric DNA into an i-motif", *Nucleic Acids Research*, 1994, **22**, 1600–1606.

(24) S. Ahmed, A. Kintanar and E. Henderson, "Human telomeric C–strand tetraplexes", *Nature Structural & Molecular Biology*, 1994, **1**, 83–88.

(25) P. Acharya, P. Cheruku, S. Chatterjee, S. Acharya and J. Chattopadhyaya, "Measurement of Nucleobase p K a Values in Model Mononucleotides Shows RNA-RNA Duplexes To Be More Stable than DNA-DNA Duplexes", *Journal of the American Chemical Society*, 2004, **126**, 2862–2869.

(26) J.-L. Mergny, J. L. Lacroix, X. Han, J.-L. Leroy and C. Helene, "Intramolecular Folding of Pyrimidine Oligodeoxynucleotides into an i-DNA Motif", *Journal of the American Chemical Society*, 1995, **117**, 8887–8898.

(27) R. J. Ellis and A. P. Minton, "Join the crowd", *Nature*, 2003, **425**, 27–28.

(28) A. Rajendran, S.-i. Nakano and N. Sugimoto, "Molecular crowding of the cosolutes induces an intramolecular i-motif structure of triplet repeat DNA oligomers at neutral pH", *Chemical Communications*, 2010, **46**, 1299.

(29) D. Miyoshi and N. Sugimoto, "Molecular crowding effects on structure and stability of DNA", *Biochimie*, 2008, **90**, 1040–1051.

(30) Y. P. Bhavsar-Jog, E. Van Dornshuld, T. A. Brooks, G. S. Tschumper and R. M. Wadkins, "Epigenetic Modification, Dehydration, and Molecular Crowding Effects on the Thermodynamics of i-Motif Structure Formation from C-Rich DNA", *Biochemistry*, 2014, **53**, 1586–1594.

(31) J. Cui, P. Waltman, V. Le and E. Lewis, "The Effect of Molecular Crowding on the Stability of Human c-MYC Promoter Sequence I-Motif at Neutral pH", *Molecules*, 2013, **18**, 12751–12767.

(32) T. Fujii and N. Sugimoto, "Loop nucleotides impact the stability of intrastrand i-motif structures at neutral pH", *Physical Chemistry Chemical Physics*, 2015, **17**, 16719–16722.

(33) S. P. Gurung, C. Schwarz, J. P. Hall, C. J. Cardin and J. A. Brazier, "The importance of loop length on the stability of i-motif structures", *Chemical Communications*, 2015, **51**, 5630–5632.

(34) S. M. Reilly, R. K. Morgan, T. A. Brooks and R. M. Wadkins, "Effect of Interior Loop Length on the Thermal Stability and p K a of i-Motif DNA", *Biochemistry*, 2015, **54**, 1364–1370.

(35) E. P. Wright, J. L. Huppert and Z. A. E. Waller, "Identification of multiple genomic DNA sequences which form i-motif structures at neutral pH", *Nucleic Acids Research*, 2017, **45**, 2951–2959.

(36) S. Dzatko, M. Krafcikova, R. Hänsel-Hertsch, T. Fessl, R. Fiala, T. Loja, D. Krafcik, J.-L. Mergny, S. Foldynova-Trantirkova and L. Trantirek, "Evaluation of the Stability of DNA i-Motifs in the Nuclei of Living Mammalian Cells", *Angewandte Chemie International Edition*, 2018, **57**, 2165–2169.

(37) M. Zeraati, D. B. Langley, P. Schofield, A. L. Moye, R. Rouet, W. E. Hughes, T. M. Bryan, M. E. Dinger and D. Christ, "I-motif DNA structures are formed in the nuclei of human cells", *Nature Chemistry*, 2018, **10**, 631–637.

(38) S. Simon, D. Roy and M. Schindler, "Intracellular pH and the control of multidrug resistance.", *Proceedings of the National Academy of Sciences*, 1994, **91**, 1128–1132.

(39) U. Schnell, F. Dijk, K. A. Sjollema and B. N. G. Giepmans, "Immunolabeling artifacts and the need for live-cell imaging", *Nature Methods*, 2012, **9**, 152–158.

(40) C. V. Kumar, J. K. Barton and N. J. Turro, "Photophysics of ruthenium complexes bound to double helical DNA", *Journal of the American Chemical Society*, 1985, **107**, 5518–5523.

(41) C. A. Puckett and J. K. Barton, "Methods to Explore Cellular Uptake of Ruthenium Complexes", *Journal of the American Chemical Society*, 2007, **129**, 46–47.

(42) C. J. Murphy and J. K. Barton, in *Methods in Enzymology*, Academic Press, 1993, vol. 226, pp. 576–594.

(43) A. Juris, V. Balzani, F. Barigelletti, S. Campagna, P. Belser and A. von Zelewsky, "Ru(II) polypyridine complexes: photophysics, photochemistry, eletrochemistry, and chemiluminescence", *Coordination Chemistry Reviews*, 1988, **84**, 85–277.

(44) M. Abrahamsson, M. Jager, R. J. Kumar, T. Osterman, P. Persson, H.-c. Becker, O. Johansson and L. Hammarstrom, "Bistridentate Ruthenium(II)polypyridyl-Type Complexes with Microsecond 3 MLCT State Lifetimes: Sensitizers for Rod-Like Molecular Arrays", *Journal of the American Chemical Society*, 2008, **130**, 15533–15542.

(45) E. A. Medlycott and G. S. Hanan, "Synthesis and properties of mono- and oligonuclear Ru(II) complexes of tridentate ligands: The quest for long-lived excited states at room temperature", *Coordination Chemistry Reviews*, 2006, **250**, 1763–1782.

(46) J. R. Lakowicz, *Principles of Fluorescence Spectroscopy*, ed. J. R. Lakowicz, Springer US, Boston, MA, 3rd edn., 2006.

(47) K. Kalyanasundaram, "Photophysics, photochemistry and solar energy conversion with tris(bipyridyl)ruthenium(II) and its analogues", *Coordination Chemistry Reviews*, 1982, **46**, 159–244.

(48) J. K. Barton, A. Danishefsky and J. Goldberg, "Tris(phenanthroline)ruthenium(II): stereoselectivity in binding to DNA", *Journal of the American Chemical Society*, 1984, **106**, 2172–2176.

(49) J. K. Barton, L. A. Basile, A. Danishefsky and A. Alexandrescu, "Chiral probes for the handedness of DNA helices: enantiomers of tris(4,7-diphenylphenanthroline) ruthenium(II).", *Proceedings of the National Academy of Sciences*, 1984, **81**, 1961–1965.

(50) G. Li, L. Sun, L. Ji and H. Chao, "Ruthenium(II) complexes with dppz: from molecular photoswitch to biological applications", *Dalton Transactions*, 2016, **45**, 13261–13276.

(51) A. W. McKinley, P. Lincoln and E. M. Tuite, "Environmental effects on the photophysics of transition metal complexes with dipyrido[2,3-a:3′,2′-c]phenazine (dppz) and related ligands", *Coordination Chemistry Reviews*, 2011, **255**, 2676–2692.

(52) E. J. Olson, D. Hu, A. Hörmann, A. M. Jonkman, M. R. Arkin, E. D. Stemp, J. K. Barton and P. F. Barbara, "First observation of the key intermediate in the 'light-switch' mechanism of $[Ru(phen)_2dppz]^{2+}$", *Journal of the American Chemical Society*, 1997, **119**, 11458–11467.

(53) F. E. Poynton, J. P. Hall, P. M. Keane, C. Schwarz, I. V. Sazanovich, M. Towrie, T. Gunnlaugsson, C. J. Cardin, D. J. Cardin, S. J. Quinn, C. Long and J. M. Kelly, "Direct observation by time-resolved infrared spectroscopy of the bright and the dark excited states of the [Ru(phen) 2 (dppz)] 2+ light-switch compound in solution and when bound to DNA", *Chemical Science*, 2016, **7**, 3075–3084.

(54) C. Metcalfe, H. Adams, I. Haq and J. A. Thomas, "A ruthenium dipyridophenazine complex that binds preferentially to GC sequences", *Chemical Communications*, 2003, **0**, 1152–1153.

(55) A. N. Boynton, L. Marcélis and J. K. Barton, "$[Ru(Me_4phen)_2dppz]^{2+}$, a Light Switch for DNA Mismatches", *Journal of the American Chemical Society*, 2016, **138**, 5020–5023.

(56) J. H. J. Hoeijmakers, "Genome maintenance mechanisms for preventing cancer", *Nature*, 2001, **411**, 366–374.

(57) R. R. Iyer, A. Pluciennik, V. Burdett and P. L. Modrich, "DNA Mismatch Repair: Functions and Mechanisms", *Chemical Reviews*, 2006, **106**, 302–323.

(58) A. N. Boynton, L. Marcélis, A. J. McConnell and J. K. Barton, "A Ruthenium(II) Complex as a Luminescent Probe for DNA Mismatches and Abasic Sites", *Inorganic Chemistry*, 2017, **56**, 8381–8389.

(59) C. Rajput, R. Rutkaite, L. Swanson, I. Haq and J. A. Thomas, "Dinuclear Monointercalating RuII Complexes That Display High Affinity Binding to Duplex and Quadruplex DNA", *Chemistry - A European Journal*, 2006, **12**, 4611–4619.

(60) S. Shi, J. Zhao, X. Gao, C. Lv, L. Yang, J. Hao, H. Huang, J. Yao, W. Sun, T. Yao and L. Ji, "Molecular "light switch" for G-quadruplex DNA: cycling the switch on and off", *Dalton Transactions*, 2012, **41**, 5789.

(61) S. Shi, J. Liu, T. Yao, X. Geng, L. Jiang, Q. Yang, L. Cheng and L. Ji, "Promoting the Formation and Stabilization of G-Quadruplex by Dinuclear Ru II Complex Ru 2 (obip)L 4", *Inorganic Chemistry*, 2008, **47**, 2910–2912.

(62) Q. Yu, Y. Liu, J. Zhang, F. Yang, D. Sun, D. Liu, Y. Zhou and J. Liu, "Ruthenium(ii) polypyridyl complexes as G-quadruplex inducing and stabilizing ligands in telomeric DNA", *Metallomics*, 2013, **5**, 222.

(63) A. Siddiqui-Jain, C. L. Grand, D. J. Bearss and L. H. Hurley, "Direct evidence for a G-quadruplex in a promoter region and its targeting with a small molecule to repress c-MYC transcription", *Proceedings of the National Academy of Sciences*, 2002, **99**, 11593–11598.

(64) W.-J. Mei, X.-Y. Wei, Y.-J. Liu and B. Wang, "Studies on the interactions of a novel ruthenium(II) complex with G-quadruplex DNA", *Transition Metal Chemistry*, 2008, **33**, 907–910.

(65) D. Bouzada, I. Salvadó, G. Barka, G. Rama, J. Martínez-Costas, R. Lorca, Á. Somoza, M. Melle-Franco, M. E. Vázquez and M. Vázquez López, "Selective G-quadruplex binding by oligoarginine-Ru(dppz) metallopeptides", *Chemical Communications*, 2018, **54**, 658–661.

(66) L. He, X. Chen, Z. Meng, J. Wang, K. Tian, T. Li and F. Shao, "Octahedral ruthenium complexes selectively stabilize G-quadruplexes", *Chemical Communications*, 2016, **52**, 8095–8098.

(67) S. Shi, J. Zhao, X. Geng, T. Yao, H. Huang, T. Liu, L. Zheng, Z. Li, D. Yang and L. Ji, "Molecular "light switch" for G-quadruplexes and i-motif of human telomeric DNA: $[Ru(phen)_2(dppz)]^{2+}$", *Dalton Transactions*, 2010, **39**, 2490.

(68) S. Shi, X. Geng, J. Zhao, T. Yao, C. Wang, D. Yang, L. Zheng and L. Ji, "Interaction of [Ru(bpy)2(dppz)]2+ with human telomeric DNA: Preferential binding to G-quadruplexes over i-motif", *Biochimie*, 2010, **92**, 370–377.

(69) S. M. Haider, S. Neidle and G. N. Parkinson, "A structural analysis of G-quadruplex / ligand interactions", *Biochimie*, 2011, **93**, 1239–1251.

(70) B. J. Pages, S. P. Gurung, K. McQuaid, J. P. Hall, C. J. Cardin and J. A. Brazier, "Stabilization of Long-Looped i-Motif DNA by Polypyridyl Ruthenium Complexes", *Frontiers in Chemistry*, 2019, **7**, 744.

(71) M. Abrahamsson, M. Jäger, T. Österman, L. Eriksson, P. Persson, H. C. Becker, O. Johansson and L. Hammarström, "A 3.0 μs room temperature excited state lifetime of a bistridentate RuII-polypyridine complex for rod-like molecular arrays", *Journal of the American Chemical Society*, 2006, **128**, 12616–12617.

(72) V. Balzani, S. Campagna, G. Denti, A. Juris, S. Serroni and M. Venturi, "Designing Dendrimers Based on Transition-Metal Complexes. Light-Harvesting Properties and Predetermined Redox Patterns", *Accounts of Chemical Research*, 1998, **31**, 26–34.

(73) J. R. Winkler, T. L. Netzel, C. Creutz and N. Sutin, "Direct observation of metal-to-ligand charge-transfer (MLCT) excited states of pentaammineruthenium(II) complexes", *Journal of the American Chemical Society*, 1987, **109**, 2381–2392.

(74) J. Wang, Y. Q. Fang, G. S. Hanan, F. Loiseau and S. Campagna, "Synthesis and properties of the elusive ruthenium(II) complexes of 4'-cyano-2,2':6',"-terpyridine", *Inorganic Chemistry*, 2005, **44**, 5–7.

(75) E. C. Constable, A. M. Cargill Thompson, N. Armaroli, V. Balzani and M. Maestri, "Ligand substitution patterns control photophysical properties of ruthenium(II)-2,2':6',"-terpyridine complexes—room temperature emission from [Ru(tpy)2]2+ analogues", *Polyhedron*, 1992, **11**, 2707–2709.

(76) M. I. J. Polson, E. A. Medlycott, G. S. Hanan, L. Mikelsons, N. J. Taylor, M. Watanabe, Y. Tanaka, F. Loiseau, R. Passalacqua and S. Campagna, "Ruthenium complexes of easily accessible tridentate ligands based on the 2-aryl-4,6-bis(2-pyridyl)-s-triazine motif: Absorption spectra, luminescence properties, and redox behavior", *Chemistry - A European Journal*, 2004, **10**, 3640–3648.

(77) H. Wolpher, O. Johansson, M. Abrahamsson, M. Kritikos, L. Sun and B. Åkermark, "A tridentate ligand for preparation of bisterpyridine-like ruthenium(II) complexes with an increased excited state lifetime", *Inorganic Chemistry Communications*, 2004, **7**, 337–340.

(78) M. Abrahamsson, H. Wolpher, O. Johansson, J. Larsson, M. Kritikos, L. Eriksson, P.-o. Norrby, J. Bergquist, L. Sun, B. Åkermark and L. Hammarström, "A New Strategy for the Improvement of Photophysical Properties in Ruthenium(II) Polypyridyl Complexes. Synthesis and Photophysical and Electrochemical Characterization of Six Mononuclear Ruthenium(II) Bisterpyridine-Type Complexes", *Inorganic Chemistry*, 2005, **44**, 3215–3225.

(79) O. A. Borg, S. S. M. C. Godinho, M. J. Lundqvist, S. Lunell and P. Persson, "Computational Study of the Lowest Triplet State of Ruthenium Polypyridyl Complexes Used in Artificial Photosynthesis", *The Journal of Physical Chemistry A*, 2008, **112**, 4470–4476.

(80) M. Jäger, R. J. Kumar, H. Görls, J. Bergquist and O. Johansson, "Facile synthesis of bistridentate Ru II complexes based on 2,6-Di(quinolin-8-yl)pyridyl Ligands: Sensitizers with microsecond ^{3}MLCT excited state lifetimes", *Inorganic Chemistry*, 2009, **48**, 3228–3238.

(81) M. Jäger, L. Eriksson, J. Bergquist and O. Johansson, "Synthesis and Characterization of 2,6-Di(quinolin-8-yl)pyridines. New Ligands for Bistridentate Ru II Complexes with Microsecond Luminescent Lifetimes", *The Journal of Organic Chemistry*, 2007, **72**, 10227–10230.

(82) C. S. Devi, B. Thulasiram, S. Satyanarayana and P. Nagababu, "Analytical Techniques Used to Detect DNA Binding Modes of Ruthenium(II) Complexes with Extended Phenanthroline Ring", *Journal of Fluorescence*, 2017, **27**, 2119–2130.

(83) C. Hiort, P. Lincoln and B. Norden, "DNA binding of Δ- and Λ-$[Ru(phen)_2dppz]^{2+}$", *Journal of the American Chemical Society*, 1993, **115**, 3448–3454.

(84) L. Wang, Y. Wu, T. Chen and C. Wei, "The interactions of phenanthroline compounds with DNAs: Preferential binding to telomeric quadruplex over duplex", *International Journal of Biological Macromolecules*, 2013, **52**, 1–8.

(85) F. E. Poynton, S. A. Bright, S. Blasco, D. C. Williams, J. M. Kelly and T. Gunnlaugsson, "The development of ruthenium(II) polypyridyl complexes and conjugates for in vitro cellular and in vivo applications", *Chemical Society Reviews*, 2017, **46**, 7706–7756.

(86) J. K. Barton, J. M. Goldberg, C. V. Kumar and N. J. Turro, "Binding Modes and Base Specificity of Tris(phenanthroline)ruthenium(II) Enantiomers with Nucleic Acids: Tuning the Stereoselectivity", *Journal of the American Chemical Society*, 1986, **108**, 2081–2088.

(87) J.-B. Lepecq and C. Paoletti, "A fluorescent complex between ethidium bromide and nucleic acids", *Journal of Molecular Biology*, 1967, **27**, 87–106.

(88) C. J. Cardin, J. M. Kelly and S. J. Quinn, "Photochemically active DNA-intercalating ruthenium and related complexes – insights by combining crystallography and transient spectroscopy", *Chemical Science*, 2017, **8**, 4705–4723.

(89) M. Vorlíčková, I. Kejnovská, K. Bednářová, D. Renčiuk and J. Kypr, "Circular Dichroism Spectroscopy of DNA: From Duplexes to Quadruplexes", *Chirality*, 2012, **24**, 691–698.

(90) N. C. Garbett, P. A. Ragazzon and J. B. Chaires, "Circular dichroism to determine binding mode and affinity of ligand–DNA interactions", *Nature Protocols*, 2007, **2**, 3166–3172.

(91) Q. Sheng, J. C. Neaverson, T. Mahmoud, C. E. M. Stevenson, S. E. Matthews and Z. A. E. Waller, "Identification of new DNA i-motif binding ligands through a fluorescent intercalator displacement assay", *Organic & Biomolecular Chemistry*, 2017, **15**, 5669–5673.

(92) D. L. Boger and W. C. Tse, "Thiazole orange as the fluorescent intercalator in a high resolution fid assay for determining DNA binding affinity and sequence selectivity of small molecules", *Bioorganic and Medicinal Chemistry*, 2001, **9**, 2511–2518.

(93) G. M. Morris, R. Huey, W. Lindstrom, M. F. Sanner, R. K. Belew, D. S. Goodsell and A. J. Olson, "AutoDock4 and AutoDockTools4: Automated docking with selective receptor flexibility", *Journal of Computational Chemistry*, 2009, **30**, 2785–2791.

(94) O. Trott and A. J. Olson, "AutoDock Vina: Improving the speed and accuracy of docking with a new scoring function, efficient optimization, and multithreading", *Journal of Computational Chemistry*, 2009, **31**, 455–461.

(95) M. M. Jaghoori, B. Bleijlevens and S. D. Olabarriaga, "1001 Ways to run AutoDock Vina for virtual screening", *Journal of Computer-Aided Molecular Design*, 2016, **30**, 237–249.

(96) M. W. Chang, C. Ayeni, S. Breuer and B. E. Torbett, "Virtual Screening for HIV Protease Inhibitors: A Comparison of AutoDock 4 and Vina", *PLoS ONE*, 2010, **5**, e11955.

(97) I. Romero, M. Rodríguez, A. Llobet, M.-N. Collomb-Dunand-Sauthier, A. Deronzier, T. Parella and H. Stoeckli-Evans, "Synthesis, structure and redox properties of a new ruthenium(II) complex containing the flexible tridentate ligand N,N-bis(2-pyridylmethyl)ethylamine, cis-fac-$[Ru(bpea)_2]^{2+}$, and its homologue attached covalently to a polypyrrole film", *Journal of the Chemical Society, Dalton Transactions*, 2000, **3**, 1689–1694.

(98) I. Ortmans, B. Elias, J. M. Kelly, C. Moucheron and A. Kirsch-DeMesmaeker, "[Ru(TAP) 2 (dppz)] 2+ : a DNA intercalating complex, which luminesces strongly in water and undergoes photo-induced proton-coupled electron transfer with guanosine-5'-monophosphate", *Dalton Trans.*, 2004, **0**, 668–676.

(99) K. McQuaid, H. Abell, S. P. Gurung, D. R. Allan, G. Winter, T. Sorensen, D. J. Cardin, J. A. Brazier, C. J. Cardin and J. P. Hall, "Structural Studies Reveal Enantiospecific Recognition of a DNA G-Quadruplex by a Ruthenium Polypyridyl Complex", *Angewandte Chemie International Edition*, 2019, **58**, 9881–9885.

(100) R. J. Kumar, S. Karlsson, D. Streich, A. Rolandini Jensen, M. Jäger, H.-C. Becker, J. Bergquist, O. Johansson and L. Hammarström, "Vectorial Electron Transfer in Donor-Photosensitizer-Acceptor Triads Based on Novel Bis-tridentate Ruthenium Polypyridyl Complexes", *Chemistry - A European Journal*, 2010, **16**, 2830–2842.

(101) L. A. Adrio, B. N. Nguyen, G. Guilera, A. G. Livingston and K. K. Hii, "Speciation of Pd(OAc) 2 in ligandless Suzuki–Miyaura reactions", *Catalysis Science and Technology*, 2012, **2**, 316–323.

(102) J. Sherwood, J. H. Clark, I. J. S. Fairlamb and J. M. Slattery, "Solvent effects in palladium catalysed cross-coupling reactions", *Green Chemistry*, 2019, **21**, 2164–2213.

(103) J.-L. Mergny, J. Li, L. Lacroix, S. Amrane and J. B. Chaires, "Thermal difference spectra: a specific signature for nucleic acid structures", *Nucleic Acids Research*, 2005, **33**, e138–e138.

(104) A. M. Pyle, J. P. Rehmann, R. Meshoyrer, C. V. Kumar, N. J. Turro and J. K. Barton, "Mixed-ligand complexes of ruthenium(II): factors governing binding to DNA", *Journal of the American Chemical Society*, 1989, **111**, 3051–3058.

(105) N. W. Luedtke, J. S. Hwang, E. Nava, D. Gut, M. Kol and Y. Tor, "The DNA and RNA specificity of eilatin Ru(II) complexes as compared to eilatin and ethidium bromide", *Nucleic Acids Research*, 2003, **31**, 5732–5740.

(106) Q. Sheng, J. C. Neaverson, T. Mahmoud, C. E. M. Stevenson, S. E. Matthews and Z. A. E. Waller, "Identification of new DNA i-motif binding ligands through a fluorescent intercalator displacement assay", *Org. Biomol. Chem.*, 2017, **15**, 5669–5673.

(107) D. Monchaud, C. Allain and M.-P. Teulade-Fichou, "Development of a fluorescent intercalator displacement assay (G4-FID) for establishing quadruplex-DNA affinity and selectivity of putative ligands", *Bioorganic & Medicinal Chemistry Letters*, 2006, **16**, 4842–4845.

(108) A. E. Friedman, J. C. Chambron, J. P. Sauvage, N. J. Turro and J. K. Barton, "A molecular light switch for DNA: $Ru(bpy)_2(dppz)^{2+}$", *Journal of the American Chemical Society*, 1990, **112**, 4960–4962.

(109) S. K. Sheet, B. Sen, S. K. Patra, M. Rabha, K. Aguan and S. Khatua, "Aggregation-Induced Emission-Active Ruthenium(II) Complex of 4,7-Dichloro Phenanthroline for Selective Luminescent Detection and Ribosomal RNA Imaging", *ACS Applied Materials and Interfaces*, 2018, **10**, 14356–14366.

(110) X. Xu, J. Li, Q. Li, J. Huang, Y. Dong, Y. Hong, J. Yan, J. Qin, Z. Li and B. Z. Tang, "A Strategy for dramatically enhancing the selectivity of molecules showing aggregation-induced emission towards biomacromolecules with the aid of graphene oxide", *Chemistry - A European Journal*, 2012, **18**, 7278–7286.

(111) L. Huang and L. Dai, "Aggregation-Induced Emission for Highly Selective and Sensitive Fluorescent Biosensing and Cell Imaging", *Journal of Polymer Science, Part A: Polymer Chemistry*, 2017, **55**, 653–659.

(112) Q. Zeng, Z. Li, Y. Dong, C. Di, A. Qin, Y. Hong, L. Ji, Z. Zhu, C. K. Jim, G. Yu, Q. Li, Z. Li, Y. Liu, J. Qin and B. Z. Tang, "Fluorescence enhancements of benzene-cored luminophors by restricted intramolecular rotations: AIE and AIEE effects", *Chemical Communications*, 2007, **1**, 70–72.

(113) Y. Dong, J. W. Lam, A. Qin, Z. Li, J. Liu, J. Sun, Y. Dong and B. Z. Tang, "Endowing hexaphenylsilole with chemical sensory and biological probing properties by attaching amino pendants to the silolyl core", *Chemical Physics Letters*, 2007, **446**, 124–127.

(114) J. D. McGhee and P. H. von Hippel, "Theoretical aspects of DNA-protein interactions: Co-operative and non-co-operative binding of large ligands to a one-dimensional homogeneous lattice", *Journal of Molecular Biology*, 1974, **86**, 469–489.

(115) G. M. Morris, R. Huey, W. Lindstrom, M. F. Sanner, R. K. Belew, D. S. Goodsell and A. J. Olson, "AutoDock4 and AutoDockTools4: Automated docking with selective receptor flexibility", *Journal of Computational Chemistry*, 2009, **30**, 2785–2791.

(116) A. T. Phan, M. Guéron and J.-L. Leroy, "The solution structure and internal motions of a fragment of the cytidine-rich strand of the human telomere 1 1Edited by I. Tinoco", *Journal of Molecular Biology*, 2000, **299**, 123–144.

(117) G. N. Parkinson, M. P. H. Lee and S. Neidle, "Crystal structure of parallel quadruplexes from human telomeric DNA", *Nature*, 2002, **417**, 376–880.

(118) E. F. Pettersen, T. D. Goddard, C. C. Huang, G. S. Couch, D. M. Greenblatt, E. C. Meng and T. E. Ferrin, "UCSF Chimera - A visualization system for exploratory research and analysis", *Journal of Computational Chemistry*, 2004, **25**, 1605–1612.

(119) M. J. Frisch, G. W. Trucks, H. B. Schlegel, G. E. Scuseria, M. A. Robb, J. R. Cheeseman, G. Scalmani, V. Barone, G. A. Petersson, H. Nakatsuji, M. C. X. Li, A. V. Marenich, J. Bloino, B. G. Janesko, R. Gomperts, B. Mennucci, H. P. Hratchian, J. V. and D. J. Fox, *Gaussian 16*, Wallingford CT, 2016.

(120) G. te Velde, F. M. Bickelhaupt, E. J. Baerends, C. Fonseca Guerra, S. J. A. van Gisbergen, J. G. Snijders and T. Ziegler, "Chemistry with ADF", *Journal of Computational Chemistry*, 2001, **22**, 931–967.

(121) M. Jäger, L. Freitag and L. González, "Using computational chemistry to design Ru photosensitizers with directional charge transfer", *Coordination Chemistry Reviews*, 2015, **304-305**, 146–165.

(122) T. Schlotthauer, B. Suchland, H. Görls, G. A. Parada, L. Hammarström, U. S. Schubert and M. Jäger, "Aryl-Decorated Ru II Polypyridyl-type Photosensitizer Approaching NIR Emission with Microsecond Excited State Lifetimes", *Inorganic Chemistry*, 2016, **55**, 5405–5416.

(123) O. A. Borg, S. S. M. C. Godinho, M. J. Lundqvist, S. Lunell and P. Persson, "Computational Study of the Lowest Triplet State of Ruthenium Polypyridyl Complexes Used in Artificial Photosynthesis", *The Journal of Physical Chemistry A*, 2008, **112**, 4470–4476.

(124) T. Österman, M. Abrahamsson, H. C. Becker, L. Hammarström and P. Persson, "Influence of triplet state multidimensionality on excited state lifetimes of bistridentate Ru II complexes: A computational study", *Journal of Physical Chemistry A*, 2012, **116**, 1041–1050.

(125) T. Österman and P. Persson, "Excited state potential energy surfaces of bistridentate RuII complexes – A TD-DFT study", *Chemical Physics*, 2012, **407**, 76–82.

(126) P. Wolski, K. Nieszporek and T. Panczyk, "G-Quadruplex and I-Motif Structures within the Telomeric DNA Duplex. A Molecular Dynamics Analysis of Protonation States as Factors Affecting Their Stability", *The Journal of Physical Chemistry B*, 2019, **123**, 468–479.

(127) Y. Sun, D. A. Lutterman and C. Turro, "Role of Electronic Structure on DNA Light-Switch Behavior of Ru(II) Intercalators", *Inorganic Chemistry*, 2008, **47**, 6427–6434.

(128) B. C. Poulsen, S. Estalayo-Adrián, S. Blasco, S. A. Bright, J. M. Kelly, D. C. Williams and T. Gunnlaugsson, "Luminescent ruthenium polypyridyl complexes with ex-

tended 'dppz' like ligands as DNA targeting binders and cellular agents", *Dalton Transactions*, 2016, **45**, 18208–18220.

(129) C. Moucheron, A. Kirsch-De Mesmaeker and S. Choua, "Photophysics of $Ru(phen)_2(PHEHAT)^{2+}$: A Novel "Light Switch" for DNA and Photo-oxidant for Mononucleotides", *Inorganic Chemistry*, 1997, **36**, 584–592.

(130) J.-P. Lecomte, A. Kirsch-De Mesmaeker, M. M. Feeney and J. M. Kelly, "Ruthenium(II) Complexes with 1,4,5,8,9,12 - Hexaazatriphenylene and 1,4,5,8 - Tetraazaphenanthrene Ligands: Key Role Played by the Photoelectron Transfer in DNA Cleavage and Adduct Formation", *Inorganic Chemistry*, 1995, **34**, 6481–6491.

(131) O. Van Gijte and A. Kirsch-De Mesmaeker, "The dinuclear ruthenium(II) complex $[\{Ru(phen)_2\}_2(HAT)]^{4+}$ (HAT = 1,4,5,8,9,12-hexaazatriphenylene), a new photoreagent for nucleobases and photoprobe for denatured DNA", *Journal of the Chemical Society, Dalton Transactions*, 1999, 951–956.

(132) A. Boisdenghien, C. Moucheron and A. Kirsch-De Mesmaeker, "$[Ru(phen)_2(PHEHAT)]^{2+}$ and $[Ru(phen)_2(HATPHE)]^{2+}$: Two Ruthenium(II) Complexes with the Same Ligands but Different Photophysics and Spectroelectrochemistry", *Inorganic Chemistry*, 2005, **44**, 7678–7685.

(133) N. Komatsuzaki, R. Katoh, Y. Himeda, H. Sugihara, H. Arakawa and K. Kasuga, "Structure and photochemical properties of ruthenium complexes having dimethyl-substituted DPPZ or TPPHZ as a ligand †", *Journal of the Chemical Society, Dalton Transactions*, 2000, 3053–3054.

(134) J. Olofsson, L. M. Wilhelmsson and P. Lincoln, "Effects of methyl substitution on radiative and solvent quenching rate constants of $[Ru(phen)_2dppz]^{2+}$ in polyol solvents and bound to DNA", *Journal of the American Chemical Society*, 2004, **126**, 15458–15465.

(135) C. Friebe, H. Görls, M. Jäger and U. S. Schubert, "Linear Metallopolymers from Ruthenium(II)-2,6-di(quinolin-8-yl)pyridine Complexes by Electropolymerization - Formation of Redox-Stable and Emissive Films", *European Journal of Inorganic Chemistry*, 2013, **2013**, 4191–4202.

(136) R. J. Kumar, S. Karlsson, D. Streich, A. Rolandini Jensen, M. Jäger, H.-C. Becker, J. Bergquist, O. Johansson and L. Hammarström, "Vectorial Electron Transfer in Donor-Photosensitizer-Acceptor Triads Based on Novel Bis-tridentate Ruthenium Polypyridyl Complexes", *Chemistry - A European Journal*, 2010, **16**, 2830–2842.

(137) M. Jager, A. Smeigh, F. Lombeck, H. Gorls, J.-P. Collin, J.-P. Sauvage, L. Hammarstrom and O. Johansson, "Cyclometalated Ru II Complexes with Improved Octahedral Geometry: Synthesis and Photophysical Properties", *Inorganic Chemistry*, 2010, **49**, 374–376.

(138) G. Ragazzon, P. Verwilst, S. A. Denisov, A. Credi, G. Jonusauskas and N. D. McClenaghan, "Ruthenium(ii) complexes based on tridentate polypyridine ligands that feature long-lived room-temperature luminescence", *Chemical Communications*, 2013, **49**, 9110.

(139) J. Madureira, C. I. V. Ramos, M. Marques, C. Maia, B. de Sousa, L. Campino, M. G. Santana-Marques and N. Farrell, "Nonclassic Metallointercalators with Dipyridophenazine: DNA Interaction Studies and Leishmanicidal Activity", *Inorganic Chemistry*, 2013, **52**, 8881–8894.

(140) A. M. Funston, C. Cullinane, K. P. Ghiggino, W. D. McFadyen, S. S. Stylli and P. A. Tregloan, "Dipyridophenazine Complexes of Cobalt(III): DNA Photocleavage and Photobiology", *Australian Journal of Chemistry*, 2005, **58**, 206.

(141) E. D. Olmon, P. A. Sontz, A. M. Blanco-Rodríguez, M. Towrie, I. P. Clark, A. Vlček and J. K. Barton, "Charge Photoinjection in Intercalated and Covalently Bound $[Re(CO)_3(dppz)(py)]^+$ –DNA Constructs Monitored by Time-Resolved Visible and Infrared Spectroscopy", *Journal of the American Chemical Society*, 2011, **133**, 13718–13730.

(142) F. L. Thorp-Greenwood, M. P. Coogan, L. Mishra, N. Kumari, G. Rai and S. Saripella, "The importance of cellular localisation of probes: synthesis, photophysical properties, DNA interactions and cellular imaging properties of rhenium dppz complexes with known cellular localisation vectors", *New Journal of Chemistry Chemistry*, 2012, **36**, 64–72.

(143) E. L. Menon, R. Perera, M. Navarro, R. J. Kuhn and H. Morrison, "Phototoxicity against Tumor Cells and Sindbis Virus by an Octahedral Rhodium Bisbipyridyl Complex and Evidence for the Genome as a Target in Viral Photoinactivation", *Inorganic Chemistry*, 2004, **43**, 5373–5381.

(144) D.-L. Ma, C.-M. Che and S.-C. Yan, "Platinum(II) Complexes with Dipyridophenazine Ligands as Human Telomerase Inhibitors and Luminescent Probes for G-Quadruplex DNA", *Journal of the American Chemical Society*, 2009, **131**, 1835–1846.

(145) R. E. Holmlin and J. K. Barton, "$Os(phen)_2(dppz)^{2+}$: A Red-Emitting DNA Probe", *Inorganic Chemistry*, 1995, **34**, 7–8.

(146) A. Wragg, M. R. Gill, C. J. Hill, X. Su, A. J. H. M. Meijer, C. Smythe and J. A. Thomas, "Dinuclear osmium(II) probes for high-resolution visualisation of cellular DNA structure using electron microscopy", *Chemical Communications*, 2014, **50**, 14494–14497.

(147) D. Herebian and W. S. Sheldrick, "Synthesis and DNA binding properties of bioorganometallic (η5-pentamethylcyclopentadienyl)iridium(iii) complexes of the type $[(\eta5\text{-}C_5Me_5)Ir(Aa)(dppz)]^{n+}$ (dppz = dipyrido[3,2-a:2′,3′-c]phenazine, n = 1–3), with S-coordinated amino acids (Aa) or peptides", *Journal of the Chemical Society, Dalton Transactions*, 2002, 966–974.

(148) K. K.-W. Lo, C.-K. Chung and N. Zhu, "Nucleic Acid Intercalators and Avidin Probes Derived from Luminescent Cyclometalated Iridium(III)–Dipyridoquinoxaline and –Dipyridophenazine Complexes", *Chemistry - A European Journal*, 2006, **12**, 1500–1512.

(149) S. Stimpson, D. R. Jenkinson, A. Sadler, M. Latham, D. A. Wragg, A. J. H. M. Meijer and J. A. Thomas, "Tuning the Excited State of Water-Soluble Ir III -Based DNA Intercalators that are Isostructural with $[Ru^{II}(NN)_2(dppz)]$ Light-Switch Complexes", *Angewandte Chemie International Edition*, 2015, **54**, 3000–3003.

(150) D. Reha, M. Kabelác, F. Ryjácek, J. Šponer, J. E. Šponer, M. Elstner, S. Suhai and P. Hobza, "Intercalators. 1. Nature of Stacking Interactions between Intercalators (Ethidium, Daunomycin, Ellipticine, and 4′,6-Diaminide-2-phenylindole) and DNA

Base Pairs. Ab Initio Quantum Chemical, Density Functional Theory, and Empirical Potential Study", *Journal of the American Chemical Society*, 2002, **124**, 3366–3376.

(151) S. E. Patterson, J. M. Coxon and L. Strekowski, "Intercalation of ethidium and analogues with nucleic acids: a molecular orbital study", *Bioorganic & Medicinal Chemistry*, 1997, **5**, 277–281.

(152) L. Lu, W. Wang, C. Yang, T.-S. Kang, C.-H. Leung and D.-L. Ma, "Iridium(III) complexes with 1,10-phenanthroline-based NN ligands as highly selective luminescent G-quadruplex probes and application for switch-on ribonuclease H detection", *Journal of Materials Chemistry B*, 2016, **4**, 6791–6796.

(153) A. K. Pal, N. Zaccheroni, S. Campagna and G. S. Hanan, "Near infra-red emission from a mer-Ru(ii) complex: consequences of strong σ-donation from a neutral, flexible ligand with dual binding modes", *Chemical Communications*, 2014, **50**, 6846.

(154) S. K. Singh and D. S. Pandey, "Multifaceted half-sandwich arene–ruthenium complexes: interactions with biomolecules, photoactivation, and multinuclearity approach", *RSC Advances*, 2014, **4**, 1819–1840.

(155) B. Therrien, "Functionalised η^6-arene ruthenium complexes", *Coordination Chemistry Reviews*, 2009, **253**, 493–519.

(156) U. Schatzschneider, "Photoactivated Biological Activity of Transition-Metal Complexes", *European Journal of Inorganic Chemistry*, 2010, **2010**, 1451–1467.

(157) S. Betanzos-Lara, L. Salassa, A. Habtemariam and P. J. Sadler, "Photocontrolled nucleobase binding to an organometallic RuII arene complex", *Chemical Communications*, 2009, 6622.

(158) A. F. A. Peacock, M. Melchart, R. J. Deeth, A. Habtemariam, S. Parsons and P. J. Sadler, "Osmium(II) and Ruthenium(II) Arene Maltolato Complexes: Rapid Hydrolysis and Nucleobase Binding", *Chemistry - A European Journal*, 2007, **13**, 2601–2613.

(159) W. Lackner, C. M. Standfest-Hauser, K. Mereiter, R. Schmid and K. Kirchner, "Photochemical displacement of the benzene ligand in $[(\eta^6\text{-}C_6H_6)Ru(CH_3CN)_2(L)]^{2+}$

and [(η^6-C_6H_6)Ru(CH_3CN)(L2)]$^{2+}$ (L=CH_3CN, PPh_3, L2=dppe, bipy)", *Inorganica Chimica Acta*, 2004, **357**, 2721–2727.

(160) E. Muetterties, J. R. Bleeke and A. C. Sievert, "Arene transition metal chemistry", *Journal of Organometallic Chemistry*, 1979, **178**, 197–216.

(161) D. E. Stephens, V. T. Nguyen, B. Chhetri, E. R. Clark, H. D. Arman and O. V. Larionov, "Organocatalytic Synthesis of Methylene-Bridged N -Heterobiaryls", *Organic Letters*, 2016, **18**, 5808–5811.

(162) M. D. Hanwell, D. E. Curtis, D. C. Lonie, T. Vandermeersch, E. Zurek and G. R. Hutchison, "Avogadro: an advanced semantic chemical editor, visualization, and analysis platform", *Journal of Cheminformatics*, 2012, **4**, 17.

(163) Y.-W. Tsai, Y.-F. Chen, Y.-J. Li, K.-H. Chen, C.-H. Lin and J.-H. Huang, "Structural Determination of Ruthenium Complexes Containing Bi-Dentate Pyrrole-Ketone Ligands", *Molecules*, 2018, **23**, 159.

(164) S. H. Dale and M. R. J. Elsegood, "Oxalate complexes of the (η^6- *p*-cymene) ruthenium(II) fragment: μ-oxalato-κ 2 O 1 , O 2 :κ 2 O 1′ , O 2′ -bis[(η^6- *p*-cymene)(triphenylphosphine-κ P) ruthenium(II)] bis(tetrafluoroborate) and (η^6 - p -cymene)(oxalato-κ 2 O , O ′)(pyridine-3,5-dicar", *Acta Crystallographica Section C Crystal Structure Communications*, 2006, **62**, m166–m170.

(165) D. A. Freedman, S. Kruger, C. Roosa and C. Wymer, "Synthesis, Characterization, and Reactivity of [Ru(bpy)(CH 3 CN) 3 (NO 2)]PF 6 , a Synthon for [Ru(bpy)(L 3)NO 2] Complexes", *Inorganic Chemistry*, 2006, **45**, 9558–9568.

(166) M. R. Elsegood and D. A. Tocher, "Studies on transition metal paracyclophane compounds. Reactions of [{M(η^6-$C_{16}H_{16}$)Cl_2}$_2$] {M = Ru, Os} with tertiary phosphines: The crystal structures of [Ru(η^6-$C_{16}H_{16}$)Cl_2(PPh_3)]·$CHCl_3$ and [Ru(η^6-C_6H_6)Cl_2(PPh_3)]·2CH_2Cl_2", *Polyhedron*, 1995, **14**, 3147–3156.

(167) M. Bennett, G. Robertson and A. Smith, "Divalent ruthenium complexes containing non-planar hexahapto-benzene", *Journal of Organometallic Chemistry*, 1972, **43**, C41–C43.

(168) T. P. Gill and K. R. Mann, "Photochemical properties of the cyclopentadienyl(η_6-benzene) ruthenium(II) cation. The synthesis and reactions of a synthetically useful intermediate: the cyclopentadienyltris(acetonitrile) ruthenium(II) cation", *Organometallics*, 1982, **1**, 485–488.

(169) T. Hayashida and H. Nagashima, "Access to Novel Ruthenium - Amidinate Complexes, (η^6-arene)Ru(η^2-amidinate)$_X$ and [Ru(η^2-amidinate)(MeCN)$_4$] + PF_6 - by Photochemical Displacement of the Benzene Ligand in (η^6-C_6H_6)Ru(η^2-amidinate)X", *Organometallics*, 2002, **21**, 3884–3888.

(170) N. W. Alcock, P. R. Barker, J. M. Haider, M. J. Hannon, C. L. Painting, Z. Pikramenou, E. A. Plummer, K. Rissanen and P. Saarenketo, "Red and blue luminescent metallo-supramolecular coordination polymers assembled through π–π interactions †", *Journal of the Chemical Society, Dalton Transactions*, 2000, **0**, 1447–1462.

(171) H. A. Day, P. Pavlou and Z. A. Waller, "i-Motif DNA: Structure, stability and targeting with ligands", *Bioorganic & Medicinal Chemistry*, 2014, **22**, 4407–4418.

(172) L. Wang, Y. Wu, T. Chen and C. Wei, "The interactions of phenanthroline compounds with DNAs: Preferential binding to telomeric quadruplex over duplex", *International Journal of Biological Macromolecules*, 2013, **52**, 1–8.

(173) M. Wang, Z. Mao, T. S. Kang, C. Y. Wong, J. L. Mergny, C. H. Leung and D. L. Ma, "Conjugating a groove-binding motif to an Ir(iii) complex for the enhancement of G-quadruplex probe behavior", *Chemical Science*, 2016, **7**, 2516–2523.

(174) S. Lin, T.-S. Kang, L. Lu, W. Wang, D.-L. Ma and C.-H. Leung, "A G-quadruplex-selective luminescent probe with an anchor tail for the switch-on detection of thymine DNA glycosylase activity", *Biosensors and Bioelectronics*, 2016, **86**, 849–857.

(175) V. Schnecke and J. Boström, "Computational chemistry-driven decision making in lead generation", *Drug Discovery Today*, 2006, **11**, 43–50.

(176) R. Lahana, "How many leads from HTS?", *Drug Discovery Today*, 1999, **4**, 447–448.

(177) W. L. Jorgensen, "The Many Roles of Computation in Drug Discovery", *Science*, 2004, **303**, 1813–1818.

(178) C. Venkatachalam, X. Jiang, T. Oldfield and M. Waldman, "LigandFit: a novel method for the shape-directed rapid docking of ligands to protein active sites", *Journal of Molecular Graphics and Modelling*, 2003, **21**, 289–307.

(179) G. Jones, P. Willett, R. C. Glen, A. R. Leach and R. Taylor, "Development and validation of a genetic algorithm for flexible docking 1 1Edited by F. E. Cohen", *Journal of Molecular Biology*, 1997, **267**, 727–748.

(180) M. Rarey, B. Kramer, T. Lengauer and G. Klebe, "A Fast Flexible Docking Method using an Incremental Construction Algorithm", *Journal of Molecular Biology*, 1996, **261**, 470–489.

(181) Z. Wang, H. Sun, X. Yao, D. Li, L. Xu, Y. Li, S. Tian and T. Hou, "Comprehensive evaluation of ten docking programs on a diverse set of protein–ligand complexes: the prediction accuracy of sampling power and scoring power", *Physical Chemistry Chemical Physics*, 2016, **18**, 12964–12975.

(182) G. M. Morris, D. S. Goodsell, R. S. Halliday, R. Huey, W. E. Hart, R. K. Belew and A. J. Olson, "Automated docking using a Lamarckian genetic algorithm and an empirical binding free energy function", *Journal of Computational Chemistry*, 1998, **19**, 1639–1662.

(183) V. Le Guilloux, P. Schmidtke and P. Tuffery, "Fpocket: An open source platform for ligand pocket detection", *BMC Bioinformatics*, 2009, **10**, 168.

(184) O. Y. Fedoroff, A. Rangan, V. V. Chemeris and L. H. Hurley, "Cationic Porphyrins Promote the Formation of i-Motif DNA and Bind Peripherally by a Nonintercalative Mechanism", *Biochemistry*, 2000, **39**, 15083–15090.

(185) S. Kumar, P. Pandya, K. Pandav, S. P. Gupta and A. Chopra, "Structural studies on ligand-DNA systems: A robust approach in drug design", *Journal of Biosciences*, 2012, **37**, 553–561.

(186) NCI, *Available Plates — Drug Synthesis and Chemistry Branch (DSCB) — Developmental Therapeutics Program (DTP)*, 2020, https://dtp.cancer.gov/organization/dscb/obtaining/available_plates.htm (visited on 05/26/2020).

(187) M. Davies, M. Nowotka, G. Papadatos, N. Dedman, A. Gaulton, F. Atkinson, L. Bellis and J. P. Overington, "ChEMBL web services: streamlining access to drug discovery data and utilities", *Nucleic Acids Research*, 2015, **43**, W612–W620.

(188) M. A. Abdelhamid, L. Fábián, C. J. MacDonald, M. R. Cheesman, A. J. Gates and Z. A. Waller, "Redox-dependent control of i-Motif DNA structure using copper cations", *Nucleic Acids Research*, 2018, **46**, 5886–5893.

(189) J. L. Rodgers and W. A. Nicewander, "Thirteen Ways to Look at the Correlation Coefficient", *The American Statistician*, 1988, **42**, 59.

(190) D. J. Rogers and T. T. Tanimoto, "A Computer Program for Classifying Plants", *Science*, 1960, **132**, 1115–1118.

(191) D. Rogers and M. Hahn, "Extended-Connectivity Fingerprints", *Journal of Chemical Information and Modeling*, 2010, **50**, 742–754.

(192) D. E. Patterson, R. D. Cramer, A. M. Ferguson, R. D. Clark and L. E. Weinberger, "Neighborhood behavior: A useful concept for validation of 'molecular diversity' descriptors", *Journal of Medicinal Chemistry*, 1996, **39**, 3049–3059.

(193) G. Maggiora, M. Vogt, D. Stumpfe and J. Bajorath, "Molecular Similarity in Medicinal Chemistry", *Journal of Medicinal Chemistry*, 2014, **57**, 3186–3204.

(194) P. Spence, *GitHub - philspence/gendock: Python package for virtual screening of small molecules to macromolecules*, 2020, https://github.com/philspence/gendock (visited on 02/05/2020).

(195) W. S. Wade, M. Mrksich and P. B. Dervan, "Design of peptides that bind in the minor groove of DNA at 5'-(A,T)G(A,T)C(A,T)-3' sequences by a dimeric side-by-side motif", *Journal of the American Chemical Society*, 1992, **114**, 8783–8794.

(196) S. White, J. W. Szewczyk, J. M. Turner, E. E. Baird and P. B. Dervan, "Recognition of the four Watson–Crick base pairs in the DNA minor groove by synthetic ligands", *Nature*, 1998, **391**, 468–471.

(197) T. Zhu, S. Cao, P.-C. Su, R. Patel, D. Shah, H. B. Chokshi, R. Szukala, M. E. Johnson and K. E. Hevener, "Hit Identification and Optimization in Virtual Screening:

Practical Recommendations Based on a Critical Literature Analysis", *Journal of Medicinal Chemistry*, 2013, **56**, 6560–6572.

(198) J.-F. Truchon and C. I. Bayly, "Evaluating Virtual Screening Methods: Good and Bad Metrics for the "Early Recognition" Problem", *Journal of Chemical Information and Modeling*, 2007, **47**, 488–508.

(199) C. Hélène, "Reading the minor groove", *Nature*, 1998, **391**, 436–438.

(200) K. M. Rahman, K. Tizkova, A. P. Reszka, S. Neidle and D. E. Thurston, "Identification of novel telomeric G-quadruplex-targeting chemical scaffolds through screening of three NCI libraries", *Bioorganic & Medicinal Chemistry Letters*, 2012, **22**, 3006–3010.

(201) Y. Chen and D. Yang, "Sequence, Stability, and Structure of G-Quadruplexes and Their Interactions with Drugs", *Current Protocols in Nucleic Acid Chemistry*, 2012, **50**, DOI: 10.1002/0471142700.nc1705s50.

(202) A. Hazra, "Using the confidence interval confidently", *Journal of Thoracic Disease*, 2017, **9**, 4124–4129.

(203) I. P. Evans, A. Spencer and G. on, "Dichlorotetrakis(dimethyl sulphoxide)ruthenium(II) and its use as a source material for some new ruthenium(II) complexes", *Journal of the Chemical Society, Dalton Transactions*, 1973, **0**, 204.

(204) M. A. Bennett, T.-N. Huang, T. W. Matheson, A. K. Smith, S. Ittel and W. Nickerson, in *Inorganic Syntheses*, John Wiley & Sons, Ltd, 2007, pp. 74–78.

(205) C. White, A. Yates, P. M. Maitlis and D. M. Heinekey, in *Inorganic Syntheses*, John Wiley Sons, Ltd, 2007, pp. 228–234.

(206) *Rigaku Corporation, CrysAlisPro (Version 1.171.40.68a)*, Tokyo, Japan, 2019.

(207) G. M. Sheldrick, "SHELXT – Integrated space-group and crystal-structure determination", *Acta Crystallographica Section A Foundations and Advances*, 2015, **71**, 3–8.

(208) O. V. Dolomanov, L. J. Bourhis, R. J. Gildea, J. A. K. Howard and H. Puschmann, "OLEX2 : a complete structure solution, refinement and analysis program", *Journal of Applied Crystallography*, 2009, **42**, 339–341.

(209) G. M. Sheldrick, "Crystal structure refinement with SHELXL", *Acta Crystallographica Section C Structural Chemistry*, 2015, **71**, 3–8.

(210) L. J. Farrugia, "ORTEP -3 for Windows - a version of ORTEP -III with a Graphical User Interface (GUI)", *Journal of Applied Crystallography*, 1997, **30**, 565–565.

(211) C. Fonseca Guerra, J. G. Snijders, G. te Velde and E. J. Baerends, "Towards an order-N DFT method", *Theoretical Chemistry Accounts: Theory, Computation, and Modeling (Theoretica Chimica Acta)*, 1998, **99**, 391–403.

(212) E. van Lenthe, E. J. Baerends and J. G. Snijders, "Relativistic regular two-component Hamiltonians", *The Journal of Chemical Physics*, 1993, **99**, 4597–4610.

(213) C. Adamo and V. Barone, "Toward reliable density functional methods without adjustable parameters: The PBE0 model", *The Journal of Chemical Physics*, 1999, **110**, 6158–6170.

(214) S. N. Steinmann and C. Corminboeuf, "Comprehensive benchmarking of a density-dependent dispersion correction", *Journal of Chemical Theory and Computation*, 2011, **7**, 3567–3577.

(215) P. J. Stephens, F. J. Devlin, C. F. Chabalowski and M. J. Frisch, "Ab Initio Calculation of Vibrational Absorption and Circular Dichroism Spectra Using Density Functional Force Fields", *The Journal of Physical Chemistry*, 1994, **98**, 11623–11627.

(216) S. Grimme, S. Ehrlich and L. Goerigk, "Effect of the damping function in dispersion corrected density functional theory", *Journal of Computational Chemistry*, 2011, **32**, 1456–1465.

(217) J. D. Chai and M. Head-Gordon, "Systematic optimization of long-range corrected hybrid density functionals", *Journal of Chemical Physics*, 2008, **128**, 084106.

(218) RDKit, *RDKit is a collection of cheminformatics and machine-learning software written in C++ and Python*, 2006, http://www.rdkit.org (visited on 06/25/2020).

Appendix

A1. The top 59 molecules that were identified in the top 100 for binding in the loop, groove and whole structure searches

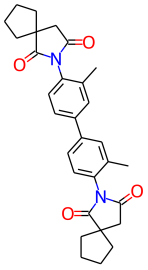

308835

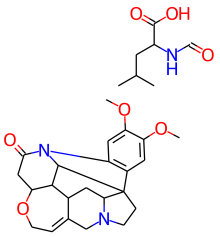

3391

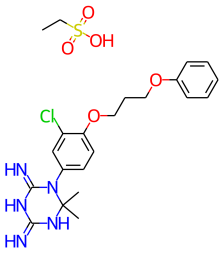

133071

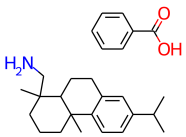

65238

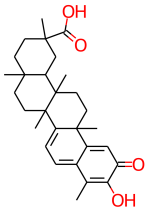

70931

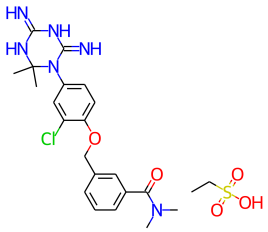

139105

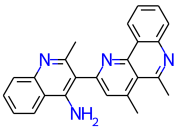

345845

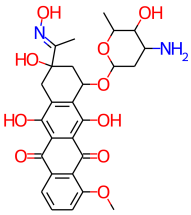

143491

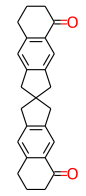

670283

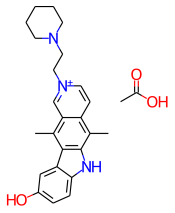

311153

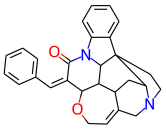

121868

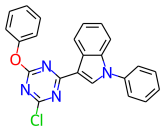

142335

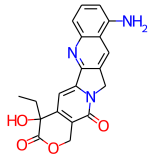

603071

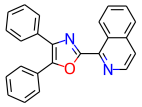

25457

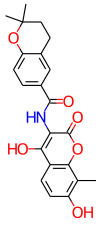

5157

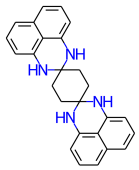

97920

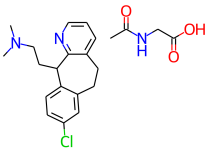

335506

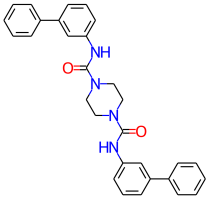

37553

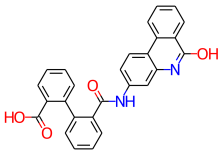

127133

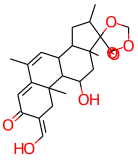

116339

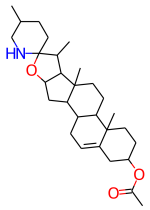

96021

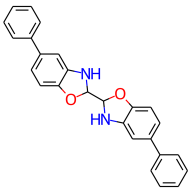

84100

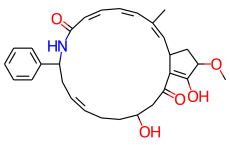

343256

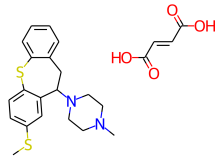

281816

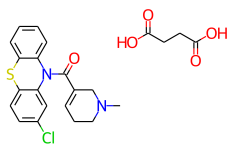

166259

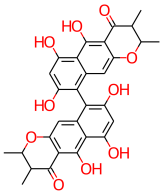

345647

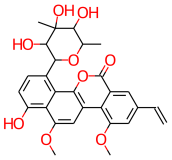

354844

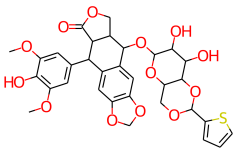

122819

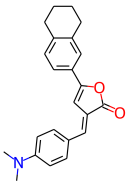

33575

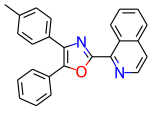

116702

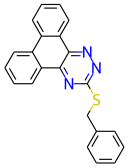

327702

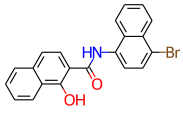

601359

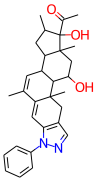

80997

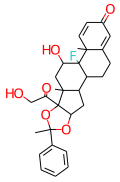

37641

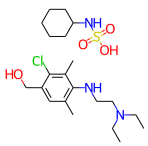

166375

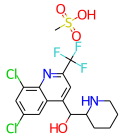

322661

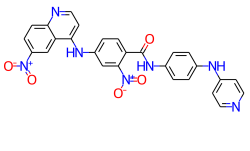

202386

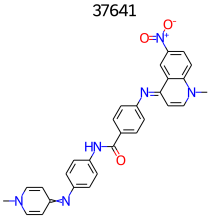

260594

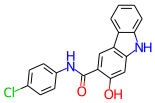

50651

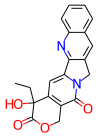

94600

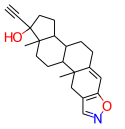

270916

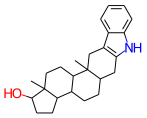

60785

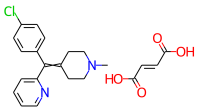

70933

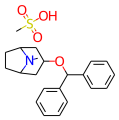

42199

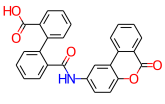

128606

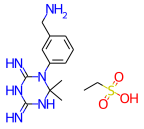

168184

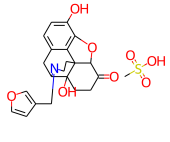

292253

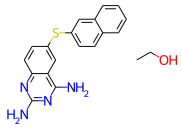

305780

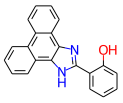

332670

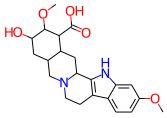

81463

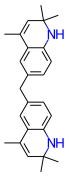

217697

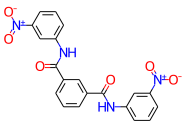

204232

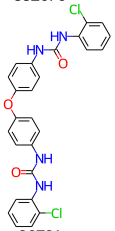

80731

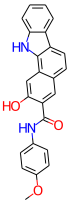

50654

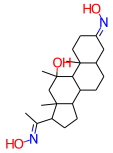

70799

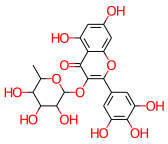

19803

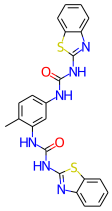

319990

A2. Molecules that appear in the top 100 for binding to the loop but not the groove. Labelled with NSC number

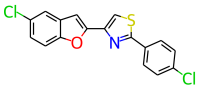

321502

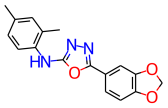

326182

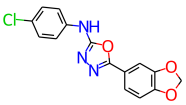

326184

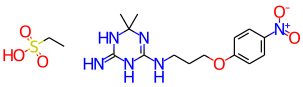

337832

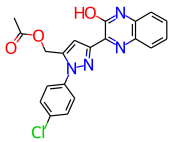

339161

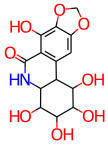

349156

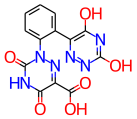

362639

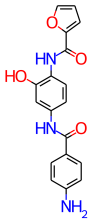

375981

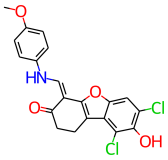

378719

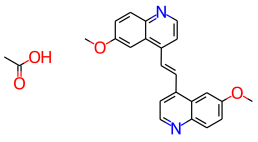

5907

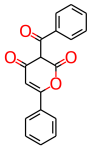

6844

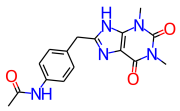

14142

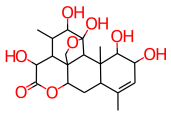

14974

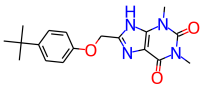

36525

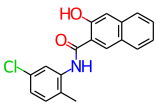

37187

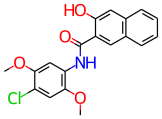

50688

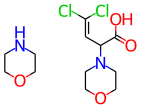

53874

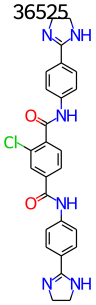

60339

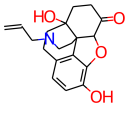

70413

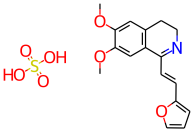

73053

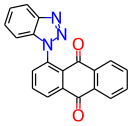

80313

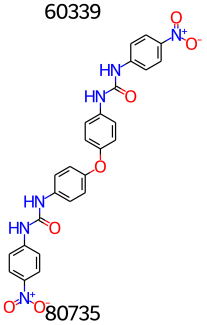

80735

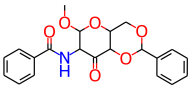

99925

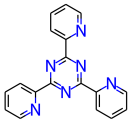

112125

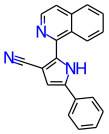

116640

117197

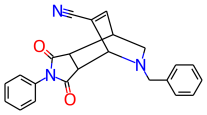

118818

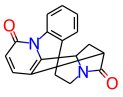

122253

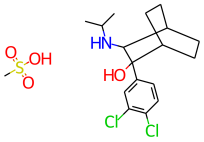

172255

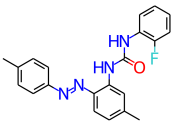

214009

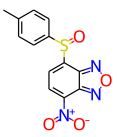

228150

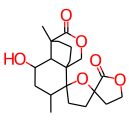

250429

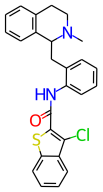

309874

A3. Molecules that appear in the top 100 for binding to the groove but not the loop. Labelled with NSC number

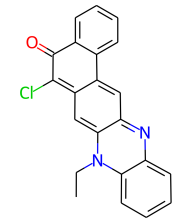

295486

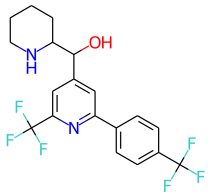

305798

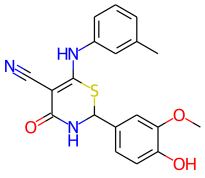

319435

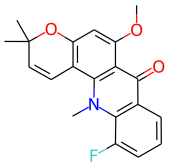

346578

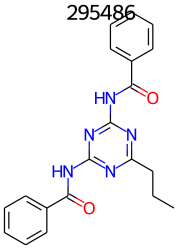

359472

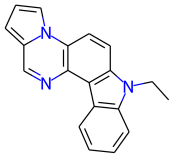

375105

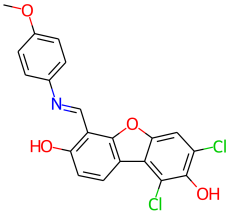

379099

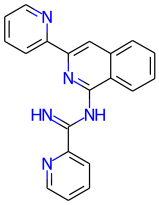

637578

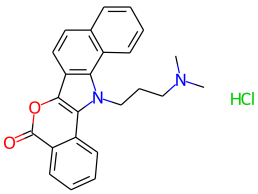

638432

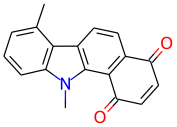

645330

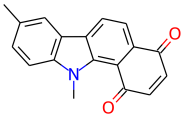

661221

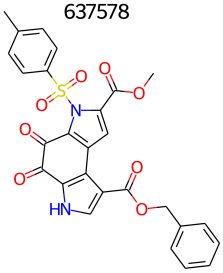

679525

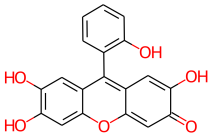

9037

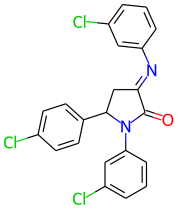

13294

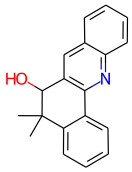

19824

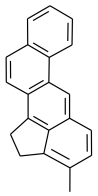

21970

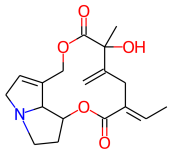

30622

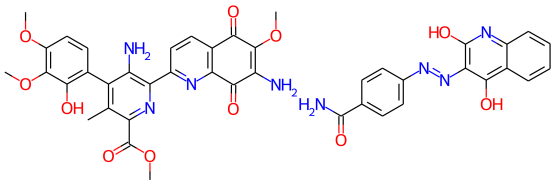

45384

45545

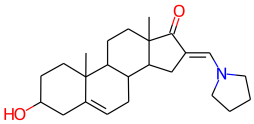

54709

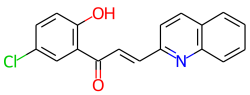

71097

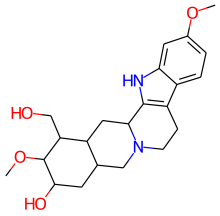

80137

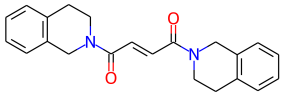

87838

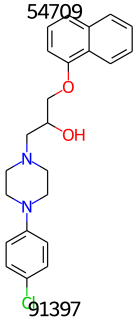

91397

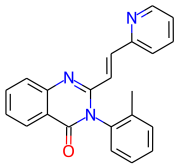

96996

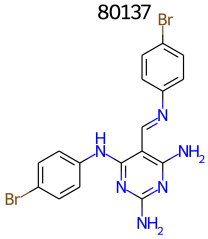

103520

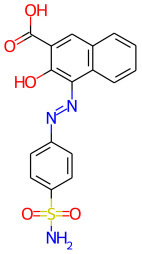

134137

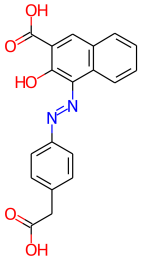

156563

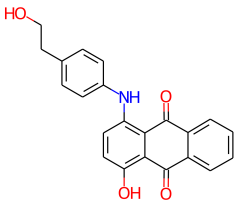

156565

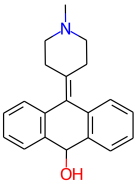

170955

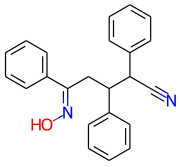

186200

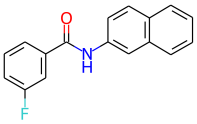

214029

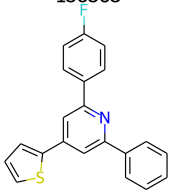

246999

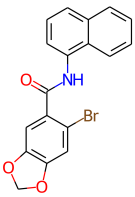

292923

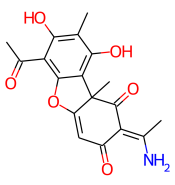

293360

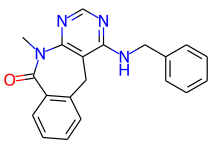

295300

A4. Matches found when searching the ChEMBL library with a Tanimoto similarity ≥0.80, labelled with either the NSC (parent molecule) or the Tanimoto similarity to the parent molecule

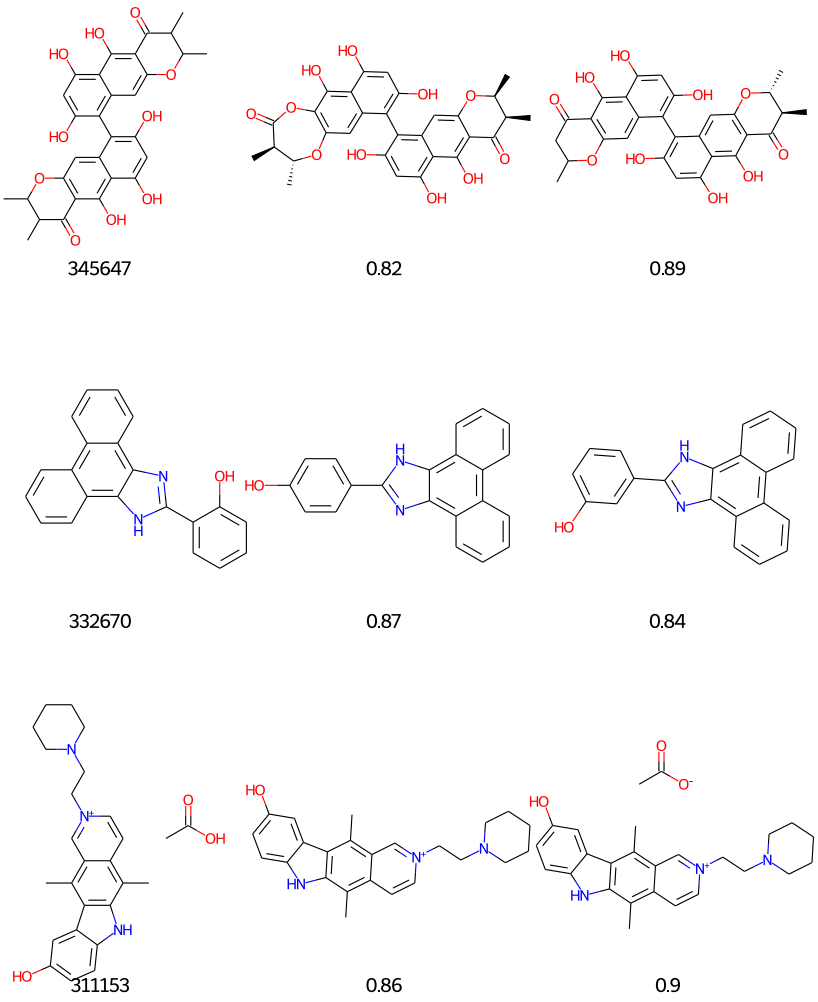

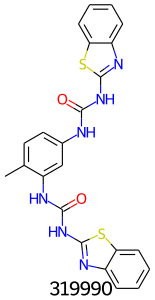

319990

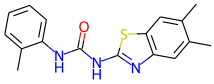

0.81

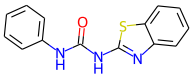

0.82

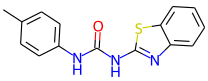

0.88

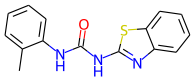

0.94

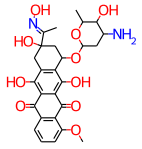

143491

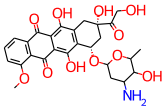

0.88

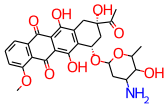

0.91

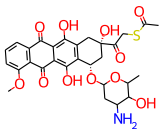

0.83

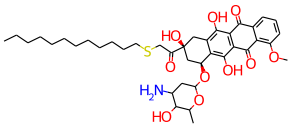

0.8

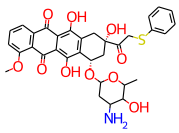

0.84

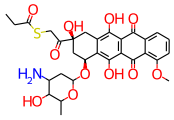

0.82

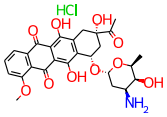

0.89

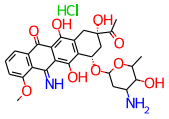

0.8

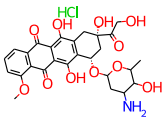

0.86

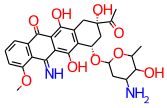

0.81

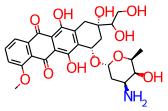

0.82

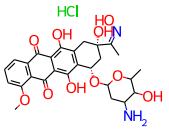

0.98

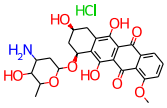

0.85

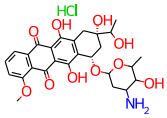

0.84

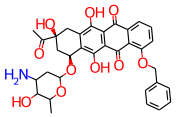

0.81

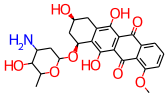

0.87

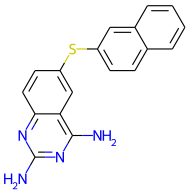

305780

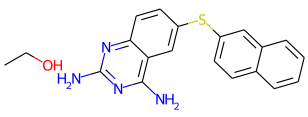

0.84

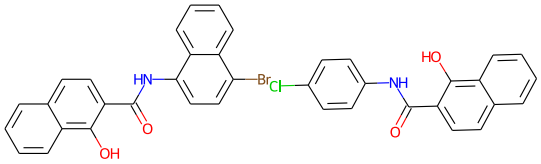

601359

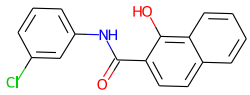

0.82

0.8

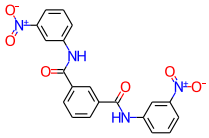

204232

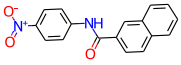

0.81

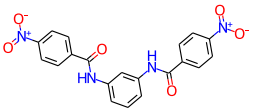

0.89

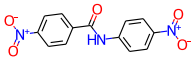

0.89

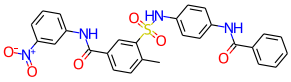

0.82

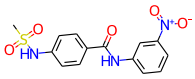

0.84

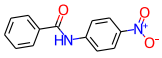

0.93

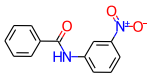

0.96

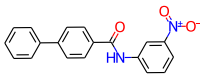

0.87

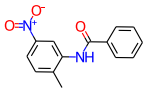

0.8

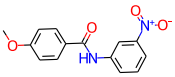

0.81

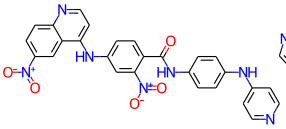

202386

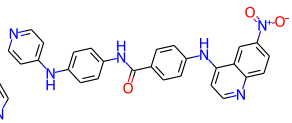

0.91

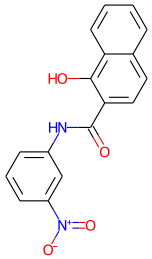

50648

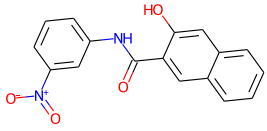

0.84

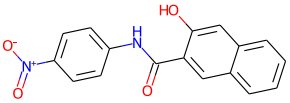

0.81

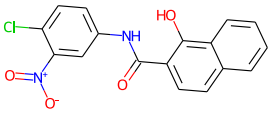

0.8

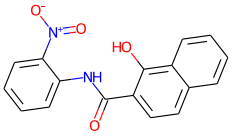

0.86

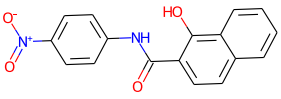

0.97

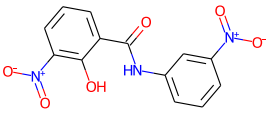

0.81

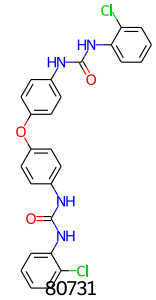

80731

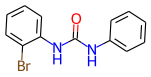

0.83

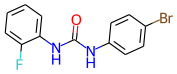

0.8

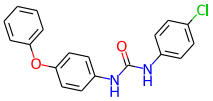

0.88

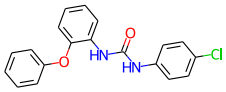

0.81

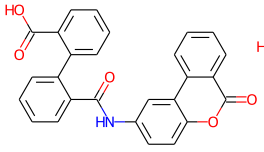

128606

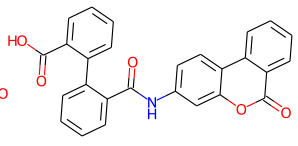

0.93

A5. Crystallographic Table for Δ,*cis*-**1a**

*Table 6.2: Crystallographic Data and Refinement Details for cis-**1a***

Empirical formula	$C_{51.5}H_{38}F_6N_6O_{6.5}Ru$
Formula weight	1059.95
Temperature/K	100.00(10)
Crystal system	trigonal
Space group	$P3_221$
a/Å	14.04740(10)
b/Å	14.04740(10)
c/Å	19.96580(10)
α/°	90
β/°	90
γ/°	120
Volume/Å^3	3412.00(5)
Z	3
ρ_{calc}g/cm^3	1.548
μ/mm^{-1}	3.531
F(000)	1617.0
Crystal size/mm^3	0.64 × 0.3 × 0.21
Crystal Description	Red, block
Radiation	Cu Kα (λ = 1.54184)
2Θ range for data collection/°	7.266 to 139.912
Index ranges	-17 ≤ h ≤ 17, -17 ≤ k≤ 17, -24 ≤ l ≤ 23
Reflections collected	91343
Independent reflections	4315 [R_{int} = 0.0644, R_{sigma} = 0.0148]
Data/restraints/parameters	4315/295/340
Goodness-of-fit on F^2	1.396
Final R indexes [I>=2σ (I)]	R_1 = 0.0920, wR_2 = 0.2658
Final R indexes [all data]	R_1 = 0.0921, wR_2 = 0.2665
Largest diff. peak/hole / e Å^{-3}	1.53/-1.58
Flack parameter	0.064(11)

A6. Crystallographic Table for $[Ni(bqp)_2][PF_6]_2$

Table 6.3: Crystallographic Data and Refinement Details for $[Ni(bqp)_2][PF_6]_2$

Empirical formula	$C_{98}F_{24}N_{12}Ni_2O_2P_4$
Formula weight	2074.4
Temperature/K	99.92(17)
Crystal system	triclinic
Space group	P-1
a/Å	11.1545(2)
b/Å	14.4489(2)
c/Å	14.7629(4)
α/°	89.201(2)
β/°	69.047(2)
γ/°	84.1090(10)
Volume/Å^3	2209.61(8)
Z	1
ρ_{calc}g/cm^3	1.559
μ/mm^{-1}	2.194
F(000)	1020
Crystal size/mm^3	0.3 × 0.1 × 0.07
Crystal Description	Orange, block
Radiation	Cu Kα (λ = 1.54184)
2Θ range for data collection/°	6.152 to 164.188
Index ranges	-14 $\leq$ h $\leq$ 12, -18 $\leq$ k$\leq$ 16, -18 $\leq$ l $\leq$ 18
Reflections collected	39012
Independent reflections	8911 [R_{int} = 0.1071, R_{sigma} = 0.0442]
Data/restraints/parameters	8911/0/640
Goodness-of-fit on F^2	1.023
Final R indexes [I>=2σ (I)]	R_1 = 0.1867, wR_2 = 0.5073
Final R indexes [all data]	R_1 = 0.1922, wR_2 = 0.5098
Largest diff. peak/hole / e Å^{-3}	3.78/-1.15

A7. Crystallographic Table for [Ru($p-$cymene)(bqp)][PF_6]$_2$

Table 6.4: Crystallographic Data and Refinement Details for [Ru(p−cymene)(bqp)][PF_6]$_2$

Empirical formula	$C_{70}H_{64}F_{24}N_8P_4Ru_2$
Formula weight	1799.31
Temperature/K	99.99(10)
Crystal system	triclinic
Space group	P-1
a/Å	12.9131(2)
b/Å	15.4480(3)
c/Å	20.5433(4)
$\alpha/°$	111.131(2)
$\beta/°$	90.657(2)
$\gamma/°$	113.701(2)
Volume/Å^3	3440.88(13)
Z	2
ρ_{calc}g/cm^3	1.737
μ/mm^{-1}	0.649
F(000)	1808.0
Crystal size/mm^3	0.25 × 0.25 × 0.25
Crystal Description	Orange, prism
Radiation	Mo Kα (λ = 0.71073)
2Θ range for data collection/°	3.766 to 62.136
Index ranges	-18 $\leq$ h $\leq$ 18, -22 $\leq$ k $\leq$ 21, -28 $\leq$ l $\leq$ 29
Reflections collected	92139
Independent reflections	18585 [R_{int} = 0.0800, R_{sigma} = 0.0564]
Data/restraints/parameters	18585/0/981
Goodness-of-fit on F^2	1.170
Final R indexes [I>=2σ (I)]	R_1 = 0.1302, wR_2 = 0.3220
Final R indexes [all data]	R_1 = 0.1421, wR_2 = 0.3271
Largest diff. peak/hole / e Å^{-3}	4.59/-1.89

A8. Crystallographic Table for [Ru(benzene)(bqp)][PF_6]$_2$

Table 6.5: Crystallographic Data and Refinement Details for [Ru(benzene)(bqp)][PF_6]$_2$

Empirical formula	$C_{29}H_{21}F_{12}N_3P_2Ru$
Formula weight	802.50
Temperature/K	100.00(10)
Crystal system	monoclinic
Space group	P21/n
a/Å	13.308(4)
b/Å	15.378(4)
c/Å	13.493(4)
α/°	90
β/°	90
γ/°	90
Volume/Å^3	2761.2(14)
Z	4
ρ_{calc}g/cm^3	1.930
μ/mm^{-1}	0.794
F(000)	1592.0
Crystal size/mm^3	0.5 × 0.3 × 0.3
Crystal Description	Orange, irregular
Radiation	Mo Kα (λ = 0.71073)
2Θ range for data collection/°	4.016 to 64.686
Index ranges	-17 $\leq$ h $\leq$ 18, -21 $\leq$ k $\leq$ 22, -17 $\leq$ l $\leq$ 17
Reflections collected	62062
Independent reflections	7751 [R_{int} = 0.0555, R_{sigma} = 0.0232]
Data/restraints/parameters	7751/0/424
Goodness-of-fit on F^2	1.122
Final R indexes [I>=2σ (I)]	R_1 = 0.0777, wR_2 = 0.2073
Final R indexes [all data]	R_1 = 0.0797, wR_2 = 0.2082
Largest diff. peak/hole / e Å^{-3}	6.03/-1.21

A9. Full Crystallographic Data

Attached externally.

A10. Autodock Vina, FID and FRET data for all ligands in the NCI Diversity Set VI Library

Attached externally.